Investigation into calcium regulation and mitochondrial metabolism in chronic myeloid leukaemia

Ahmed Khalaf

BSc, MRes

Thesis submitted to the University of Glasgow in fulfilment of the requirements for the degree of Doctor of Philosophy

School of Cancer Sciences

College of Medical, Veterinary and Life Sciences

University of Glasgow

March 2023

Abstract

Chronic myeloid leukaemia (CML) is a myeloproliferative disease characterised by accumulation of myeloid cells in the bone marrow (BM) and blood circulation. On a molecular level, CML is caused by a chromosomal translocation between chromosome 9 and chromosome 22, resulting in a formation of deformed short chromosome called Philadelphia chromosome. This translocation results in a replacement of a negative regulator domain in Abelson (*ABL*) tyrosine kinase with breakpoint cluster region (*BCR*), leading to constitutive ABL kinase protein activity. Since the BCR::ABL kinase inhibitor imatinib was discovered in 2000, the survival rates of CML patients have dramatically improved. Nevertheless, not only mutations within *BCR::ABL1* limit BCR::ABL inhibitor potency but also the fact that CML is a haematopoietic stem cell (HSC) driven disease (BCR::ABL positive HSCs are referred to as leukaemic stem cells; LSCs). LSCs adopt both intrinsic and BM extrinsic factors to resist current therapy and underpin the disease persistence experienced in the clinic.

It has been previously reported that LSCs rely more on mitochondrial OXPHOS for their survival compared to their normal HSCs counterparts. Targeting such metabolic vulnerability sensitised those LSCs to eradication by BCR::ABL inhibitors. Since current OXPHOS inhibitors have drawbacks in the clinic, such as short half-life or residual side effects, screening for novel and safe OXPHOS inhibitors is critical.

To deliver this approach, the Helgason lab conducted a drug repurposing screen to identify novel OXPHOS inhibitors which can be safely used in clinics. The drug screening analysis identified the Ca^{2+} channel blocker lomerizine as one of the most promising OXPHOS inhibitor. Ca^{2+} is one of the main ions in BM niche and has been shown to catalyse mitochondrial OXPHOS in HSCs. Our transcriptome analysis of LSCs revealed that Ca^{2+} channels such as TRPC6 and CACNA1D are upregulated in CD34+CD38- LSCs when compared with their normal counterparts. Also, stem cell enriched CML CD34+ cells have higher possession of ER mass and subsequent mitochondrial Ca^{2+} level than normal counterparts. Both *in vitro* and *ex vivo* studies using CML cell lines and CD34+ patient samples revealed that imatinib therapy does not affect the CACNA1D and TRPC6 mediated Ca^{2+} influx, which is targeted by lomerizine single treatment or when combined with imatinib. Also, by

deleting genes using clustered regularly interspaced short palindromic repeats (CRISPR) Cas9, results confirmed the reliance of CML on TRPC6 and CACNA1D to provide ER and mitochondria with Ca^{2+} ions as a cofactor for tricyclic acid (TCA) cycle dehydrogenases. An *in vitro* and *ex vivo* metabolomics was performed, cell growth, and stem cell functional assays on CML cell lines and stem cell enriched patient samples that supported the impact of lomerizine on CML through inhibition of mitochondrial Ca^{2+} and impacting metabolism.

In preclinical models of CML, the effective combination between lomerizine and imatinib using well-established CML murine models where combination treatment enhanced survival of mice xenografted with CML KCL22 cells. Also, combination of lomerizine with imatinib significantly decreased level of LSCs in BM of mice transplanted with primary CD34+ CML cells.

Overall, current research showed for first time that Ca^{2+} influx via CACNA1D and TRPC6 is important for OXPHOS in therapy resistant LSCs, rendering them sensitive to the combination of lomerizine, as a Ca^{2+} channel blocker, and imatinib.

Table of Contents

List of Tables

List of Figures

Acknowledgement

First, I appreciate the help of my supervisor, Professor Vignir Helgason for allowing me to join his lab and get the chance to learn down the line all these amazing waves of experience in the pre-clinical field of myeloid leukaemia biology and therapy. I would like to thank everyone in the Helgason lab, especially, Dr Edward Kalman (Eric) who gratefully supported me both personally and professionally. I never had enough words to express how grateful I am for his kind assistance. I would also like to thank Dr Kevin Rattigan for his advice and assistance. Also, this project was a continuation of Dr Lucie De Beauchamp, who was approachable and informative colleague. I am grateful to my close colleague Fei Yan for sharing scientific discussions. I would also thank Dr Joe Jones for his assistance in drafting articles.

I would like to recognise the Paul O'Gorman Leukaemia Research Centre and the Biorepository NHS Research Lab at Queen's Elizabeth Hospital for gathering human samples from our generous donors. Also, many thanks to flow cytometry, mouse house, and metabolomics colleagues at the CRUK Beatson Institute for their dedication to training and experimental management.

I would like to thank my assessors, Professors Chris Halsey, and Kristina Kirschner, for their helpful feedback and encouragement. I would also like to thank Dr Hassan Almasoudi, Abdulkarim Aldosari, Mariana Cendejas Orozco, and Mary Scott (Laboratory of Prof Vetrie D) for their kind help. In addition, I would like to thank Aqeel Faisal Taqi for his contribution to molecular techniques and for being a close friend.

I never forget to acknowledge Dr Ahmed Mohamed Sidky (Professor Darren G. Monckton's lab) for his insightful academic coaching. I would also like to thank my colleague, Ahmed Elshaarrawi, from the University of Tennessee, Knoxville, U.S.A., for our lengthy virtual sessions to analyse bioinformatics data. I would like to thank Mr Hakem Albilasi for the pleasant moments we shared.

I am grateful to Dr Vega Garcia's lab in Madrid, Spain, as well as Prof. Roberta A. Gottlieb and Dr Aleksandr Stotland at Cedars Sinai in the United States, for generously sharing Mito-Timer plasmids. In addition, I'd like to thank Dr Jin Rui Liang and Prof. Jacob Corn lab in Zurich, Switzerland, for providing the Tom20 and ER autophagy reporter constructs, and for their invaluable assistance. I'd like to thank the Newton Musharafa committee for their PhD scholarship.

Lastly, I would like to thank Citadel Capital Holdings (Qalaa Holdings) for their confidence in investing in me to travel and earn my master's degree in 2015-2016 from the University of Nottingham. I would also like to thank Prof. David Heery for overseeing the difficult second half of my master's degree. Without their assistance, I would not have reached this position of success.

In addition to the scientific community, I'd like to thank people on the other side of my life who made me realise that every life matters. I am grateful to my wife, Yasmine Ali, and my children, Mostafa, and Mohamed, for providing home all beautiful days we continuously have sharing. I am honoured to be the father and husband of such a beautiful family.

Many friends and families, like Mr. Ali Bekdash and his beloved family, lived close to me in Maryhill, Glasgow, and made me always feel I was not far from my home. I would also like to thank our pharmacists, Mr. Tariq Sharif and Mr. Abdelqyoum, for their kind help. I will never forget to express my gratitude for Mr. Aras Amin, Mr. Khaled Elbadry, and Mr. Khalifa's good friendship. My sincere appreciation to Ms. Margaret for her tremendous support given to my family.

I would want to thank my friends in Egypt, especially Dr Mohamed Ahmed Abdelrahman, who in this difficult life continually inspires me with his extreme example of true friendship. Additionally, I am appreciative of Mr. Rady Ali Gad and his family for their unwavering support of our young family.

I'd like to thank my friends Mohamed Mouawad Abo Gabal, Ahmed Saad Gholly, Mahmoud Omar Gowhar, Mohamed Refaat Ahmed Ismael, Belal Mohamed Attwa, Mahmoud Abdelhadi Barghout, Ahmed Hamid, and Taha Samir Hamid for being such wonderful, true friends who were with me from elementary school until I graduated from university in Egypt.

I would like to acknowledge my big family, especially my uncles, Eng. Sayed El Khateib, and Mr. Hassaan Abdelmaksoud Khalaf, and my cousin Ahmed Hassan Abdelmaksoud Khalaf, for their support throughout our lives and during difficult times.

I would like to remember family members who passed away before we celebrated this occasion together. Mr. Mohamed Gaber Faisal (Abo Mahmoud), who passed away before I began my doctoral studies. He was a model father, older brother, and loyal supporter. I wish to dedicate this PhD to his spirit and to his family. I would also like to recall my dear sister Doaa Khalaf, whom I have not seen in ten years and who passed away during the time I was writing my thesis. She was truly kind person and very committed to the entire family. Her husband, Farhan Amer, and their young children have my condolences. In addition, I would like to welcome Doaa Mohamed Khalaf, who was born at the same time as her aunt passed away. Finally, I am grateful to my dad who passed away in 18.02.2023, just 10 days after passing my PhD Viva Voce. His spirit will not fade away from our hearts.

My Ph.D. is dedicated to my parents, Mr. Hassanein Abdelmaksoud Khalaf and Ms. Sharbat Korany Ahmed Hassan El Khateib, and to everyone who truly believes that small hands carrying enormous dreams can make them come true.

“We will show them Our signs in the universe and in their own selves, until it becomes manifest to them that this is the truth” (Quran; 41:53).

Author's Declaration

I declare that, except where explicit reference is made to the contribution of others, this dissertation is the result of my own work and has not been submitted for any other degree at the University of Glasgow or any other institution.

Ahmed Khalaf

Abbreviations

ABL	Abelson murine leukaemia virus
ADP	Adenosine diphosphate
AGC	Aspartate glutamate carrier (Aralar citrin shuttle)
ALL	Acute lymphoid leukaemia
AML	Acute myeloid leukaemia
AMP	Adenosine monophosphate
AMPK	Adenosine monophosphate kinase
ANOVA	Analysis of variance
ANT	Adenine nucleotide translocase
APC	Allophycocyanin
ATP	Adenosine triphosphate
AWERB	Animal Welfare and Ethical Review Board
BCA	bicinchoninic acid
BCR	breakpoint cluster region
BM	Bone marrow
BSA	Bovine serum albumin
BVDF	Polyvinylidene fluoride
CaMK	Calmodulin kinase
CCCP	Carbonyl cyanide m-chlorophenyl hydrazone
CCE	Capacitive Ca^{2+} entry
CFC	Colony-forming cells
CLL	Chronic lymphocytic leukaemia
CLP	Common lymphoid progenitor
CML	Chronic myeloid leukaemia
CMP	Common myeloid progenitor
CRISPR	Clustered regularly interspaced short palindromic repeats
CRKL	Crk-like protein
CTV	Cell trace violet
DAG	Diacyl glycerol
DAPI	4′,6-diamidino-2-phenylindole
DMEM	Dulbecco's Modified Eagle Medium
DMSO	Dimethyl sulfoxide
EBSS	Earle's Balanced Salt Solution
ECAR	Extracellular acidification rate
ECL	Enhanced chemiluminescence
EDTA	Ethylenediaminetetraacetic acid
EGTA	Ethylene glycol tetra acetic acid

ELISA	Enzyme-linked immunosorbent assay
EPHOSS	Extra Physiologic Oxygen Shock/Stress
ER	Endoplasmic reticulum
ERAD	ER associated degradation
ETC	Electron transport chain
FACS	Fluorescence-activated cell sorting
FDA	Food and drug administration
FDR	False discovery rate
FMO	Fluorescence minus one
GAPDH	Glyceraldehyde 3-phosphate dehydrogenase
GMP	Granulocytes macrophages progenitors
GPCR	G-protein coupled receptor
GSEA	Gene set enrichment analysis
HBSS	Hank's Balanced Salt Solution
HPC	Haematopoietic progenitor cells
HPLC	High-performance liquid chromatography
HSC	Haematopoietic stem cell
IDH	Isocitrate dehydrogenase
IMDM	Iscove's Modified Dulbecco's Medium
IVIS	In vivo Imaging System
LDH	Lactate dehydrogenase
LPC	Leukaemic progenitor cell
LSC	Leukaemic stem cells
MAM	Mitochondrial associated membrane
MBS	Myristoyl Binding Site
MCU	Mitochondrial Ca^{2+} uniporter
MEP	Megakaryocytes erythrocytic progenitors
MNT	Myristolylated N-terminal
MPP	Multilineage potential progenitor
MTG	Mito-tracker green
NAD+	Nicotinamide adenine diphosphate
NADH	Nicotinamide adenine dinucleotide
NADPH	Nicotinamide adenine dinucleotide phosphate
NES	Normalised enrichment score
NFAT	Nuclear factor of activated T cell
NMP	nucleotide monophosphate
NTP	nucleotide triphosphate
OCR	Oxygen consumption rate
OGC	Oxaloacetate glutamate carrier
OXPHOS	Oxidative phosphorylation

PBS	Phosphate buffered saline
PCA	Principal component analysis
PCR	Polymerase chain reaction
PDH	Pyruvate dehydrogenase
PDX	Patient derived xenograft
PE	Phycoerythrin
PKA	Protein kinase A
PMCA	Plasma membrane Ca^{2+} ATPase
RFP	Red fluorescence protein
RIPA	Radio immunofluorescence precipitation assay
RNA	Ribonucleic acid
ROCC	Receptor operated Ca^{2+} channel
ROS	Reactive oxygen species
RPMI	Roswell Park Memorial Institute
SCF	Stem cell factor
SEM	Standard error of mean
SERCA	Sarco/endoplasmic reticulum Ca^{2+} ATPase
SFM	Serum-free medium
SOCE	Stored operated Ca^{2+} entry
TAE	Tris acetate EDTA
TBST	TRIS-buffered saline tween
TCA	Tricyclic acid
TET	Ten-eleven translocation
TFEB	Transcription factor EB
TKI	Tyrosine kinase inhibitor
TMRM	Tetramethyl rhodamine
TRPC	Transient receptor potential channel
UPR	Unfolded protein response
UV	Ultraviolet
VDAC	Voltage dependent anion channel
VGCC	Voltage gated Ca^{2+} channel
WT	Wild type
αKDH	α ketoglutarate dehydrogenase

1 Introduction

1.1 Haematopoiesis

Haematopoiesis is derived from Greek prefix "*haema*", which means blood, and "*poiesis*", meaning to make. It is continuous generation of blood cell repertoire throughout life [1]. During the first seven weeks of foetal development, *primitive* haematopoiesis occurs in the foetal yolk sac. The foetal liver, spleen, and thymus participate in haematopoiesis for a short period until haematopoietic progenitors reach foetal blood circulation by week 10. Haematopoietic progenitor cells slowly move from blood to the liver, becoming the main organ for performing haematopoiesis until week 16, when they migrate to BM to perform what is called *definitive* haematopoiesis in adults [2, 3]. At cellular level, haematopoiesis is initiated in haematopoietic stem cells (HSCs), which require migration and residing in BM niche or spleen during foetal development. Those HSCs, besides their capacity to self-renew by symmetrical division, can produce heterogenous blood components by asymmetrical division, as first reported by Till and McCulloch in early 60's when they noticed formation of a group of myeloid, erythroid, and megakaryocytic cells " individual colonies" when BM cells were engrafted into sub-lethally irradiated murine hosts [4]. Interestingly, those HSCs were found as a rare population within BM niche at a ratio of 0.05% of total resident cells that can replenish blood circulation with 1.5 million short life span cells, indicating how important those HSCs are [5].

1.1.1 HSCs hierarchy

Since Till and McCulloch established the stem cell and clonal expansion concept, several subsequent studies have helped to accumulate our current knowledge about hierarchical patterns where whole haematopoiesis occurs from a single HSC [6, 7]. The haematopoietic hierarchy begins with HSCs, transforming into lineage-restricted progenitors and terminally differentiated cells. Those HSCs can generate Short-Term HSCs (ST-HSCs) and Long-Term HSCs (LT-HSCs) [8]. LT-HSCs have a high capacity for self-renewal, whereas ST-HSCs have a lower capacity but a higher differentiation potential into multilineage potential progenitor cells (MPPs). LT-HSCs and ST-HSCs are usually found in quiescence until exposed to

stress conditions that push them to wake up and enter cell cycle [9]. Because of LT-HSCs and ST-HSCs' ability to self-renew, they differ from their subsequent MPPs, which have almost no regeneration capacity and are committed to differentiating into oligopotent and unipotent lineage-specific cells. MPPs give rise to common myeloid progenitor cells (CMP) that continue to differentiate into granulocytes, monocytes, macrophages, microglial cells, and dendritic cells. In contrast, common lymphoid progenitor cells (CLP) continue to differentiate into natural killer cells, T cells, and B cells [5, 10] (Figure 1-1).

This classic road map for HSC hierarchy was confirmed by tracing various differentiating cells using chromosomal aberration and foreign gene integration in 1970, followed by establishing a hierarchy based on cell purification by surface markers expression in 1990. However, multiple revisions for hierarchy were done since the 2000s based on data generated from highly developed genetic barcoding, which is also revisited by 2010 using single cell omics profiling [7].

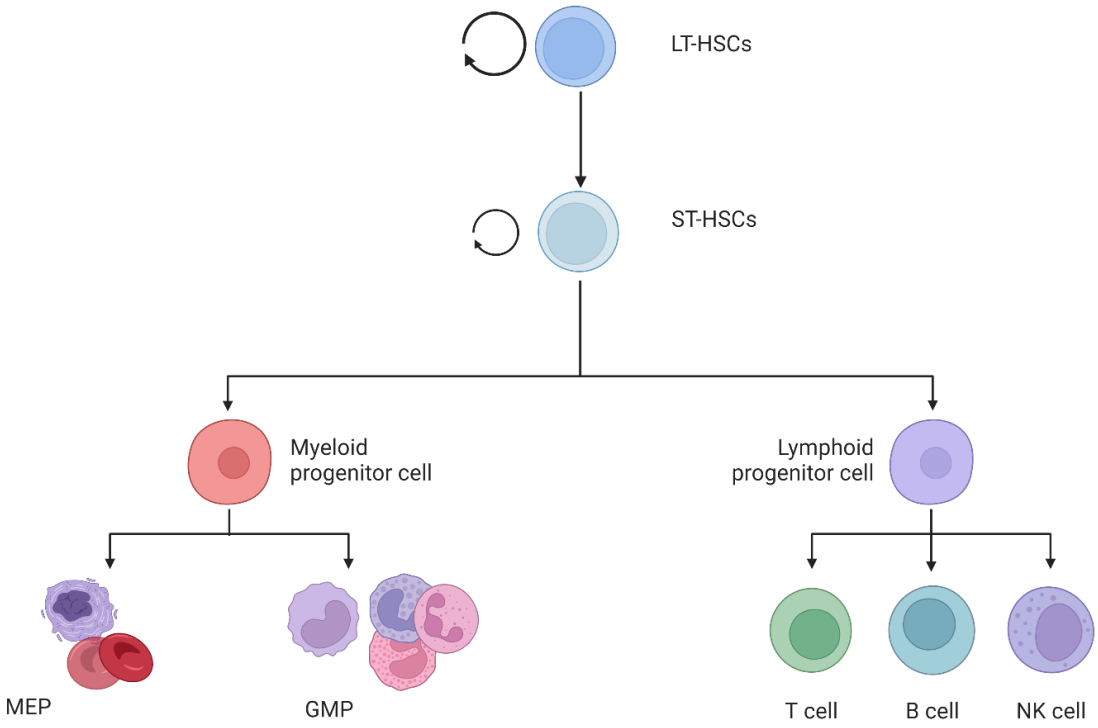

Figure 1-1: Classic roadmap of haematopoiesis.

Classic roadmap of differentiation trajectories of HSCs that set at the top of the haematopoiesis hierarchy. By possessing multipotent stem cell characteristic, HSCs can self-renew and differentiate into either oligopotent common myeloid or lymphoid progenitors (CMP and CLP). Both of CMP and CLP have less self-renew capacity and more prone to differentiate into unipotent blood components that have more definitive short half-life and cannot self-renew themselves, proposing the importance of HSCs for supporting the propensity of blood repertoire throughout life span. Figure is generated using BioRender website.

1.1.2 HSC characterisation

Explicitly addressing characteristics of HSCs necessitated isolating those populations and following up with functional assays. One of cell-specific features is based on unique expression of specific cell surface markers (cluster of differentiation; CD) that are usually proteins integrated into cell membrane and can be identified with flow cytometry. Using flow cytometry/cell sorting, primitive human haematopoietic progenitors and stem cells are enriched in CD34+ population in both adult and foetal BM but not in CD34- population, which is known to participate in HSC pool size and maintenance in BM niche [11, 12]. However, CD34 is not limited to HSCs but is extended to MPPs [13]. Different cell surface markers have been used to demonstrate HSC in CD34+ populations from different haematopoietic organs. HSCs from both foetal and adult BM express CD38 at very low levels [14]. However, CD38 is not a perfect marker to specify HSCs because the broad expression makes it difficult to select or isolate HSCs. Other surface markers have been expressed explicitly in HSCs, such as CD133, CD90, and EPCR (CD201) [15].

In order to characterise HSCs *in vitro,* coculturing HSCs in a layer of adherent stromal cells in a plate will provide HSCs with growth factors they require for long-term HSC maintenance as seen by differentiating into different specific colonies based on their self-renewal potential in long-term cultured media [16]. The long-term colony-initiating cell (LTC-IC) assay allows investigation of BM cell cultures. The stem cells are treated and then replated in a semi-solid growth medium. The stem cells will produce colonies after 5-8 weeks, which are subsequently quantified [17]. Without stromal support, HSC can also form colonies in liquid or semi-solid cultures. In these cultures, different cytokine combinations are utilised to encourage proliferation or maintenance of progenitor cells, an assay known as colony-forming cell assay (CFC) [18]. However, in culture, HSCs do not achieve same self-renewal or differentiation as *in vivo*. Given that HSCs can perform haematopoiesis, HSCs can recapitulate BM niche with blood progenitors within 10-14 days of transplantation after stress conditions such as irradiation [19]. This enables researchers to investigate *in vivo* BM repopulating capacity of HSCs in sub-lethally irradiated (often immunocompromised) mice.

Therefore, HSCs are at inception of a crucial process, and there is tight control over their ability to self-renew and differentiate. Despite haematopoiesis being a

tightly regulated process, it is also highly vulnerable to dysfunction if the integrity of HSCs is compromised.

1.2 Ca^{2+} homeostasis

Ca^{2+} is a ubiquitous element found in human body, where 1-1.5 kg of it exists, comprised of 99% in bone and 1% in fluid [20]. When the level of Ca^{2+} in the blood becomes lower than standard level, parathyroid hormone (PTH) is secreted to generate the active form of vitamin D3 (calcitriol). Because of this, Ca^{2+} is absorbed from intestine through calbindin (expressed in response to calcitriol transcriptional activity). Calcitriol, acidity, and amino acids such as arginine and lysine increase intestinal Ca^{2+} absorption. Ca^{2+} in blood is usually found bound to a variety of proteins or in free ionised Ca^{2+} forms. The level of Ca^{2+} in blood is regulated through binding to albumin transporter protein. However, it is not only albumin that determines Ca^{2+} levels. Further, Matrix γ-carboxyglutamic acid (GLA) protein is another Vitamin K2 dependent protein that binds to and regulates Ca^{2+} deposition to arterioles or cartilage [21]. Alkalinity enhances Ca^{2+} protein binding, and acidity induces Ca^{2+} ionisation [22]. When blood Ca^{2+} exceeds 10 mg/dL, the thyroid hormone calcitonin inhibits PTH release, leading to renal tubules quickly excreting the surplus. Ca^{2+} functions in muscle contraction, nerve conduction, and secretion of hormones such as insulin and vasopressin. Ca^{2+} is also known as factor IV when it is chelated by gamma carboxyl group of glutamic acid residues of prothrombin, which convert to thrombin required for coagulation. Vitamin K enhances this process through post-translational carboxylation of glutamic acid residues of prothrombin. The exact mode of action found in anticoagulants, such as EDTA, which also chelates Ca^{2+} ions.

1.2.1 Intracellular Ca^{2+} homeostasis

There are various mechanisms by which intracellular Ca^{2+} levels are regulated. In a steady-state, the concentration of Ca^{2+} in cytosol and mitochondria is extremely low (~100nM) [23]. The ER stores up to 100 times Ca^{2+} found in the rest of the cell [24]. As shown in Figure 1-2, extracellular Ca^{2+} levels are usually higher than intracellular levels, and the plasma membrane is impermeable to Ca^{2+} diffusion unless cells become activated by altering membrane voltage, which results in voltage gated Ca^{2+} channel (VGCC) activation [25]. Mobilisation of Ca^{2+} from ER to

cytosol occurs through phospholipase C (PLC), a cytosolic enzyme that degrades plasma membrane phosphatidylinositol diphosphate (PIP2) into diacylglycerol (DAG) and inositol triphosphate (IP3) [26]. In turn, IP3 bind to its ligand gated Ca^{2+} channel (IP3R) on ER membrane, causing mobilisation of Ca^{2+} to cytosol. The junction between ER and mitochondria is called mitochondrial associated membrane (MAM), which links mitochondrial voltage dependent Ca^{2+} channel (VDAC) with IP3R through glucose-regulated protein 75 [27]. The release of Ca^{2+} by IP3R to MAM forms a Ca^{2+} microdomain with a higher Ca^{2+} concentration, from which Ca^{2+} diffuses to mitochondria. In turn, mitochondrial Ca^{2+} level spikes 10-20 fold more than cytosolic level [23]. Mitochondrial Ca^{2+} uptake requires sustained Ca^{2+} release from ER [28]. Ca^{2+} can also get transferred from ER to nuclear pores (Ca^{2+} microdomain of nucleoplasm) [29]. Depleted ER Ca^{2+} stores are sensed by STIM1 on the surface of ER. Stored operated Ca^{2+} entry (SOCE) allows refilling of depleted ER stores when STIM1 EF-hand domain associates with and activates ORAI1 (Ca^{2+} release activated channel protein 1), which is located on plasma membrane [30]. PLC can also activate other receptor operated Ca^{2+} channels (ROCC), such as transient receptor potential cation subfamily C (TRPC). ROCC allows Ca^{2+} influx through DAG mediated confirmational changes, which allow Ca^{2+} influx [31, 32]. TRPC1 has been reported to co-assemble with STIM1 in response to depleted ER stores, which complicates our understanding of SOCE activity [33]. Not only do plasma membrane and ER increase cytosolic Ca^{2+} levels, but lysosomal vesicles also mobilise Ca^{2+} to cytosol through its MCOLN1 receptors [34].

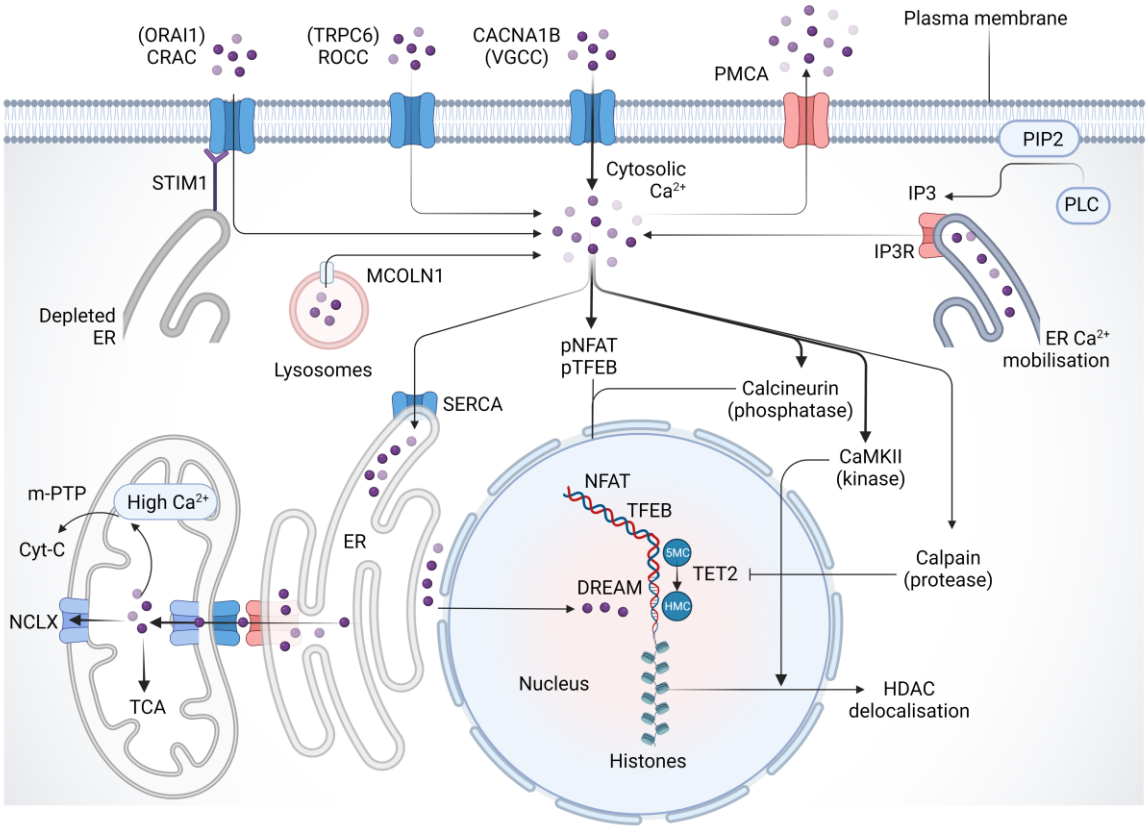

Figure 1-2: Cellular Ca^{2+} signalling in mammalian cells.

Ca^{2+} ions enter cytosol through plasma membrane channels such as VGCC. PLC produces IP3, responsible for mobilising Ca^{2+} from ER to either cytosol or through MCU and VDAC axis to mitochondria. As a response to ER Ca^{2+} depletion, STIM1 on ER interacts with ORAI1 on plasma membrane to allowing an influx of Ca^{2+} into cytosol. Ca^{2+} can also get transferred to nucleus, mainly through nucleoplasm microdomain between ER and nuclear pores. Lysosomes are reported to allow Ca^{2+} release to cytosol through MCOLN1. The intracellular Ca^{2+} activates calcineurin, which is required for dephosphorylation and colocalising transcriptional factors to nucleus, for example, NFAT and TFEB. Ca^{2+} binds to and activates calmodulins, which are required for cell cycle progression and delocalisation of HDAC out of nucleus. Another important Ca^{2+} binding protein is calpain, which degrades TET2 enzymes that convert 5 methyl cytosines on histones to 5 hydroxy methyl cytosine. Ca^{2+} can also directly bind to DREAM transcriptional repressor factor. However, Ca^{2+} overload is harmful to cells, as it can activate mitochondrial PTP, ultimately leading to apoptosis. Thus, cytosolic Ca^{2+} can direct different fates: either it replenishes SERCA, it can activate cytosolic signalling, or it gets pumped out of cell through PMCA. Figure is generated using BioRender website.

1.2.2 VGCC channels

The plasma membrane possesses various categories of Ca^{2+} channels. VGCCs are plasma membranes of distinct subunits: α1, β, and γ. The ion-conducting pore is formed by one of the α1 subunits, whereas the accompanying β and γ subunits have a variety of roles, including gating modulation [35]. The VGCC opens once electrical and chemical gradients differ between extracellular and intracellular components. When this occurs, the concentration of Ca^{2+} passively changes up to 100-fold in cytosol [25]. VGCCs have been categorised according to their capacity to keep Ca^{2+} current. For instance, long (L-VGCC) requires higher depolarisation and is kept open longer, whereas transient (T-VGCC) requires lower voltage and loses its activity faster compared to L-VGCC [25]. Scientists categorised VGCC according to their α subunit (Table 1-1) [25]. The auxiliary subunits, such as CACNβ1-4, facilitates or activate pore-forming unit activity instead [36]. Studies also reported that expression of CACNA1D could not elicit Ca^{2+} influx without co-expression of CACNβ2 in *Xenopus* oocytes [37]. To go further, co-expression of β3 stimulates α1-mediated Ca^{2+} flux in the same manner as β1/β2 in *Xenopus* oocytes [38]. Huang *et al*. hinted at interaction between CACNβ4 and CACNA1D [39]. Their study confirmed the overexpression of CACNβ4 and its role in regulating Ca^{2+} flux, which was affected by splice variants of Cav1.3 [39]. A different study showed that dihydropyridine (DHP) inhibitor isradepine selectively inhibited CACNA1D and also inhibited the ability of β subunits to reverse this effect [40]. Surprisingly, the interaction of the Cav1.3 (CACNA1D) channel with the auxiliary β subunits is crucial for their plasma membrane localisation. This was revealed when exogenously expressed cav1.3 showed a significant increase in surface localisation when heterologous β4-subunits were overexpressed by four folds in Hippocampal Dendritic Spines [41].

Table 1-1: Different types of VGCC.

Channel	Other names	Type	Voltage	DHP[1]
Cav1.1	CACNA1S	L	High	Sensitive
Cav1.2	CACNA1C	L	High	Sensitive
Cav1.3	CACNA1D	L	High	Sensitive
Cav1.4	CACNA1F	L	High	Sensitive
Cav2.1	CACNA1A	P/Q (Purkinje)	High	Resistant
Cav2.2	CACNA1B	N (neural)	High	Resistant
Cav2.3	CACNA1E	R (residual)	Intermediate	Resistant
Cav3.1	CACNAIG	T	Low	Resistant
Cav3.2	CACNA1H	T	Low	Resistant
Cav3.3	CACNA1I	T	Low	Resistant

The table is adapted from [25, 42].

1.2.3 TRPC channels

PLCγ stimulation can activate TRPC channels in general, with certain members also being activated by diacylglycerols, for example, TRPC3 and TRPC6 [31]. G-protein coupled receptors are activated by pathological stress or hypertrophic agonists, causing PLC to produce DAG and inositol triphosphate (IP3) [26]. IP3 stimulates the release of Ca^{2+} from internal reserves and Ca^{2+} influx via TRPC. When intracellular Ca^{2+} reaches a certain level, calcineurin/NFAT pathway is activated. NFAT is translocated into nucleus and causes additional TRPC genes to be transcribed [26]. The activation of TRPC in response to the emptying of ER Ca^{2+} stores is known as capacitive Ca^{2+} entry (CCE) or stored operated Ca^{2+} entry (SOCE) [32]. To examine this phenomenon, scientists have previously stimulated ER Ca^{2+} depletion with sarco/endoplasmic reticulum Ca^{2+} ATPase (SERCA) receptor inhibitor (thapsigargin) [43] or ionophores that stimulate emptying of ER such as ionomycin to measure the extent of CCE. Three hypotheses may explain how ER depletion leads to the activation of CCE. The first is the direct link between activated IP3R or ryanodine (RYR) receptors on ER and TRP. The second mechanism is the presence of a diffusible second messenger from stimulated ER that triggers SOCE or CCE. The third option is TRP vesicle fusion with plasma membrane bilayer in response to ER depletion [44].

---

[1] DHP stands for 1,4-dihydropyridine Ca^{2+} channel blockers.

1.2.4 Intracellular Ca^{2+} signalling

The amplitude and duration of intracellular Ca^{2+} spikes determine a specific Ca^{2+} mediated signalling output [45]. For example, numerous cellular proteins bind Ca^{2+} ions, which affects their function, including EF-hand S100A proteins, calcineurin phosphatase, and calmodulins [46]. When Ca^{2+} binds to calcineurin, it dephosphorylates NFAT (nuclear factor of activated T cells), resulting in NFAT nuclear translocation. Subsequently, NFAT induces transcription of various genes involved in physiological and developmental processes [47, 48]. Calcineurin also participates in the dephosphorylation and nuclear translocation of TFEB, a master transcriptional factor of autophagy genes [49]. Calmodulin is another Ca^{2+} binding protein that leads to the recruitment of a series of other kinases involved in many processes, including cell cycle progression [50]. Ca^{2+} participates in histone acetylation modification through histone deacetylases (HDACs) delocalised out of nucleosomes, mainly through CaMKII involvement [51]. Ca^{2+} regulates many biological processes as a second messenger through interactions with various Ca^{2+} binding proteins, such as S100A proteins [52]. The EF-hands S100 protein family regulates proliferation, differentiation, cytoskeleton dynamics, stress response and apoptosis and its members are expressed in a cell-specific pattern [53]. Calpains are a group of proteases activated by Ca^{2+} ions, which degrade TET2 enzyme [54]. The TET family is composed of 3 isoforms that hydroxylate 5 methyl cytosine (5 MC) into 5 hydroxy methyl cytosine (5 HMC), which is known to demethylate cytosine DNA residues [55]. Autophagy has also been reported to get regulated by Ca^{2+} signalling. This regulation occurs through different mechanisms, including TFEB-induced expression of autophagy genes and adenosine monophosphate kinase (AMPK), the main driver of ULK1-mediated autophagy [56, 57]. Transcriptional regulation of DNA through direct binding of Ca^{2+} to transcriptional repressor called DREAM has also been reported [58]. The nuclear factor of activated T cell isoform 4 (NFAT4) requires an additional nuclear Ca^{2+} wave to become fully activated [47]. Ca^{2+} plays an important role in metabolism and energy supply. A Ca^{2+} overload leads to unfavourable cycling and differentiation of various stem cells [59]. Therefore, cells must maintain a homeostatic Ca^{2+} level actively. One-way cells can remove Ca^{2+} is through plasma membrane efflux pumps (PMCAs) that actively pump a large Ca^{2+} gradient from cytosol out of the cell [60]. In addition, ER Ca^{2+} ATPase pumps (SERCA) also

transport Ca^{2+} into ER sheets [61]. Thus, an increased understanding of the Ca^{2+} signalling in the maintenance or expanding of HSCs and its dysregulation that may lead to or correlate to blood malignancies is a topic of interest.

1.3 HSC maintenance and Ca^{2+}

Microscopy of intravascular and interstitial BM of the skull calvarium bone by SC Yeh *et al*. showed that extracellular Ca^{2+} distribution *in vivo* ranges from 0.5 to 1.6 mM [62]. They found that HSCs reside in BM domains with elevated Ca^{2+} levels (0.8 - 1.6 mM) without existence in domains with low Ca^{2+} levels [62].

This raises the question of whether BM extracellular Ca^{2+} plays a role in maintaining HSCs (Figure 1-3). Early evidence highlighted a role for BM Ca^{2+} in supporting HSC engraftment to BM niche. The current understanding is that BM Ca^{2+} is sensed by Ca^{2+} sensing receptors required for migration and adhesion of HSCs in BM niche [63]. CXCR4 also mediates HSC adhesion to BM niche [63-65]. Schajnovitz *et al*. revealed that the secretion of CXCR4 ligand (CXCL12) from resident stromal cells occurs in a Ca^{2+} dependent fashion [66]. This supports proper haematopoiesis after birth due to the prerequisite of foetal liver stem cells migrating to BM to generate HSCs and initiate haematopoiesis [67]. Mice lacking Ca^{2+} sensing receptors were found to die at 7-10 days after birth [63]. Besides CXCL12 secretion, BM Ca^{2+} interacts with progenitors to inhibit further HSC cycling and exhaustion.

Furthermore, Kelly *et al*. reported that cytosolic Ca^{2+} is responsible for secretion of antigen-stimulated interleukin 10 (IL10) in human macrophages [68]. IL10 release from these myeloid/monocytes subsequently leads to the activation of IL10 ß receptor on HSCs (IL10Rß), which halts HSC myeloid commitment or differentiation [69]. This suggests another protective role of extracellular Ca^{2+} against HSC pool exhaustion and placement of Ca^{2+} as a coordinator between HSCs and haematopoietic progenitors to decide on HSC proliferation or quiescence.

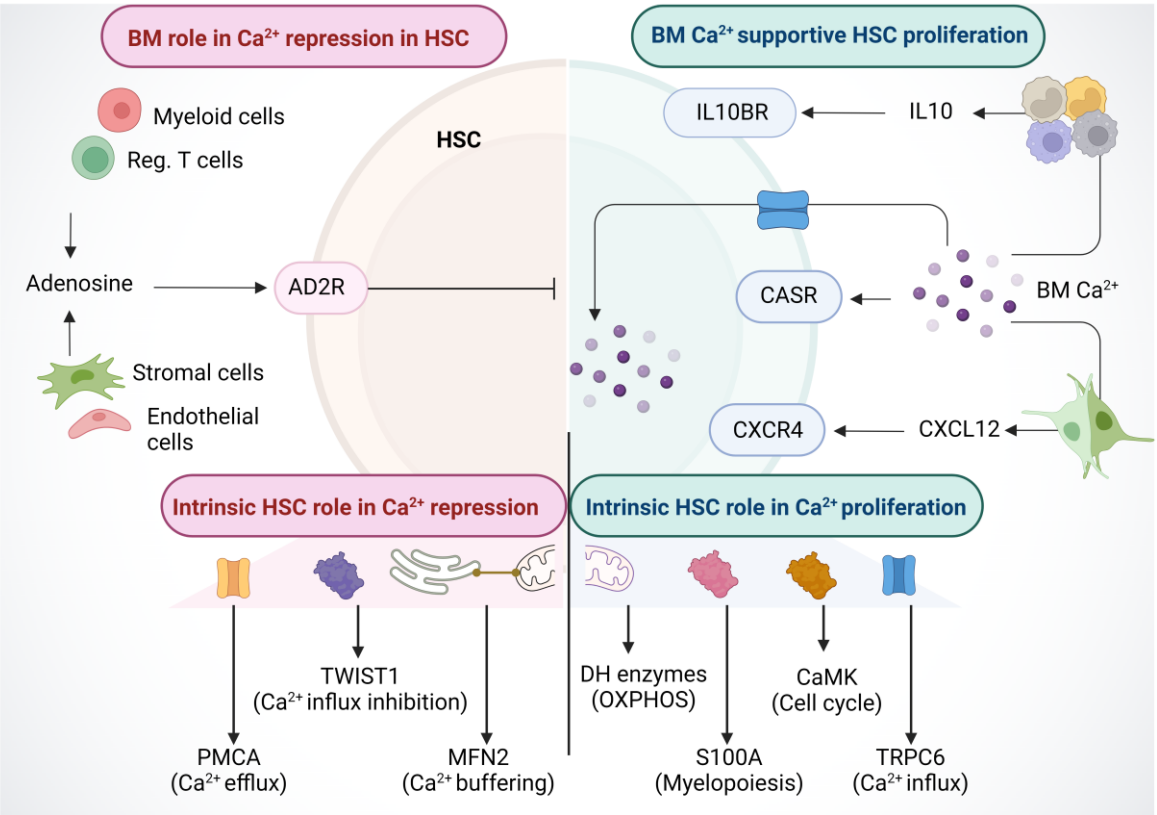

Figure 1-3: BM regulates HSC maintenance.

There is a bidirectional crosstalk role between Ca^{2+} in BM and BM signalling that helps in HSC maintenance. For instance, BM Ca^{2+} mediates the maintenance of HSCs by regulating secretomes in BM niche, such as, IL10 secretion from monocytes and CXCL12 from BM stromal cells. The BM Ca^{2+} defines the level of intracellular Ca^{2+} of HSCs, which then triggers Ca^{2+} mediated signalling required for proliferation and cell cycling. The BM niche also regulate the extent of Ca^{2+} influx to HSCs to avoid exhaustion of HSCs. For instance, adenosine secretion from resident cells binds to adenosine receptors (AD2R) on HSCs which represses Ca^{2+} influx. At intracellular level, HSCs itself could use Ca^{2+} signalling to induce mitochondrial respiration, perform myelopoiesis through S100A proteins, or induce cell cycle through calmodulins. However, HSCs can also inhibit intracellular Ca^{2+} signalling by buffering this Ca^{2+} into ER and mitochondria tethered by MFN2, upregulation of TWIST1 protein that inhibits CACNA1B Ca^{2+} influx or pumping out Ca^{2+} by PMCA. This maintains HSC Ca^{2+} signalling through BM niche and intracellular arms. Figure is generated using BioRender website.

1.3.1 HSCs and Ca^{2+} *in vivo*

Findings by Luchsinger and Fukushima could raise the role BM niche plays in supporting HSCs proliferation signalling through modulating Ca^{2+} influx to avoid exhausting HSCs. For instance, changes in BM niche, such as increased production of growth factors and cytokines and transplantation procedures and injuries, can stimulate HSCs to cycle or remain dormant. Fukushima *et al*. suggested that HSCs can switch between quiescence and cycling *in vivo,* which is impossible *in vitro* due to loss of dormancy in 40 hours *in vitro* [70, 71]. Some studies revealed that resident progenitors play the switch between active and dormant state through regulating Ca^{2+} level. A2 adenosine receptors repressed Ca^{2+} influx by inhibiting L-VGCCs [72]. Umemoto *et al*. showed that myeloid progenitors significantly reduced intracellular Ca^{2+} levels and mitochondrial potential (ΔΨm) in HSCs because myeloid cells secrete adenosine, leading to the induction of HSC A2 adenosine receptors [73]. Without adenosine, 5-FU induces Ca^{2+} influx with subsequent HSC exhaustion. Similarly, BM resident regulatory T lymphocytes inhibit HSC exhaustion through CD73/CD93 that convert AMP into adenosine in BM niche, promoting HSC quiescence and enhancing allogenic HSC engraftment after transplantation [74]. Sinusoidal endothelial and mesenchymal stromal cells also highly express CD73, which is critical for HSC maintenance [75].

Hypoxia is another dimension of BM niche that helps in maintaining HSCs. The long-term function of hypoxia-inducible factor-1α (HIF-1 α), a transcriptional factor that drives cellular signalling in response to hypoxia through slowing LT-HSCs [76, 77]. Technically, HSCs are commonly found in hypoxic BM niche, usually not considered during culturing and assays *in vitro*. Even those HSCs examined under low oxygen (0.1-5 % O_2) are collected in ambient air and exposed to Extra Physiologic Shock and Stress (EPHOSS) [78]. Mantel *et al*. discovered that number of HSCs and progenitors and their functions are enhanced when cells are collected and processed in 3% O_2 and never exposed to ambient air oxygen level [79]. HIF-1α stabilisation shifts HSC metabolism towards glycolysis, ensuring reduced reactive oxygen species (ROS) generation [80]. This begs the research question of whether EPHOSS alters Ca^{2+} levels and allows Ca^{2+} signalling to drive differentiation, and those of low Ca^{2+} levels similarly mitigate EPHOSS stress response.

1.3.2 HSCs maintenance in low Ca^{2+} *in vitro*

Luchsinger *et al*. showed that culturing HSCs at low Ca^{2+} levels (0.02 mM CaCl2) maintain lower intracellular Ca^{2+}, and this enhances HSCs repopulating capacity when these are engrafted into the murine model (Figure 1-4). The low extra and intracellular Ca^{2+} represses calpains, an intracellular Ca^{2+} sensitive protein. The repression of calpains leads to a stabilisation of TET2. This TET2 stabilisation is required for maintaining HSC stemness and quiescence [70]. They proposed that HSCs also reduce intracellular Ca^{2+} by upregulating the expression of plasma membrane Ca^{2+} ATPase efflux pumps (PMCA; Atp2b1 and Atp2b4). These preferentially stabilise the Ca^{2+} balance in cultured HSCs against SOCE activity [70]. Umemoto *et al*. agree with Luchsinger *et al*. that suppressing Ca^{2+} influx contributes to the maintenance of HSCs upon cytokine stimulation, using a combination of stem cell factor and thrombopoietin *in vitro*. In these stressed HSCs, the Ca^{2+} channel blocker nifedipine prolonged cell division intervals at the G1 cell cycle phase by inhibiting Ca^{2+} influx. This block made cells retain stem cell characteristics, indicating symmetric stem cell expansion [73]. Subsequent research by Luchsinger *et al*. showed that Mitofusin isoform 2 (MFN2) protein tethers ER to mitochondria, which leads to a buffering of Ca^{2+} into ER and protecting HSC commitment to lymphoid lineage [81]. Thus, Luchsinger model shows that maintaining low intracellular Ca^{2+} in HSCs is highly beneficial prior to cell transplantation to enhance engraftment.

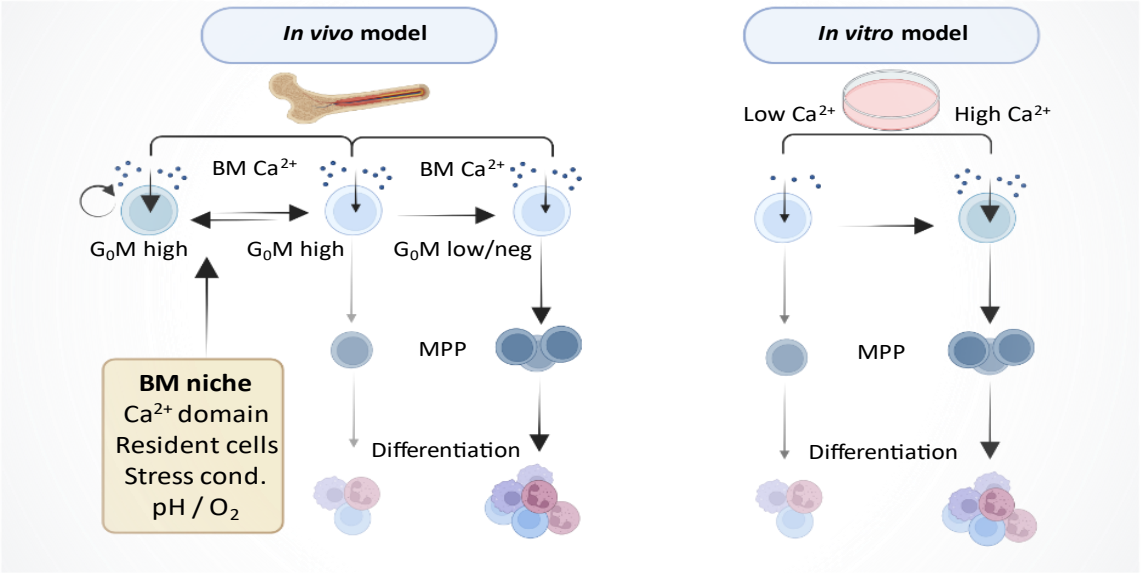

Figure 1-4: Intracellular Ca^{2+} in HSCs.

In vitro model shows that bulk HSCs can be maintained in a low Ca^{2+} in culture. It is shown that culturing HSCs in high Ca^{2+} forces HSCs to lose their quiescence. ***In vivo*** model shows that true self-renewable LT-HSCs (G0M high; most populations are quiescent) possess higher intracellular Ca^{2+} levels than those with G0M low LT-HSCs. The G0 low and G0M neg are more committed HSCs to differentiation. Both G0M high-Ca^{2+} high and G0M high-Ca^{2+} low LT-HSCs are interchangeable only in vivo, which would be challenging to replicate *in vitro*. Also, BM niche seems to regulate the interchangeable format. Figure is generated using BioRender website.

1.4 Mitochondrial metabolism

The oxidation of “metabolic fuels” such as carbohydrates, lipids, and proteins provide cellular energy. It is subsequently utilised to maintain energy-dependent processes such as macromolecule synthesis, muscular contraction, active ion transport, and thermogenesis. The oxidation process produces free energy that can be stored in phosphoanhydrine “high-energy bonds” within molecules such as nucleoside diphosphate and nucleoside triphosphate (i.e., adenosine 5′ diphosphate and adenosine 5′ trisphosphate, Adenosine diphosphate (ADP), and adenosine triphosphate (ATP), respectively). ATP is the primary link between energy-producing and energy-demanding processes involving synthesis, hydrolysis, or transfer of the terminal phosphate group [82].

As shown in Figure 1-5, The primary source of energy for cellular metabolism is glucose, which is catabolised via glycolysis, the tricarboxylic acid cycle (TCA or Krebs cycle), and lastly, OXPHOS to produce ATP. Both the TCA cycle and OXPHOS occur in mitochondria. However, initial conversion of glucose to pyruvate occurs in cytosol. Ultimately, pyruvate is transformed into acetyl coenzyme A (acetyl-CoA), which enters the TCA cycle and allows for continuous generation of NADH. In addition, it is important to note that acetyl-CoA can be produced by lipid and protein catabolism [82]. NADH synthesis occurs when TCA cycle dehydrogenase enzymes release CO_2 and H+ out of carbon substrate, reducing NAD^+ and FAD^+ [83]. NADH and FADH2 are ETC electron donors that travel via the ETC, which has five complexes, including ATP synthase. Oxygen accepts these electrons to form H_2O. Complexes I, III, and IV pump hydrogen protons (H^+) from inner mitochondria to the mitochondrial intermembrane space (IMS), creating a proton gradient that negatively charges the inner mitochondrial space and positively charges the intermembranous region (about −180 to −200 mV). A charge difference creates mitochondrial membrane potential. Due to this potential, H^+ protons return to the interior of the mitochondria by complex V. ATP synthase employs this protonmotive force to make 32 ATP molecules from ADP counterparts [84]. Once produced, ATP can be transported into IMS through nucleotide exchanger adenine nucleotide translocase (ANT), which passively exchanges ATP with ADP. Once in IMS, ATP can traverse the outer mitochondrial membrane through VDAC.

Besides glucose, lipids can be used as fuel for the TCA cycle. Free fatty acids are transferred into mitochondria via carnitine shuttle. Once in the mitochondria, free

fatty acids undergo ß oxidation to generate acetyl-CoA. The total oxidation of common fatty acid palmitate produces 104 ATP [85]. Also, there are a variety of catabolic mechanisms via which amino acids enter the TCA cycle, e.g. glutamine, which enters the TCA cycle through conversion first into glutamate, followed by α ketoglutarate, an intermediate of the TCA cycle [86].

Warburg proposed cancer cells' need to undergo aerobic glycolysis, where cells utilise glucose to feed the pyruvate lactate shuttle despite the presence of oxygen [87]. Further, many cells need to secure high energy levels to meet the proliferation rate through providing ATP and metabolic intermediates such as citrate as a cofactor in many processes, including fatty acid synthesis. Considering the dynamic nature of metabolic switches, HSCs must adapt within BM niche to ensure self-renewal and proliferation. For example, most of the time, HSCs remain quiescent and rely on glycolysis with low dependency on OXPHOS. However, in the case of stress insult, OXPHOS is induced to support HSCs with ATP molecules required for their proliferation or activating cellular signalling in response to insult [88]. Ca^{2+} is one of several elements that participate in this switch in HSCs [73].

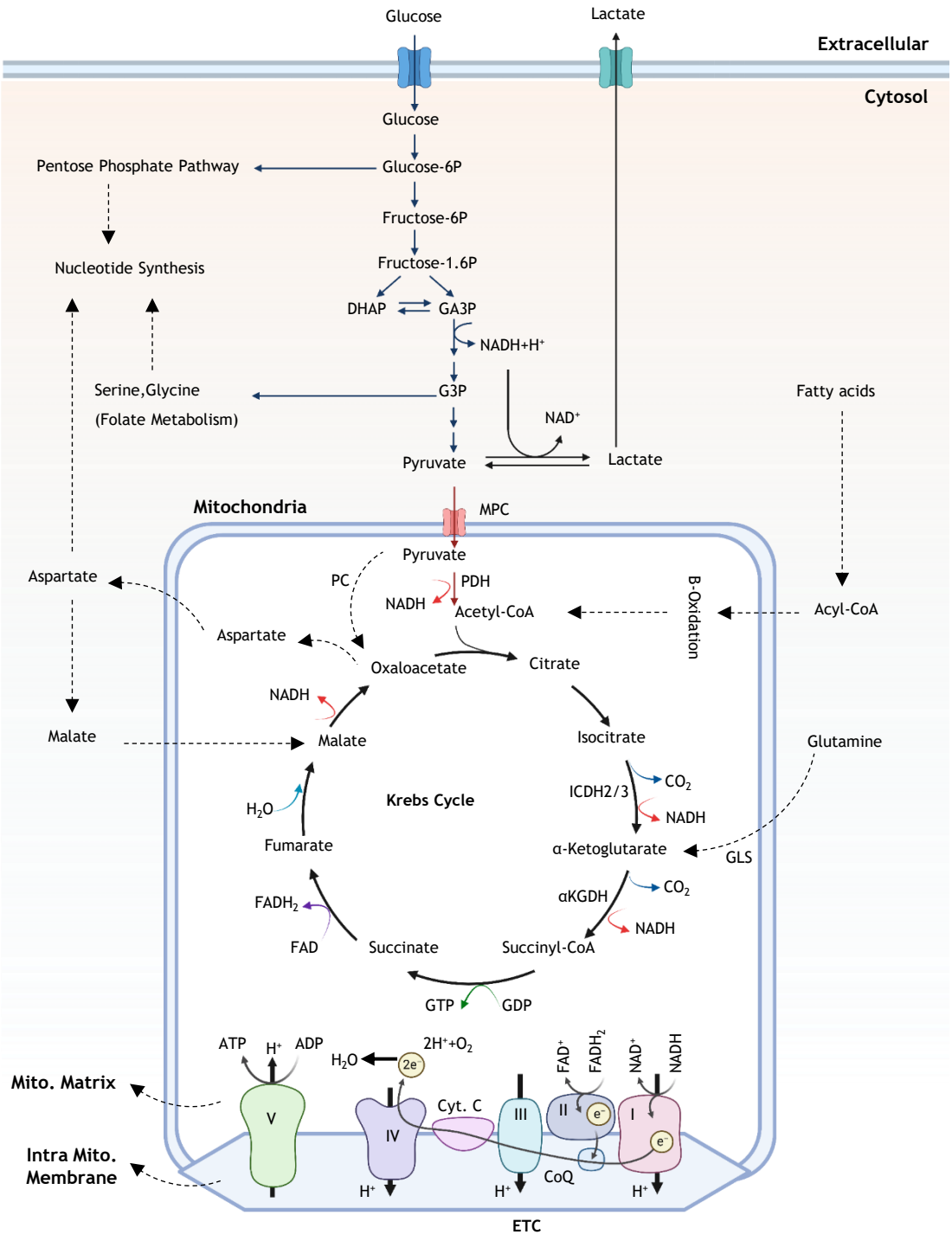

Figure 1-5: Metabolic Pathways in Mammalian cells.

Glucose generates two pyruvate molecules to fuel anaerobic glycolysis (fermentation) that produces lactate or oxidises inside mitochondrial Krebs cycle machinery. Other carbon sources that can support Krebs cycle; are fatty acid through β oxidation and glutamine that gets converted to glutamate by glutaminase the mitochondrial enzyme (GLS) and glutamate dehydrogenase converts it further to αKG (Glutaminolysis). Adapted from [89] and regenerated using BioRender website.

1.4.1 Metabolism and Ca^{2+}

Ca^{2+} supports mitochondrial metabolism in different scenarios to enable the cell to generate energy (Figure 1-6). For example, OXPHOS aims to generate ATP energy molecules. Previous studies correlated the Ca^{2+} within mitochondria and the level of generated ATP. For example, chelation of Ca^{2+} using EDTA significantly reduced ATP pool [90]. However, EDTA has been shown to chelate other divalent cations, including Mg^{2+} and Ca^{2+}. Denton and McCormack demonstrated for the first time that free intramitochondrial Ca^{2+} activated mitochondrial dehydrogenases, increasing NADH and ATP generation [91, 92]. The activation mechanism of those dehydrogenases by Ca^{2+} is different. For example, pyruvate dehydrogenase (PDH) reaches its V_{max} through indirect Ca^{2+} activity. PDH is activated by Ca^{2+} dependent phosphatase dephosphorylation [91]. Contrary to PDH, Ca^{2+} directly modulates α-ketoglutarate dehydrogenase (αKDH) through direct binding to Ca^{2+} ions [93]. Also, isocitrate dehydrogenase (IDH) is directly activated by Ca^{2+} binding.

Several studies indicate that Ca^{2+} dependent dehydrogenases are not the only mechanism for Ca^{2+} dependent ATP synthesis. Harris *et al*. and Scholz *et al*. showed that Ca^{2+} could impact F1-F0-ATPase in cardiac cells [94, 95]. This occurs because F1-F0 ATPase gets activated only when Ca^{2+} reaches Km of 200 nM, which increases ATP synthesis [96]. However, this is thought to be due to either post-translational modification of F1-F0-ATPase or to a changing mitochondrial potential due to induced reductive NADH production by dehydrogenase activity, helping in potential mitochondrial gradient [96, 97]. Conversely, the chemiosmotic theory proposes that the increased mitochondrial Ca^{2+} uptake is driven by ETC activity, which generates a negatively charged electrochemical gradient inside the mitochondrial matrix by efflux of H^+ protons through complex I, III, IV. This mitochondrial potential of ΔΨ of – (150–180) mV favours cation entrance, such as Ca^{2+}. As proof of the chemiostatic theory, mitochondrial uncoupler CCCP resettles ΔΨ and disrupts MCU-mediated Ca^{2+} influx [98]. Moreau *et al*. demonstrated similar findings that the accumulation of H^+ inside mitochondrial matrix leads to MCU inactivation [99]. This strategy has been thought of as a tool that cells can use during ATP synthesis to avoid Ca^{2+} overload. This occurs because ATP synthesis can influence mitochondrial Ca^{2+} signalling through inflow of H^+ again into the matrix during ATP generation by ATPase. This

strategy may avoid a mitochondrial Ca^{2+} accumulation that represses PTP-mediated apoptosis [100].

In addition, Ca^{2+} regulated transporters influence mitochondrial metabolism without reaching the mitochondrial matrix. For example, aralar and citrin are aspartate/glutamate carriers (AGC) engaged in malate-aspartate NADH shuttle through inner membrane EF-hand-based regulatory sites involved in malate-aspartate NADH shuttle [101]. This equilibrates the NAD^+/NADH ratio from cytosol to mitochondrial matrix across the mitochondrial inner membrane. These transporters are activated at physiological Ca^{2+} concentrations of around 300 nM [102]. Overexpression of WT those AGC transporters (but not mutants lacking Ca^{2+} binding sites) increased ATP production in response to cell stimulation, suggesting that Ca^{2+} effectors in different mitochondrial fractions (matrix, intermembrane space) may cooperate in ATP production [103]. The direct contribution to OXPHOS by the AGC shuttle's activity is likely minimal due to high demand for NADH in mitochondria that exceeds those of AGC activity. However, AGC shuttle removes cytosolic NADH, which may play a role in enhanced pyruvate oxidation through repressing dehydrogenase (LDH) activity that requires NADH [104]. In this way, Ca^{2+} activation of NADH shuttle system may avoid pyruvate "waste" to lactate via lactate dehydrogenase deactivation.

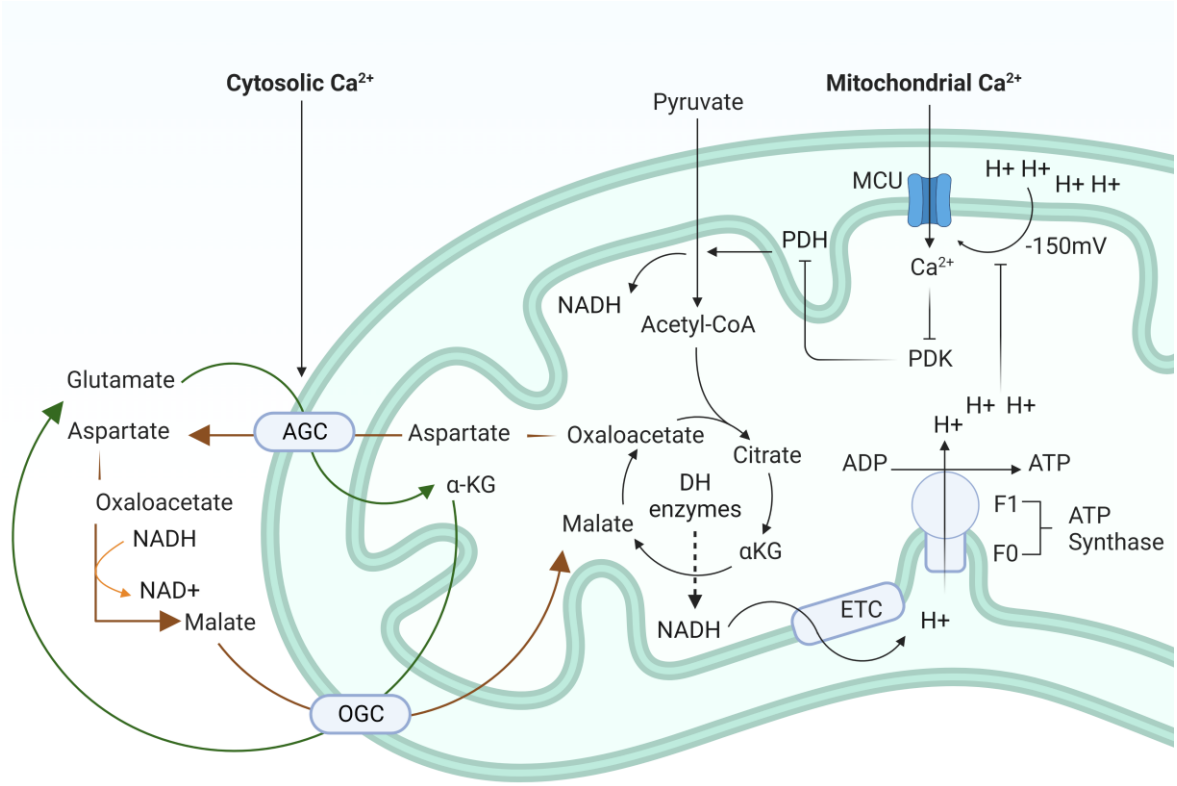

Figure 1-6: Ca^{2+} homeostasis in mitochondrial metabolism.

Cytosolic Ca^{2+} activates AGC, known as aralar and citrin. By coupling that shuttle with OGC shuttle, metabolites can be recycled by cytosolic part of the reaction, supporting the TCA cycle again with malate. The reaction of oxaloacetate conversion to malate consumes NADH and generates NADH equivalent inside mitochondria, supporting the NAD^+/NADH balance inside mitochondria. Another side of AGC activity is that it competes with LDH for NADH consumption, supporting pyruvate oxidation rather than expanding it into lactate. On the other hand, Ca^{2+} inside mitochondria supports mitochondrial metabolism by indirectly activating PDH and directly activating IDH and αKDH enzymes, which leads to production of more NADH required for ETC complex I, III, and IV activities. The acidity inside inner mitochondrial membrane generates negative potential inside mitochondria matrix, which enhances Ca^{2+} influx to mitochondria via MCU channel. MCU Ca^{2+} influx to mitochondria is partially repressed by ATP synthase, which equilibrates the negative potential by allowing proton influx in exchange for ADP conversion to ATP. This reduces chances of apoptosis due to Ca^{2+} overload. Figure is generated using BioRender website.

1.4.2 HSC metabolism and Ca^{2+}

Fukushima *et al*. showed that murine LT-HSCs are quiescent and have higher intracellular Ca^{2+} ions than bulk HSCs, suggesting a distinct dependency on Ca^{2+} levels of BM niche [71]. Fukushima *et al*. noticed that the SOCE gene set (SOCE; *Trpc6, Stim1, Orai1*) is enriched in quiescent LT-HSCs compared to bulk HSCs [71]. There is increasing evidence of cellular signalling driven by Ca^{2+} binding molecules mediating HSC maintenance, such as calmodulin kinases and EF-motif binding S100A proteins [105-108]. However, none of the reported Ca^{2+} binding proteins studies correlated their findings to dysregulated Ca^{2+} levels. One elegant study directly correlating Ca^{2+} level to metabolism regulation of HSCs was done by Umemoto *et al*. [73]. As highlighted above, LT-HSCs have a low basal energy level that relies on glycolysis [109, 110]. However, cells keep mitochondrial mass as a reservoir that allows LT-HSCs to respire, proliferate, and reconstitute BM niche during stress conditions [71, 111]. The proliferation of HSCs is an energetic process that requires active mitochondrial respiration following mitochondrial Ca^{2+} influx [73]. Mitochondrial respiration is also indispensable for HSC survival and lineage commitment [112, 113]. Results indicate that Ca^{2+} and hypoxia in BM niche regulate HSC maintenance and proliferation by regulating the balance between glycolysis and OXPHOS. To understand how Ca^{2+} regulates metabolism, it is important to look at how OXPHOS and glycolysis occur in cellular context.

1.5 Ontogeny of leukaemia

The Greek word leukaemia is derived from coining of "*haima*", which means blood, and "*leukos*", which stands for white, which reflects the accumulation of white blood cells [114]. The story of leukaemia started when research run by John Hughes Bennett in Edinburgh in 1845s described a case of hypertrophy of the spleen and liver in which death took place from suppuration of the blood [115]. Six weeks later, Rudolph Virchow, in Berlin 1846s, described an enlarged spleen and milky white blood and called it "Weisses Blut" to describe white blood cell accumulation in blood circulation [116]. Despite the assumption in 1914s by Boveri that malignancies arise from disruption of genetic materials, it was not proven until 1950s when cytogeneticists were able to show the content of 46 human chromosomes followed by comparing normal and leukaemic samples chromosomes. Today, it is agreed that leukaemia of myeloid origin arises from the clonal expansion of myeloid cells following dysregulation in primitive haematopoietic cells, including HSCs. It is unclear what precipitating factor could lead to this transformation in HSCs, possibly radiation or toxic material exposure [117, 118]. These factors are assumed to imply epigenetic and genetic dysregulation in HSCs that could lead to forming a preleukaemic transition phase to leukaemia "leukemogenesis". The fact that HSCs have a self-renewal capacity makes the situation worse because it allows them to persist despite stress-induced mutations in their genetic content over time. This transformation of HSCs produces another version of dysregulated cells that harbours stem cell self-renewal capacity and defective clonal expansion due to their mutational landscape, known as leukaemia stem cells (LSCs) [119, 120]. Leukaemic cells have been categorised according to the type of clonal progenitors that harbour genetic dysregulation to produce immature cells, including either myeloid leukaemias or lymphocytic leukaemias. To distinguish between them, CMPs are enriched with high levels of CD150, but CLP is less enriched with CD150 compared to CMP population [70]. Leukaemia has been further categorised according to the rate of disease onset, either an acute or chronic onset of leukaemia.

1.5.1 Chronic myeloid leukaemia (CML)

One of those consequences of LSC deviated clonal expansion is CML. In 1960, it was Nowell and Hungerford who noticed abnormal acentric small chromosomes in

patients [121]. In 1973, Janet Rowley dissected the reason behind this abnormal chromosome. She discovered chromosomal translocation t(9;22) (q34;q11), which results in fusion gene *BCR::ABL1*, named Philadelphia chromosome [122, 123]. This defective chromosome expresses an oncoprotein that has a constitutive tyrosine kinase activity. The BCR::ABL oncogene is similarly detected in all CML individuals and thus is considered a hallmark of the disease [124, 125].

1.5.2 Molecular signalling of BCR::ABL

CML occurs with an incidence rate in United Kingdom of 1.2 cases per 100,000 individuals [126]. Since the risk of getting CML increases with age, the average age of people diagnosed worldwide is 60 [127]. Exposure to benzene and prior irradiation have been linked to an increased risk of developing CML [117, 118]. BCR::ABL tyrosine kinase activity induces many cellular signalling events—for example, the transcription factor STAT5 and its downstream pCRKL [128]. PI3K kinase and its Akt downstream signalling are required for derepressed proliferation and were also reported [129]. This signalling also includes mTOR activation, which is required for proliferation [130]. Furthermore, RAS and its downstream ERK kinase activity have been reported to be directly stimulated by BCR::ABL activity that promotes cell proliferation [131].

1.5.3 CML progression

CML can progress from chronic to the so-called blast phase, in which the number of myeloid blasts in BM and blood increases by over 20%, and symptoms of the disease worsen [132]. This occurs as a tri-phase progression, from chronic, accelerated, to finally, blast phase. The symptoms are mild in the chronic phase and much worse in the blast phase of the disease, which is almost incurable due to altered signalling, impaired DNA stress response and accumulation of more genetic mutations [133] (Table 1-2).

Table 1-2: Diagnostic genetic alteration in CML phases.

Alterations	Chronic	Accelerated	Blast
Blast count	<10%	~20%	>20%
Cell of origin	HSCs		HSPCs
Additional chromosomal alterations	Only BCR::ABL1	Trisomy 8, isochromosome 17q, trisomy 19, complex karyotype, or abnormalities of 3q26.228	Trisomy 8, isochromosome 17, duplication of Ph chromosome or chromosome 19, 21, or 17, loss of chromosome Y or monosomy 7
Epigenetics			ASXL1, DNMT3A, RUNX1, and TET2
Other kinases			Fyn, CaMKIIγ
DNA damage	Low		Impaired
Tumour suppressors			RB1, TP53, and CDKN2A29

This table was reviewed by Rahul Kumar and Danielle Krause [134].

1.5.4 History of CML treatment

Throughout 250 years, CML has been revolutionised with various treatments (). In 1865s, arsenic was the first drug reported to be effective in CML. Treatment was palliative for most cases during the last century, including splenic irradiation, various cytostatic agents, including busulfan, which was standard for nearly three decades, and intensive combination therapy [135]. The first reported curative strategy began with stem cell transplantation in 1969, initially described in syngeneic twins [136]. Despite progress in engraftment between different individuals, transplantation still shows poor responses and technical challenges such as rejection of engraftment, hard-to-find stem cell donors, and the inability to expand *ex vivo* [137]. Another therapeutic strategy, interferon (IFN) plus hydroxyurea or low-dose cytarabine (ara-C), offered the possibility of extending survival, particularly in low-risk patients and those with cytogenetic remission [138-140].

Since 1998s, the breakthrough discovery of imatinib as the first introduced tyrosine kinase inhibitor (TKI) represented a new hope for CML patients. In the international IRIS study (International Randomized Study of IFN-α plus Ara-C vs STI571), imatinib considerably exceeds interferon plus cytarabine (IFN/Ara-C) in terms of complete cytogenetic response (CCyR) rates and progression-free survival

in patients with newly diagnosed chronic-phase chronic myelogenous leukaemia [141]. Scientists discovered imatinib from TKI drug screening. It acts through binding to ATP binding pocket of BCR::ABL protein and inhibits its ability to phosphorylate downstream candidate proteins, such as p210BCR::ABL adaptor protein (CRKL). When imatinib was studied in a clinical phase-I trial, a complete haematologic response was achieved in 54 patients who failed to respond to IFNα treatment after two weeks. However, the variable outcome was in cytogenic response [142]. The inhibited activity of BCR::ABL was reported in blood withdrawn from patients receiving imatinib by reduced levels of phosphorylated CRKL, the major Substrate of BCR::ABL. Successful TKI therapeutic regimens have afforded CML patients a five-year survival rate of nearly 80% [143]. However, a Stop Imatinib (STIM) clinical trial launched in France in 2007s revealed that imatinib discontinuation could lead to relapse from complete CML phenotypic disease in around 50% of patients for up to 2 years after starting TKI treatment [144]. Another study showed consistent findings in patients who received IFNα prior to imatinib [145].

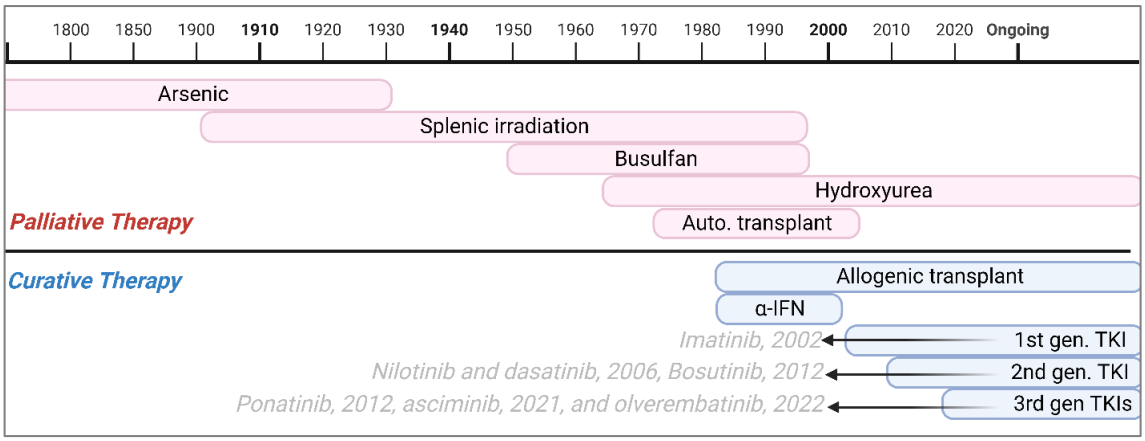

Figure 1-7: History of CML treatment within the last 250 years.

Different treatment strategies have been approached. Cytotoxic drugs, and splenic irradiation were the only available palliative cure of CML patients until 1970s. Patients started to receive autologous and allogenic transplantation which enhanced survival in 50% of CML patients, alongside hydroxyurea. Despite the enhanced treatment outcome by using interferons, the successful achievement occurred once the first of TKIs was reported in 2000s (imatinib) which enhanced survival rate in CML patients by 85%. Following the discovery of imatinib, scientists discovered wide spectrum second and third generations of other TKIs that are used in more advanced or resistant cases to imatinib. Figure is generated using BioRender website.

1.5.5 Guide to interpreting CML responses to imatinib

Since imatinib revolutionised CML treatment, scientists set up parameters to monitor disease progression and remission after treatment [146]. There are 3 categories of CML response towards therapy: haematologic, cellular, and molecular, indicating the treatment outcome (Table 1-3).

Table 1-3: Guidance for treatment outcomes in CML.

Types of responses		Feature	Test used
Haematologic	Complete haematologic response (CHR)	Blood count and spleen size return to normal	Complete blood count (CBC)
		No blasts in the blood	
		No disease symptoms	
Cytogenic	Complete cytogenic response (CCyR)	No cells have Philadelphia Ch.	BM cytogenetics or FISH.
	Partial (PCyR)	1-35% of cells Philadelphia Ch.	
	Major (MCyR)	35% of cells have Philadelphia Ch.	
	Minor response	> 35% of cells have Philadelphia Ch.	
Molecular	Complete molecular response (CMR)	No *BCR::ABL1* gene detected	qPCR using the international scale
	Major molecular response (MMR)	> 3 log reduction (1/1000) in *BCR::ABL1* or 0.1% *BCR::ABL1*	

This table is adapted from [147].

1.5.6 Resistance to imatinib

Several reasons have subsequently been suggested for the resistance of CML individuals to imatinib treatment, which can be categorised as BCR::ABL kinase domain dependent or BCR::ABL independent. The largest proportion of imatinib resistance that accounts for 80% of reported cases comes from point mutations within *BCR::ABL1*, which expresses a BCR::ABL with impaired imatinib binding efficiency to its kinase domain, such as confirmational changes of threonine to isoleucine at position 315 (T315I BCR::ABL CML) known as a gatekeeper position for BCR::ABL mutation [148, 149].

The second generation of TKIs included more potent BCR::ABL inhibitors, such as dasatinib, bosutinib, and nilotinib [150-152]. Even though those drugs enhanced survival rates and complete cytogenic response compared to imatinib, they are

still less efficient in inhibiting T315I mutant BCR::ABL. Other BCR::ABL mutations also render nilotinib and dasatinib less effective therapy against BCR::ABL. Those BCR::ABL mutations include E255K, Y253H, F359C/N BCR::ABL resistant to nilotinib, and F317L BCR::ABL dasatinib resistant [153].

Ponatinib, a third-generation TKI, inhibits T315I BCR::ABL mutant version of the disease and is currently the most effective treatment against CML resistant to first and second generation approved TKIs [154]. In clinics, these inhibitors are often used in a certain order based on how patients react. However, about 1% to 5% of people with CP-CML do not respond to any BCR::ABL TKIs and end up with blast phase CML, the advanced form of the disease [155]. Furthermore, ponatinib has since been withdrawn from shelves due to reported cardiovascular adverse effects concurrently with T315I inhibition [156].

In 2021s, asciminib was approved for medical use in U.S.A as a novel CML therapy for patients with reported T315I mutated BCR::ABL [157]. The Myristolylated N-terminal of normal ABL kinase represses kinase activity upon binding to its Myristoyl Binding Site (MBS) within the ABL domain. However, the translocation of *BCR* and *ABL* led to the replacement of MNT with BCR protein, leading to the loss of MNT with subsequent loss of repression of ABL through MBS, which leads to constitutive ABL kinase activity (Figure 1-8). The mechanism of action of asciminib relies on allosteric binding to MBS pocket. Once asciminib engages in this pocket, ABL kinase becomes inactivated, which abolishes BCR::ABL activity [157]. There is no overlapping between imatinib and asciminib binding sites, enabling asciminib to target T315I mutant version of BCR::ABL. However, another mutation with MBS pocket limits asciminib activity, such as A337V and P223S [158]. Olverembatinib, another recent ATP binding pocket inhibitor, was approved in China and Canada for chronic and accelerated phases of CML in July 2022 [159]. Olverembatinib has effectively repressed most *BCR::ABL1* mutants, including those expressing T315I-BCL-ABL [160]. However, olverembatinib has displayed off-target effects not reported for previous TKIs, such as grade 1 skin pigmentation, grade 3-4 thrombocytopenia, and hypertriglyceridemia, which may limit its applicability to all patients [161].

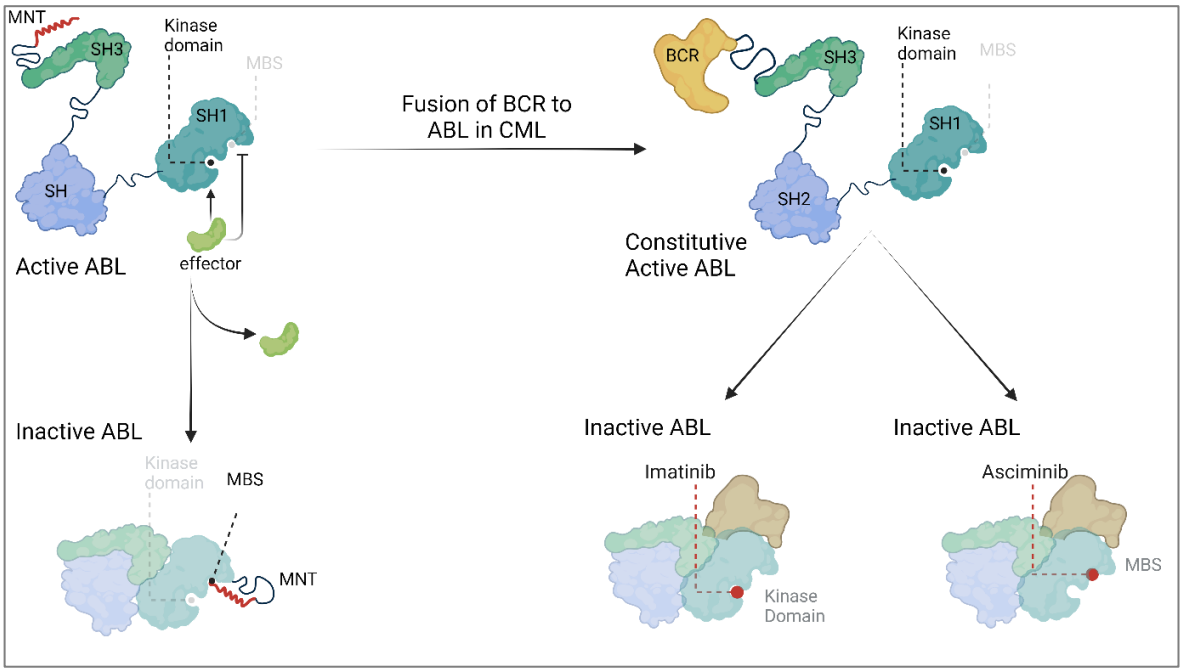

Figure 1-8: Asciminb and imatinib mode of action.

The WT ABL kinase is induced by signalling inhibiting Myristolylated N-terminal (MNT) binding to MBS. When signalling is relieved, ABL is inhibited by binding MNT to MBS due to confirmational changes that restrict kinase activity. In CML, MNT is lost and substituted with BCR, which does not have an affinity to MBS, leading to constitutive activity of ABL. Asciminib works similarly to MNT through allosteric occupying MBS. Imatinib binds to a different domain that also represses ABL kinase activity. Figure is generated using BioRender website.

The other form of BCR::ABL independent resistance to therapy arises from amplifying BCR::ABL copy number, as reported in a few CML cases, which causes cells to resist treatment [162]. BCR::ABL independent mutations responsible for treatment failure were related to e.g. a drug transporter responsible for the absorption of imatinib from gastrointestinal tract to circulation, such as organic cation transporter-1 (OCT-1) [163]. Other BCR::ABL independent mutations have been reported to participate in resistance to imatinib treatment during the progression from the chronic to blast phase of the disease, such as a mutation in LYN kinase [164]. LYN kinase and extra mutations related to progression from chronic to blast phase displayed in table 2 have been reported to limit therapeutic efficacy. Patients in blast phase have a poor five-year survival rate of 20% [117]. It is not only those intrinsic mechanisms that confer TKI resistance but also de novo mechanisms induced upon TKI treatment, such as autophagy, a process thought to confer CML cells and LSCs resistance to imatinib treatment [165, 166]. TKI treatment induces localisation of FOXO-3a to nucleus, enhancing anti-apoptotic signalling that makes cells more resistant to BCR::ABL inhibition [167-169].

Most of these mechanisms cause non-mutational therapy resistance, and this has been linked to those extra attributes of LSCs, such as quiescence, self-renewal, and high reliance on mitochondrial OXPHOS. Also, the localisation of CML LSCs within the immune protective BM niche limits imatinib to penetrate and eradicate those cells within their niches [170]. This all indicates that the efficacy of BCR::ABL inhibition is not enough to achieve deep molecular remission in CML, which requires four times log-fold reduction in Philadelphia chromosome detection (DR4 ≤ 0.01%), necessitating the search for more targeted therapies against CML.

1.6 Leukaemic stem cells

The expression of *BCR::ABL* does not offer committed progenitors the ability to self-renew [171]. This suggests that CML chromosomal translocation originates in HSCs with intrinsic ability to self-renew. Those disrupted HSCs (LSCs) can generate whole progenitor lineage expressing BCR::ABL [172]. CML LSCs are similarly like HSCs (CD34+ and CD38-) [173]. These LSCs markers are still the gold standard for initially characterising CML LSCs [174]. However, more work has been done to precisely separate CML LSCs from HSCs through abnormal expression of other cell surface antigens, such as CD25, CD26, CD9, CD123, CD93, CD96, and immune checkpoint antigens, such as CTLA4, CD274 (PD-L1), and TIM-3 [175]. Some LSC surface markers show higher clinical utility than others, such as CD26 and CD93 [176, 177]. Although LSCs are the source of CML, their functional capabilities and molecular signatures are mostly mutation independent. BCR::ABL activity does not appear to be required for CML LSC survival, as noticed in murine models [178]. Giustacchini *et al*. could distinguish BCR::ABL+ and BCR::ABL- LSCs from CML patients using an RNA sequencing approach [179]. Surprisingly, they showed that these LSCs have a dormant signature at transcriptional level, which is linked to poor treatment response and disease persistence [179]. Thus, LSCs appear to play a key role in clonal dynamics identified in CML due to their ability to self-renew.
Given that the most primitive LSCs are dormant or quiescent [180], suggesting quiescence as mutation independent therapy resistance characteristics of LSCs. Reinforcing this, Corbin *et al*. found that CML LSCs do not rely on BCR::ABL for survival, shifting the focus of current CML research to the identification of targetable vulnerabilities that could be used to sensitise LSC quiescent population to conventional TKI therapy and potentially cure the disease [181].

1.6.1 LSC metabolism

Since Otto Warburg proposed that transforming cells need aerobic glycolysis, numerous researchers have continued refining Warburg's aerobic glycolysis model. Heiden *et al.*, for instance, hypothesise that the increase in glycolysis seen in cancer cells is not utilised for energy production but rather to supply rapidly proliferating cells with all intermediate metabolites required to build biomass, notably nucleotides [182]. Also, those cells with less functional mitochondria or mitochondrial-independent metabolisms, such as pancreatic, breast and ovary cancers, are concrete examples supporting Warburg concept [183].

However, mounting evidence suggests that CML LSCs rely on OXPHOS and not glycolysis, contrary to Warburg. For instance, Kuntz and colleagues showed that the TCA cycle flux and mitochondrial respiration are higher in CD34+ CML LSCs than in CD34- LSCs. They also found that the most primitive CD34+CD38- LSCs relied more on OXPHOS than non-leukaemic HSCs [184]. Giustacchini *et al.* performed a single cell RNA sequencing and showed that in a CML sample from the same patient, BCR::ABL+ LSCs overexpressed genes related to OXPHOS more than normal HSCs [166]. Reinforcing that, Abraham and colleagues found that the upregulated OXPHOS in CML LSCs is partly regulated by the NAD-dependent deacetylase sirtuin-1 (SIRT1), which is required for PGC1-α expression [185]. The authors found that direct PGC-1α inhibition did not fully inhibit CML pathogenesis *in vivo*, unlike SIRT1 inhibition.

Further literature supports increased carbon sources for the TCA cycle independently of glucose. For example, myeloid leukaemia cells can transform their BM niche domain to help perform certain purposes. It might include facilitating the propensity of TCA carbon sources, such as free fatty acids. Ye and his colleagues showed that blast phase CML cells can promote lipolysis in their adipose niche, which releases free fatty acids [186]. All these results indicate that profound metabolism rewiring may help in leukemogenesis.

Notably, not only disease transformation but also resistance of those cells to introduced therapy could be a consequence of this metabolic rewiring. Tumour cells undergo metabolic reprogramming, a hallmark of carcinogenesis, which may explain the resistance of leukaemic cells to anti-cancer therapy like TKI treatment [187, 188]. Also, LSCs rely on adipose tissues as a reservoir for their energy demands. LSCs expressing increased levels of CD36 tend to show more flexibility

to escape therapy due to increased lipolysis [186]. They found that when $CD36^+$ or $CD36^-$ LSCs were compared, $CD36^+$ LSCs were preferentially more resistant to dasatinib treatment [186]. All this has driven scientists to test whether inhibition of OXPHOS is potential key to undermining resistance of LSCs to current chemotherapy. Kuntz *et al*. revealed that tigecycline, a mitochondrial protein translation inhibitor, synergistically eradicated CML LSCs combined with imatinib but did not harm HSCs [188].

In conclusion, although normal HSCs primarily rely on glycolysis [189], CML LSCs, as well as treatment-resistant cells, seem to be far more OXPHOS-dependent and unable to rely only on glycolysis. Because LSC persistence and resistance to therapy remain the most difficult hurdles in treating myeloid leukaemia, OXPHOS seems to be a therapeutically important target in this disease. Although various compounds have shown that this pathway may be targeted in individuals, success in the clinic has been harder to achieve, and significant safety concerns persist. Also, to our expertise, no OXPHOS inhibitor has yet been explored in clinical trials to treat CML.

1.6.2 Ca^{2+} and OXPHOS in CML LSCs

Ca^{2+} plays an important role in OXPHOS. OXPHOS is critical in CML LSC survival. However, no literature directly correlates Ca^{2+} signalling to OXPHOS in CML LSCs. This further emphasises the need to dissect molecular signalling that defines connection between ER and mitochondria. Promyelocytic leukaemia (PML) is known to facilitate Ca^{2+} flux to mitochondria through the activation of IP3R. PML recruits PP2A that relieves Akt-mediated inhibition of IP3R [190]. The lectin chaperones calnexin and calreticulin, as well as their associated co-chaperone ERp57, are other resident Ca^{2+} binding proteins in MAM that participate in sequestering Ca^{2+} within ER and help in proper ER-mediated protein folding [191]. The dissociation of Ca^{2+} bound to calnexin relies on their shuttling to contact sites between ER and mitochondria by PACS2 (phosphofurin acidic cluster sorting protein 2), allowing Ca^{2+} transfer between those two organelles [192, 193]. Also, glucose-regulated protein 75 (GRP75) tethers ER to mitochondria through tethering IP3R to VDAC, respectively, allowing the formation of a tunnel for Ca^{2+} to flow from ER to mitochondria [194]. All those regulatory proteins have not been evaluated yet regarding their involvement in leukaemia progression, especially

those leukaemias that rely on mitochondrial metabolism. Findings indicate that Ca^{2+} plays a role in acute myeloid leukaemia (AML) and CML disease progression and participates in CML therapy resistance, highlighting possible role of Ca^{2+} ions in regulating survival in sensitive and resistant CML.

Given the direct role of Ca^{2+} in catalysing dehydrogenases, regulating the abundance of TCA cycle metabolites generation could be enhanced by Ca^{2+} involvement. The TCA cycle metabolites, α-KG, participates in epigenetic regulation of DNA through their involvement in histone demethylation [195, 196]. Despite all assumptions, Ca^{2+} mediated changes in metabolism and epigenetics have not been fully studied yet and could be an elegant cause of HSC transformation in myeloid leukaemia.

Hypothesis and Aims

This project aims to address our hypothesis that Ca^{2+} homeostasis is dysregulated in CML LSCs in comparison to its normal counterparts and investigate if this impacts OXPHOS in CML. Further the research project aims to investigate the impact of Ca^{2+} influx inhibition using lomerizine, a compound identified through drug repurposing screen, and validate it as a potential OXPHOS inhibitor in CML. Furthermore, the aim was set to investigate the impact of targeting specific Ca^{2+} channels such as TRPC6 and CACNA1D using genetic approach to define their importance for mitochondrial metabolism and Ca^{2+} homeostasis in CML. Lastly, this project aims to investigate if Ca^{2+} inhibition using lomerizine targets tumour burden and patient derived LSC BM engraftment using advanced *in vivo* models.

2 Methods and Materials

2.1 Methods

2.1.1 Cell culture

2.1.1.1 Primary samples collection

All patient samples were generously donated with ethical permission and informed consent (REC 10/S0704/60 & REC 15/WS/003). CML samples were taken from chronic phase CML (Ph+) patients by leukapheresis at the time of diagnosis, prior to TKI therapy (Table 2-25). Normal cells were extracted from the femoral head BM of individuals undergoing hip replacement (Table 2-25). Other CD34+ samples were collected from individuals with other haematological diseases (not affecting the CD34+ population), also referred to as “normal”.

2.1.1.2 BM cells separation from hip samples

To prepare normal femoral head BM cells, it was first gently squished in PBS and then strained through 40 µm cell strainer to eliminate cartilage. The cloudy suspension was spun down for 10 minutes at a speed of 400 x g. Following suspension of the pellet in 7 ml of PBS, it was put into a falcon tube containing 8 ml of histopaque (Sigma Aldrich, UK). The BM leukocytes were separated in a histopaque density gradient by centrifugation for 30 minutes at 400 x g without brakes. After that, the mononuclear cell layer was moved into a new falcon tube, topped with PBS, and centrifuged for 10 minutes at a speed of 400 x g. Cells were then resuspended in 1 ml PBS that was ready for CD34+ selection.

2.1.1.3 Isolation of CD34+ cells

Dr Alan Hair conducted CD34+ CML cell isolation at Paul O’Gorman Research Centre (Glasgow, UK) by leukapheresis. Isolation of CD34+ normal cells was performed in Helgason lab where CD34 isolation was performed using CD34 Microbead Kit (Miltenyi Biotech, UK). Isolated mononuclear cells collected BM were resuspended in 200 µl PBS and 100 µl of kit FcR blocking reagent, followed by incubating for 10 minutes. The cell mixture was topped up with 100 µl of kit CD34 Microbeads, followed by 30 minutes of incubation at 4^{o} C. Mixtures were topped up with PBS. The cell suspension was centrifuged for 10 minutes at 300xg,

followed by resuspending in 500 µl PBS. The cell suspension was filtered on a 40 µM cell strainer and the filtrate was loaded into a PBS-hydrated LS selection column fixed on top of a magnetic column. Column loaded with cells was washed 3X to remove nonspecific binding debris. Cells were collected by pushing the syringe plunger into the column.

2.1.1.4 CML cell lines used in this study

K-562 (ATCC # CCL-243™) are immortalised erythroleukemic cells that belongs to female CML patient with chronic myelogenous leukaemia who was 53 years old. Another cell line called KCL22 (ATCC # CRL-3349™)which is a cell line with lymphoblast-like morphology that was derived from a 32-year-old woman who had chronic myeloid leukaemia during blast crisis in 1999 from pleural effusion. Both of those K562 and KCL22 cell lines are sensitive to imatinib and other generations of TKIs. The paired KCL22 sensitive and KCL22 resistant clones can serve as valuable cell line models for tyrosine kinase inhibitor sensitivity and resistance. During this stud, two imatinib resistant cell lines were used, ponatinib resistant (PonRes) KCL22 which resists effect of different types of TKIs, including imatinib despite the absence of *BCR::ABL1* mutational landscape. The other imatinib resistant KCL22 cell line harbours point mutation within the kinase motif of *BCR::ABL1* which generates mutated version of BCR::ABL with the substitution of threonine to isoleucine at position 315 (T315I) that can resist imatinib effect. PonRes KCL22 resistant cell lines have been generated and verified previously by Helgason lab former PhD colleagues, Dr. Elodie Kuntz [197]. Also, T315I KCL22 cells were generous gift from Professor Bruno Calabretta which was verified in Helgason lab by former PhD colleague, Dr. Rebacca Mitchell [198]. There are other manipulated cell lines that are modified using CRISPR-Cas9 gene deletion of ATG7 or ULK1 were also previously generated and verified in Helgason lab.

2.1.1.5 Recovery of cell lines and primary cells

Cells were thawed in 37^{o}C water bath followed by transferring them to 15 ml falcon tube. Cells were then washed with PBS or culture media, followed by centrifugation to remove residual dimethyl sulfoxide (DMSO). Cell pellets were resuspended in SFM supplemented with physiological growth factors (φGF) (Recipe: Table 2-23). CD34+ CML or non-CML primary cells were thawed in 37^{o}C

water bath, followed by transferring them to 15 ml falcon tube. A 10 ml DAMP (DNase I Albumin Magnesium PBS buffer) solution (Recipe: Table 2-25) was added to cell suspension dropwise over 5-10 minutes, then left the mixture for another 10 minutes. Cells were centrifuged, and cell pellet was washed using DAMP twice. Cells were then centrifuged at 300Xg for 10 minutes. Cell pellets were resuspended and maintained in fresh media.

2.1.1.6 Cell line maintenance in culture

Erythro-leukaemic cell lines (K562 or KCL22) were passaged for no more than a month after initial liquid nitrogen thawing. Cells were cultured in RPMI 1640 media (Thermo Fisher, UK) supplemented with penicillin-streptomycin, glutamine, 105 FBS and glucose/galactose if required (Recipe:Table 2-23). The cell count density did not exceed 1.5*105 /mL to avoid over-confluency and secure high viability. For cell passage, cells were pelleted at 350g for 5 minutes, and cells were resuspended in fresh media. HEK293FT was maintained in complete Dulbecco's Modified Eagle Medium (DMEM) (Table 2-23). Cells were passaged every 3 days, followed by trypsin-EDTA to detach cells from a petri dish. HEK293FT cells were maintained at $0.5x10^6$ cells/ml.

2.1.1.7 Monitoring cell proliferation

Cell lines were seeded at $5x10^4$ cells/ml using RPMI and incubated for 3 days. Cell densities were performed at 24h intervals using CASY automated cell counter. Primary cell expansion was performed using the same approach according to an experimental plan.

2.1.1.8 Cell expansion assays

Catalytic reduction of resazurin into resorufin is accompanied by a colour shift from blue to pink and reflects the activity of a viable cell. This fluorometric shift (570/600 nm) was measured using Tecan 200 infinite plate reader after 3 hours of incubation with 50 μM resazurin (Table 2-13).

2.1.1.9 Cryopreservation of cell lines and primary cells

Cell lines maintained at $0.2*10^6$ cells/ml were centrifuged and resuspended in freezing media (90% FBS+10% DMSO). Primary cells were cryopreserved using 50%

FBS+40% IMDM+10% DMSO instead. The cell suspension was kept on ice for less than 5-10 minutes, followed by freezing in an isopropranolol hydrated container at -80^{o}C for 72 hours before cryopreserving them.

2.1.2 Clonal expansion assays

CFC was performed by gently mixing 70000 cells in 3 ml of semi-solid Methocult H4034 Optimum (Stem Cell Technologies, UK), then left for 14 days, followed by counting colonies using the bright field microscope. Cells also were assayed for LTC-IC by counting CFC content after 5-week coculturing CML cells with 1X10^{4} of two pre-established genetically engineered murine fibroblasts. M2-10B4 (secretes IL-3 and G-CSF) and S1/S1 (produces IL3 and SCF) in MyeloCult™ H5100 (Stem Cell Technologies, UK) supplemented with hydrocortisone in a Collagen I coated plate and followed by gently replacing media each week.

2.1.3 Flow cytometry Ca^{2+} assays

2.1.3.1 Cytosolic and mitochondrial Ca^{2+} level

Flow cytometry dyes and stains for this and the following section are reported (Table 2-12, Table 2-13).

Basal cytosolic and mitochondrial Ca^{2+} levels were measured by staining cells with 5 μM of Indo-1, AM, cell-permeant, and rhodamine AM ester (Rhod-2) for 30 minutes and data acquired by flow cytometry using BD LSRFortessa™ Cell Analyser. The reason behind selecting ester-based chemical dyes is that dyes are inactive until exposed to lysis by esterase enzymes located in either cytosol or mitochondria, ensuring enhanced precise detection of Ca^{2+} level within the cellular site of interest. Briefly, Indo-1 is a UV light—excitable, ratiometric Ca^{2+} indicator. The emission maximum of indo-1 shifts from ~475 nm in Ca^{2+} free medium to ~400 nm when the dye is saturated with Ca^{2+}. Then the level of freely available cytosolic Ca^{2+} was measured as the bound emission fluorescence intensity ratio at 400 nm with the fluorescence intensity at 475 nm. The indo-1 emits at 581 nm after excitation at 552 nm. Indo-1 is combined with 5 μM of the mitochondrial Ca^{2+} dye (Rhod2 AM). The reaction is analysed as a kinetic process of the change in the level of Ca^{2+} versus time (unit=seconds). During the Ca^{2+} level assay by flow cytometry (BD LSRFortessa™; BD Biosciences; Wokingham, UK), cells were exposed to a high concentration of Ca^{2+} stressors (Table 2-10). The

immediate response of cells to stressors was acquired. The kinetic analysis was done by FlowJo software V 10.6.01, BD Biosciences and statistically presented by Graphpad Prism 8.

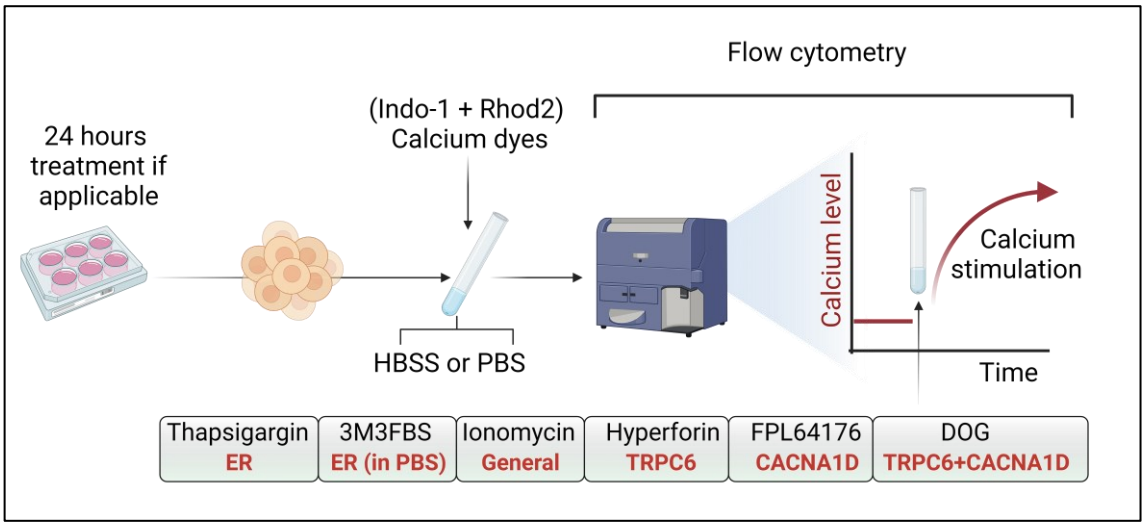

Figure 2-1: Measurement of Ca^{2+} level stimulation.

Cells were initially collected and washed after 24 hours of exposure to treatment. Cells resuspended either in either HBSS (Extracellular 2 mM Ca^{2+}) or PBS (Ca^{2+} free to exclude extracellular Ca^{2+} impact on Ca^{2+} level assay) before staining cells with indo-1 (Cytosolic Ca^{2+} indicator) alongside with Rhod-2 (Mitochondrial Ca^{2+} indicator) for 30 minutes. Cells then exposed to flow cytometry to measure basal Ca^{2+} level. During acquiring data over time (seconds), a specific stimulator is spiked in cells and their acute effect on Ca^{2+} level is recorded. The difference between stimulation level and basal is considered for statistical analysis. Figure is generated using BioRender website.

2.1.3.2 ER Ca^{2+} level assay using dye based Ca^{2+} indicators

Cells stained with Indo-1 and Rhod2 dyes were immediately stimulated with 3 µM thapsigargin, an ER Ca^{2+} mobiliser, to measure ER Ca^{2+} transfer to mitochondria or cytosol. Ca^{2+} levels were measured through instant stimulating cells with 5 µM ionomycin without extra cellular Ca^{2+} supply (PBS without Ca^{2+}) to stimulate Ca^{2+} influx and mobilise Ca^{2+} from ER stores. The immediate response of cells to stressors was acquired. The kinetic analysis was done by FlowJo software V 10.6.01 (BD Biosciences) and statistically presented by Graphpad Prism 8.

2.1.3.3 ER Ca^{2+} level using genetically encoded Ca^{2+} indicator

As previously reported, ER Ca^{2+} level was measured by expressing genetically encoded Ca^{2+} indicator lentiviral construct into K562 cells as reported [199]. As a control, cells were pre-treated with 5 µM 2-Aminoethoxydiphenyl borate, an IP3R inhibitor [200], to retain ER Ca^{2+} content, then measured with flow cytometry upon mobilisation using 25 µM m-3M3FBS a PLC mediated IP3R stimulator when cells suspended in Ca^{2+} free PBS. The immediate response of cells to stressors was acquired.

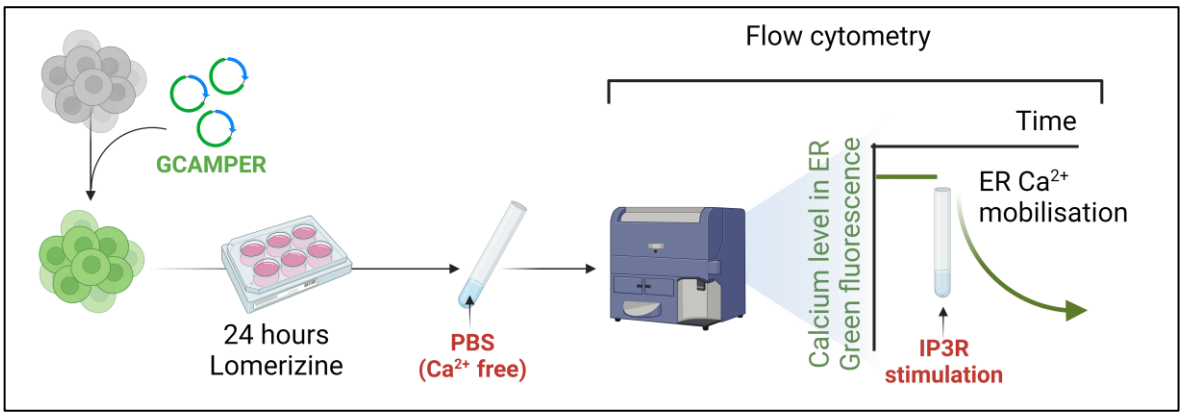

Figure 2-2: ER Ca^{2+} dynamics measurement using GCAMPER.

K562 cells were initially transduced with low affinity green fluorescence ER Ca^{2+} indicator named GCAMPER. GCAMPER expressing cells were collected and washed after 24 hours of exposure to treatment. Cells resuspended in PBS (Ca^{2+} free to exclude extracellular Ca^{2+} impact on Ca^{2+} level assay). Cells then exposed to flow cytometry to measure basal ER Ca^{2+} level. The difference after exposing cells to treatment was unnoticeable, assumably due to low affinity of the GCAMPER construct the can detect Ca^{2+} changes in µM-mM concentration. So, it was important to measure ER Ca^{2+} content after forcedly ER Ca^{2+} mobilisation (Fluorescence intensity drops) when a specific stimulator is spiked in cells and their acute effect on Ca^{2+} level is recorded. The difference between stimulation level and basal is considered for statistical analysis. Figure is generated using BioRender website.

2.1.3.4 Measurement of TRPC6 and CACNA1D mediated Ca^{2+} influx

Ca^{2+} levels were measured following staining with Indo-1 and Rhod2. After measuring basal Ca^{2+} levels, cells were stimulated with 25 µ 1,2-dioctanoyl-cn-glycerol (DOG), an analogue of DAG known to activate TRPC6 and CACNA1D, 25 µM hyperforin, known to activate TRPC6 Ca^{2+} influx, or 25 µM FPL64176 (FPL), known to activate CACNA1D Ca^{2+} influx (Table 2-10). The immediate response of cells to stressors was acquired. The kinetic analysis was done by FlowJo software V 10.6.01, BD Biosciences and statistically presented by Graphpad Prism V8.

2.1.4 Other flow cytometry

Other flow cytometry dyes and stains are described in Table 2-12 and Table 2-13.

2.1.4.1 Apoptosis assay

Programmed cell death (or apoptosis) usually occurs associated with phosphatidylserine translocation to the cell membrane indicating early apoptosis. Annexin V conjugated with FITC or Allophycocyanin (APC), a Ca^{2+} dependent phospholipid binding protein, has a high binding affinity towards phosphatidylserine, enabling to measure cells undergoing early apoptosis by flow cytometry. Also, 7-AAD dye stains cells that undergo necrosis. During flow cytometry analysis, coupling annexin V and 7-AAD enables the cytometer to detect cells that undergo early or late apoptosis.
For cell lines, $2x10^5$ cells in 100 µl HBSS were stained with 3 µl APC-annexin V and 3 µl 7-AAD in a dark room for 15 minutes. For primary cells, $2x10^5$ cells in 100 µl HBSS were stained with 3 µl FITC-annexin V and 3 µl 7-AAD or 3 µl DAPI (like 7-AAD) in a dark room for 15 minutes, and then apoptosis level was measured with flow cytometry following adding 300 µl HBSS to the cell suspension.

2.1.4.2 Erythroid maturation

CD71 and glycophorin A (GlyA) were used to indicate erythroid maturation to erythrocytes. Erythroid maturation was assessed in CML CD34+ cells. CML CD34+ cells were cultured in SFM media for 5 days. Cells ($2x10^5$) were stained with 3µL of GlyA (PerCP/Cy5.5) and 3µL of CD71 (PE) in a 50µL PBS, following 20 minutes of incubation at dark room temperature. Following PBS wash, expressions of CD71

and GlyA were measured on the Fluorescence-activated Cell Sorting (FACS) Verse flow cytometer (BD Biosciences).

2.1.4.3 Oxidative stress

MitoSOX red (Thermo Fisher, UK) is a permeable dye that targets mitochondria explicitly due to the presence of a triphenyl phosphonium cation. Its oxidation by superoxide in the mitochondria results in red fluorescence. CellROX (Thermo Fisher, UK) is a cell-permeable dye that binds and gets oxidised by cytosolic ROS leading to emitting fluorescence that remains in cells.
Cells ($3x10^5$) were stained with 10 µM MitoSOX red or CellROX deep red in 1 ml PBS at room temperature in a dark place for 30 minutes. Following PBS washing, cells were resuspended in 500 µl PBS. MitoSOX dye was used to measure mitochondrial ROS level, using a 7-AAD channel on BD FACS Verse. Meanwhile, CellROX dye was used to measure cytosolic ROS level, using APC channel on BD FACS Verse.

2.1.4.4 Mitochondrial mass

Mitochondrial dyes such as Mito-tracker green or Mito-tracker deep red are cell-permeant dyes that selectively translocate to thiol groups of cysteine residues of mitochondrial proteins their fluorescence reflects the mitochondrial mass. Cells ($3x10^5$) were stained with 100 nM Mito-tracker deep red, followed by incubating at 37^{o}C and 5% CO_2 for 30 minutes. Cells were washed with PBS twice and directly analysed with flow cytometry.
The outer mitochondrial membrane 20 (Tom20) translocase is a ubiquitously expressed protein. The lentiviral construct of eGFP-Tom20 as a mitochondrial localised signal was expressed in CML cell lines, quantifying mitochondrial mass level. Cells ($0.3x10^5$) expressing eGFP-Tom20 were centrifuged and resuspended in 500 µl PBS followed by flow cytometry analysis. The eGFP Tom20 construct was a gift from JR Liang and Jacob Corn labs.

2.1.4.5 Mitochondrial membrane potential

Mitochondrial potential occurs due to protracting protons into mitochondrial inner membrane by mitochondrial complexes (I, III, IV). Those protons are critical for ATP generation by facilitating complex V activity. This change results in -180 mV inside mitochondrial matrix, which reflects the level of mitochondrial activity.

Tetramethyl rhodamine Methyl Ester Perchlorate (TMRM) is a potentiometric dye with high affinity to mitochondrial matrix negative charges, enabling quantifying the level of mitochondrial activity. To assess mitochondrial membrane potential, $3x10^5$ cells were stained with 10 nM TMRM for 30 minutes, followed by PBS twice, and fluorescent intensity was recorded by flow cytometry (excitation: 560 nm and emission: 590 nm). Also, cells were assayed for mitochondrial membrane potential by staining with 2 μM JC-1 Dye (another mitochondrial Membrane Potential Probe). The ration of monomeric mitochondrial (green fluorescence) and mitochondrial aggregates (red fluorescence) indicates the loss of mitochondrial potential.

2.1.4.6 Mitochondrial turnover

Mitophagy flow cytometry analysis was performed using cells expressing retroviral construct mKeima and measured by getting the ratio of fluorescence intensities of mitochondria outside lysosomes (pH=7-8) and those inside lysosomes (pH=4) as previously described [201]. Mitochondrial biogenesis flow cytometry analysis was performed using cells expressing lentiviral pLVX puro Mito-Timer (Construct was kindly gifted from Dr Vega Garcia, Spain [202]).

2.1.4.7 ER flow cytometry assay

ER specific autophagy was measured by expressing Ribosome-associated membrane protein 4 (RAMP4), as previously reported [203].
In addition, ER mass was measured by either staining cells with 3 μM of Bodipy ER tracker red (Thermo Fisher, UK) for 30 minutes before analysing with flow cytometry that gets excited at 587/615 as detected using TRITC or Alexa555 channels on flow cytometry. ER mass was also measured by overexpressing the lentiviral mCherry RAMP4 construct that can be measured with flow cytometry using mCherry spectrum with an excitation peak at 587 nm and an emission peak at 610 nm (kindly gifted by JR Liang and Jacob Corn labs).

2.1.4.8 Cell division assay

CellTrace™ Violet (CTV; Life technologies, UK) diffuses quickly into cells, where it is broken by intracellular esterase enzymes to produce a highly fluorescent derivative that can emit at 405/450 nm. This derivative covalently binds to intracellular amines, resulting in fluorescent staining that is persistent and well-

retained, even during cell divisions. This feature enables the dye to get divided when cells proliferate, resulting in reduction in fluorescence intensity by half.
Primary CD34+ CML cells ($1x10^5$ cells/ml) were stained with 0.1 µM CTV Proliferation dye for 30 min at 37°C. The chemical reaction was quenched by adding up to 50 mL PBS containing 10% FBS into cell suspension. The fraction of stained cells was subjected to measure maximum CTV using pacific blue on BD FACS Verse flow cytometry. The remaining cells were resuspended in SFM completed medium with physiological growth factors in 37°C and 5% CO_2. After 72 hours, CTV staining and CD34 expression levels were assessed by flow cytometry, BD FACS Verse. The ideal CTV histogram generated from FlowJo software produced sequential dilutions of the dye intensities. The distribution of events was split into 3 consecutive populations representing sequential cell divisions (undivided cells; D0=maximum intensity at day 0, single cell division; D1, cells divided twice; D2, cells divided 3 times; D3). The population count on every division was calculated using FlowJo software and plotted using Prism software.

2.1.4.9 Expression of stem cell markers in primary cells

Stem cell enrichment was determined by measuring the level of CD34 and CD133 surface marker expression (CD34+CD133+) or CD34 and CD38 surface marker expression (CD34+CD38-).
Primary CML cells ($1x10^5$ cells) were stained with 4 µL CD34 (APC) and 4 µL CD133 (PE) in 100 µL PBS. The cell suspension was left in dark at room temperature for 20 minutes. The cell suspension was washed and resuspended in 300 µL PBS, followed by subjecting to flow cytometry analysis.

2.1.5 Cell sorting analysis

For isolation of cells expressing lentiviral RAMP4, Tom20, ER-Phagy tandem reporter, or mKeima constructs were sorted with a FACSAria Fusion Cell sorter, BD Biosciences.

2.1.6 Protein quantification

2.1.6.1 Protein extraction in RIPA buffer

Cells were centrifuged and washed twice with ice-cold PBS. Any residual PBS was accurately aspirated. Cell pellet ($1.5x10^6$) was vigorously lysed with 100 µL of commercially available RIPA buffer supplemented with Roche Phostop and cOmplete ULTRA Tablets-EASYpacks, and 10% SDS, using insulin syringes (Table 2-17). Cell lysates were kept on ice for 10 minutes, followed by centrifugation at 16,000xg for 20 minutes at 4^{o}C. The supernatant was stored at -80^{o}C until further use.

2.1.6.2 Cellular protein quantification

The BCA Protein Assay, which stands for "Bicinchoninic Acid", is used to quantify the total amount of protein present in a sample. The fundamental idea behind this technique is that proteins catalyse the reduction of copper ions from Cu^{2+} to Cu^{1+} in an alkaline solution via the biuret reaction, which then produces a purple colour when interacting with bicinchoninic acid. The purple colour is measurable at 562nm λ using Tecan 200 infinite plate reader. Standards of known protein quantity (0-2 µg of bovine serum albumin; BSA) were prepared in 1:2 serial dilutions for quantification. In a clear flat bottom 96 well plate, 10 µL of standard serial dilution BSA were mixed with 190 µL of BCA (Solution A+ Solution B in 1:50 v/v). Simultaneously, 2 µL of sample protein lysates were mixed with 198 µL of BCA (Solution A+ Solution B in 1:50 v/v). The plate loaded with standards and samples was incubated in non-CO_2 incubator at 37^{o}C for 30 minutes, followed by measuring absorbance on Tecan 200 infinite plate reader. The quantity of protein in samples is determined when compared against BSA standard curve values.

2.1.6.3 Protein resolving and quantification

15 µg protein lysate per sample was combined with NuPAGE LDS Sample Buffer (4X) and DDT as reducing agents (Table 2-17). The mixture was boiled at 95°C for 5 minutes before loading into NuPAGE 4-12 % Bis-Tris gel. To figure out the molecular weight of resolved proteins, 5 µL of protein ladder designed to visualise proteins that have molecular weight ranges from 10-250 kDa. Following the loading ladder and samples, running at a constant 100V for 90 minutes with 1X

NuPAGE MES SDS Running Buffer was performed. The wet transfer approach was utilised to transfer resolved proteins from SDS-PAGE to BVDF membrane. The transfer occurred in an ice-cold tank filled with 1X Bio-Rad transfer buffer at 150 mA continuous current for 90 minutes.

The PVDF membrane was washed and blocked with 3% BSA, then incubated on a rotating shaker with 3% BSA in TRIS-buffered saline tween (TBST) containing a recommended concentration of one of the primary antibodies overnight in a cold room. The membrane then was conjugated with Horseradish Peroxidase secondary antibody for 3 hours at room temperature, followed by immunoblotting with either SuperSignal™ West Femto Maximum Sensitivity substrate or Pierce™ enhanced chemiluminescence (ECL) Western blotting substrate. The protein chemiluminescence signal was detected using Odyssey Fc Imaging System, LI-COR Biosciences. Please refer to (Table 2-16, Table 2-17) for Western blot materials and antibodies used.

2.1.7 Cyclic AMP-PKA activity

The level of adenylate cyclase activity was measured by measuring its downstream cAMP mediated PKA activity detection kit according to supplier's protocol. The enzymatic reaction of cAMP/PKA consumes ATP molecules and leads to competition with luciferin, reducing relative luminescence levels as recorded with Promega GloMax Multiplus Plate Luminometer (Table 2-13).

2.1.8 CRISPR-Cas9 technology

CRISPR-Cas9 can be used to edit the human genome by providing cells with plasmid vector (lenti-CRISPR V2) that harbours gRNA relevant to the gene of interest and a Cas9 enzyme construct cuts DNA when gRNA binds to its complementary sequence in human genome.

This approach can be applied upon following these steps:

All plasmid constructs used are reported (Table 2-20).

2.1.8.1 Lenti-CRISPR V2 digestion

Lenti-CRISPR v2 was digested at 37ºC for 3 hours using following contents:

		Add
8	µg	lenti-CRISPR v2
2	µl	BsmBI enzyme V2
6	µl	NEB buffer 10X concentrate
35	µl	Nuclease free water

Finally, 1µl FastAP was added, and reaction mixture was left for another 1 hour. Also, Fast digest Esp3I enzyme was used (BsmBI Isoschizomer) as follows:
The reaction tube was mixed thoroughly and incubated at 37ºC for 30 min using a heat block or incubator.

		Add
X	µl	Nuclease free H_2O
3	µl	10X FastDigest Green buffer (simple flicks, avoid vortex)
2	µg	lenti-CRISPR v2
1	µl	FastDigest enzyme
3	µl	10 mM DTT

FastDigest Green buffer has the same role of Gel Loading Dye, Purple (6X) (New England Biolabs, UK). FastAP Thermosensitive Alkaline Phosphatase (1 U/µL) was added for another 30 minutes.
FastAP and digestion enzyme isoschizomers were heat deactivated at 60°C for 10 minutes, and reaction mixture was chilled on ice before electrophoresis. The digested plasmid was run in a 2% Tris EDTA acetate (TAE) based agarose gel at 100V for 90 minutes. Digested fraction (~11 kb) was precisely cut and purified using QIAquick Gel Extraction Kit (Qiagen). Digested plasmid was quantified using NanoDrop 2000 Spectrophotometer (Thermo Fisher, UK).
N.B: Different vectors modified from Lenti-CRISPR V2 were tested to ensure appropriate interpretation of CRISPR mediated KO: pLentiCrispr-V2-m-Orange (V2mO) (Plasmid #140206, Addgene) possesses orange fluorescence and puromycin antibiotic selection markers. LentiCRISPRv2GFP (Plasmid #82416, Addgene) possesses a GFP selection marker.

2.1.8.2 Cloning gRNA into linearised Lenti-CRISPR V2 vector

To successfully select gRNA oligomers targeting interest genes, gRNAs were customed using the same guides reported by Zang lab (https://zlab.bio/guide-design-resources). Both gRNA oligos were annealed and amplified using polymerase chain reaction (PCR) reaction as follows: Mixture was vortexed before adding T4 PNK ligase (avoid enzyme Vortexing).

6.5	µl	deionised H_2O
1	µl	10X T4 ligation buffer with 10mM ATP
1	µl	Forward oligo (100 µM) (Vortex properly)
1	µl	Reverse oligo (100 µM) (Vortex properly)
1	µl	T4 polynucleotide kinase ligase (flick it 5X)

The phosphorylation/annealing reaction was incubated in a thermocycler using following parameters: 37ºC for 30 minutes, 95ºC for 5 minutes, and then ramping down to 25ºC at 5ºC/minute and finally 10 minutes at 4ºC. The mixture was 200X diluted in nuclease free water (5 µl reaction mixture: 1000 µl water), then collected and stored at -20º C, ready for following ligation with linearised vector reaction.

Digested lenti-CRISPR v2 was then ligated with annealed oligos for 20 minutes at room temperature as follows:

50ng	Digested Lenti-CRISPR v2
1µL	Diluted annealed oligos
5µL	2X Quick Ligase Buffer (NEB)
1µL	Quick Ligase (NEB)
XµL	deionised H_2O up to 10µL total volume

Ligation product was transformed into Mix & Go *Stbl3 E. Coli* bacteria, followed by plating into agar plates supplemented with 100 µg/mL Ampicillin. Single growing colonies were picked and left to grow in 250 ml lysogeny broth (LB) at 37ºC, with shaking at 225rpm overnight. Bacterial culture was pelleted by spinning down at 4000 RPM for 10 minutes. The CRISPR-Cas9 ligated gRNA plasmid was extracted from bacterial pellet by using a Maxiprep kit (Invitrogen). The concentration of gRNA V2 plasmid was quantified using NanoDrop 2000 Spectrophotometer (Thermo Fisher).

N.B: To exclude individual handling errors during synthesis of gDNA construct, same gDNA constructs were ordered from GeneScript (GenScript Biotech, Oxford, UK) using those gRNA oligomers:

TRPC6: TGTATAGGATG AGCCTGATG

CACNA1D guide 1: CAGCAAGCGGACC AGCCGAA

CACNA1D guide 2: TACATCCTAATGCTTATGTT

2.1.8.3 Virus particles generation and infection of CML cells

To generate lentiviral particles that harbour the gRNA plasmid, HEK293FT cells should reach 75% confluency. To achieve that, HEK293FT ($5x10^5$) cells were seeded on a 10 cm^2 petri dish for 3 days. Once confluency was achieved, the following mixture listed was prepared. 183µl of 2.5 M $CaCl_2$ was added dropwise to DNA mixture. Following this, 1.5ml of 2xHBS (Recipe:Table 2-24) was added dropwise to $CaCl_2$-conjugated DNA mixture. The solution must be a little turbid but not precipitating. The suspension was incubated for 20 minutes at 37ºC.

Lentivector	14.2 µg
Packaging plasmid	12.45 µg
Envelope plasmid (pVSVg)	4.5 µg
Nuclease free Water	X µL
	1317 µL final total volume

To HEK293FT at 75% confluent cells with 5 ml completed fresh IMDM medium, the DNA suspension was added dropwise. Cells were gently incubated in 5% CO_2 and 37ºC for 8 hours. Media was gently aspirated and replaced with a 10 ml fresh completed IMDM medium, followed by incubation for 4 days. Medium colour should turn yellowish, indicating that HEK293FT cells were viable growing, ensuring replication of viral particles. The yellowish medium was harvested and passed through a 0.45 µm syringe filter. At least 35 ml of harvested filtered medium per condition was ultra-centrifuged at 25000xg for at least 90 minutes to pellet the virus particles. The supernatant was gently removed, and yellowish pellet was resuspended in 100 µL PBS. The suspension was collected in 1.5 ml Eppendorf tube and put on a shaker at 800 RPM and 25ºC for 3 hours. Serial volumes of concentrated viral particles were added to 10000 leukaemic cell lines in 200 µL of completed RPMI medium in a 96-well plate. The transduced cells were incubated for 6 days in a humidity chamber to avoid evaporation. Another 500 µL of completed RPMI medium was added on the fourth day to support cell growth. Control pLKO-GFP viral concentrate was included as a positive control to monitor the best viral concentration that successfully generated 100% transduced cells (cells that express GFP). Cells were collected and resuspended in 4 ml of completed RPMI supplemented with 1 µg/ml puromycin. The cell suspension was incubated for another 3 days. Cells were collected in 15 ml falcon tubes,

centrifuged, and washed twice with PBS at 200xg low speed, then reintubated for another 5 days in 5 µg/ml puromycin.
For cells transduced with viral particles of lenti-CRISPR V2 GFP or m-Orange origin, the selection of successful cells was based on expressing fluorescence markers, using BD FACSAria™ Fusion sorter, instead of puromycin selection in culture.

2.1.9 DNA extraction and sequencing

To validate successful gene editing, DNA editing was verified using next-generation sequencing. Genomic DNA from cell lines generated was extracted and purified by GeneJet Genomic DNA purification kit (Table 2-21). In order to amplify genomic DNA that flanks the gDNA motif, a set of oligonucleotide primers were designed using the UCSC genome browser (https://genome-euro.ucsc.edu/cgi-bin/hgGateway) and Primer3 V0.4.0 platforms (https://bioinfo.ut.ee/primer3-0.4.0/).

Table 2-1: Set of Primers used for PCR the gRNA flanking regions.

Primer name	Type	Guide	Sequence	Melting temp.	GC%	Length
CACNA1D	F	1	GCTGAAGCGAGAATAAGG	56.1 ºC	55 %	20
CACNA1D	R	1	AGGACACTGAACCCGAAT CA	56 ºC	50 %	20
CACNA1D	F	2	TGGAGGGAAATGCTTATA	53.6 ºC	39.1	23
CACNA1D	R	2	GCAGCATCACCAGCCTTAAA	55.9 ºC	50 %	20
TRPC6	F	1	TCATGAGGCCGTTCAATCCT	56.4 ºC	50 %	20
TRPC6	R	1	TCGAGGACCAGCATACAT GT	55.8 ºC	50 %	20
TRPC6	F	2	GACTCGGCACCAGATTGAAG	55.8 ºC	55 %	20
TRPC6	R	2	AAGCATCACTGGGGTCTGAG	56.5 ºC	55 %	20

Using PCR, genomic DNA was amplified using high fidelity *Taq* polymerase (Table 2-18). Amplicons were purified using the Monarch PCR and DNA Cleanup Kit. Amplicons were verified using 2% agarose gel electrophoresis. Only a single tight band at around 600 was visualised using an ultraviolet illuminometer. PCR amplicons were quantified using Nanodrop 2000.
DNA sequencing was performed using The Applied Biosystems (BigDye Terminator v3.1) for the setup of sequencing reactions and precipitation of sequenced DNA. PCR amplicons were sequenced using Applied Biosystems PRISM 3130xl (16 capillaries) sequencer. To view sequencing results on software platforms such as Snapgene or Vector NTI, raw sequencing output was initially curated using ABI

Prism Seqscape software, where results are provided as an Applied Biosystems sequence trace file ". *ab1*". Sequencing analysis verified successful genomic editing using online platforms, such as Tide (http://shinyapps.datacurators.nl/tide/) and Chromas V2.6.6.

2.1.10 Bacterial transformation

All lentiviral or retroviral-based plasmid constructs (Table 2-19) were transformed using Mix&Go *E. coli* Transformation Kit & Buffer set, according to manufacturer protocol (Table 2-21).

2.1.11 Metabolomics

2.1.11.1 Isotope labelling

The RPMI supplemented with 11 mM fully labelled glucose isotope ([$^{13}C_6$] glucose) (Cambridge biosciences, UK) was used as a growth medium for K562 cell line at a concentration of 0.2 × 10^6 cells/ml for 24 hours. Primary cells were recovered overnight in SFM completed medium supplemented with unlabelled metabolites. At least 50% of recovery must be achieved to avoid mis interpretation of results because of a high level of apoptotic cells that may interfere with the final judgement. Recovered primary cells were then plated in the presence of11 mM [$^{13}C_6$] glucose or 100 µM [$^{13}C_{16}$] palmitate for 24 hours at a concentration of 0.2 × 10^6 cells/ml in a serum-like culture medium (Plasmax) that comprises trace elements required for proliferation found in the plasma of human blood for 24 hours (Table 2-23).

2.1.11.2 Extraction of metabolites

Cells were counted using an automated CASY counter; counts were recorded for normalisation at the end of the experiment. Equal cell counts of different conditions were considered for extraction. Cell lines or primary cells were washed twice with ice-cold PBS. To extract intracellular metabolites, cells were centrifuged and lysed with ice-cold extraction solvent (methanol, acetonitrile, and high-performance liquid chromatography (HPLC) grade water at 5:3:2 ratios) within 5 minutes on ice. The cell lysates were centrifuged at 16,000xg for 10 minutes at 4^{o}C. Finally, supernatants were collected and kept in -80^{o}C till being

subjected to LCMS analysis. Please refer to (Table 2-15) for the extraction solvent recipe.

2.1.11.3 Metabolites analysis (LCMS)

Cell lysates were exposed to the Q-Exactive Orbitrap mass spectrometer coupled with the UltiMate 3000 HPLC system (Thermo Scientific). The HPLC was composed of a ZIC-pHILIC column (SeQuant, 15 × 0.21 cm, 5 µm) with a ZIC-pHILIC guard column (SeQuant, 2 × 0.21 cm, Merck KGaA). The organic mobile phase was acetonitrile, and the aqueous mobile phase solvent was composed of 0.1% NH_4OH with 20mM $(NH_4)_2CO_3$. The metabolites were separated over a linear spectrum from 80% organic to 80% aqueous at 45^oC. The flow rate was 200 µL/minute for 22.2 minutes. All metabolites were acquired across a 75–1,000 m/z mass range and 35,000 (at 200m/z) resolution using the Q-Exactive mass spectrometer with electrospray ionisation and polarity switching mode. The mass detection accuracy was below 5 p.p.m for all metabolites.

2.1.11.4 Statistical analysis of metabolite levels

Metabolites' raw peak intestines retention times were calculated against known standard metabolites values using TOXOID. TraceFinder software platform was used for detecting those peak intensities, reflecting what metabolite and the level of this metabolite. Peak intensities of metabolites were normalised against the standard solvent artefacts. Those normalised intensities were corrected according to cell number and peak volume. Finally, the relative isotopologue levels were visualised using Autoplotter V2.4 online platform. Bioinformatics and statistical analysis of differential targeted labelling was performed using Metaboanalyst V5.0 online platform.

2.1.12 Seahorse metabolic assays

Metabolic processes occur when cells require energy molecules to support their sustainability. By this, cells burn different carbon sources and consume oxygen from the medium required to perform OXPHOS. Also, cells can utilise glucose as a carbon source to fuel glycolysis producing lactate (acidity to the medium). Live cell metabolic experiments were performed using the Agilent Seahorse XFe96 analyser. The Seahorse analyser is a device that can monitor two media

parameters: oxygen consumption rate (OCR) and extracellular acidification rate (ECAR). ECAR reflects cells' glycolytic activity, and OCR reflects cells' OXPHOS activity. The OCR assay on intact cells is titled as mitostress test. The ECAR assay on intact cells is titled Glycostress.

On the day before the assay, because CML cells are non-adherent, the kit cell plate was coated with 25 µL/well with Cell-Tak mixture (Corning, UK) for 30 minutes (0.02mg/mL Cell-Tak mixture was prepared by mixing appropriate Cell-Tak stock volume in 2.5 ml of 0.1 M $NaHCO_3$, and pH was adjusted to 7.4 with 0.1 M NaOH) (Seahorse media additives: Table 2-23). The cell plate was then washed with distilled water or PBS and left at room temperature overnight to dry. Kit cartridge plate was loaded with 200 µL calibrant solution and wrapped in parafilm to avoid evaporation before overnight placing at 37°C in the non-CO_2 incubator.

On the experimental day, cells were collected by centrifugation, counted, resuspended in completed Seahorse media (Table 2-23) and seeded in Cell-Tak coated plate to achieve $0.1x10^6$ in 175 µL per well. Cell loaded plate was spun down at 200xg for 1 minute and then left for 25 minutes at 37°C in a non-CO_2 incubator.

An assay cartridge was loaded with stressors at 25 µL/ port in Seahorse media (Table 2-23), which is left on non-CO_2 incubator for 10 minutes before loading into the analyser. After analyser finished calibration and loading cartage, cell plate was loaded to the analyser to read out either the mitostress profile or Glycostress profile.

As shown (Figure 2-2), the mitostress analysis was designed for measuring OCR, where basal OCR was first acquired, followed by sequential injections of stressors from sensor cartridge as follows: (A) 1 µM oligomycin, an ATP synthase (complex V) inhibitor, (B) 1.6 µM carbonyl cyanide-4-(trifluoromethoxy) phenylhydrazone (CCCP), a mitochondrial complex-IV uncoupler, and (C) 1 µM antimycin A (complex III) and 1 µM rotenone (complex I) (all from Sigma Aldrich).

The Glycostress assay was designed to measure the acidity of the medium, where basal ECAR was acquired, followed by sequential injections of stressors from the sensor cartridge as follows: (A) 11 mM glucose (B) 1 µM oligomycin that inhibits OCR and forces cells to use glycolysis (C) 4 µM 2-deoxy glucose, phospho-glucose isomerase inhibitor (all from Sigma Aldrich). The profile output was then analysed using the Seahorse desktop software Wave (Agilent).

2.1.13 Respiratory complexes activity

Another modified OCR-based approach was designed to measure mitochondrial activity through permeabilising cell membrane *in situ* (Figure 2-3). The OCR assay on permeabilised cell membrane directly measured different mitochondrial respiratory chain complexes' activity.

Drugs can indirectly modify mitochondrial activity by controlling mitochondrial mass, fission fusion status, or degrading mitochondria by activating mitophagy. Those therapeutic activities may interfere with the analysis output. To avoid misinterpreting results from this experimental approach, drugs that specifically block one of the mitochondrial complexes should not target cells longer than 4 hours.

Seahorse cell assay media was replaced with mannitol and sucrose buffer (MAS-BSA) (220 mM mannitol, 10 mM KH2PO4, 70 mM sucrose, 5 mM MgCl2, 1 mM EGTA, 2 mM HEPES, 4 mg/mL FFA-BSA, pH at 7.2: Table 2-23). The assay plate cartridge was hydrated as before. Cells were loaded to kit assay plate precoated overnight with Cell-Tak at $1X10^5$ / well as previously mentioned. Plated cells were acclimatised at 37^oC in a non-CO_2 incubator for less than 10 minutes. During the acclimatisation of cell plate, the assay sensor cartridge was loaded with different mitochondrial complexes substrates and cell membrane permeabiliser (saponin). Baseline OCR measurements were recorded for intact cells. Then, cells were stressed and permeabilised simultaneously by injecting stressors from sensor cartridge ports. It has been shown that once the membrane is permeabilised and ADP and substrate injected, mitochondria respire at the maximal rate, called state III. State III describes the activity results from complex V (ADP dependent; state II or state IV) and the activity of the complex of interest (complex substrate dependent; known as state I). The complex V activity (state I) is lost either due to ADP depletion or after injecting oligomycin as a complex V inhibitor. Thus, state III and state II or IV has been shown to ascribe the respiratory control ratio (RCR) that reflects the complex activity [204]. Please refer to (Table 2-8, Table 2-25) for membrane permeabilisation OCR materials.

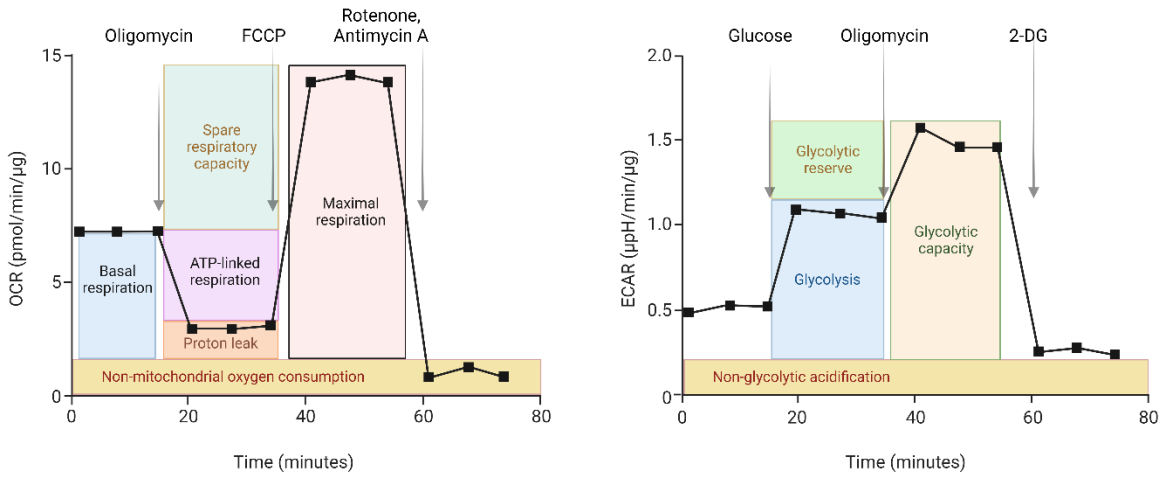

Figure 2-2: Mitostress and Glycostress metabolic profiles by Agilent Seahorse.

The figure on the left-hand side illustrates the mitostress test profile. Cells' OCR is assessed after a series of injections of oligomycin, which inhibits complex V of the ETC; CCCP, which disrupts the proton gradient and mitochondrial membrane potential; and Rotenone, which inhibits complex I and III, respectively.
The right-hand side figure illustrates the Glycostress test profile. The ECAR of cells is measured after injections of glucose, which promotes glycolysis; oligomycin, which inhibits complex V of the ETC and further promotes glycolysis; and 2-deoxy-glucose (2-DG), a glucose analogue that inhibits glycolysis by competing for glucose hexokinase binding site (Images are adapted from Agilent Seahorse website and designed with BioRender online platform).

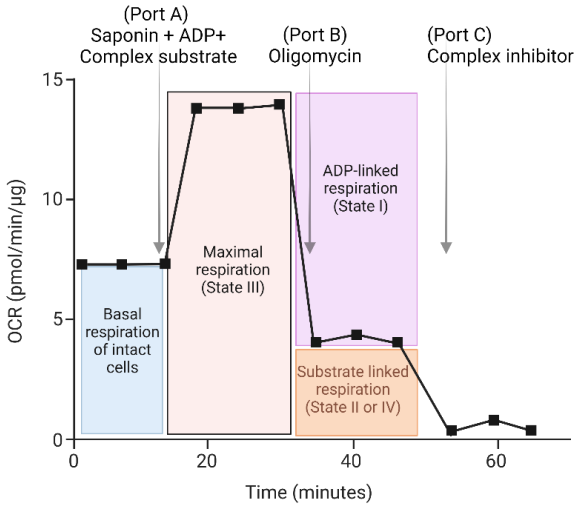

Figure 2-3: Membrane permeabilisation and mitochondrial complex activity measurement.

OCR is used to measure mitochondrial complex activity. First, the basal OCR level of intact cells is recorded. Then cells are stressed and permeabilised through injecting a series of complex substrates and inhibitors: ***Port A*** Cell membrane is permeabilised with saponin. Respiratory chain complex V is activated by ADP injection. Lastly, one of the specific complex substrates are injected alongside saponin and ADP. The final working concentrations of ADP (1 mM), saponin (30 µg/mL) and (complex I substrate; 10 mM pyruvate, 5 mM malate), (complex II;10 mM succinate, 1 µM rotenone), or (com-IV; 0.5 mM TMPD, 2 mM ascorbate). ***Port B*** complex V is inhibited by injecting oligomycin; oligomycin A (1.5 µM). ***Port C*** Only one specific complex inhibitor is injected to completely shut down the remaining complex activity; complex I (1 µM rotenone), complex II (2 µM antimycin A), and complex-IV (20 mM azide). The profile output was then analysed using the Seahorse desktop software Wave (Agilent).

2.1.14 IDH3 activity

The nicotinamide adenine diphosphate (NAD^+) dependent IDH3 activity was performed using the IDH activity assay kit according to the manufacturer's protocol (Sigma Aldrich, UK). The IDH3 activity was assayed in cell extracts using the IDH3 substrate and the cofactor NAD^+ in an enzyme reaction, resulting in a colourimetric product (450 nm) proportional to NADH production. The enzyme activity was calculated according to the NADH standard curve. Each unit of IDH3 reflects the amount that will produce 1.0 µmol NADH, which is traced calorimetrically every 5 minutes for an hour.

2.1.15 Animal studies

All animal experiments were carried out under the Animals Scientific Procedures Act of 1986 and following the University of Glasgow Animal Welfare and Ethical Review Board (AWERB) under a Home Office Licence. All experiments were performed under Prof Vignir Helgason's licence (# PPL number PP2518370) and Ahmed Khalaf's Personal Licence (# PIL number I82823224). Mice were accommodated in a pathogen-free facility with day/night cycles (12 hours each). Mice were given unlimited access to food libitum, soft hydrogels (when required) and water.

2.1.15.1 NRGW41 mouse model

In 2017, the Eaves lab developed the NRGW41 immunocompromised mouse model [205]. These mice lack the $Prkdc^{scid}$ allele, which increases ionising radiation sensitivity. Due to the absence of the stem cell growth factor receptor KIT in these mice, human cell engraftment is proved. The absence of interleukin-2 (IL2) receptor gamma chain and recombination activating gene 1 (Rag1) impairs the maturation of T and B-cells.

2.1.15.2 KCL22 xenograft

KCL22 expressing lentiviral firefly luciferase cells were selected with 5 µM puromycin *in vitro* culture for 10 days. NOD-NOD-$Rag1^{-/-}$-$IL2Rgc^{-/-}$ -W^{40} variant (NRG-W41) female mice have transplanted IV with luciferase expressing KCL22 cells (4 x 10^6 cells/mouse). Transplantation and extramedullary tumour formation were monitored using *in vivo* imaging system for small animals (IVIS, PerkinElmer, UK) luciferase bioluminescence imaging. Imaging was performed after 30 minutes

of cell transplantation wherein transplanted mice were anaesthetised with isoflurane gas 5 minutes before imaging to monitor tumour burden. To visualise cells, anaesthetised mice were injected subcutaneously with 200µL D-luciferin and analysed by imaging luciferase bioluminescence (photon radiance approach) via *in vivo* imaging system (IVIS) at 550 nm and 620 nm filters spanning to efficiently record positive signals. This procedure was repeated weekly to monitor tumour burden. Transplanted mice were imaged for tumour development during this procedure following luciferin injection and anaesthesia. Before drug administration, mice must show a luminescent IVIS signal indicating engraftment/tumourigenesis. Drug treatment started in the third week. Mice were randomly allocated into four groups (6 mice/group): vehicle (saline) control, lomerizine (80 mg/kg once daily morning I.P.), imatinib (50 mg/kg oral gavage twice daily), and a combination of lomerizine with imatinib group. Imaging of mice was expected to be done every week after treatment.

2.1.15.3 Patient derived xenograft (PDX)

Female NRGW41 mice aged 8-13 weeks were sub-lethally irradiated (2X 100 cGy). After 24 hours, mice were transplanted with 200 µl of PBS containing 2% FBS and 1.3 x 10^6 human CD34+ CML cells via the tail vein. Seven weeks after the transplant, successful transplantation was measured following the same protocol. One of those mice was culled, and bones (tibia, femur, and hip bones), spleen, and blood were collected and processed to isolate cells of interest, as described in the following section.

The rest of the mice were left for another week before initiation of treatment after week 8 of transplantation. Mice were randomly allocated into four groups (5-6 mice/group): vehicle control, lomerizine (80 mg/kg once daily morning I.P.), imatinib (100 mg/kg oral gavage twice daily), and a combination of lomerizine with imatinib group. Mice were treated for another 4 weeks before culling them using the schedule-I method. Culled mice were dissected where bones, spleen, and blood were collected further to assess their engraftment and level of stem cells.

i) Isolation of cells for analysis

Blood cells (600 µl/mouse) had to be processed by incubating for 10 minutes at room temperature with 2 mL of red blood cell lysis buffer (8.02 g/L ammonium acetate, 1 g/L potassium bicarbonate, 0.02 g/L EDTA in purified water). Remaining cells in lysed mixture were washed with 2 mL of PBS and centrifuged at 400 x g for 5 minutes. In a total 400 µL, 200 µl were stained with each antibody mixture.

The spleen was crushed between a 40 µm cell strainer and a 10 ml-syringe plunger before being flushed with a 20 ml solution of 2% FBS PBS. The cell suspension was centrifuged at 400 x g for 5 minutes, followed by decantation of supernatant and cells were resuspended in a total volume of 400 µL; 200 µl were stained with each antibody's mixture.

Clean bones (tibia, femur, and hip bones) / mice were collected and cut into two halves. The cut pieces of bones were split into two 0.5 ml Eppendorf tubes with a tiny needle hole at its bottom and fitted into a 1.5 ml Eppendorf tube containing 200 µl 2% FBS/PBS. The double tubes were centrifuged at 12000 x g for 15 seconds to allow cell leakage to 2% FBS/PBS. Cells were resuspended into 1 ml of 2% FBS/PBS and then strained against a 40 µm cell strainer. Cells were split into two halves and centrifuged at 400 x g for 5 minutes. One-half was used to store BM cells. The other half cells were resuspended into 400 µl 2% FBS/PBS. In a total of 400 µL, 200 µl were stained with each antibody mixture.

ii) PDX analysis by flow cytometry

A CASY cell counter was used to measure cell concentrations. Flow cytometry was used to analyse the cells further, as described below.

To adjust flow cytometry gates appropriately, compensation beads were used instead of cells to set appropriate single channels on flow cytometry. After setting the gating strategy on flow cytometry, fluorescence minus one (FMO) were pooled using a small fraction from all samples to avoid wasting cells from a single arm.

The actual measurement of those extracted cells (BM cells, spleen cells, or blood circulating cells) was characterised by measuring the level of human myeloid cells (human CD45+ CD33+) and human myeloid stem cells (human CD45+ CD34+ CD133-/CD38-) using a specific panel of antibodies staining and flow cytometry analysis (Table 2-2). To prevent nonspecific antibody binding, 0.5 µL murine Fc block was

added per sample. Cells were incubated in the dark for 20 minutes at room temperature. Cells were then washed with 1 mL PBS, centrifuged for 5 minutes at 350 x g, resuspended in 250 µl PBS, and analysed with Attune X flow cytometer (BD Biosciences).

Table 2-2: Panel of antibodies used to assess PDX successful engraftment.

Target	Species	Fluorophore	Use x µL/ sample	Attune channel
murine CD45	Murine	APC	1.25	RL1
human CD45	Human	FITC	10	BL1
CD33 PE	Human	PE	3	YL1
CD19	Human	PE-Cy7	1	YL4
Fc block	Murine	--------	0.5	

Table 2-3: Panel of antibodies used to assess level of engrafted human stem cells.

Target	Species	Fluorophore	Use x µL/ sample	Attune channel
CD45	Murine	APC-Cy7	1.25	RL3
CD45	Human	FITC	10	BL1
CD34	Human	APC	2	RL1
CD38	Human	PerCP	2	BL3
CD133	Human	PE	2	YL1
Fc block	Murine	--------	0.5	

2.1.16 Bioinformatics analysis

2.1.16.1 Dataset attributes

Raw data of two publicly available HuGene-1_0-st-v1 Affymetrix arrays on the ArrayExpress website were analysed with the following attributes:

E-MTAB-2581: Leukaemic peripheral blood cells were obtained from individuals with chronic phase CML using leukapheresis at the point of diagnosis. Normal samples were mobilised from BM of donors. Both tissue $CD34^+$ cells were enriched using the sterile CliniMACS system (Miltenyi Biotec, Bisley, UK) and cryopreserved in liquid nitrogen. They were frozen and recovered overnight in a serum-free medium (SFM) supplemented with a cocktail of physiological growth factors. This was followed by a cell sorting method employing CD34-APC and CD38-FITC tagged antibodies. Cells were sorted as either $CD34^+CD38^-$ as haematopoietic stem cells (HSC) or $CD34^+CD38^+$ haematopoietic progenitor cells (HPC).

E-MTAB-2594: Cells were treated with 5μM imatinib, 150 nM dasatinib, or 5 nM nilotinib for 8 hours (CD34+38) or 7 days (CD34+) without including growth factors. After 7 days of treatment, viable cells were collected, and cDNA was extracted for chip hybridisation. So, extracted cDNA came from cells that are persistent to TKI treatment.

2.1.16.2 R and R-Studio analysis

i) Quality control and normalisation

The probe intensities are presented using a graphical boxplot with one box for each chip. The (oligo: boxplot) function in the R platform can extract the expression matrix as an argument. It performs a log2-transformation as the default setting. However, the variation of probe intensity varies between different arrays.

ii) Background effect exclusion, calibration, and summarisation

The oligo package in the R platform performs background correction and normalisation. It collects different representative probes for single genes (probeset) summarisation in a single step via a deconvolution for background correction, quantile normalisation, and the RMA (robust multichip average) calculations for summarisation [206] (Figure 2-3, Figure 2-4)

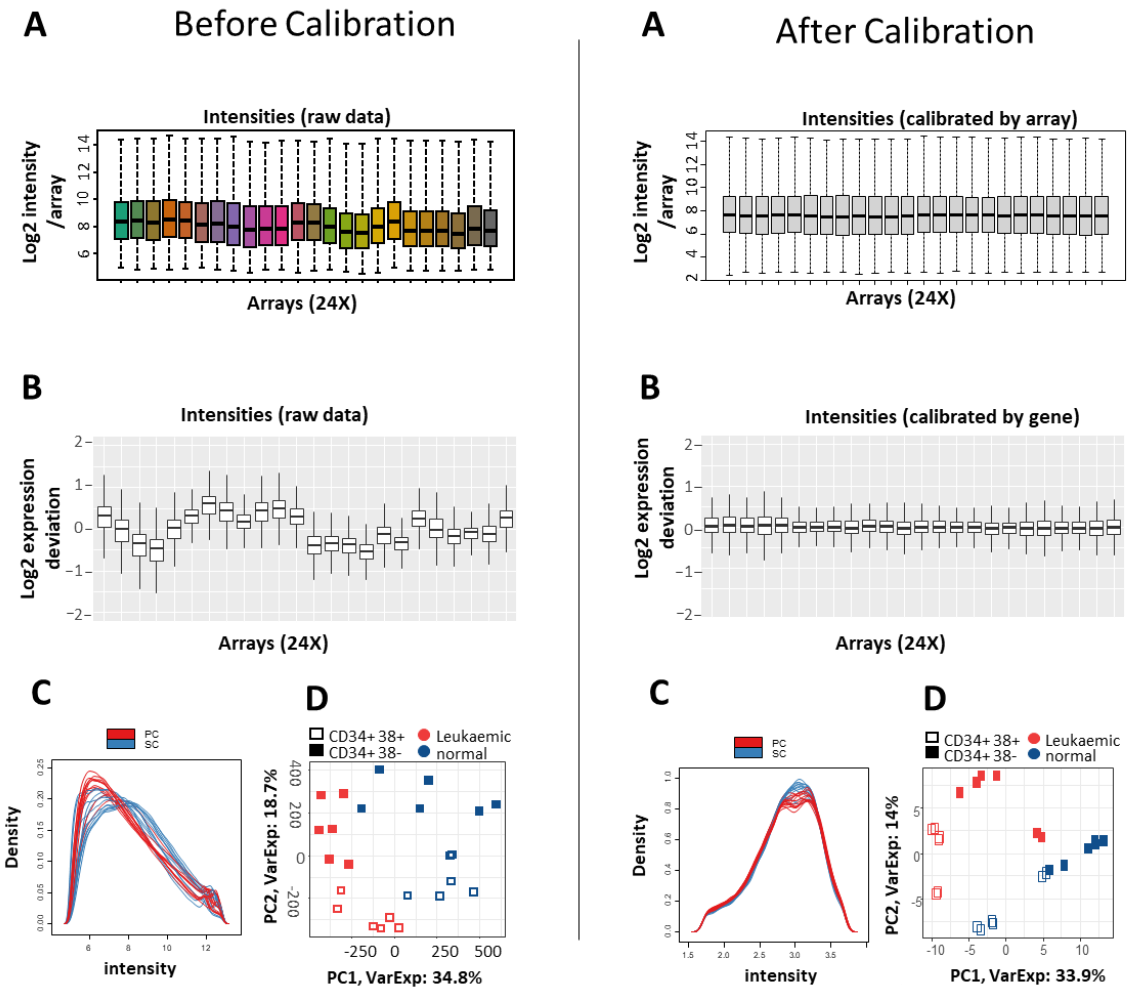

Figure 2-3: E-MTAB-2581 microarray calibration.

Twenty-four raw microarray data (left panel) were downloaded and normalised with RMA package (right panel). (A) $\log_2$ expression intensities per array. (B) relative log2 gene expression deviation per array is performed by getting median $\log_2$ intensity of each gene across all arrays. (C) density plot showing distribution of lowly to overly expressed genes for all arrays as a median intensity (x) against density (y). (D) representative principal component analysis (PCA) output of clustered normal stem cells (CD34+/CD38-), normal progenitors (CD34+/CD38+), or their leukaemic stem and progenitor counterparts. PCA plot depicts distribution of gene profile of each cell phenotype.

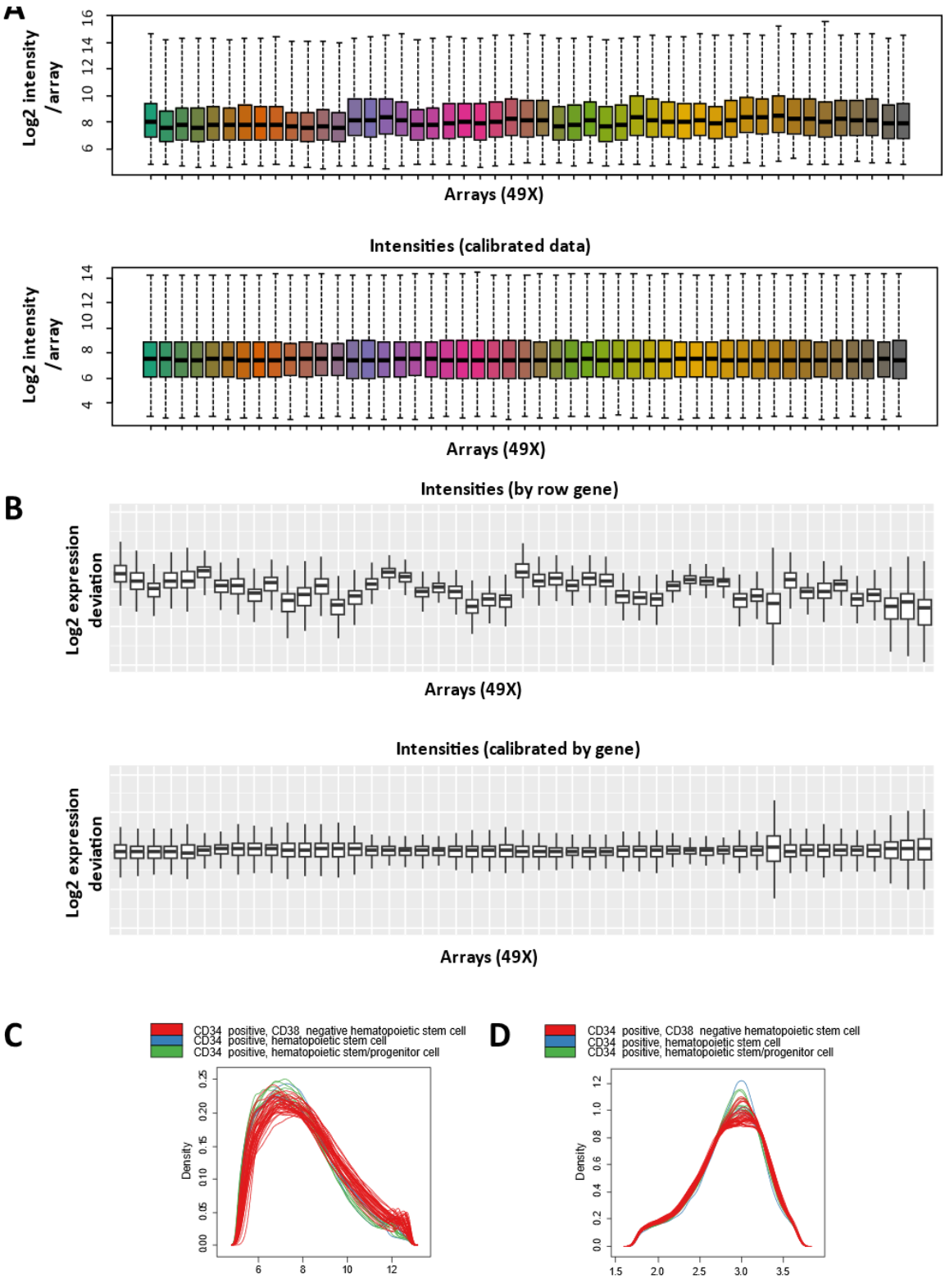

Figure 2-4: E-MTAB-2594 microarray calibration.

Forty-nine raw microarray data were downloaded and normalised with RMA package
(A) log2 expression intensities per array. (B) Relative log2 gene expression deviation per array is performed by getting median log2 intensity of each gene across all arrays. (C) density plot showing distribution of lowly to overly expressed genes for all arrays as a median intensity (x) against density (y).

iii) Filtration of low expressed or hard-to-detect genes

Low expressed genes are arbitrarily removed from datasets to enhance analysis quality control. However, after normalisation, histograms of the density distribution of datasets showed a superior level of fidelity and did not require any genetics filtration.

iv) Annotation of the probest clusters

The function selected from (AnnotationDbi) into the R platform to query the genetic symbols and affiliated brief descriptions for the probest clusters. For each cluster, the gene symbol (SYMBOL) was manually attributed plus a brief description of the representative gene (GENE NAME). However, to proceed, multi-mapped genes were removed from data sets because probest can be denoted to different genes, and this may be the reason for data to be lost which cannot be avoided.

v) Extraction of differential expression genes by linear model

The linear model is applied to expression data to determine which genes are differentially expressed between the different conditions of the specified data set. Linear models are the "workhorse" of experimental data analysis. The linear model can be easily applied via recalling the “limma” package into R platform [207].

vi) Multiple testing, false discovery rate (FDR)

The probability concept is used to describe how far the null hypothesis can get accepted where the difference between arrays is not significant. The less probability fraction of one unit, the more confidence to accept the alternative hypothesis. Benjamini & Hochberg known or FDR algorithms were used at probability threshold (≤ 5%) [208].

vii) Gene set enrichment analysis (GSEA)

The GSEA was performed with GSEA (v4.1.0) from the Broad Institute (http://www.gsea-msigdb.org/gsea/index.jsp); q values were computed using one thousand permutations of the phenotypic label. Enrichment statistics were calculated by hypergeometric distribution [209].

2.1.17 Statistical analysis and graphical illustrations

Data were visualised and analysed by Graphpad Prism (V 7 and V 8.1.0). No specific statistical method was used to determine sample size; however, the author used at least 3 biological or technical replicates to perform any statistical analysis. The statistical test was applied mainly for those who follow a normal distribution. For example, to compare 2 samples, an unpaired Student's t-test was used. To compare between more than 2 samples, an analysis of variance (ANOVA) was applied. Most of the cases, Tukey test was applied for multiple comparisons if number comparisons were between more than 3 means. If comparisons were between only 3 means, the Fishers Least Significant Difference (LSD) test was considered. Significance was considered only when a cut-off of $P < 0.05$ was defined as statistically significant. Only, for Seahorse Flux assays, two-way ANOVA were performed. For *in vivo* survival curve, the log-rank (Mantel-Cox) test was used to assess the statistical difference between different mice groups.
All graphical illustrations were designed using licensed BioRender online platform.

2.2 Materials

2.2.1 Incubation and growth of cells

Table 2-2:: Cell culture and incubation media.

Product	Manufacturer	Cat. N
Dulbecco's Phosphate Buffered Saline (DPBS)	Gibco	14190-094
Dulbecco's Modified Eagle Medium (DMEM)	Gibco	21969-035
Glucose-free Earle's Balanced Salt Solution (EBSS)	Gibco	14155048
Hank's Balanced Salt Solution (HBSS) (10X), Ca^{2+}, Magnesium, No Ph. Red	Gibco	14065049
Iscove's Modified Dulbecco's Medium (IMDM)	Gibco	21980
MethoCult™ H4034	Stem Cell Technologies	4034
MyeloCult™ H5100	Stem Cell Technologies	0515
Roswell Park Memorial Institute Media (RPMI) 1640	Gibco	31870-025

Table 2-3: Additives to the growth medium.

Product	Manufacturer	Cat. Number
2-Mercarptoethanol	Life Technologies	21985023
Bovine Serum Albumin (BSA)	Gibco	11021045
BSA insulin and transferrin (BIT) 9500 Serum Substitute	Stem_Cell_Technologies	9500
FBS	Gibco	10500064
Glucose	Sigma Aldrich	G7021
L-Glutamine	Life Technologies	25030-024
Low density lipoprotein	Sigma Aldrich	L4646
Sodium pyruvate	Gibco	11360070
Transferrin	Sigma Aldrich	T4132-100MG
[13C16] palmitate	Cambridge Isotope Laboratories	CLM-6059

Table 2-4: Cell culture selection antibiotics.

Product	Manufacturer	Cat. Number
Ampicillin	Sigma Aldrich	A5354-10ML
Blasticidin S hydrochloride	Fisher Scientific	10658203
Penicillin-Streptomycin	Life Technologies	15140-122
Puromycin Dihydrochloride	Life Technologies	12122530

Table 2-5: Growth factors for primary cell culture.

Product	Manufacturer	Cat. Number
Human Flt3-Ligand	PeproTech	300-19
Human granulocyte colony-stimulating factor (G-CSF)	PeproTech	300-23
Human granulocyte-macrophage CSF (GM-SCF)	PeproTech	300-03
Human insulin solution	Sigma Aldrich	I9278-5ML
Human interleukin-6 (IL-6)	PeproTech	200-06
Human leukaemia inhibitory factor (LIF)	PeproTech	300-05
Human macrophage inflammatory protein α (MIP-1α)	PeproTech	300-08
Human serum albumin	National Blood Transfusion Service	
Human stem cell factor (SCF)	PeproTech	300-07

Table 2-6: Seahorse media additives.

Product	Manufacturer	Cat. Number
Carbonyl cyanide 3-chlorophenylhydrazone (CCCP)	Sigma Aldrich	C2759
2-Deoxyglucose	Sigma Aldrich	154-17-6
ADP	Sigma Aldrich	72696-48-1
Antimycin A	Sigma Aldrich	A8674
Sodium Azide	Sigma Aldrich	26628-22-8
Cell-Tak	Corning	354240
D-Mannitol	Sigma Aldrich	69-65-8
EGTA	Sigma Aldrich	67-42-5
Malate	Sigma Aldrich	97-67-6
Oligomycin	Sigma Aldrich	O4876-5MG
Rotenone	Sigma Aldrich	R8875
Saponin	Sigma Aldrich	8047-15-2
Seahorse XF Base Medium	Agilent Technologies	102353
Seahorse XFe96 FluxPak (includes calibrant)	Agilent Technologies	102416-100
Succinate	Sigma Aldrich	110-15-6
Sucrose	Sigma Aldrich	57-50-1
TMBD	Sigma Aldrich	637-01-4

Table 2-7: Buffering reagents for cell culture.

Product	Manufacturer	Cat. Nu.
HEPES	Sigma Aldrich	H3375-100G
Sodium bicarbonate ($NaHCO_3$)	Sigma Aldrich	S5761
Sodium chloride (NaCl)	Sigma Aldrich	S5886
Sodium hydroxide (NaOH)	Sigma Aldrich	S0899
Sodium phosphate dibasic dihydrate (Na2HPO4 · 2H2O)	Sigma Aldrich	10028-24-7

2.2.2 Drug reagents

Table 2-8: Drugs used for treatment.

Product	Manufacturer	Cat. Number
2-Aminoethoxydiphenyl borate	Sigma Aldrich	D9754
3-nitrocoumarin	MedChem Express	HY-111919
BI-749327	Axon Medchem B.V.	3036
Bafilomycin	Sigma Aldrich	88899-55-2
EGTA	Tocris Bioscience	67-425
Hydroxychloroquine Sulphate	Merck	PHR1782-1G
IACS-010759 -10759	Selleckchem	S8731
Imatinib Mesylate	LC Laboratories	I-5508
Lomerizine	APExBIO; Stratech Ltd	B1782
Lomerizine	Abcam Plc	ab142528
N-acetyl-L-cysteine (NAC)	Sigma Aldrich	A9165-25G
Nicardipine hydrochloride	Medchem Express	HY-12515A

Table 2-9: Drug solvents.

Product	Manufacturer	Cat. Number
Dimethyl Sulfoxide (DMSO)	Sigma_Aldrich	D2660
Pluronic™ F-127	Thermo Fisher Scientific	P3000MP
Tween 80	Sigma Aldrich	9005-65-6

Table 2-10: Ca^{2+} stimulators.

Product	Manufacturer	Cat. Number	Target
Thapsigargin	Bio-Techne	67526-95-8	ER Ca^{2+}
3M3FBS	Sigma Aldrich	T5699	PLC or ER Ca^{2+}
Ionomycin	TOCRIS Biosciences	56092-82-1	Ca^{2+} mobiliser
1,2-dioctanoyl-cn-glycerol	Sigma Aldrich	317505	TRPC6 and CACNA1D
Hyperforin	Hello Bio	HB3933	TRPC6
FPL	Tocris Biosciences	2A/252413	CACNA1D

2.2.3 Drug preparation

Lomerizine was dissolved in 80% DMSO + 20% Pluronic solution at 20 mM stock concentration. Lomerizine stock solution was aliquoted and kept at -20^{o}C. Imatinib was dissolved in DMSO at a concentration of 4 mM and was stored at -20^{o}C. IACS-010759 (IACS-010759) was dissolved in DMSO at a concentration of 10 mM and stored at -20^{o}C. BI-749327, TRPC6 inhibitor was dissolved in DMSO at a concentration of 1mM and stored at -20^{o}C (cells did not receive more than 2-5 µM for 3 days: not exceeding 0.5% V/V DMSO). Nicardipine, CACNA1D inhibitor, was dissolved in DMSO at a concentration of 10 mM and stored at -20^{o}C.

For *in vivo* studies, 1 g lomerizine was suspended in 25 ml 0.9 % NaCl (Saline) to facilitate dissolving, followed by thorough dissolving in 2.5 ml DMSO (almost dissolved). The solution was highly acidic and required pH calibration back to 7.4, which is suitable for *in vivo* studies. To calibrate the pH, 1 M NaOH was added to the solution and vortexed till it generated a milky suspension. To revert it to a clear solution, 3 drops of Tween 80 were added with continuous Vortexing, which was sufficient to emulsify the suspension. The addition of 1 M NaOH followed by Tween 80 was repeated till pH reached 7, because Tween 80 could not abolish the turbidity of the suspension when it reached that point. Overall, the consumed Tween 80 during calibration should not exceed 9-15 drops (~ 1.5 ml) to ensure optimum solubility. To achieve lomerizine at 80 mg/ kg concentration, saline was added to the lomerizine stock solution to get up to 80 ml. The volume each mouse that weighs 30 g should receive was 150 µl intraperitoneally once daily. Unfortunately, lomerizine came out of from the solution and formed milky precipitation again through storage lifetime, so it is important to store the stock solution at -80^{o}C and send it to the mouse unit regularly (Table 2-8).

2.2.4 Justification for drug concentrations throughout the study

Lomerizine was used at 5-10 μM for *in vitro* studies. The claim for selecting this concentration was since different concentration of lomerizine showed ability to inhibit OCR in KCL22 cells after 60 minutes exposure to 4 μM lomerizine. Further, 5 μM lomerizine was able to reduce the value of IC50 of imatinib to half according to resazurin assay (Figure 4-5). Going further, 10 μM of lomerizine was able to inhibit 60% of K562 cell growth in galactose media compared to 20% growth inhibition in glucose cultured media as shown previously in drug repurposing screening performed by Helgason lab [210]. Imatinib also has been used for *in vitro* studies from 0.5-1 μM concentration. This was selected based on resazurin assay that proposes 0.5 μM imatinib as IC50 after 72 hours of exposure in K562 and KCL22 cells. In addition, throughout this study author tested 1 μM imatinib and 10 μM of lomerizine for 24 hours assays, such as Ca^{2+} assays. Further drug concentrations were optimized for their instant stimulation of Ca^{2+} response during recording the Ca^{2+} level by flow cytometry (Table 2-11).

Table 2-11: Effective concentrations of drugs for 24 hours *in vitro* treatments.

Compound	Target	Action	conc (μM)	Ref
Lomerizine	VDCC	Inhibitor	5-10	[211]
Lomerizine	TRPC	Inhibitor	5-10	[212]
BI749327	TRPC6	Inhibitor	1-5	[213]
3-nitrocoumarin	PLCγ	Inhibitor	1-5	[214]
EGTA	Ca^{2+}	Chelation	0.1	[215]
Thapsigargin	SERCA	Deplete ER Ca^{2+}	0.1	[216]
Ionomycin	Ca^{2+} ionophore	Stimulator	5	[217]
m-3M3FBS	PLCγ	Stimulator	50	[218]
DOG	Ca^{2+} influx	Stimulator	25	[219]
Hyperforin	TRPC6	Stimulator	50	[220]
FPL	CACNA1D	Stimulator	5	[221]
Nicardipine	CACNA1D	Inhibitor	10	[222]

2.2.5 Flow cytometry reagents

Table 2-12: Flow cytometry chemical dyes.

Product	Manufacturer	Cat. Number
7-AAD	BD Biosciences	559925
Cell trace violet (CTV)	Life Technologies	C34557
CellROX deep red	Thermo Fisher	C10422
DAPI	Biolegends	422801
ER tracker Red	Thermo Fisher	E34250
Indo-1, AM ester	Thermo Fisher	I1223
JC-1 Mitochondrial membrane potential dye	Thermo Fisher	65-0851-38
Mito-tracker deep red	Thermo Fisher	M22426
MitoSOX™ Red Mitochondrial Superoxide indicator	Life Technologies	M36008
Mito-tracker™ green	Life Technologies	M46750
Rhodamine-2, AM ester (Rhod2)	Thermo Fisher	R1244
Tetramethylrhodamine (TMRM)	Thermo Fisher	T668

Table 2-13: Flow cytometry antibodies.

Product	Manufacturer	Cat. Number
APC Anti-Human Annexin V	BD Biosciences	550475
APC Anti-Human CD34	BD Biosciences	555824
APC Anti-Human CD71	Biolegend	334108
FITC-Annexin V	BioLegend	640906
PE Anti-Human CD11b	BioLegend	301306
PE Anti-Human CD133	Milteney Biotec	130-113-108
PE Anti-Human CD71	BD Biosciences	555537
PerCP/Cy5.5 Anti-Human CD235a (Glycophorin A)	BioLegend	349110

Table 2-14: Colorimetric and Luminescence materials.

Product	Manufacturer	Cat. Number
Resazurin	Sigma Aldrich	199303
Luciferin Monopotassium Salt	Fisher Scientific	15225733
Luciferin Monopotassium Salt	PerkinElmer	122799-2

2.2.6 LCMS metabolite extraction

Table 2-15: Metabolite extraction solvent for LCMS.

Product	Manufacturer	Cat. Number
Acetonitrile	VWR International Ltd	83639.32
Methanol (HPLC grade)	Fisher Scientific	67-56-1
Water (HPLC grade)	-----	-----

2.2.7 Western blot

Table 2-16: Western Blot antibodies.

Primary Antibodies		
Product	Manufacturer	Cat. Number
CACNA1D	Thermo Fisher Scientific	PA5-07674
CACNA1D	ProteinTech	22276-1-Pr
GAPDH	Cell Signalling Technology	5174S
GAPDH	Cell Signalling	5174s
TRPC6	ProteinTech	18236-1-AP
TRPC6	Thermo Fisher Scientific	PA5-20256
ß-tubulin	Cell Signalling Technology	2146S
Secondary Antibodies		
Anti-mouse IgG, HRP-linked	Cell Signalling Technology	7076S
Anti-rabbit IgG, HRP-linked	Cell Signalling Technology	7074S

Table 2-17: Western Blot materials.

Product	Manufacturer	Cat. Number
10x Tris/Glycine Buffer for Western blots	Bio-Rad	1610734
ECL Western blotting Substrate	Fisher Scientific	10005943
Methanol	Fisher Scientific	M/4056/17
NuPAGE™ 4-12% Bis-Tris Protein Gels, 1.0 mm, 10-well	Life Technologies	NP0321BOX
NuPAGE™ LDS Sample Buffer (4X)	Life Technologies	NP0007
NuPAGE™ MES running buffer	Life Technologies	NP0002
PageRuler™ Plus Prestained Protein Ladder	Thermo Fisher	26619
PhosSTOP (phosphatase inhibitors)	Roche	4906845001
Pierce™ BCA Protein Assay Kit	Thermo Fisher Scientific	23225
Pierce™ BSA Standard Ampules, 2 mg/mL	Thermo Fisher Scientific	23209
Pierce™ enhanced chemiluminescence (ECL) Western blotting Substrate	Thermo Fisher Scientific	32106
Protease inhibitors cocktail	Sigma	P8340
PVDF Transfer Membrane	Thermo Fisher	88520
Sodium dodecyl sulphate (SDS)	Sigma Aldrich	L5750
SuperSignal™ West Femto Maximum	Thermo Fisher	34094
Tween 20	Sigma Aldrich	P9416-100ML

2.2.8 Enzymes, bacteria, and plasmids

Table 2-18: Enzymes used in current study.

Product	Manufacturer	Cat. Number
high fidelity Taq polymerase	New England Biolabs	M0267S
BsmBI2 Enzyme	New England Biolabs	R0580
T4 Polynucleotide Kinase	New England Biolabs	M0201S

Table 2-19: Bacteria used for plasmid transformation.

Product	Manufacturer	Cat. Number
One Shot™ Stbl3™ *E. coli*	Thermo Fisher	C737303
Mix&Go *E. coli*	Cambridge biosciences	T3001

Table 2-20: Plasmids used in the current study.

Fluorescent Tracker Plasmids			
Product	Manufacturer	Cat. Number	Target
GCAMPER	Addgene	65227	ER Ca^{2+} sensor
mKeima	Addgene	72342	Mitohagy reporter
RAMP4	JR Liang and Jacob Corn labs		ER Tracker
TetOn-mCherry-eGFP-RAMP4	Addgene	109014	ER autophagy
Tom20 GFP	JR Liang and Jacob Corn labs		Mitochondrial tracker
CRISPR Cas9 Plasmids			
Product	Manufacturer	Cat. Number	Target
LentiCRISPRv2GFP	Addgene	82416	V2 vector
pCMV-VSV-G	Addgene	8454	Envelope virus
pLentiCrispr-V2-m-Orange (V2mO)	Addgene	140206	V2 vector
psPAX2	Addgene	12260	Packaging virus

2.2.9 General kits

Table 2-21: General kits.

Product	Manufacturer	Cat. Number
Promega cAMP-Glo™ Assay Kit	Promega UK Ltd	V1501
NAD+ IDH activity kit	Sigma Aldrich	MAK062
QIAquick Gel Extraction Kit	Qiagen	28704
Quick Ligation™ Kit	New England Biolabs	M2200S
RNeasy Mini Kit	Qiagen	74104
Monarch PCR and DNA Cleanup Kit	New England Biolabs	T1030S
GeneJet Genomic DNA purification Kit	Thermo Fisher	K0721
Invitrogen™ PureLink™ HiPure Plasmid Maxiprep Kit	Invitrogen	K210006
CD34 MicroBead Kit	Milenyibiotec	130-046-702

2.2.10 Other materials

Table 2-22: Other materials.

Product	Manufacturer	Cat. Number
Ca^{2+} chloride (CaCl2)	Sigma Aldrich	1023780500
Compensation beads	Thermo Fisher	01-2222-42
Histopaque 1119	Sigma Aldrich	11191
Magnesium chloride	Sigma Aldrich	208337
Polybrene Transfection Reagent	Merck	TR-1003-G
Potassium Chloride (KCl)	Thermo Fisher	10684732
RNase Inhibitor	Thermo Fisher	N8080119
Substrate SYBR™ Safe DNA Gel Stain	Thermo Fisher	S33102
Separation columns	Miltenyi Biotec	130-042-401

2.2.11 Culture media recipes

Table 2-23: Recipes for cell culture medias.

Complete RPMI	
Name	Final concentration
RPMI 1640	N/A
FBS, heat inactivated	10%
L-Glutamine	2mM
Penicillin-Streptomycin (Pen/Strep)	100 IU/mL
Complete DMEM	
DMEM 1X With sodium pyruvate	N/A
FBS, heat inactivated	10%
L-Glutamine	2mM
Pen/Strep	100 IU/mL
Serum-free media (SFM)	
IMDM	N/A
BIT (BSA/Insulin/Transferrin)	20%
2-Mercaptoethanol	0.2%
Low Density Lipoprotein	40µg/ml
L-Glutamine	2mM
Pen/Strep	100 IU/mL
SFM supplemented with physiological growth factors (φGF)	
SFM	N/A
SCF	0.2ng/ml
IL-6	1ng/ml
G-CSF	1ng/ml
GM-CSF	0.2ng/ml
MIP-a	1ng/ml
LIF	0.05ng/ml
DAMP solution	
DPBS	N/A
Magnesium Chloride	1M
Trisodium Citrate	0.155M

Human serum albumin		0.2
DNase I		2500U/ml
Plasmax (primary cells)		
Plasmax base media		N/A
L-Glutamine		0.65mM
Pyruvate		100µM
Pen/Strep		100IU/mL
AlbuMAX II Lipid-Rich BSA		0.50%
Insulin		10µg/mL
Transferrin		7.5µg/mL
2-Mercaptoethanol		0.2%
Plasmax media is prepared fresh where EBSS is supplemented with amino acids, vitamins, salts, trace elements and uric acid [223].		
Seahorse XF Media (Mito Stress Test)		
XF Seahorse Base Media		N/A
Glucose		11.1 mM
L-Glutamine		2mM
Seahorse XF Media (Glycostress Test)		
XF Seahorse Base Media		N/A
L-Glutamine		2mM
3X MAS buffer (Seahorse media)		
milliQ water		Up to 1 L
Mannitol		120.23 g
Sucrose		71.88 g
KH2 PO4		4.08 g
MgCl2		150 mL of 100 mM solution
HEPES		6 mL of 1.0 M solution
EGTA		1.14 g
Must be Kept in +4ºC. It may crystallise by time. Dissolve with glacial HCL then readjust it to 1M KOH.		
1X MAS buffer		
MAS Buffer 3X		66 mL
(FAF) BSA		400 mg (add fresh)
milliQ water		~ 200 ml
Adjust pH to 7.2 with 1M KOH or 1M HCL (It is a MUST)		
Mitochondrial Complex substrates (Added according to the targeted complex)		
Reagent	Final (mM)	Equivalent µl for 4000 µl 1X MAS
Pyruvate	5	1600
Glutamine	5	800
Malate	5	160
Succinate	1	128
TMPD	0.5	16
Na-ascorbate	2	64
ADP	1	64
Saponin	0.03 µg/ml	96

Oligomycin	0.00125	9
Rotenone	0.002	8
AA	0.002	8
Sodium azide	25	1000
Calculations based on Loading 25 µL to assay cartridge		

2.2.12 Buffers and lysis reagents

Table 2-24: Recipe for buffering and lysis reagents.

Protein Lysis Buffer	
Name	Final concentration
RIPA Buffer	N/A
PhosphoSTOP	10%
Protease Inhibitor	10%
SDS	10%
Metabolite lysis buffer (in glass)	
Acetonitrile	20%
Methanol (HPLC grade)	50%
Water (HPLC grade)	N/A
2X HEPES-Buffered Saline (HBS) (pH=7.0-7.1)	
H_2O 480ml	480ml
NaCl 8g	8g
KCl	0.37g
Glucose	1g
HEPES	5g
Na2HPO4*7H2O (100x)	500µl

2.2.13 Primary samples

Table 2-25: Primary samples and corresponding experiments.

Bank ID	Tissue	% Ph+ at diagnosis	Growth, apoptosis Day 3	CFC	CD34+ CD133+	LTC-IC	Ionomycin Ca^{2+} level	Seahorse OCR	LCMS	ER, DOG Ca^{2+} level	LSC (CD34+CD38-)	JC-1/ER mass	CTV	Ca^{2+} modifiers
nonCML029	TCL	-								×		×		
nonCML30	Hodgkin	-								×		×		
nonCML042	Lymphoma	-								×		×		
nonCML044	Lymphoma	-								×		×		
BB190647	Hip BM	-	×		×									
BB190773	Hip BM	-	×	×	×									
BB190809	Hip BM	-	×	×	×									
BB190833	Hip BM	-	×	×	×									
BB190898	Hip BM	-	×	×	×									
CML339	CP-CML	96	×	×	×	×	×	×		×	×	×	×	×
CML393	CP-CML	87							×					
CML399	CP-CML	97					×			×	×	×	×	×
CML441	CP-CML	98	×	×	×	×								
CML442	CP-CML	90				×								
CML444	CP-CML	86										×	×	×
CML454	CP-CML	100	×	×	×									
CML459	CP-CML	99						×						
CML460	CP-CML	100	×	×	×	×	×	×		×	×	×	×	×
CML497	CP-CML	100	×	×	×									
CML-470	CP-CML	100	The single sample used for PDX in vivo studies											

Table 2-26: CML individuals' samples information.

	sex	Age at diagnosis	Stage of disease	Hasford/Sokal score	Karyotype	Total white cell count (10^9/L)
CML339	F	40	CP	1604/1.47	Three-way translocation 2,9&22 Bcr-Abl result when the sample was acquired b3 splice p210	295
CML393	M	40	CP	Spleen size not documented	46,XY,t(9;22;15)(q34;q11.2;p11.2)[10] Subsequent FISH using BCR/ABL probes confirm presence of BCR-ABL rearrangement with fusion signal present on derivative chromosome 22.BCR signal located on long arm of normal chromosome 22 & on short arm of der (15). ABL signal present on long arm of both normal chromosome 9 & derivative chromosome 9. Signal pattern on all 5 cells Bcr-abl result when the sample was acquired 287%	380
CML441	M	63	CP	High	10 out of 10 cells 9;22 no additional changes	223
CML442	F	61	CP	Hasford low 715.74 Sokal low 0.76	FISH (100% BCR/ABL)	192.8
CML444	M	45	CP	---	Standard t(9;22) only	313
CML454	M	56	CP	---	46,XY,t(9;22)(q34;q11)[10]	205
CML460	F	31	CP	---	46,XX,t(9;22)(q34;q11.2)[20]	148.4
CML470	M	69	CP	---	46 XY t9;22 nil else.	538
CML399			CP			
CML459			CP			
CML497			CP			

Equipment
Table 2-27: Equipment.

Name	Supplier
7000 Series Triple Quadrupole MS System	Agilent
FACSAria Fusion Cell sorter	BD Biosciences
BD LSRFortessa™	BD Biosciences
BigDye Terminator v3.1	Applied Biosystems
CASY Cell Counter and Analyser	Roche
FACS Verse	BD Biosciences
Infinite M200 Pro Plate Reader	Tecan
IVIS Spectrum In Vivo Imaging System	PerkinElmer
Nanodrop 2000	Thermo Fisher
Odyssey FC	LiCor
Peltier Thermal Cycler PTC 225	MJ Research
PRISM 3130xl (16 capillaries) sequencer	Applied Biosystems
Promega GloMax Multiplus Plate Luminometer	Promega
Q-Exactive Orbitrap MS system	Thermo Fisher
Seahorse XFe96 Analyser	Agilent
Ultimate 3000 HPLC System	Thermo Fisher
Zeiss LSM 770	Carl Zeiss

2.2.14 Software and online tools

Table 2-28: Software and online tools.

Name	Supplier
Prism GraphPad V8	https://www.graphpad.com/scientific-software/prism/
R x64 4.1.2	https://cran.r-project.org/bin/windows/base/
R-Studio	https://www.rstudio.com/
Metaboanalyst V5	https://www.metaboanalyst.ca/docs/About.xhtml
Autoplotter V2.4	https://mpietzke.shinyapps.io/AutoPlotter/
Tide	http://shinyapps.datacurators.nl/tide/
Chromas V2.6.6	http://technelysium.com.au/wp/chromas/
UCSC genome browser	https://genome-euro.ucsc.edu/cgi-bin/hgGateway
Primer3 V0.4.0	https://bioinfo.ut.ee/primer3-0.4.0/
Cytoscape V 3.9.1	https://cytoscape.org/
BiocManager	https://cran.r-project.org/web/packages/BiocManager/vignettes/BiocManager.html
GSEA_4.2.2	https://www.gsea-msigdb.org/
WAVE	https://www.agilent.com/
BioRender	https://biorender.com/
TOXOID	Thermo Fisher
TraceFinder	Thermo Fisher
Prism Seqscape software	Applied Biosystems

3 TRPC6 and CACNA1D maintains OXPHOS *in vitro*

3.1 Introduction

The role of Ca^{2+} in CML metabolism and specifically in LSCs remains unknown. Notably, Ca^{2+} ions are required as a cofactor for mitochondrial dehydrogenases activity in micromolar range, to form metabolites such as pyruvate, isocitrate, and α-ketoglutarate [93, 224]. Mitochondrial dehydrogenases support the TCA by facilitating proton (H^+) transfer from TCA cycle intermediate carbon sources to NAD+ to produce NADH-reducing cofactors. NADH, in turn, supports ETC with proton (H^+) that changes membrane potential and allows fluency of electrons through the 4 complexes (I, II, III, and IV). Those ETC complexes act as electron acceptors.

Further, Ca^{2+} ions have been shown to participate with complex V (ATP synthase) to release ATP "energy molecules". In cardiac mitochondria, an ATP synthase is conjugated with another inhibitory factor protein. In order for ATP synthase to get activated, the ATP synthase inhibitory factor protein has to dissociate which occurs upon its binding to Ca^{2+} [90]. Helgason lab has revealed that in CML, LSCs (CD34+CD38-) rely on mitochondrial OXPHOS due to higher mitochondrial content and mitochondrial activity than their normal counterparts or their preceding leukaemic committed progenitors [184]. All previous findings suggest potential role of Ca^{2+} ions in CML and in LSC's mitochondrial respiration.

It is plausible that TRPC6 and CACNA1D participate in Ca^{2+} homeostasis in CML and are likely involved in therapy resistance. One of the underlying causes of therapy resistance is the reliance of cells on mitochondrial OXPHOS. Ca^{2+} ions have been reported to act as a cofactor for mitochondrial dehydrogenases. Therefore, it has been aimed to delete TRPC6 or CACNA1D from the CML cell lines; K562 and KCL22 and investigate the impact on mitochondrial metabolism and CML survival.

To better understand the role of Ca^{2+} ions in CML LSCs, targeted transcriptome Mapping genes for Ca^{2+} homeostasis and signalling from publicly available datasets was performed in LSCs and their corresponding leukaemic progenitor cells (LPCs) and HSCs. Also, Ca^{2+} related gene expression levels were further assessed in CML after treatment with TKIs, such as imatinib, nilotinib, and dasatinib, at different treatment time points.

The following publicly available datasets were analysed to get insights into Ca^{2+} related transcriptional landscape in LSCs and compare that with those levels in their normal or committed progenitors. The first dataset is a microarray (ArrayExpress ID: E-MTAB-2581). E-MTAB-2581 includes 24 arrays of CML cells which possess four cell populations (6 arrays/condition; 2 arrays/patient samples; 3 samples/condition): HSCs (CD34+CD38-), LSCs (CD34+CD38-), HPCs (CD34+CD38+) and LPCs (CD34+CD38+). LSCs and LPCs were acquired from CP-CML individuals, whereas HSCs and HPCs (referred to as normal) were acquired from non-CML individuals.

3.2 LSCs are enriched with mitochondria and metabolic hallmarks

Initially, E-MTAB-2581 arrays were calibrated using RMA method (Figure 2-3) comparing LSCs and their normal HSCs. GSEA signature analysis from E-MTAB-2581 reveals a trend of enriched mitochondrial metabolic pathways such as hallmarks of OXPHOS in LSCs as shown to have normalised enrichment score (NES) at around 2.2 (A). Also, glycolysis hallmarks are shown to be enriched in LSCs compared to normal counterparts at NES 1.95. Enrichment of such signatures suggest higher metabolic demand in CML LSCs when compared to their normal counterparts. GSEA analysis also reveals an enriched signature of VGCC in LSCs compared to their normal counterparts (NES=1.43, nominal p Value=0.05). These results indicate a potential increase in Ca^{2+} influx activity in LSCs compared to their normal counterparts. This assumption is based on initial thought that mitochondria require Ca^{2+} to catalyse mitochondrial dehydrogenases and ATP production by ATP synthase. Text mining has been performed to assemble a list of well-known Ca^{2+} channels in mammalian cells. Next , the expression levels of this list was assessed which reveals upregulation in *CACNA1D* and *CACNB4* gene transcripts in LSCs compared to their normal counterparts (B). *CACNA1D* (cav1.3) and *CACNB4* (cavß) participate in VGCC activity. Also, another one of upregulated genes in LSCs is Ca^{2+} binding protein *S100A16*. Previously published GSEA revealed enrichment of mitochondrial membrane architecture and OXPHOS after overexpression of *S100A16* [225]. Furthermore, our analysis also reveals an upregulated *TRPC6* in LSCs. Also, the analysis was performed on the same filtered genes in LSCs as

compared to their normal counterparts and assessed their expression levels in LPCs (C). The analysis reveals that *CACNA1D* and *CACNB4* are upregulated in LSCs compared to their committed progenitors. Also, *TRPC6* shows a modest (non-significant) upregulation in LSCs versus LPCs. Findings indicate that *CACNA1D* expression is a specific attribute of primitive LSCs when compared to their normal or committed progenitors. All our findings suggest that upregulation of *CACNA1D* and *TRPC6* should be investigated in greater depth in CML.

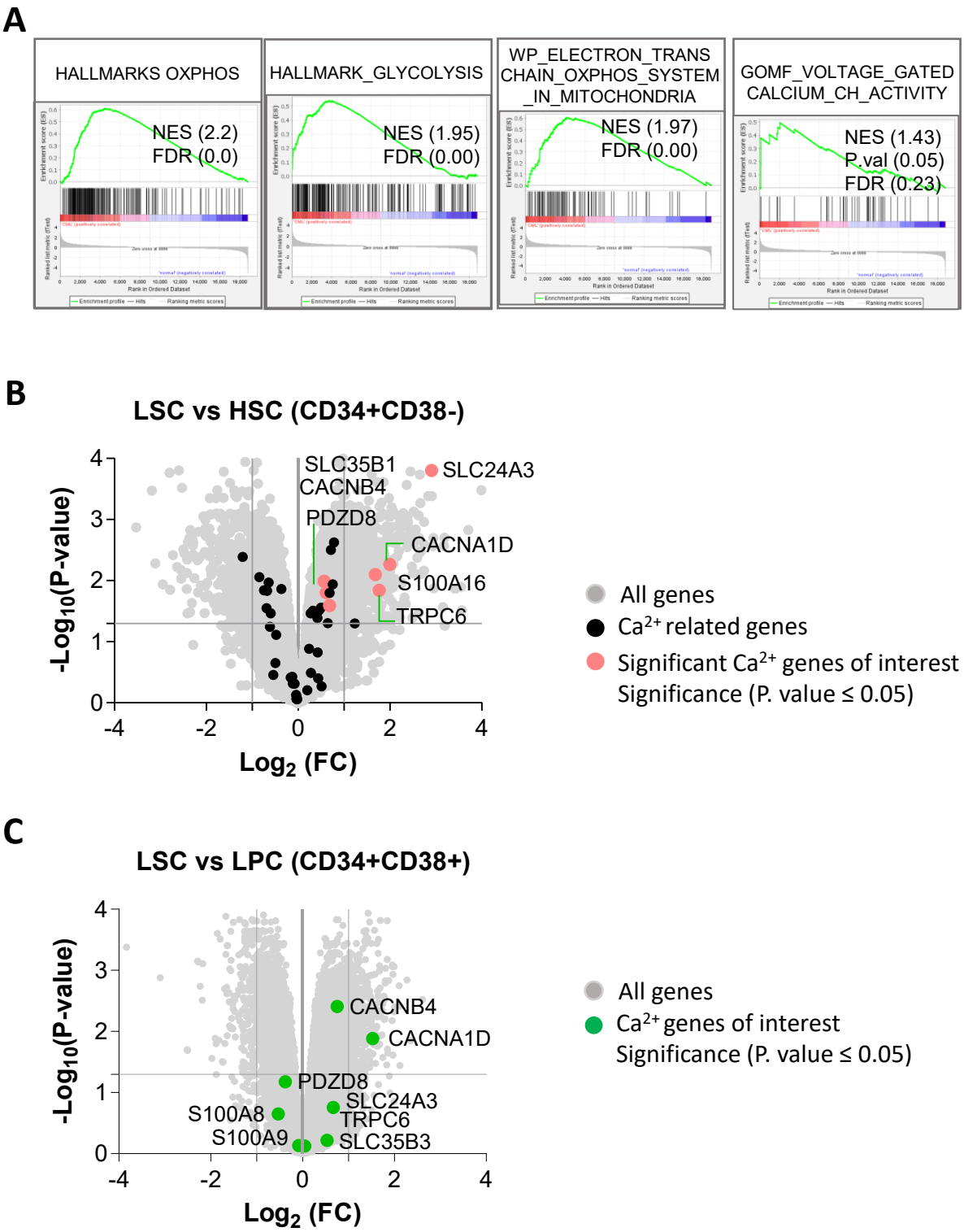

Figure 3-1: Ca^{2+} influx-related pathways are upregulated in LSCs.

(A) Enrichment analysis shows enriched metabolism, and voltage gated Ca^{2+} channel activity in LSCs as compared to their normal counterparts. (C) A representative volcano plot shows differentially expressed genes in LSCs vs HSCs, highlighting Ca^{2+} -related genes. (D) A representative volcano plot shows differentially expressed genes in LSCs vs LPCs, highlighting Ca^{2+} -related genes of interest. Each comparison condition is pooled from n=3 individual samples. Analysis is based on Benjamini & Hochberg algorithms were used at probability cut-off at Y axis (≤ 5%).

3.3 Imatinib increases *S100A8/9* and *SLC24A3* without altering *CACNA1D* or *TRPC6* levels in LSCs

The transcriptional differences related to Ca^{2+} signalling between CML LSCs treated with imatinib or second generation TKI; nilotinib or dasatinib at two different time points (8 hours and 7 days, in the absence of growth factors) were investigated (E-MTAB-2594 array express) (Figure 2-4).

Analysis of the 8 hours timepoint depicts no significant effect of any of the TKIs on Ca^{2+} signalling in CD34+CD38- CML transcriptome compared to their untreated counterparts (Figure 3-2A). Because E-MTAB-2594 dataset does not include 48 hours timepoint, Another unpublished RNAseq of CML exposed to imatinib for 48 hours was added to analysis panel, revealing a global transcriptional change (Figure 3-2B). Surprisingly none of Ca^{2+} gene signatures show any significant change apart from solute carrier SLC24A3 which is known as to pump Ca^{2+} outside the cell.

To focus on the effect of imatinib treatment on specific Ca^{2+} channels or binding proteins at transcriptome level, the expression levels of previously selected Ca^{2+} related genes were assessed. The analysis of single genes reveals that imatinib does not alter the expression of *CACNA1D* or *TRPC6* either at 8 hours or after 7 days of treatment compared to untreated CML counterparts (Figure 3-2, Figure 3-3A & 3B). The same data analysis for nilotinib and dasatinib revealed nearly the same transcriptomic change as imatinib (Figure 3-4).

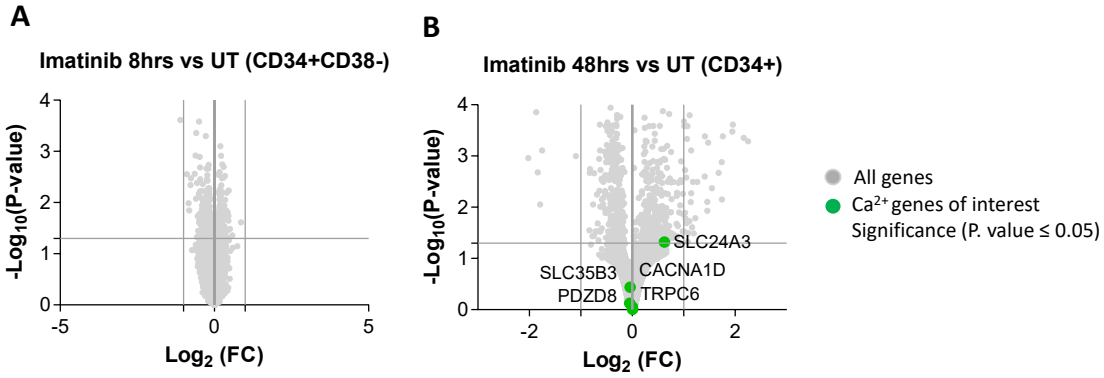

Figure 3-2: Imatinib does not alter majority of Ca^{2+} related genes in LSCs after 48 hours.

(A) Representative scatter plot shows differentially expressed genes at 8 hours of imatinib treatment versus their untreated CD34+ CML cells (B) A representative scatter plot of RNAseq data showing differentially expressed genes at 48 hours of imatinib treatment versus their untreated CD34+ CML cells. RNAseq data were generated by Helgason lab (unpublished). Each comparison condition is pooled from n=6 individual samples for E-MTAB-2594 sequencing (8 hours of 2 µM imatinib *in vitro*). Each comparison condition is pooled from n=4 individual samples for bulk RNA sequencing (48 hours). Analysis is based on Benjamini & Hochberg algorithms were used at probability cut-off at Y axis (≤ 5%).

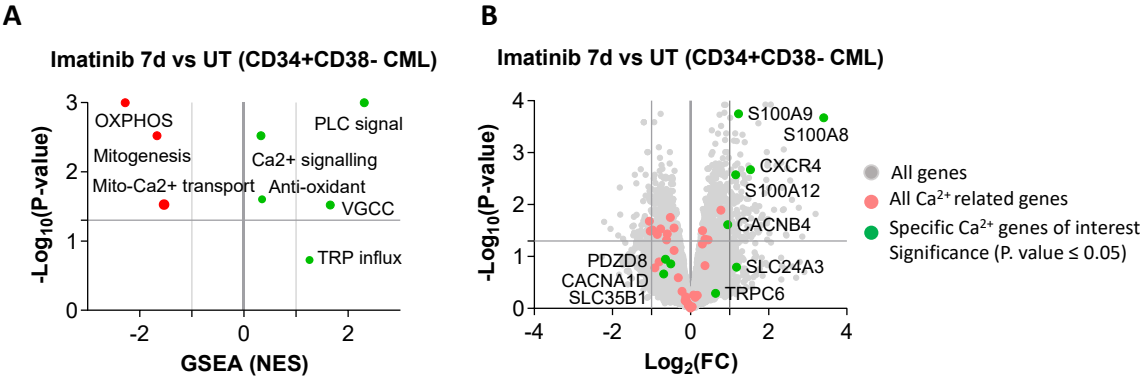

Figure 3-3: Imatinib modifies Ca^{2+} signalling in LSCs after 7 days of exposure.

(A) Scatter plot demonstrates enrichment scores of different gene sets in LSCs treated with imatinib for 7 days versus LSCs. (B) A representative volcano plot shows differentially expressed genes in LSCs treated with imatinib for 7 days vs LSCs, highlighting Ca^{2+} -related genes. The log_2 (FC) cut off=1. Each comparison condition is pooled from n=6 normal samples and n=5 CML samples for E-MTAB-2594 sequencing (7 days of 2 µM imatinib *in vitro*). Analysis is based on Benjamini & Hochberg algorithms were used at probability cut-off at Y axis (≤ 5%).

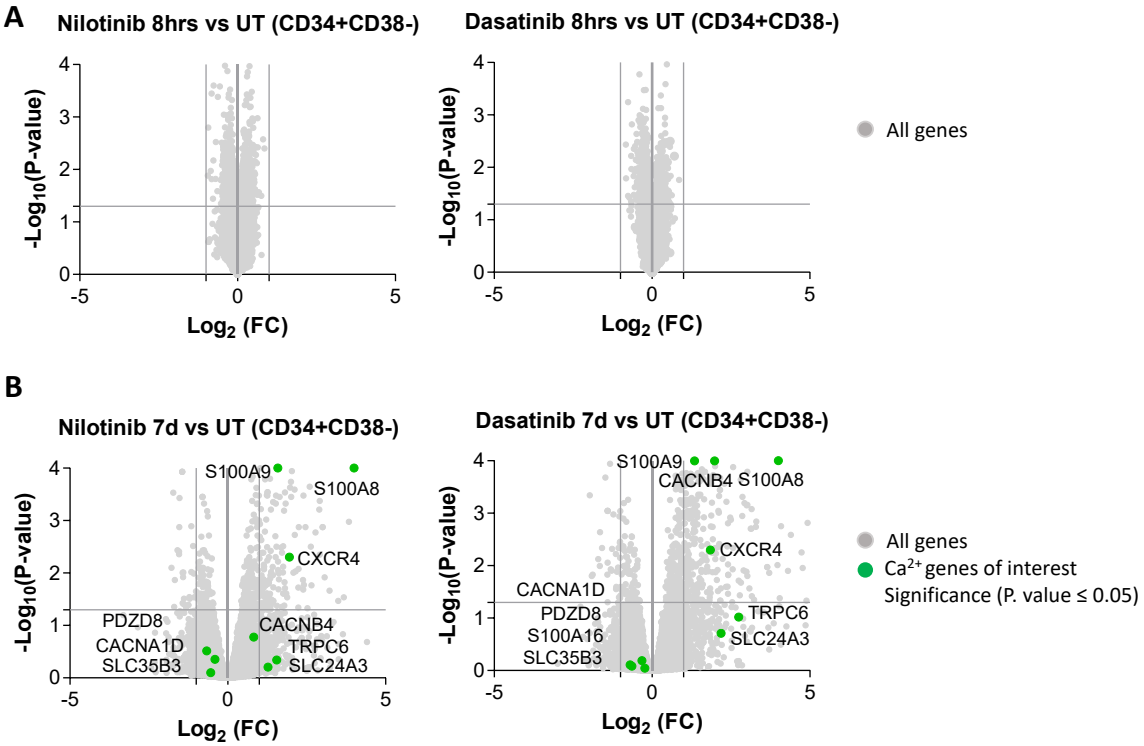

Figure 3-4: Impact of nilotinib and dasatinib on HSC and LSC Ca^{2+} signature.

(A) Representative scatter plot shows differentially expressed genes at 8 hours of nilotinib and dasatinib treatment versus their untreated CD34+CD38- CML cells (B) graphical presentation of upregulated Ca^{2+} related genes in LSCs versus HSCs dataset and TKI versus untreated LSCs dataset for same genes. Data were pooled from two different data sets, including E-MTAB-2581 and E-MTAB-2594. Log_2 (FC) cut-off= 1. Each comparison condition is pooled from n=6 normal samples and n=5 CML samples for E-MTAB-2594 sequencing (8 hours or 7 days of 150 nM dasatinib or 5 µM nilotinib *in vitro*). Analysis is based on Benjamini & Hochberg algorithms were used at probability cut-off at Y axis (≤ 5%).

3.4 LSCs have higher ER signature and mass

Helgason lab previously highlighted that CML LSCs possess higher mitochondrial mass and activity [184], leading to the assumption that CML LSCs may have higher basal mitochondrial Ca^{2+} levels. CD34+ CML and non-CML cells were stained with cytosolic and mitochondrial Ca^{2+} ion dyes to test this assumption and measured with flow cytometry (Figure 3-5). The results show that CML LSCs have higher basal mitochondrial Ca^{2+} levels and subsequent lower cytosolic Ca^{2+} levels, indicating that CML has higher Ca^{2+} ions buffering capacity within mitochondria. However, it is unknown if CD34+ enriched LSC CML also possesses higher ER mass as a main Ca^{2+} storage organelle.

Further transcriptome data analysis of previously mentioned microarray datasets was performed, comparing GSEA analysis related to ER biological processes in LSCs and their HSCs counterparts. The analysis reveals that LSCs (CD38-CD34+) are enriched in ER related processes such as unfolded protein response (UPR; NES= 1.85), UPR hallmarks (NES=2.13), and Reactome of ER Phagosome (NES=2.12), and GOCC ER protein-containing complexes (NES=1.84) (Figure 3-6A).

Given that ER retains the highest cellular Ca^{2+} ions concentration (in μM range) [226], previous studies showed that ligand induction of IP3R leads to immediate mitochondrial response due to spatial proximity between mitochondria and ER. This proximity leads primarily to concurrent mitochondrial dehydrogenase enzyme stimulation (IDH, αKDH, PDH) [224, 227]. Thus, a potential role of ER and mitochondria in CML LSC OXPHOS was assumed. To extend on the role of ER in CML Ca^{2+} homeostasis, CD34+ CML and non-CML cells were stained with ER tracker to quantify ER mass. Analysis reveals that CD34+ CML possesses higher ER mass than their normal counterpart, supporting previous findings that CML have higher Ca^{2+} buffering capacity, either through ER or mitochondria (Figure 3-6B).

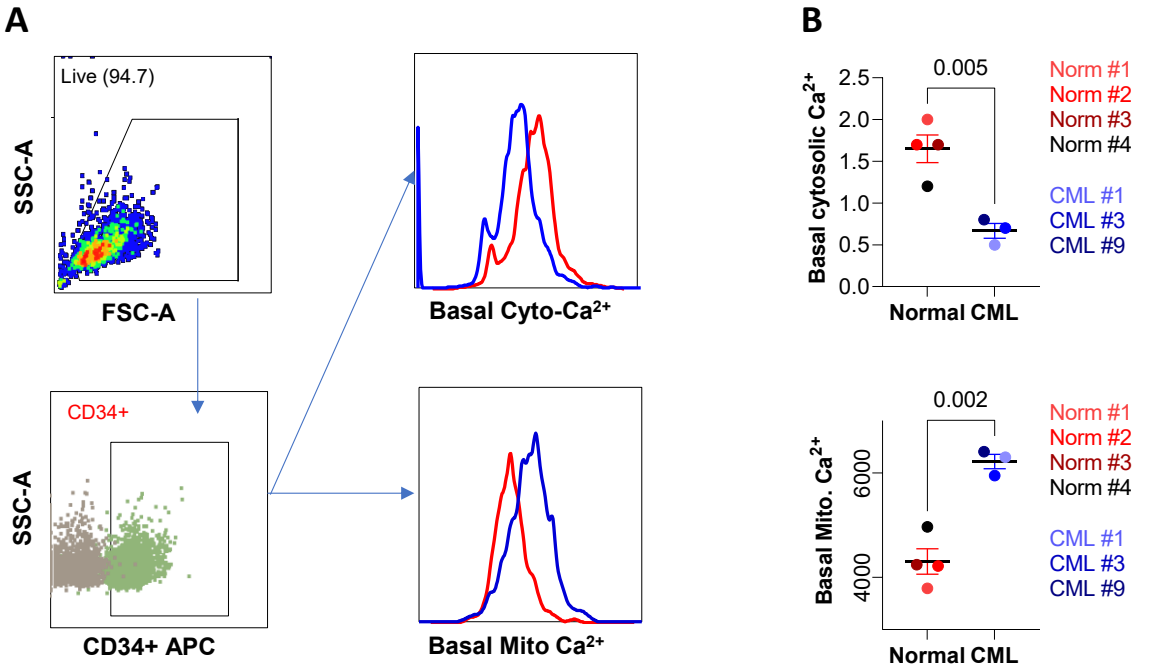

Figure 3-5: CD34+ CML have higher mitochondrial Ca^{2+} buffering capacity.

(A) Representative flow cytometry histogram shows basal cytosolic and mitochondrial Ca^{2+} levels in CD34+ CML cells (blue) and CD34+ normal cells (red). (B) Dot plot of basal Ca^{2+} level analyses in CD34+ CML cells. Results represent samples collected from individuals with CML (n=3) and non-CML (n=4), where Student's t-test was used to calculate significance.

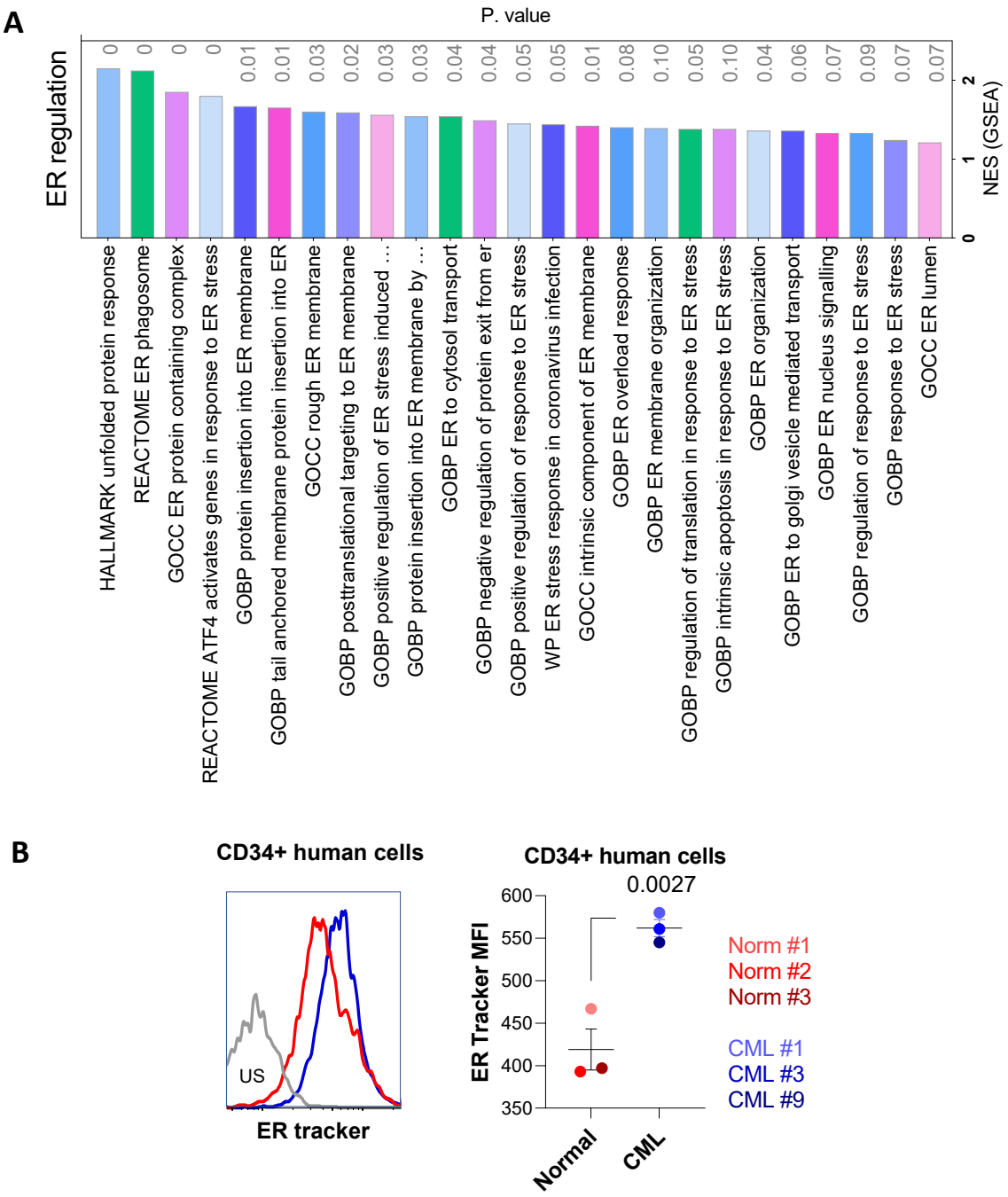

Figure 3-6: CD34+ CML cells have higher ER signature and ER mass.

(A) Enrichment analysis of gene sets related to ER in LSCs versus HSCs (E-MTAB-2581 arrays). (B) Representative histogram of ER mass in CD34+ CML cells (blue) and CD34+ normal cells stained with ER tracker™ red (BODIPY™ TR), followed by quantification using flow cytometry. Samples are collected from individuals with or without CML (n=3) and statistical analysis was performed with Student's t-test to calculate significance.

It was not clear if CML have a higher capacity to allow extracellular Ca^{2+} influx through plasma membrane Ca^{2+} channels.
To test this objective, CD34+ CML and non-CML cells were immediately stimulated with 25 µM diacylglycerol (DAG) analogue (DOG), followed by measuring both cytosolic and mitochondrial Ca^{2+} levels. Results show that CD34+ CML cells are more sensitive to DOG stimulation and show significantly higher cytosolic Ca^{2+} level with modest non-significant increase in mitochondrial Ca^{2+} level (Figure 3-7A).

To investigate if mitochondrial Ca^{2+} mainly comes from ER Ca^{2+} stores, CD34+ CML and non-CML cells were instantly stimulated with 2.5 µM thapsigargin that mobilises all ER Ca^{2+} to surrounding organelles and cytosol, followed by measuring the impact of this stimulation on cytosolic and mitochondrial Ca^{2+} levels. Results indicate that CML have higher ER Ca^{2+} content and this Ca^{2+} is transferrable to either cytosol or mitochondria when cells are stimulated or stressed (Figure 3-7B).

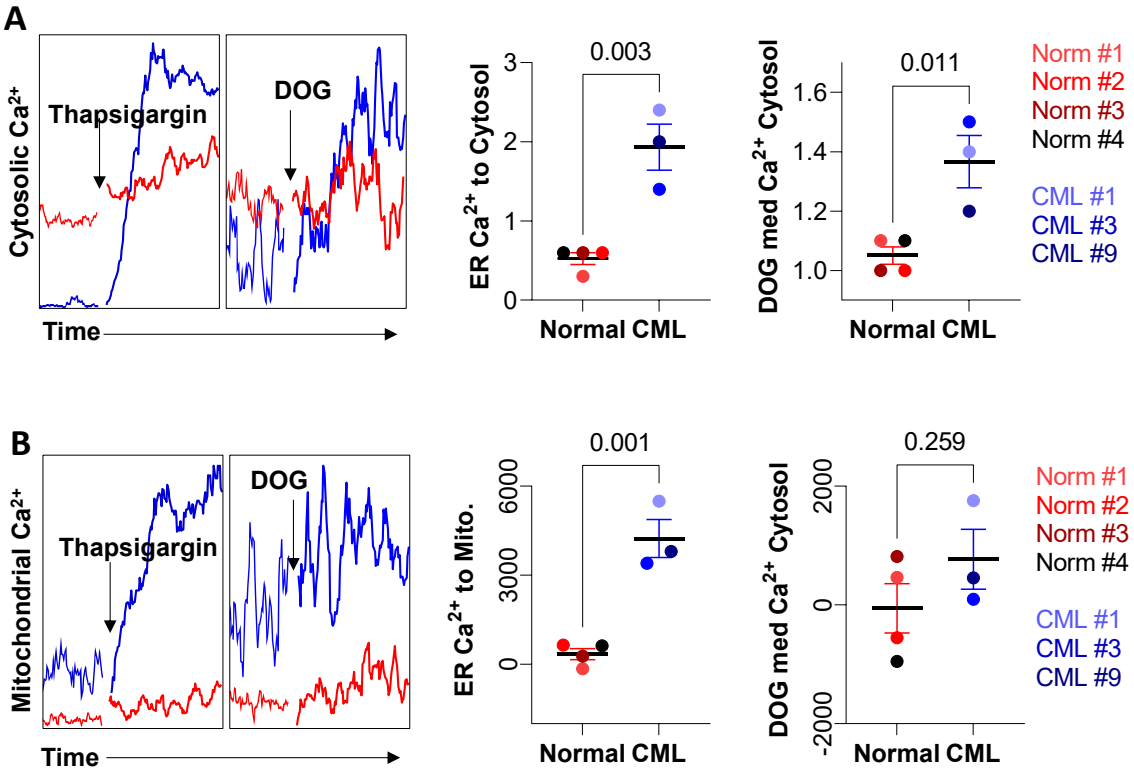

Figure 3-7: CD34+ CML cells have higher ER Ca^{2+} than normal counterparts.

(A) Representative kinetic flow cytometry data of Ca^{2+} levels in CD34+ CML cells (blue) and CD34+ normal cells (red), instantly stimulated with 2.5 µM thapsigargin or 25 µM DOG (DAG analogue) for 200 seconds. (B) Representative cytosolic and mitochondrial Ca^{2+} levels in CD34+ CML and their normal counterparts. The results represent samples from individuals with CML (n=3) and non-CML (n=4). Statistical analysis was performed with Student's t-test to calculate significance.

3.5 Impact of imatinib on ER and mitochondrial mass

Another experimental approach was performed to quantify mitochondria in KCL22 and K562 cell lines after their exposure to 0.5 μM imatinib for 72 hours by staining cells with Mitotracker Green (MTG) (Figure 3-8). Results show that imatinib significantly reduces mitochondrial content in KCL22 with trend reduction in K562 cells, proposing necessity for quantification of mitochondrial content using more accurate assay, through generating TOM20 expressing CML cells.

In order to deliver this approach, ER (mCherry-RAMP4) and mitochondrial (eGFP-TOM20) fluorescent expressing WT, ATG7 knock out (KO), ULK1 KO KCL22 and K562 cell lines were generated using constructs described before (See materials & methods, Table 2-20). The transfected cells will subsequently be named RAMP4-TOM20 (RT cells). WT RT KCL22 and K562 cells were treated for 24 hours with 1 μM imatinib, followed by visualising mitochondrial and ER content with confocal microscopy (Zeiss LSM 780®). Imatinib seems to reduce eGFP-Tom20 and mcherry-RAMP4 fluorescence intensity in WT RT K562 and WT RT KCL22 cells, reflecting possible reduction in ER and mitochondrial mass as visualised once using confocal microscopy (Figure 3-9).

As expected, mitochondrial mass reduction upon imatinib treatment significantly reduces mitochondrial ROS, cytosolic ROS, and mitochondrial potential in K562 cells (Figure 3-10). Author included CCCP known mitochondrial uncoupler as a positive control that is known to disrupt mitochondrial membrane potential. Further, N-acetyl cysteine (NAC) known as antioxidant compound was included as a positive control that showed ability to scavenge ROS from untreated cells.

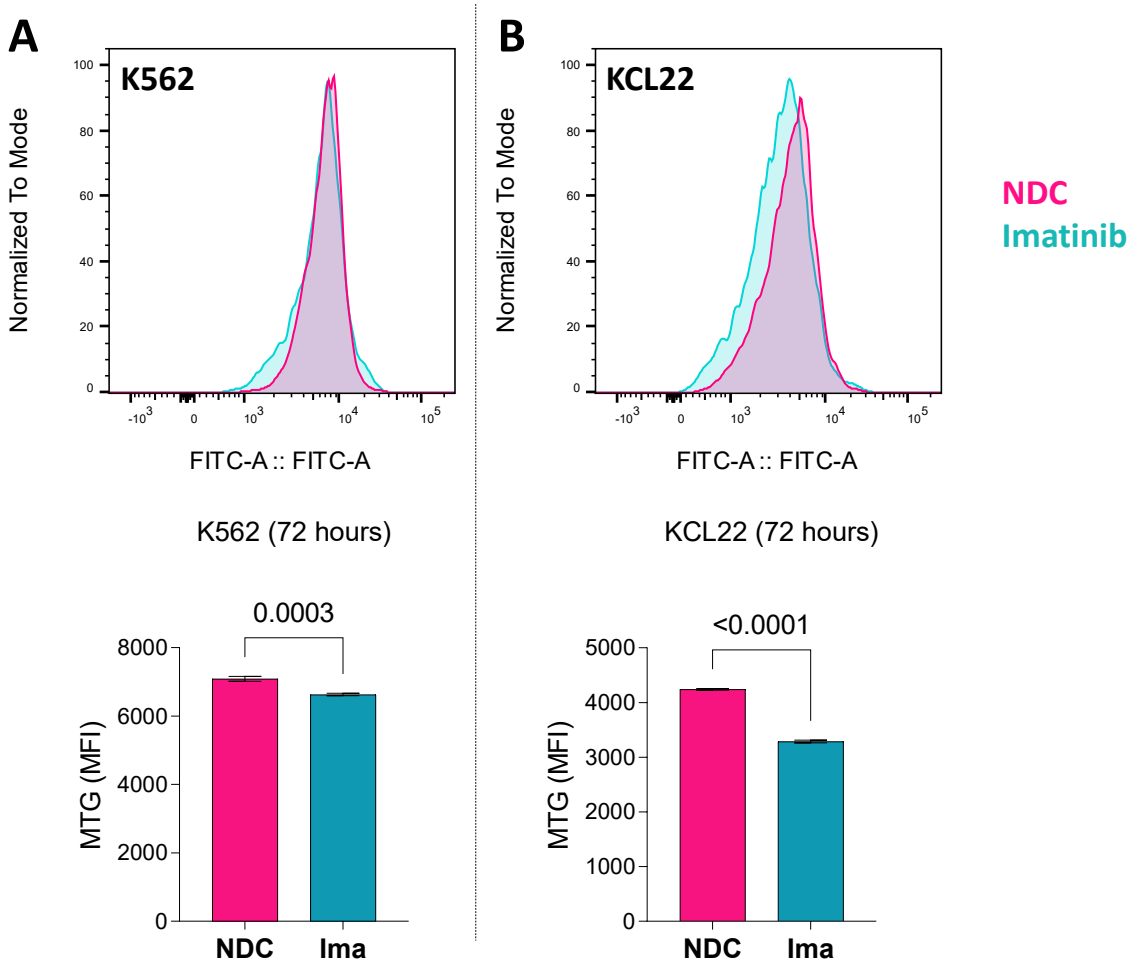

Figure 3-8: Imatinib shows trend reduction in mitochondrial content in CML cell lines.

Level of mitochondrial mass as measured by quantification of Mito Tracker green (MTG) fluorescence intensity using flow cytometry (FITC channel) after exposure of K562 cells (A) or KCL22 cells (B) to 0.5 μM imatinib for 72 hours. Experiment was performed once, n=3 technical replicates each cell line. Error bars are shown as SDM +/- MFI and Student t-test is performed to measure statistical significance.

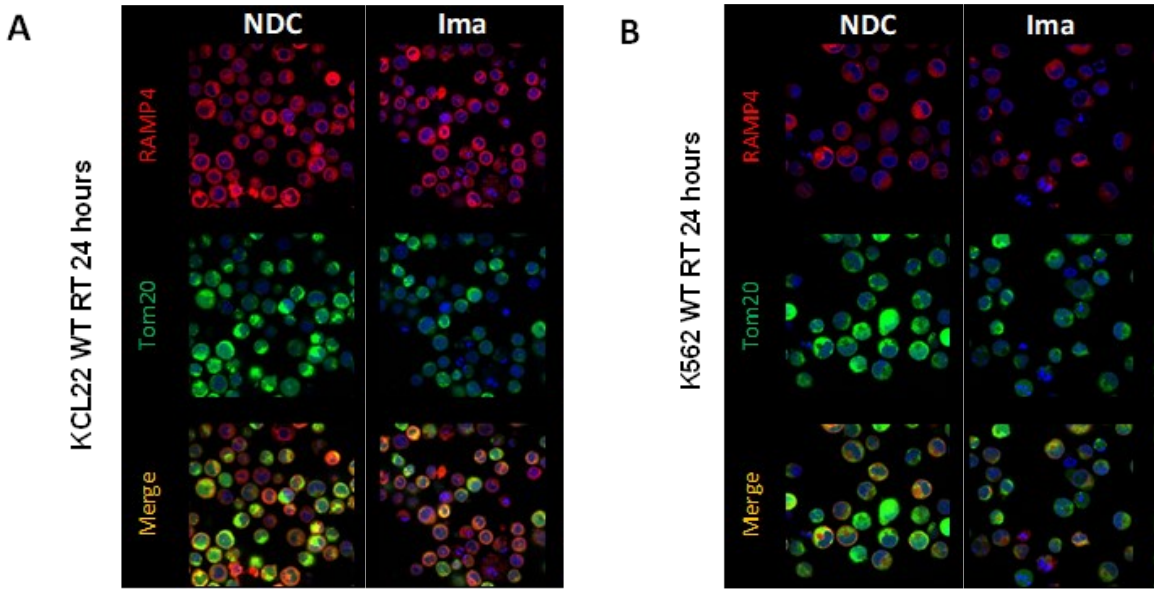

Figure 3-9: imatinib shows trend reduction in ER and mitochondrial mass in CML cells.

Confocal microscopy visualisation of mitochondrial mass (eGFP Tom20) and ER mass (mCherry RAMP4) alongside Hoechst nucleus staining after treatment with 1 μM imatinib for 24 hours using Zeiss780 confocal microscopy in double positive sorted (A) KCL22 and (B) K562 cells. Cells are shown at 10 μm scale at 40X magnification, where imaging (n=1 technical replicate).

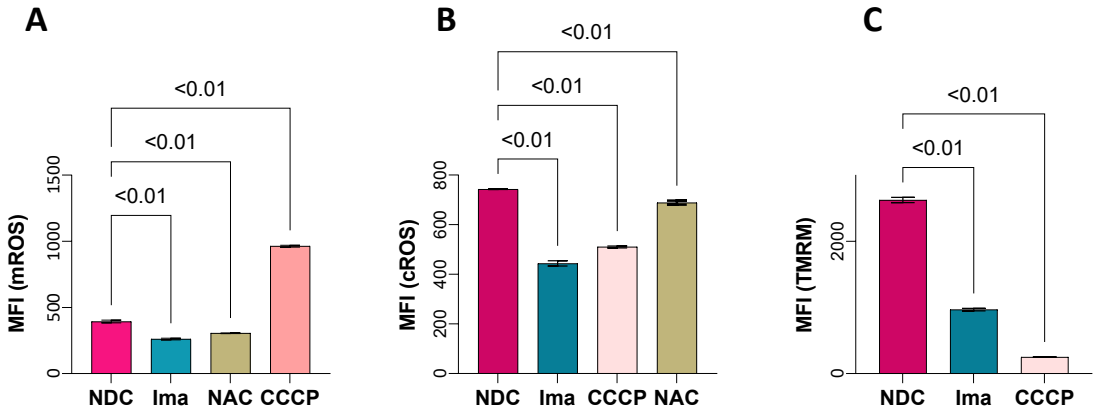

Figure 3-10: Imatinib reduces mitochondrial activity in K562 cells.

(A) Bar plot shows mitochondrial ROS in WT K562 treated with 0.5 μM imatinib for 72 hours. (B) Bar plot shows cytosolic ROS in WT K562 treated with 0.5 μM imatinib for 72 hours. (C) Bar plot shows mitochondrial membrane potential in WT K562 treated with 0.5 μM imatinib for 72 hours. 200 μM N-acetyl cysteine and 10 μM CCCP were used as a control (n=4 technical replicates), using flow cytometry. Statistical analysis was performed with one-way ANOVA and Tukey was performed to correct for multiple comparisons.

Similarly, to measure impact of imatinib on mitochondrial and ER mass, CD34+ CML were cultured in SFM supplemented with physiological growth factors and treated with imatinib for 24 hours. The cells were stained with mitochondrial and ER fluorescence trackers and quantified with flow cytometry (Figure 3-11A & 10C). Imatinib significantly reduces ER and mitochondrial mass. To measure the effect of imatinib on CD34+ CML mitochondrial potential, cells were stained with membrane-permeable JC-1 dye that is extensively utilised in apoptosis research to assess mitochondrial health. JC-1 green fluorescence emission shows potential-dependent accumulation of JC-1 dye in mitochondria at (529 nm) for monomeric form of the probe, which switches to red fluorescence at (529 nm) with concentration-dependent production of red fluorescent J-aggregates. In turn, a decrease in the (red/green) fluorescence intensity ratio indicates mitochondrial depolarisation. Results of JC-1 staining reflects trend reduction in mitochondrial potential after 24 hours of imatinib treatment (Figure 3-11B).

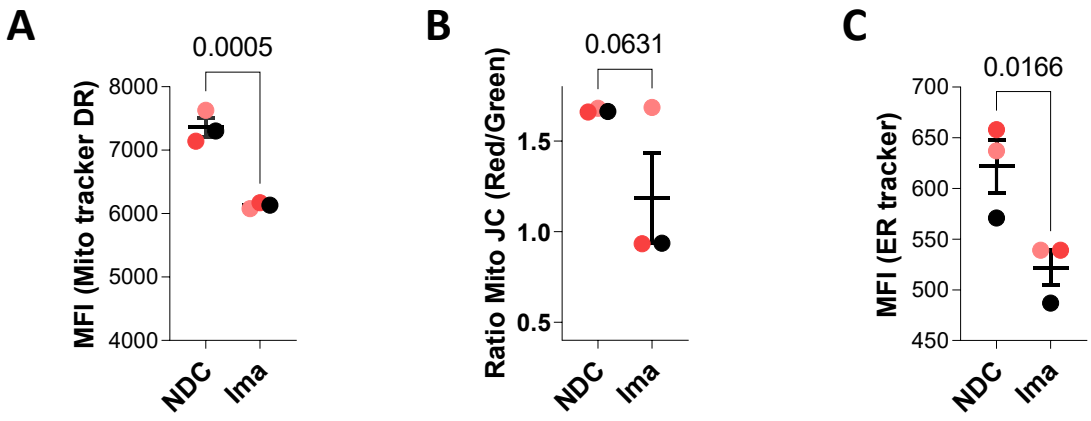

Figure 3-11: Imatinib reduces mitochondrial and ER mass in CD34+ CML cells.

(A) Level of mitochondrial mass as measured by Mito-tracker red using flow cytometry, n=3. (B) Level of mitochondrial potential as measured by Mito-JC mitochondrial staining of CD34+ CML treated 1 μM imatinib for 24 hours followed by flow cytometry, where n=3 CML patient samples.
(C) ER mass of CD34+ CML treated with 1 μM imatinib for 24 hours, n=3 CML patient samples using flow cytometry. Statistical analysis was performed with one-way ANOVA and Tukey was performed to correct for multiple comparisons.

Findings reflect consistency to results of flow cytometry in WT RT K562 and KCL22 cell lines (Figure 3-12; left bar graphs of WT cells). Bafilomycin A1 was included in this experiment due to its known impact on autophagosome-lysosome fusion to determine the activity of autophagic flux through interfering with lysosomal acidification and preventing the protons passage into the lysosomal structure [228]. Thus, author used bafilomycin as a positive control that may lead to accumulation of mitochondria and other organelles such as ER. Bafilomycin as a positive control shows ability to enhance level of detected mitochondria in WT cells without altering ER level compared to untreated cells (Figure 3-12).

Further, the reason for reduced mitochondrial and ER mass upon imatinib treatment was not clear. Helgason lab previously reported that imatinib triggers increased canonical ATG7- or ULK1-mediated autophagy [229]. The author speculated that mitochondrial mass and ER mass reduction arose from activating mitochondrial-specific autophagy (mitophagy) and ER specific autophagy (Reticulophagy; ER-Phagy). To test this, mitochondrial and ER mass were quantified with flow cytometry in RAMP4 and TOM20 (RT) expressing WT, ATG7 KO, and ULK1 KO cell lines upon exposure to 1 μM imatinib for 24 hours (Figure 3-12; middle and right bar blots of ATG7& ULK1 KO cells). Unexpectedly, imatinib reduces mitochondrial and ER mass in autophagy deficient cell lines at 24 hours, indicating that imatinib induces ATG7 or ULK1 independent mass reduction.

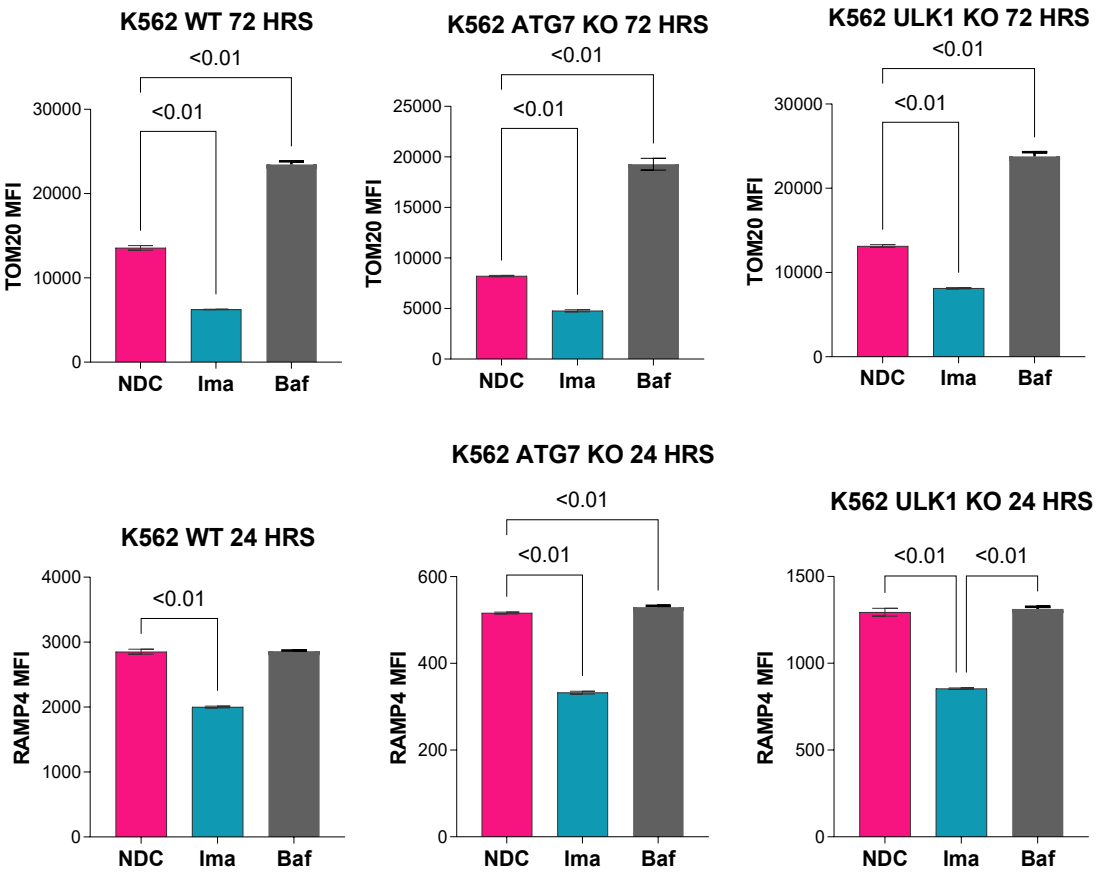

Figure 3-12: Imatinib reduces mitochondrial and ER mass in K562 cells.

Bar plots showing level of mitochondrial mass (TOM20) and ER mass (RAMP4) in WT K562, ATG7 KO and ULK1 KO K562 cells that are expressing GFP Tom20 following 24 and 72 hours of treatment with 1 μM imatinib as measured by flow cytometry. Error bars are presented as SDM+/- mean, where n=5 technical replicates. Statistical analysis was performed with one-way ANOVA and Tukey was performed to correct for multiple comparisons.

3.5.1 Imatinib induces ER-Phagy in K562 cells.

To further investigate the reason for reduced ER mass upon imatinib treatment, ER specific autophagy (ER-Phagy) reporter designed by Liang *et al*. were generated in WT KCL22 cells. In brief, Liang *et al*. developed a doxycycline-inducible ER-Phagy reporter with an N-terminal ER localisation sequence followed by tandem GFP and monomeric RFP sequences followed by ER retention sequence known as KDEL [203]. ER-Phagy reporter dual green and red fluorescence are detected under cytosolic pH=7-8. Only red fluorescence signal is detected when ER is trapped in low pH (pH=3-5; inside lysosomes) because green fluorescence is quenched and in low pH. When ER-Phagy reporter expressing WT KCL22 cells were exposed to 1 μM imatinib, cells induce ER-Phagy, both at 24 hours and 48 hours, concluding that imatinib induces ER-Phagy (Figure 3-13). To author's knowledge, there is no known ER-Phagy compound stimulator to include as positive control. The reason for using oligomycin A and antimycin A (OA+AA), or CCCP because those compounds are known as mitophagy drivers, as will be illustrated in next section, that may also enhance ER-Phagy. Also, bafilomycin known autophagy inhibitor was included as positive control. However, unlike mitophagy, OA+AA or CCCP compounds do not significantly interfere with ER-Phagy process, indicating independent regulation of both mitophagy and ER-Phagy (Figure 3-13). Bafilomycin significantly inhibits ER-Phagy which is expected but contradicting with initial findings that bafilomycin does not interfere with ER mass complicating our understanding to mechanism of ER mass regulation which require thorough investigation.

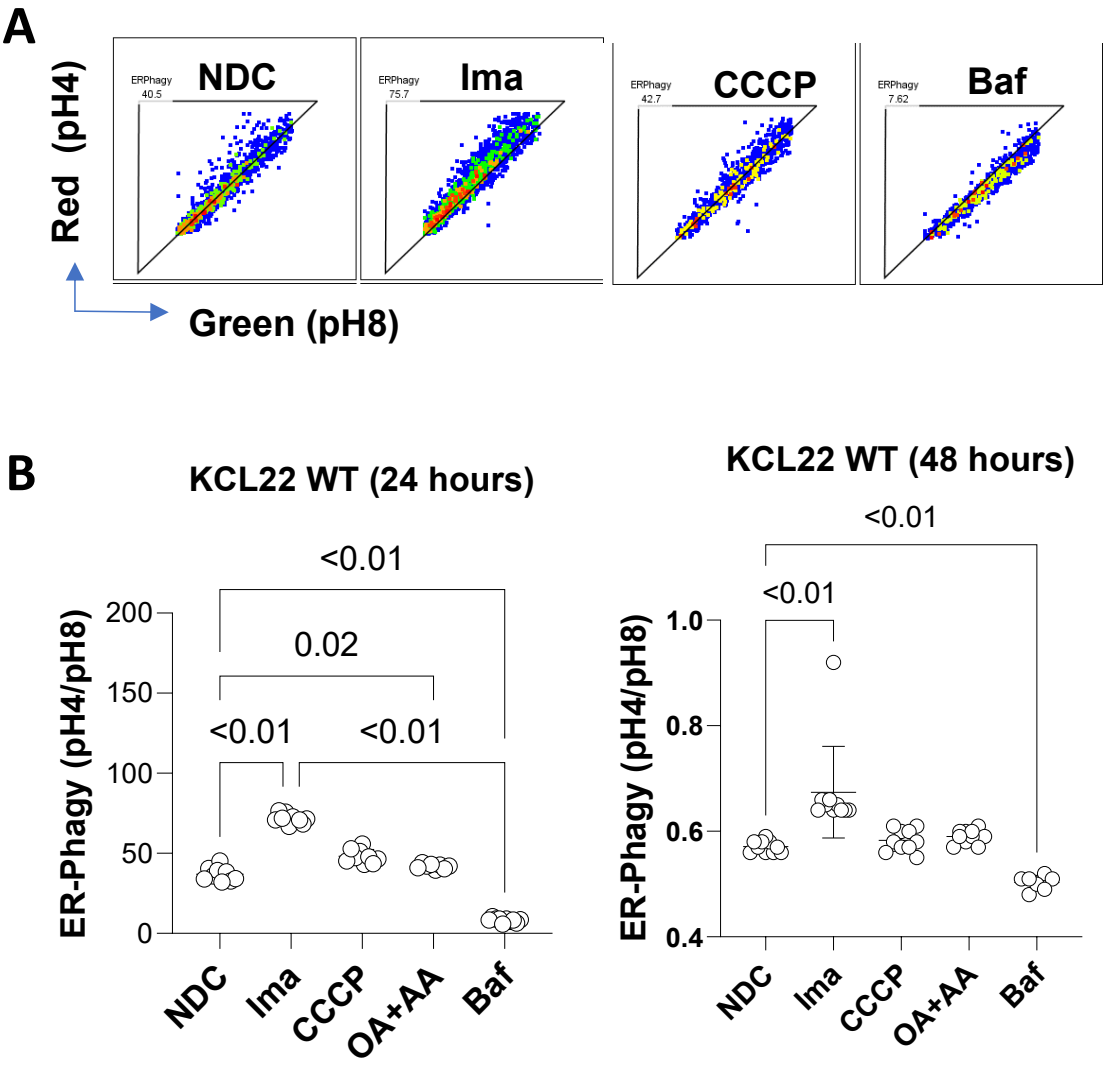

Figure 3-13: Imatinib induces ER-Phagy in KCL22 cells.

(A) Flow cytometry highlights the fraction of cells with ER in acidified pH (lysosomes), depicted by expressing ER-Phagy reporter in WT KCL22 cell line. (B) Representative dot plot shows the ratio between green fluorescence to red fluorescence (ER-Phagy level) upon treating KCL22 expressing ER-Phagy reporter using 1 µM imatinib, 10 µM CCCP, 5 µM (OA+AA), or 100 nM bafilomycin for 24 and 48 hours (n=10 technical replicates). Statistical analysis was performed with one-way ANOVA and Tukey was performed to correct for multiple comparisons. Data were pooled from two different data sets, including E-MTAB-2581 and E-MTAB-2594.

To identify candidate genes that could participate in ER-Phagy upon imatinib treatment, the transcriptome datasets of ER related degradation pathways involved genes were analysed. The strategy applied to transcriptome datasets were performed by extracting top-upregulated genes from ER related GSEA enriched in LSCs compared to HSCs. The expression level of those upregulated genes was similarly assessed in transcriptome dataset which compares between 7 days of imatinib treatment versus untreated CML LSCs. Results reveals enrichment of fatty acid recycling genes that have been reported to have 100% confidence localisation in ER, according to https://compartments.jensenlab.org/Search (Figure 3-14). The same strategy was applied on ER degradation genes by text mining and revealed that some genes are upregulated in LSC versus their normal HSC counterparts without major impact after exposure to imatinib for 7 days. Thus, those ER related genes are potential candidates that is worth further investigation in CML.

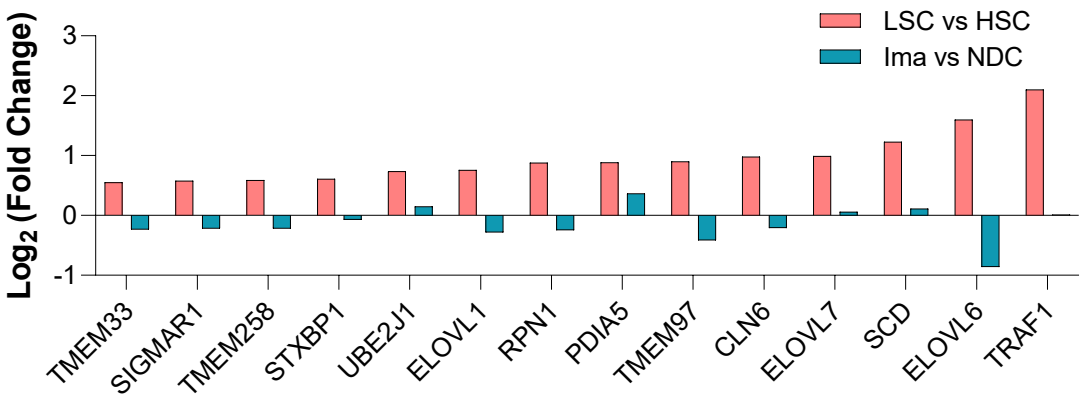

Figure 3-14: Effect of imatinib on ER genes in CD34+ CML cells.

Expression levels of top significant ER related genes from CD34+ CD38- CML versus CML transcriptome dataset and their expression in CD34+ CD38- CML after exposure to 7 days imatinib versus their untreated CML cells. Genes were extracted from top enriched in ER related GSEAs and those related to ER as reported in literature (text mining). Data were pooled from two different data sets, including E-MTAB-2581 and E-MTAB-2594.

3.5.2 Imatinib does not alter mitophagy in CML cell lines.

Next, author aimed to investigate the reason for reduced mitochondrial content caused by imatinib treatment in CML cells. Imatinib induces autophagy in CML [165], however, autophagy deficient cells did not correct imatinib mediated mitochondrial mass reduction (Figure 3-12). Experimentally, mitophagy reporter, mKeima, can stay stable in different pH conditions and has bimodal excitation according to the pH condition [201]. For example, mKeima construct is optimally excited at a short wavelength (440nm) when it is at neutral pH and excited at a longer wavelength (586nm) when protein exists in pH=4 (mitochondria is targeted to lysosomal degradation; mitophagy) (Figure 3-15). Both excitations emit at the same wavelength (620 nm). both excitation emissions can get measured simultaneously. However, it was tended to differentially measure two emissions sequentially by deactivating one of excitation lasers through switching of photomultiplier (PMT= 0) while the other laser was active (PMT~ 350) (Figure 3-15).

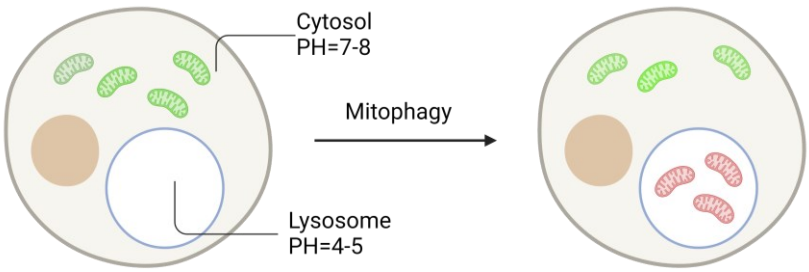

Figure 3-15: Mitophagy assessment using mKeima construct.

Nevertheless, the mitochondrial mass reduction could be related to other ATG7 or ULK1 independent lysosomal degradation (mitophagy). Thus, mKeima expressing WT, ATG7 KO, or ULK1 KO of two CML cell lines (K562 and KCL22 cells) were generated. To investigate if imatinib induces mitophagy, mKeima expressing cell lines were treated with 1μM imatinib for 48 hours. Results reveals that imatinib does not alter mKeima ratios (mitophagy level) in K562 or KCL22 cells (Figure 3-16), suggesting mitophagy independent mitochondrial mass reduction in CML upon imatinib treatment. Author included OA+AA combination as a positive control that significantly enhances mitophagy (Figure 3-16).

Functional impact on mitochondrial and cytosolic Ca^{2+} levels when WT, ATG7 KO, and ULK1 KO K562 cells were treated with 1μM imatinib for 24 hours was investigated (Figure 3-17A-C). Results indicate that ULK1 or ATG7 deletion significantly increases the level of mitochondrial Ca^{2+} ions, accompanied by a significant reduction in cytosolic Ca^{2+} ions, compared to vector control K562 cell lines. This indicates that autophagy deficient cell lines have more mitochondrial content and more Ca^{2+} ions buffering capacity of through these mitochondria. However, mitochondrial Ca^{2+} level is significantly reduced when ATG7 KO or ULK1 KO K562 cells treated with 1μM imatinib for 24 hours. Thus, while the increase in basal mitochondrial Ca^{2+} levels in ATG7 and ULK1 KO cells is likely due to block in autophagy, imatinib reduced the level of mitochondrial Ca^{2+} in an autophagy independent manner.

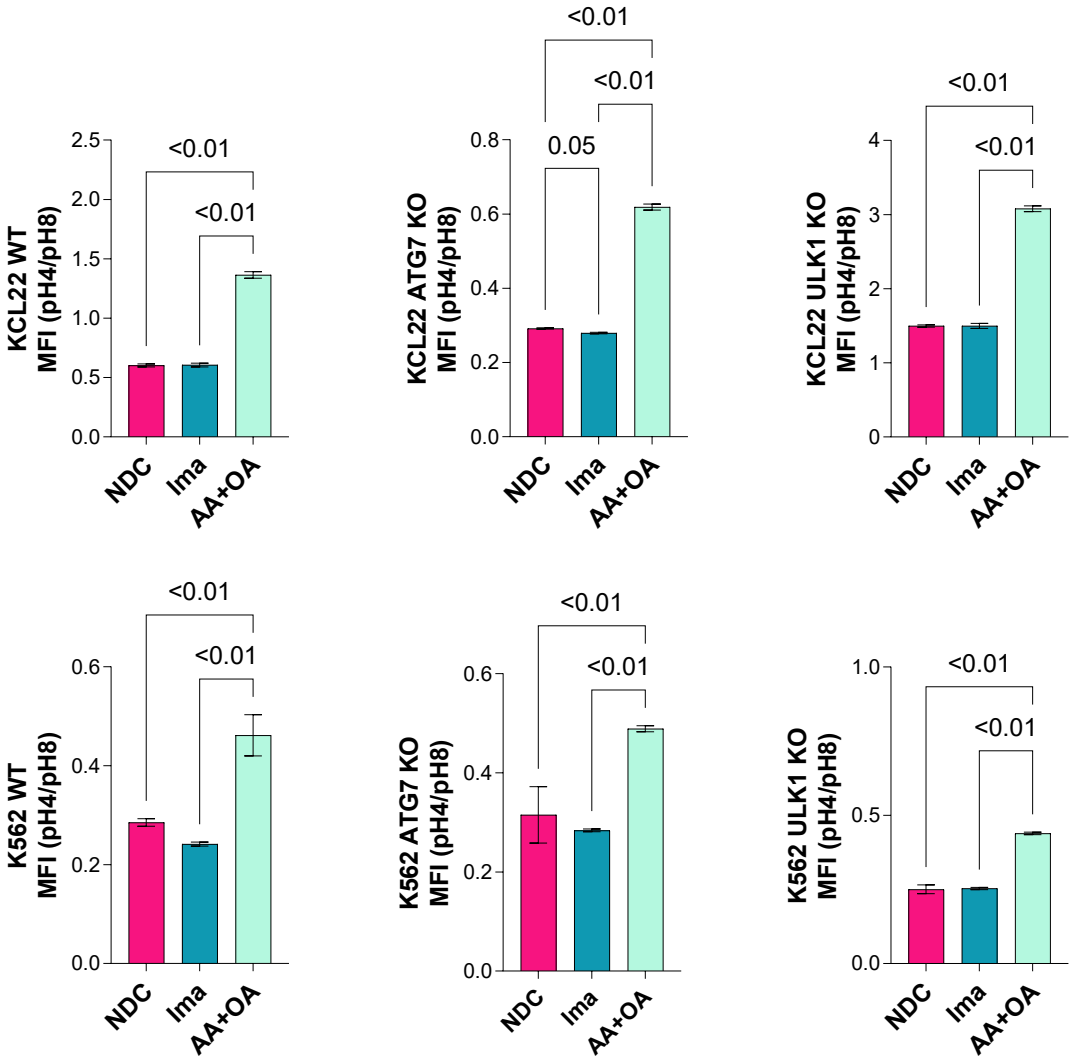

Figure 3-16: Imatinib does not alter mitophagy in KCL22 or K562 cells.

Bar plots show level of mitophagy (ratio of pH4/pH8 mitochondrial levels) using mKeima expressing cells treated with 1 μM imatinib or 5 μM (AA+OA) for 24 hours. Statistical analysis was performed with one-way ANOVA where n=3 technical replicates and Tukey was performed to correct for multiple comparisons.

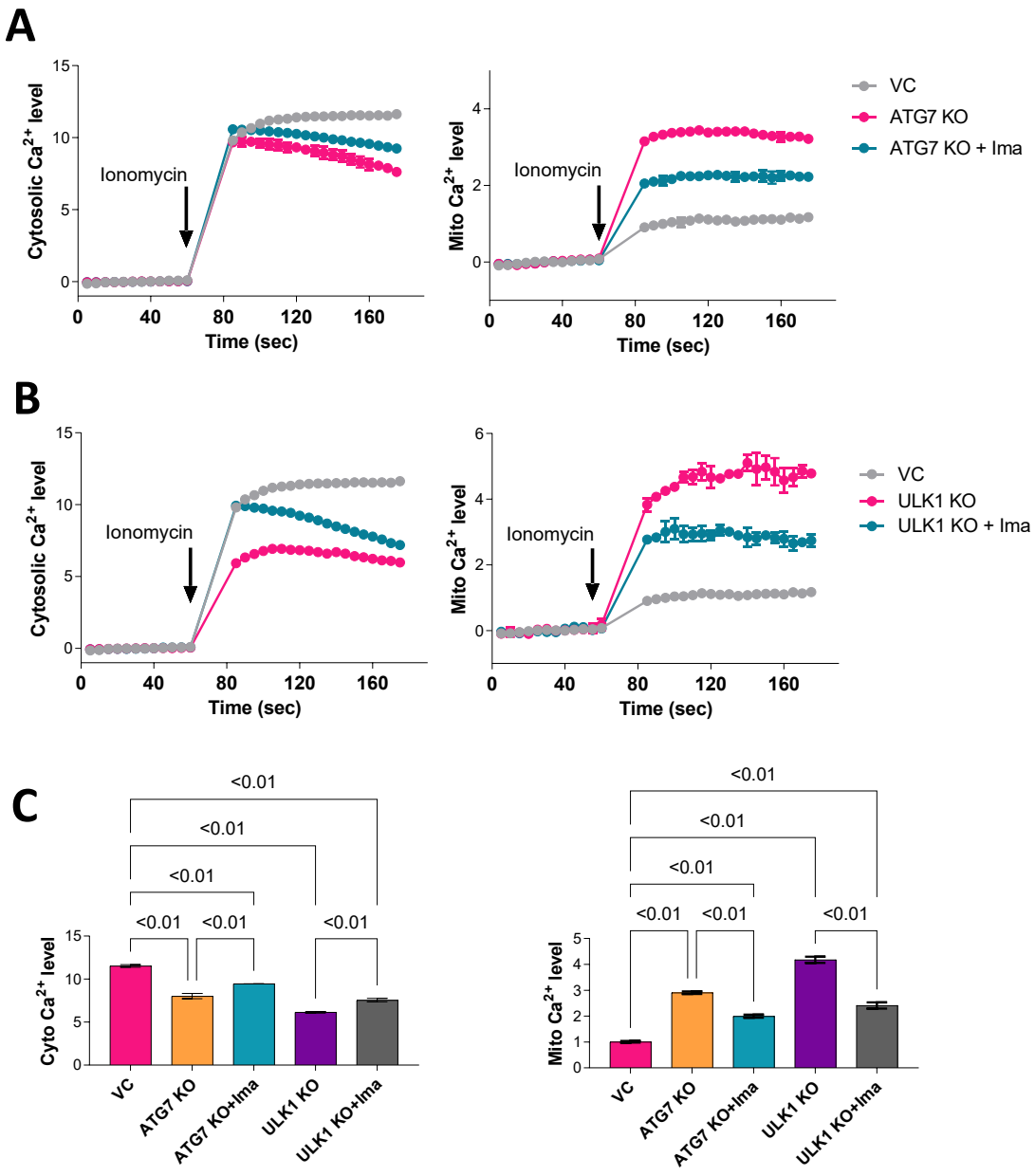

Figure 3-17: Imatinib reduces mito. Ca^{2+} in autophagy deficient cells.

(A) Representative kinetic flow cytometry Ca^{2+} levels in vector control, ATG7 KO, and ATG7 KO K562 cells exposed to 1 μM imatinib for 24 hours and stained with Indo-1 and Rhod-2 Ca^{2+} indicators. Cells are stimulated with 2.5 μM ionomycin during acquiring event on cytometer. (B) Representative kinetic flow cytometry Ca^{2+} levels in vector control, ULK1 KO, and ULK1 KO K562 cells exposed to 1 μM imatinib for 24 hours. Cells are stimulated with Ca^{2+} ionophore ionomycin during acquiring event on cytometer. (C) Representative statistical analyses of cytosolic and mitochondrial Ca^{2+} levels in WT, ATG7 KO, and ULK1 KO K562 cells (n=4 technical replicates). Statistical analysis was performed with one-way ANOVA and Tukey was performed to correct for multiple comparisons.

3.5.3 Imatinib reduces mitogenesis in CML cells

Yet, it is not clear if mitochondrial mass reduction arises from other degradation pathways such as proteasomal degradation or peroxisome mediated degradation, or it is simply reduced because of inhibited mitochondrial *de novo* synthesis. Mitochondrial biogenesis reporter, lentiviral construct called Mito-Timer designed by Garcia lab, Spain, were expressed in WT and ATG7 KO K562 cells. In brief, Mito-Timer based red fluorescent protein, ds Red, has a mutation known as a fluorescent timer, or DsRed1-E5, whose fluorescence changes over time from green to red as protein matures. The Mito-Timer construct is a maturation-based construct that can be targeted to measure *de novo* synthesised mitochondria [202, 230]. As shown in Figure 3-18, WT and ATG7 KO K562 cells expressing Mito-Timer were induced with 2 µg/ml doxycycline for 8 hours before treatment to induce expression of Mito-Timer for mitochondrial maturation process tracking. Induced cells were treated with 1 µM imatinib, 100 nM bafilomycin for 32 hours in K562 cells. Same treated cells were exposed for another induction pulse at 2 µg/ml doxycycline for extra 8 hours cells without washing out imatinib, followed by quantification of green (fresh mitochondria) and red fluorescence (mature mitochondria).

Results show that imatinib significantly reduces the level of green fluorescence after second pulse of induction (mitochondrial biogenesis), revealing that reduced mitochondrial mass is mitogenesis dependent (Figure 3-19A).

In addition, autophagy inhibition with *ATG7* deletion in K562 cells progressively reduces mitochondrial biogenesis, highlighting a possible role of autophagy inhibition on mitochondrial biogenesis inhibition, which may contribute to the mitochondrial mass loss (Figure 3-19B). Bafilomycin, known autophagy inhibitor, however, enhances mitochondrial biogenesis which may reflect either off target effect of bafilomycin or due to its acute effect on cellular functions. The assumed consequence may be subsequent differentiation of LSCs to mature erythrocytes when autophagy is blocked [229], although this still requires more thorough investigations.

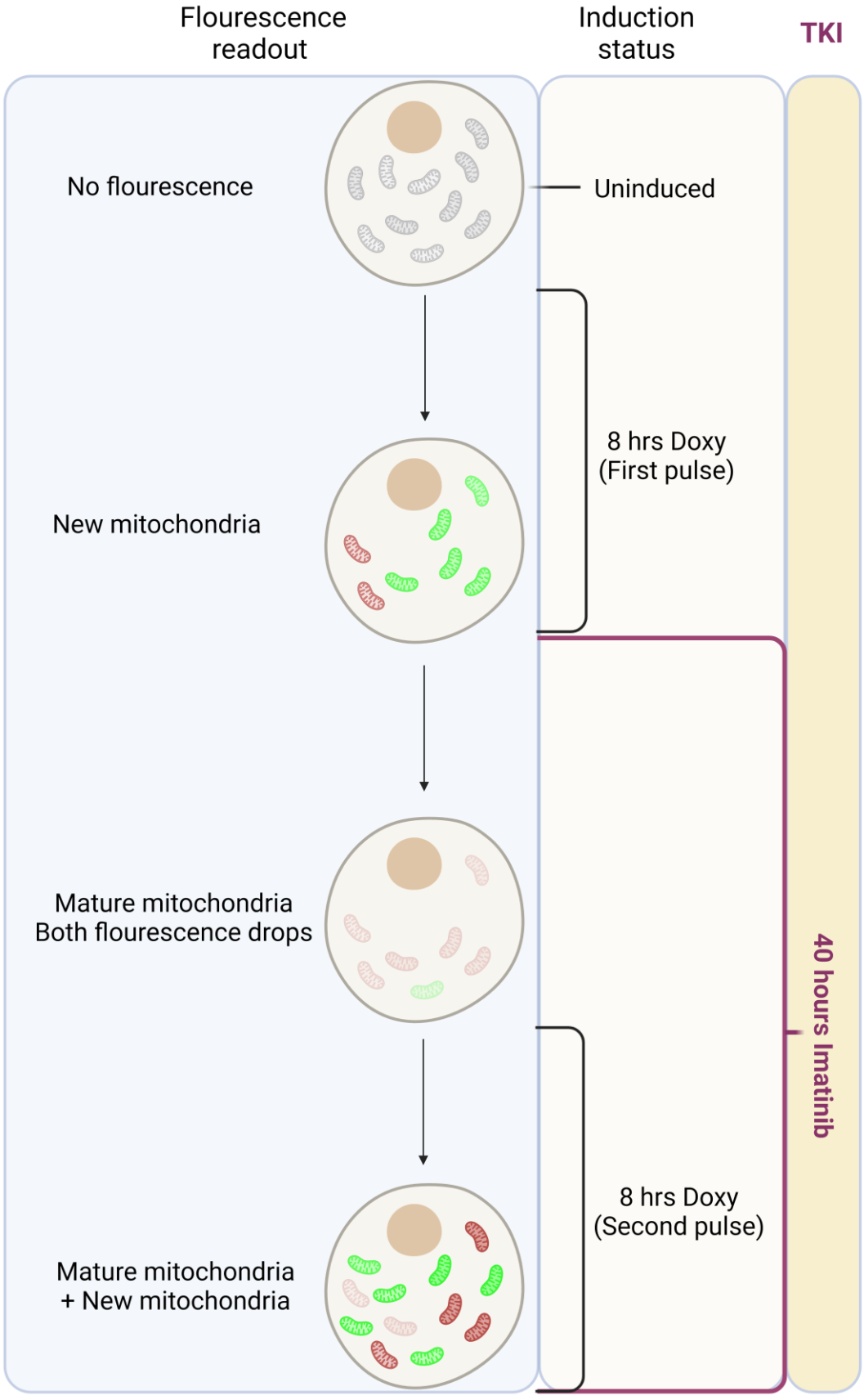

Figure 3-18: Experimental design of Mito-Timer expressing K562 cells.

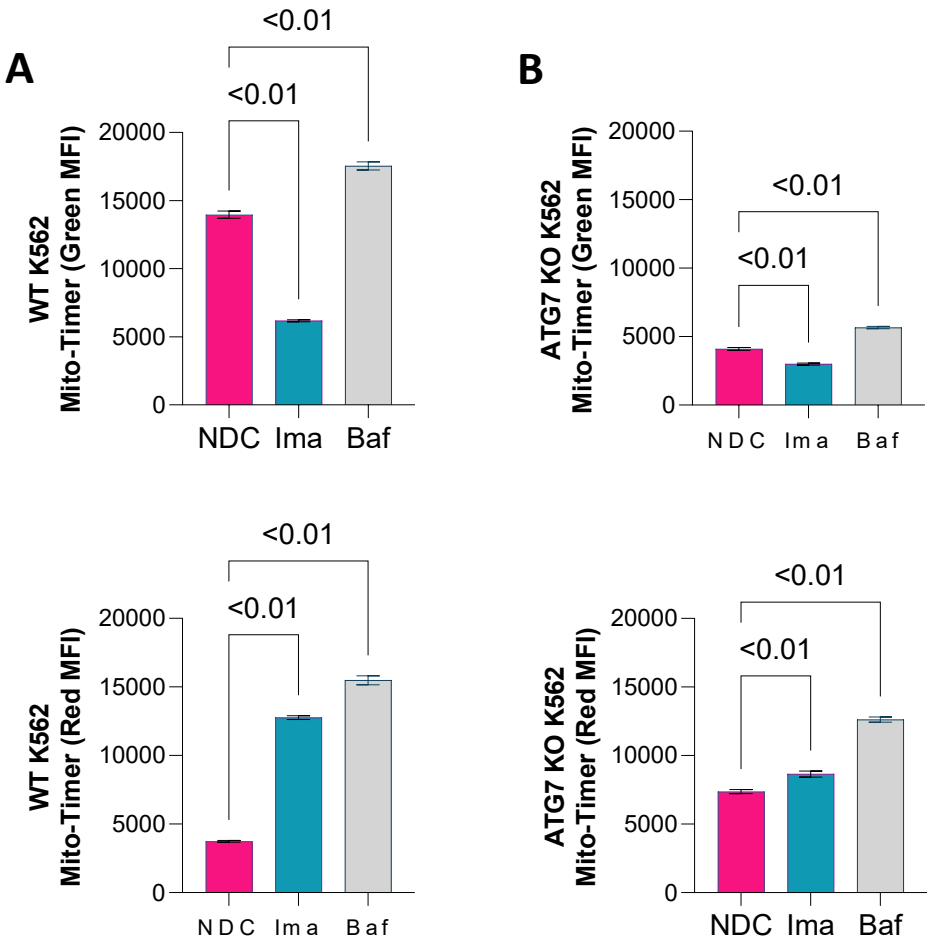

Figure 3-19: Imatinib inhibits mitochondrial biogenesis in K562 cells.

Flow cytometry analysis in Mito-Timer expressing WT K562 cells (A) and ATG7 KO K562 cells (B) after exposure to 1 μM imatinib or 100nM bafilomycin where new mitochondria (green) are shown and mature mitochondria (Red). Statistical analysis for n=8 technical replicates (Error bars are shown as SDM+/- MFI). Statistical analysis was performed with one-way ANOVA and Tukey was performed to correct for multiple comparisons.

The global Ca^{2+} signalling transcriptome landscape of CD34+CD38- CML after exposure to 2 µM imatinib for 7 days were investigated. The GSEA output reveals down-regulated hallmarks of OXPHOS and mitochondrial biogenesis at NES of -2.2 and -1.72 significantly, compared to untreated CML (Figure 3-20).

These findings indicate reduced mitochondrial gene expressions on transcriptional level, which is expected to cause reduced mitochondrial biogenesis.

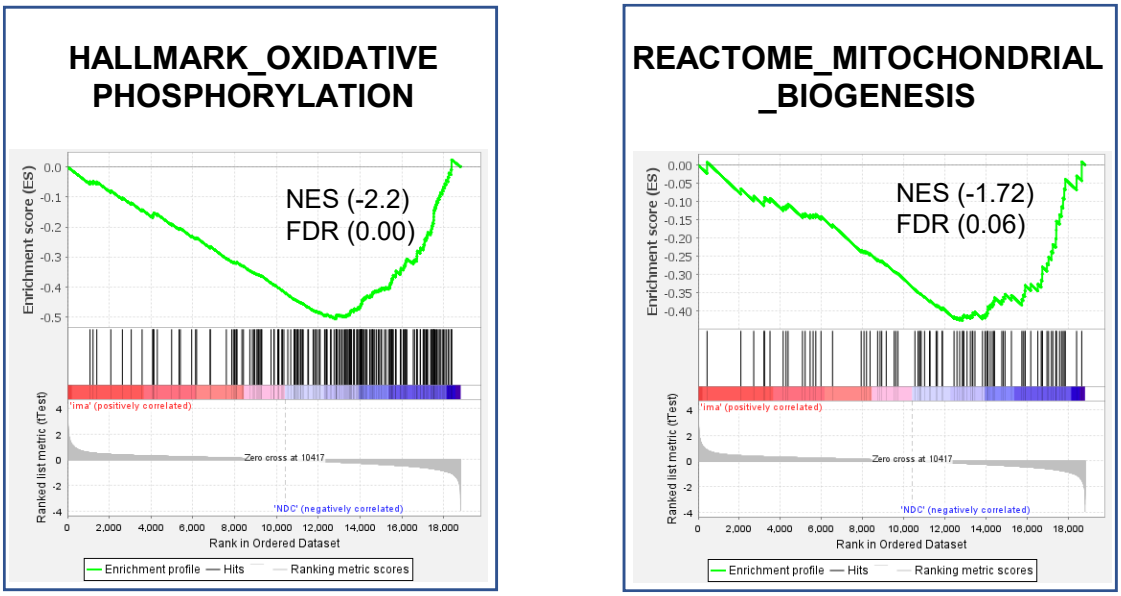

Figure 3-20: Imatinib reduces mitogenesis transcriptionally in LSCs.

GSEA of mitochondrial biogenesis Reactome from E-MTAB-2594 dataset comparing imatinib treated versus untreated CML cells.

3.6 TRPC6 or CACNA1D gene disruption in CML cells

To specifically address if CACNA1D and TRPC6 important for Ca^{2+} homeostasis and OXPHOS in CML cells, CACNA1D or TRPC6 deficient K562 and KCL22 cells were generated using CRISPR-Cas9 KO technology.

Fluorescent-based vector constructs were used; pLentiCrispr-V2-m-Orange (V2mO; Plasmid # 140206, Addgene) and LentiCRISPRv2GFP (Plasmid # 82416, Addgene). After transfecting cells with those gRNAs, cells were sorted based on their fluorescence expression (Figure 3-21A & 20B). Unfortunately, corresponding proteins are still detectable, indicating either lack of selectivity of primary antibodies or the gRNA construct synthesis was not successfully efficient. Despite verified genetic MCU deletion as shown at protein level disappears (Figure 3-22A), data showed that it cannot replicate the same approach with TRPC6 and CACNA1D in manipulated cells (Figure 3-22 B&C).

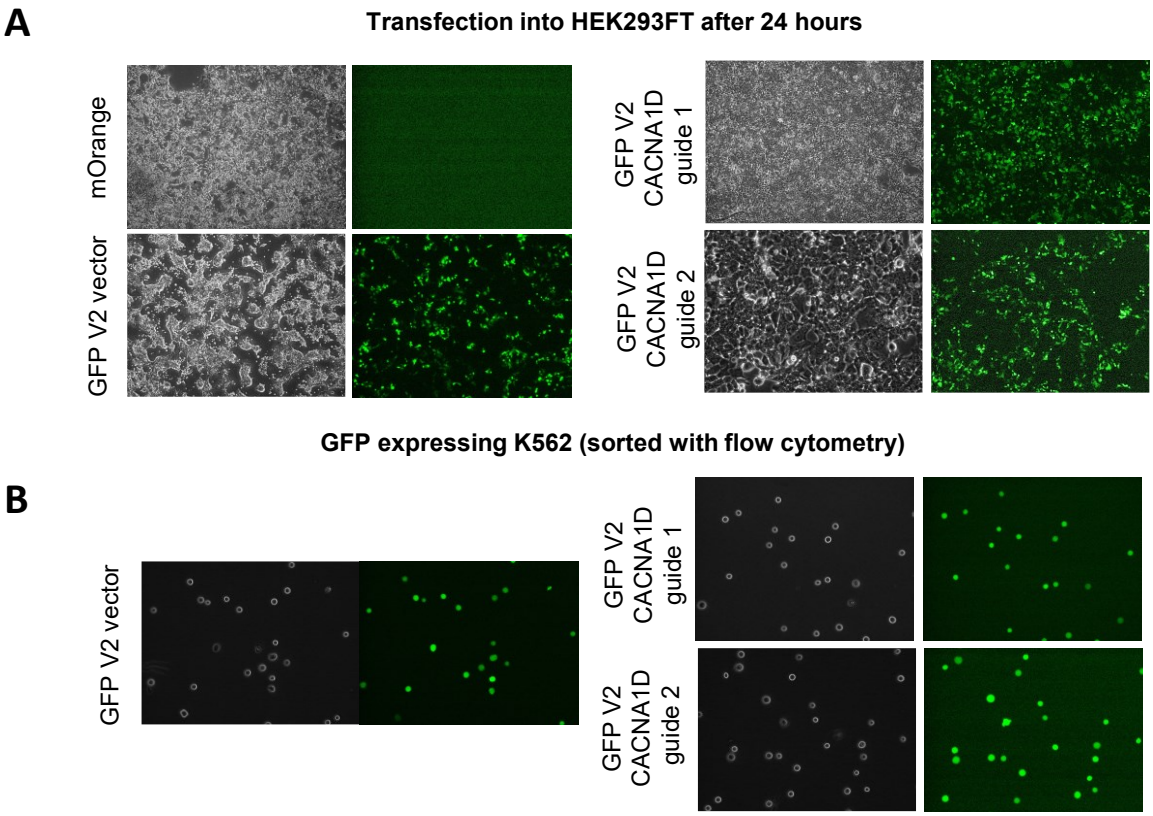

Figure 3-21: KO cells generation using GFP lenti-V2 constructs.

(A) Fluorescence imaging after 24 hours in HEK293FT cells transfected with GFP lenti-V2 construct using $CaCl_2$ reagent. Virus was collected from HEK293FT cells, concentrated, then transduced into K562 cells using 5ug/mL polybrene. (B) K562 cells were grown and sorted using FACS then imaged.

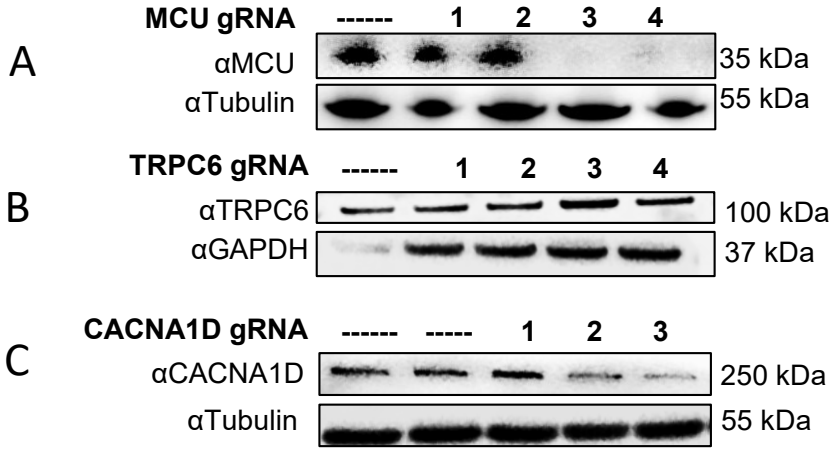

Figure 3-22: Immunoblotting of MCU, CACNA1D and TRPC6 in KO cells.

(A) Cell lysates of MCU protein in MCU KO K562 cells (B Cell lysates of TRPC6 protein in TRPC6 KO in K562 cells. (C) Cell lysates of CACNA1D KO in K562 cells.

3.6.1 Verification of TRPC6 and CACNA1D gene disruption in CML cells

Previous research findings confirmed that TRPC6 protein was still detectable after TRPC6 deletion (using CRISPR Cas9) despite immunoblotting in different primary antibodies against TRPC6 [231]. Further, TRPC6 is endogenously expressed at low levels and CRISPR-Cas9 genetic deletion was efficiently reported by western blot in TRPC6 overexpressing HEK293T cells using the same gRNA similar to those used in current studies [232]. Further, according to author's knowledge, there is no supporting previous research to show any successful verification of CACNA1D deletion at protein level. Based on this, other experimental approaches, such as DNA genetic disruption within gRNA and functionally through measuring cell response to specific Ca^{2+} influx stimulator, is used to confirm successful CRISPR-Cas9 KO strategy for targeting TRPC6 and CACNA1D.

Successful motif amplification of genomic *TRPC6* and *CACNA1D* was verified after DNA extraction using primers that flank gRNAs (Materials and Methods; Table 2-1, Figure 3-23). After sequencing those amplicons, DNA sequencing verified the disruption within the 20 nucleotides of gRNA of CACNA1D or TRPC6 in both manipulated cell lines (Figure 3-24A). Results also verified that sequence of whole amplicon (around 500 base pairs) is disrupted as visualised by using Tide software platform, showing that most editing within amplicon was nucleotides deletion rather than insertion of new nucleotides, and aberrant sequence was initiated within gRNA (Figure 3-24B).

Functionally, to verify the impact of TRPC6 gene disruption, TRPC6 KO cells significantly reduces TRPC6 mediated Ca^{2+} influx (hyperforin; TRPC6 stimulator) but not CACNA1D mediated Ca^{2+} influx (FPL; CACNA1D stimulator, Figure 3-25A). Similarly, CACNA1D KO reduces CACNA1D mediated Ca^{2+} influx but not TRPC6 mediated Ca^{2+} influx (Figure 3-25B).

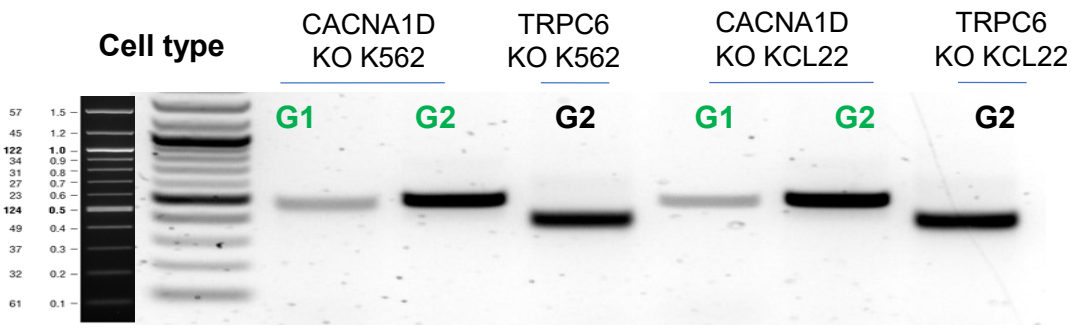

Figure 3-23: Genomic PCR of CACNA1D and TRPC6 validation.

Gel electrophoresis shows PCR products in K562 and KCL22 KO cells using primers corresponding to motifs that flanks gRNA of gene of interest.

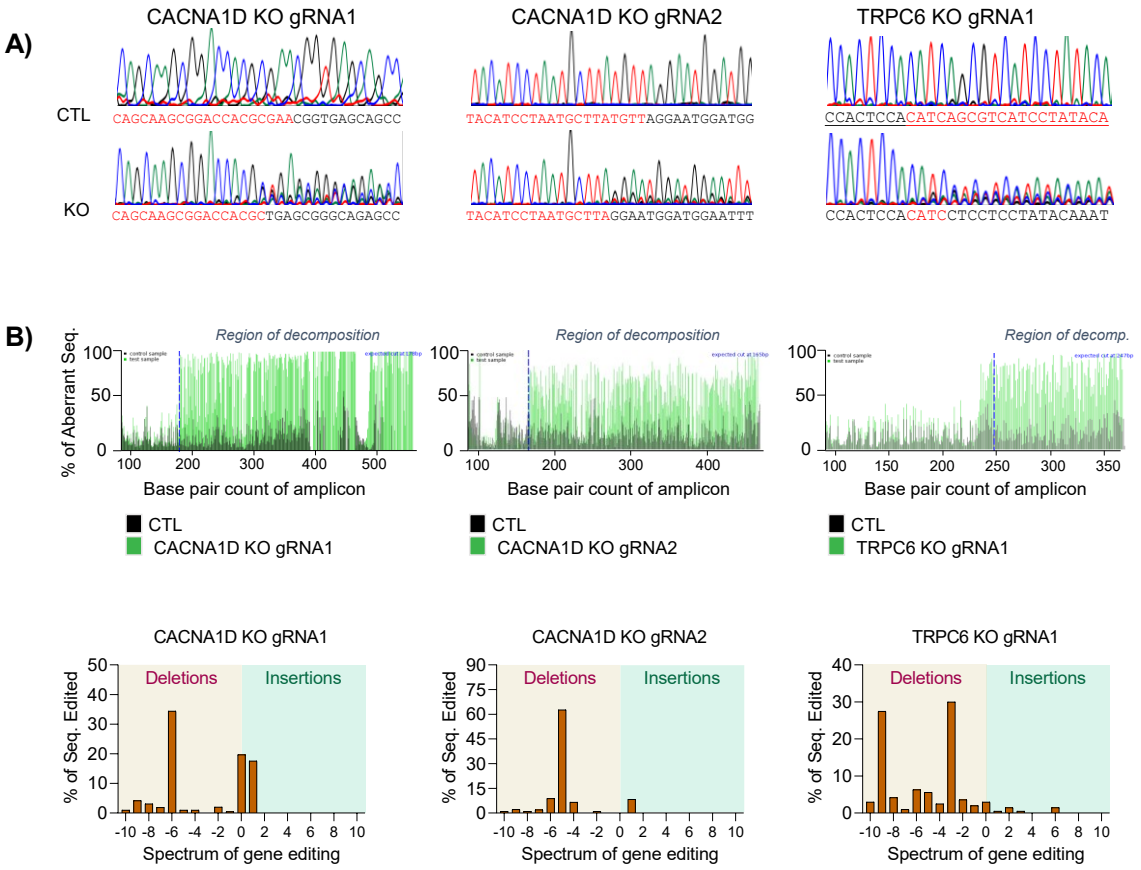

Figure 3-24: Sanger sequencing of genomic CACNA1D and TRPC6 amplicons.

(A) Sequencing of gRNA of vector and KO cells. Illustration was generated by Chromas software (B) Region of decomposition within whole PCR amplicon, where each vertical line represents a base pair. The green indicates aberrant base pair, and the length represents the % of decomposition. The point highlighted on x axis where lies within the gRNA region indicating that the change occurs in response to disruption of the sequencing. The bar graph indicates that genome editing results in deletion rather than insertion because of genetic disruption. Graphs were generated by Tide platform.

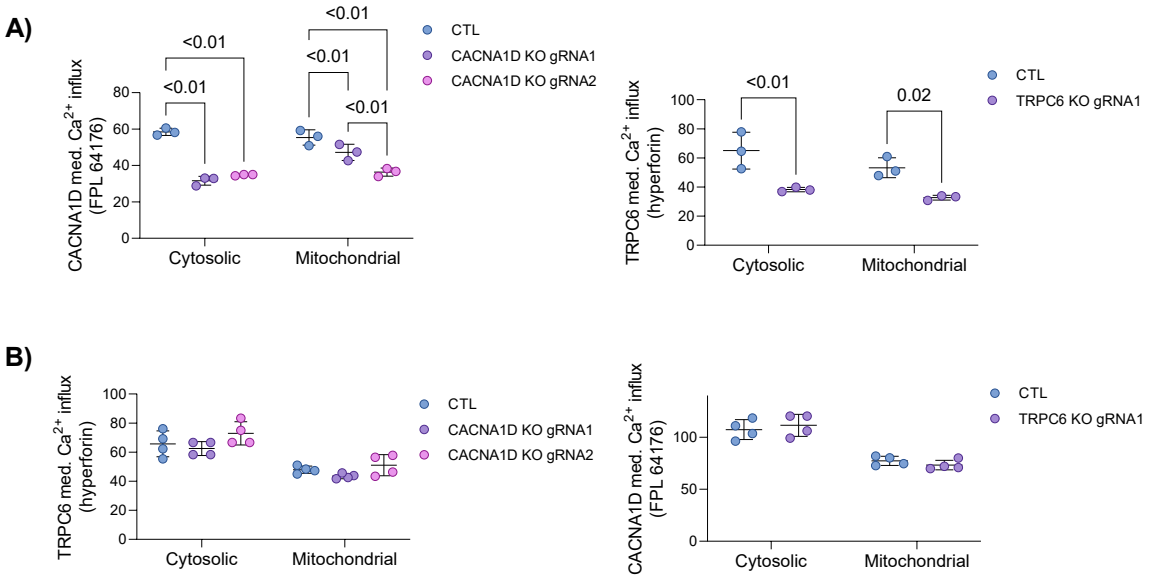

Figure 3-25: TRPC6 and CACNA1D gene disruption inhibits Ca^{2+} influx in K562 cells

(A) Flow cytometry shows the mitochondrial and cytosolic Ca2+ levels in TRPC6 KO K562 cells in response to hyperforin (TRPC6 stimulator) or in CACNA1D KO K562 upon stimulation with FPL64176 (CACNA1D stimulator). Error bars show the mean ± S.D.M.
(B) Flow cytometry shows the mitochondrial and cytosolic Ca2+ levels in CACNA1D KO K562 cells in response to hyperforin (TRPC6 stimulator) or in TRPC6 KO K562 upon stimulation with FPL64176 (CACNA1D stimulator). Error bars show the mean ± S.D.M.

3.7 TRPC6 and CACNA1D inhibits CML cell expansion

The effect of TRPC6 and CACNA1D on CML cell line growth expansion was addressed, where TRPC6 KO, CACNA1D KO, or vector control K562 and KCL22 cells were cultured for 3 days in presence or absence of 1 μM imatinib.

Cell counts were recorded using a CASY cell counter daily (Figure 3-26). Results show that TRPC6 or CACNA1D KO cells significantly reduces cell growth (Figure 3-26). Furthermore, imatinib significantly reduces cell expansion in KO cell lines compared to imatinib treated vector control cells (Figure 3-26). Further, imatinib significantly enhances apoptosis in KO cell lines compared to vector control cells (Figure 3-26). These findings indicate that TRPC6 or CACNA1D are important for CML cells expansion, and their disruption sensitises CML cells to imatinib therapy. Some of the growth rates were identical to each other's, such as those of combination conditions, leading to masking each other during graphical illustration.

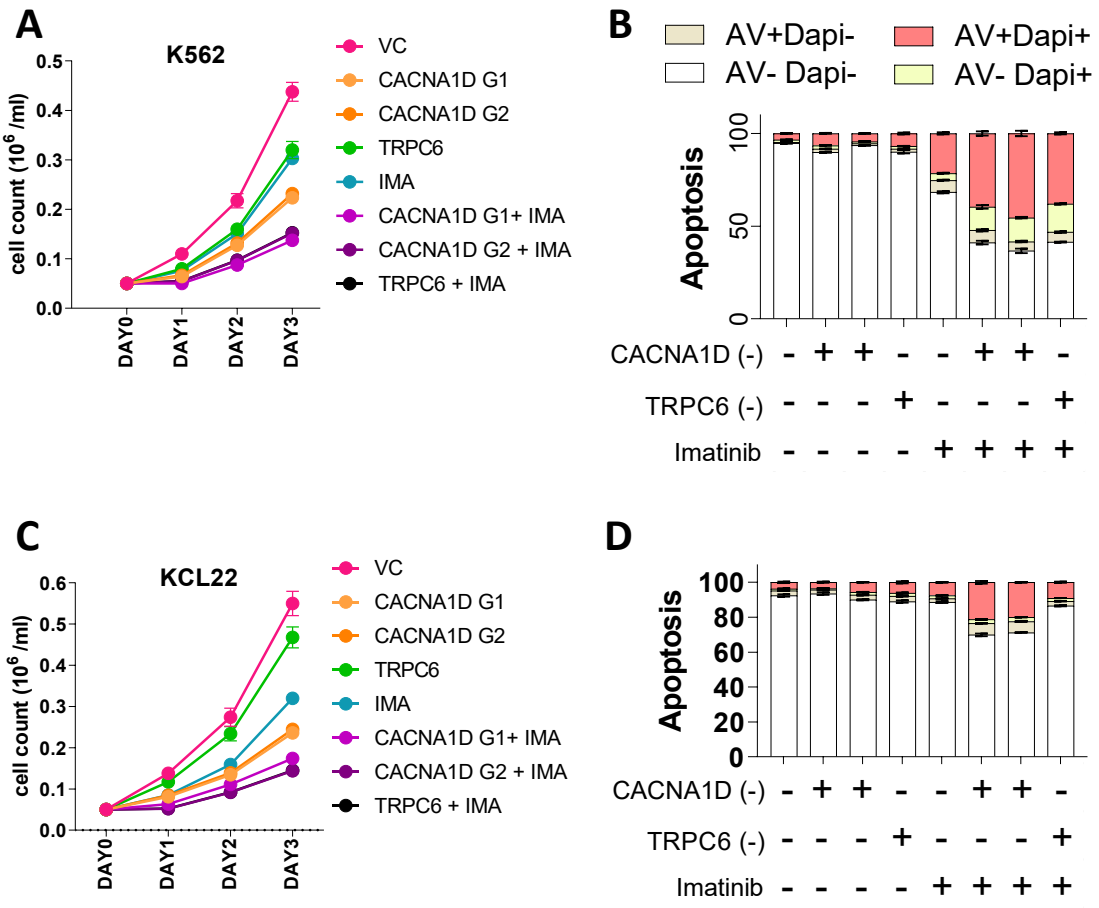

Figure 3-26: CACNA1D and TRPC6 deletion reduces CML cell expansion.

(A) Level of growth expansion in days 0-3 in CACNA1D and TRPC6 KO K562 cell lines treated with or without 1 μM imatinib for 72 hours, n=4 technical replicates. (B) Fractions of necrosis (DAPI+), early and late apoptosis (Annexin V) in CACNA1D and TRPC6 KO K562 cell lines treated with or without 1 μM imatinib treatment for 72 hours as measured by flow cytometry (n=4 technical replicates). (C) Level of growth expansion in days 0-3 in CACNA1D and TRPC6 KO KCL22 cell lines treated with or without imatinib for 72 hours, n=4 technical replicates. (D) Fractions of necrosis (DAPI+), early and late apoptosis (Annexin V) in CACNA1D and TRPC6 KO KCL22 cell lines treated with or without 1 μM imatinib treatment for 72 hours as measured by flow cytometry (n=4 technical replicates).

3.7.1 CACNA1D or TRPC6 deletion inhibits Ca^{2+} influx in K562 and KCL22 cells

It was not known if TRPC6 or CACNA1D majorly participates in regulating CML Ca^{2+} level. To address this role TRPC6 and CACNA1D plays in Ca^{2+} influx in CML cells, the level of cytosolic and mitochondrial Ca^{2+} ions were measured using specific Ca^{2+} indicators, Indo-1, and Rhod-2, followed by quantification of Ca^{2+} levels by flow cytometry. The impact of CACNA1D gene deletion was specifically investigated on Ca^{2+} influx to K562 and KCL22 cells. Previously, CACNA1D was specifically stimulated using small molecule called FPL to stimulate CACNA1D Ca^{2+} influx [221].

Similar approach was performed through acutely stimulating cells with 50 μM FPL. Results show that Ca^{2+} influx is impaired in CACNA1D KO or imatinib treated CACNA1D KO K562 cells, but not WT cells or WT K562 cells treated with imatinib in response to FPL mediated Ca^{2+} influx to cytosol (Figure 3-27A). Despite significant reduction of K562 cells response to FPL stimulation upon CACNA1D deletion, CACNA1D deletion does not significantly alter the response of Ca^{2+} level to FPL stimulation in KCL22 cells, possibly because of FPL over saturation (Figure 3-27C).

Further, CACNA1D KO from K562 and KCL22 cells significantly reduces mitochondrial Ca^{2+} influx in response to FPL stimulation, indicating that CACNA1D but not imatinib treatment inhibits Ca^{2+} influx to cells through impaired CACNA1D channel activity Figure 3-27B & 25D).

To specifically address if TRCPC6 KO blocks Ca^{2+} influx, same approach was performed to measure Ca^{2+} influx following treatment with 50 μM hyperforin, a specific TRPC6 stimulator [220]. TRCP6 KO in K562 cells impairs Ca^{2+} influx alone or when treated with imatinib, but not WT alone or WT exposed to imatinib in response to hyperforin-induced Ca^{2+} influx to cytosol and mitochondria (Figure 3-28).

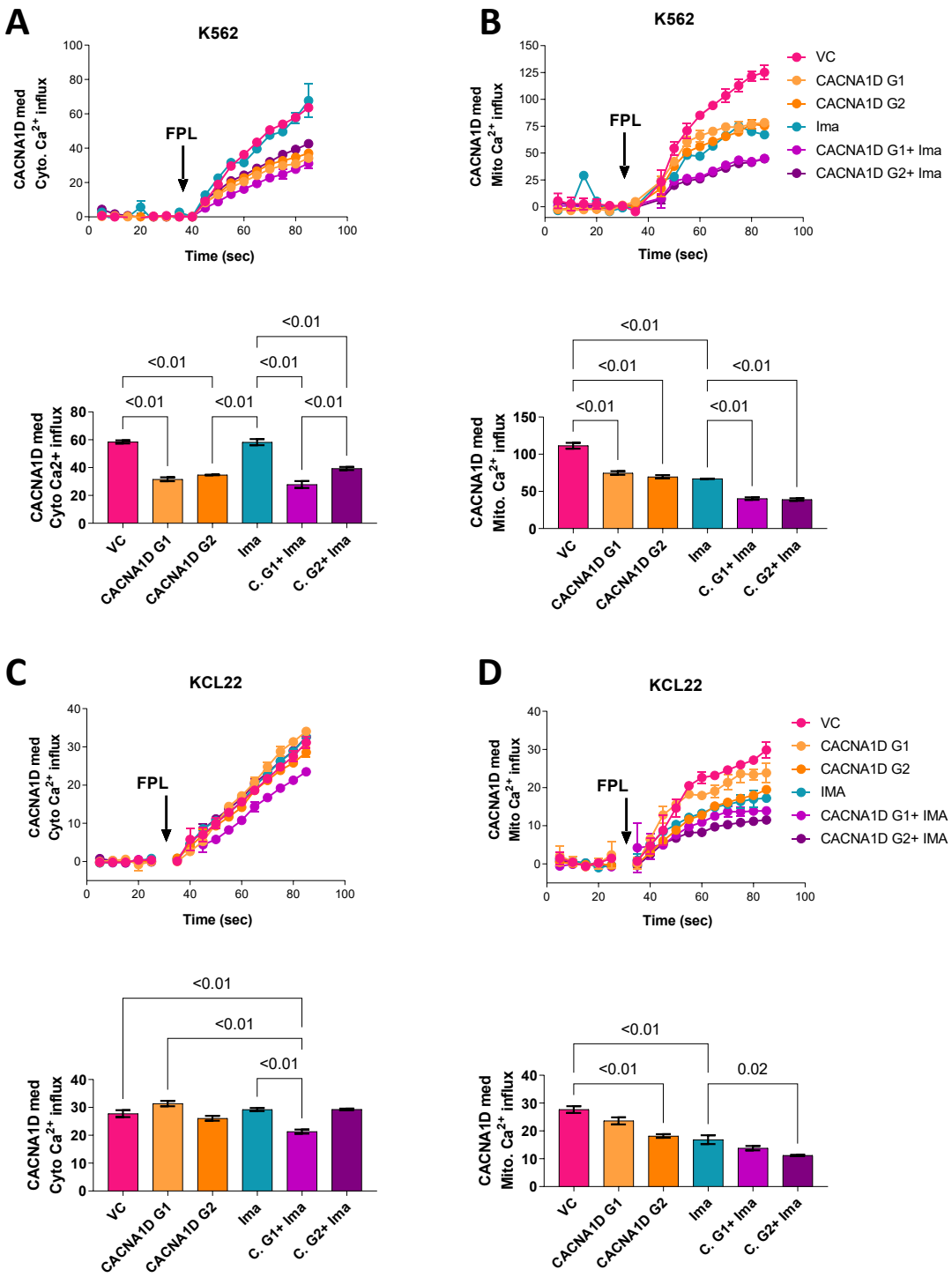

Figure 3-27: CACNA1D deletion inhibits Ca^{2+} influx in K562 and KCL22 cells.

(A) Representative kinetic flow cytometry analysis of cytosolic Ca^{2+} level in CACNA1D KO K562 cells treated for 24 hours with or without 1 µM imatinib. Cells were stimulated with 25 µM FPL during acquiring flow cytometry data. (B) Representative kinetic flow cytometry analysis of mitochondrial Ca^{2+} level in CACNA1D KO K562 cells treated for 24 hours with or without 1 µM imatinib. Cells were stimulated with 25 µM FPL during acquiring flow cytometry data. (C) Representative kinetic flow cytometry analysis of cytosolic Ca^{2+} level in CACNA1D KO KCL22 cells treated for 24 hours with or without 1 µM imatinib. Cells were stimulated with 25 µM FPL during acquiring flow cytometry data. (D) Representative kinetic flow cytometry analysis of mitochondrial Ca^{2+} level in CACNA1D KO KCL22 cells treated for 24 hours with or without 1 µM imatinib. Cells were stimulated with 25 µM FPL during acquiring flow cytometry data. Error bars were shown as SDM+/- MFI of n=3 independent technical replicates. Statistical analysis was performed with one-way ANOVA and Tukey was performed to correct for multiple comparisons.

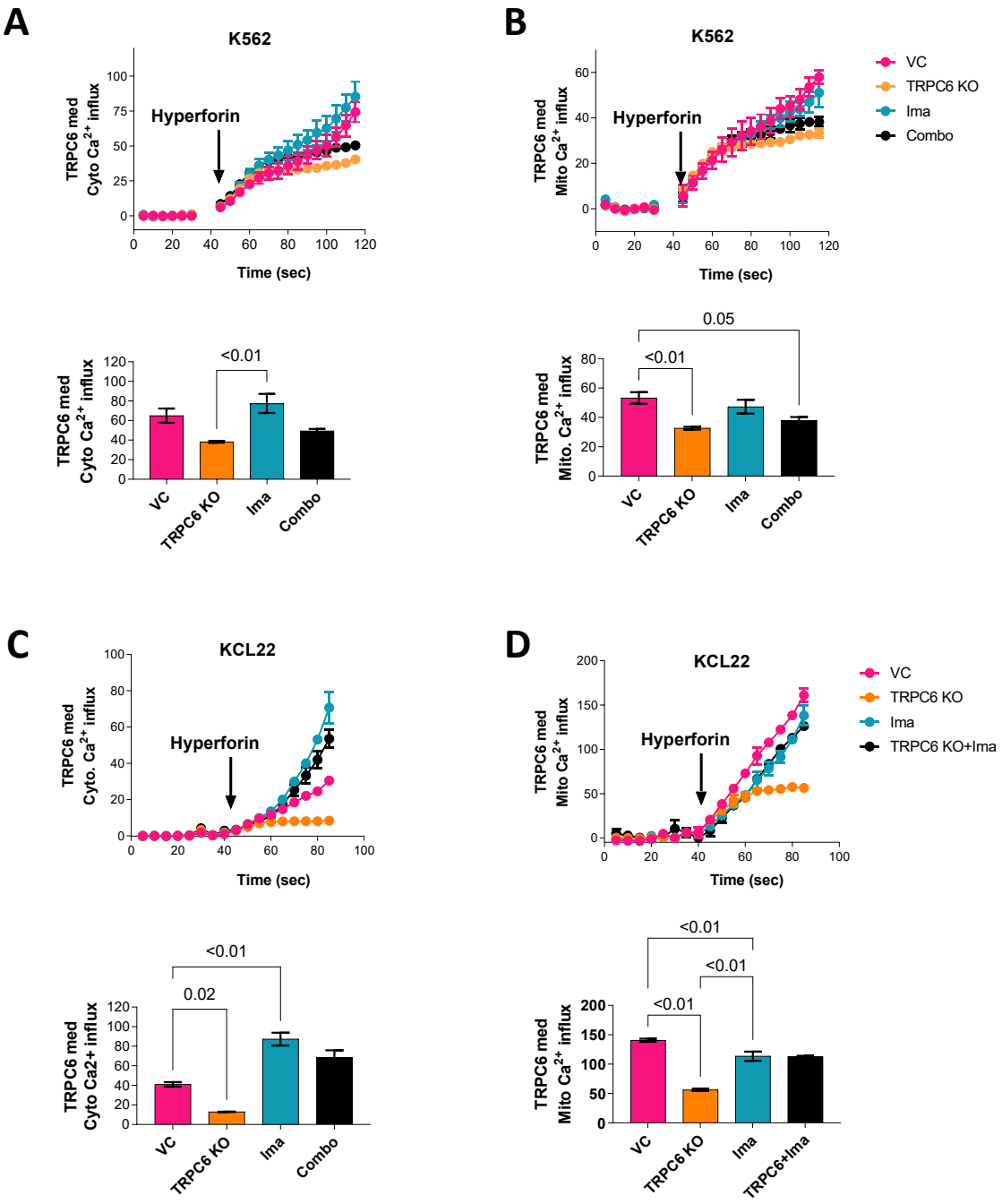

Figure 3-28: TRPC6 deletion inhibits Ca^{2+} influx in K562 and KCL22 cells.

(A) Representative kinetic flow cytometry analysis of cytosolic Ca^{2+} level in TRPC6 KO K562 cells treated for 24 hours with or without 1 μM imatinib. Cells were stimulated with 25 μM FPL during acquiring flow cytometry data. (B) Representative kinetic flow cytometry analysis of mitochondrial Ca^{2+} level in TRPC6 KO K562 cells treated for 24 hours with or without imatinib. Cells were stimulated with 25 μM FPL during acquiring flow cytometry data. (C) Representative kinetic flow cytometry analysis of cytosolic Ca^{2+} level in TRPC6 KO KCL22 cells treated for 24 hours with or without imatinib. Cells were stimulated with 25 μM FPL during acquiring flow cytometry data. (D) Representative kinetic flow cytometry analysis of mitochondrial Ca^{2+} level in TRPC6 KO KCL22 cells treated for 24 hours with or without 1 μM imatinib. Cells were stimulated with 25 μM FPL during acquiring flow cytometry data. Cells were stimulated with 25 μM FPL during acquiring flow cytometry data. Error bars were shown as SDM+/- MFI of n=3 independent technical replicates. Statistical analysis was performed with one-way ANOVA and Tukey was performed to correct for multiple comparisons.

3.7.2 TRPC6 or CACNA1D deletion depletes ER Ca^{2+} transfer to mitochondria

Yet, it is unclear whether Ca^{2+} influx through TRPC6 and CACNA1D regulates Ca^{2+} ion storage capacity of ER. To investigate this approach, corresponding Ca^{2+} levels was measured in TRPC6 and CACNA1D KO K562 and KCL22 cells alone or after exposure to imatinib for 24 hours. Cells were also stimulated with 2.5 μM thapsigargin, which mobilises Ca^{2+} acutely from ER to cytosol or mitochondria. Results reveals significant reduction in Ca^{2+} mobilisation from ER to cytosol or mitochondria in response to CACNA1D deletion in K562 and KCL22 cells (Figure 3-29). Further, results show that TRPC6 deletion significantly reduces ER Ca^{2+} mobilisation to cytosol and mitochondria in K562 cells (Figure 3-30 A&B). In KCL22 cells, TRPC6 deletion significantly reduces ER Ca^{2+} mobilisation to cytosol of imatinib treated KCL22 cells compared to WT KCL22 that are exposed to imatinib (Figure 3-30C). TRPC6 deletion significantly reduces ER Ca^{2+} mobilisation to mitochondria without altering ER Ca^{2+} mobilisation to cytosol (Figure 3-30D).

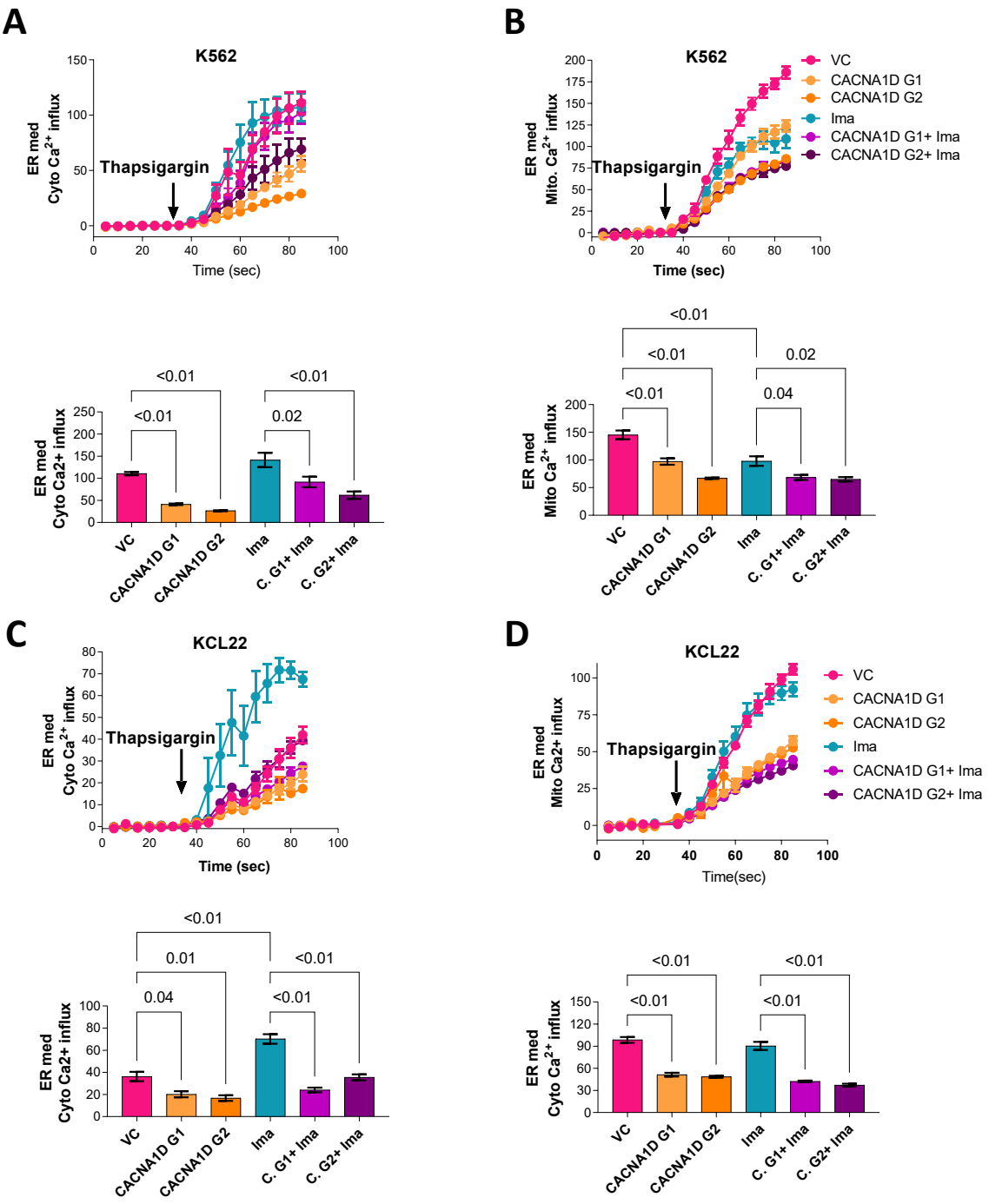

Figure 3-29: CACNA1D deletion inhibits ER Ca^{2+} mobilisation.

(A) Representative kinetic flow cytometry analysis of cytosolic Ca^{2+} level in CACNA1D KO K562 cells treated for 24 hours with or without 1 μM imatinib. Cells were stimulated with 2.5 μM thapsigargin during acquiring flow cytometry data. (B) Representative kinetic flow cytometry analysis of mitochondrial Ca^{2+} level in CACNA1D KO K562 cells treated for 24 hours with or without 1 μM imatinib. Cells were stimulated with 2.5 μM thapsigargin during acquiring flow cytometry data. (C) Representative kinetic flow cytometry analysis of cytosolic Ca^{2+} level in CACNA1D KO KCL22 cells treated for 24 hours with or without 1 μM imatinib. Cells were stimulated with 2.5 μM thapsigargin during acquiring flow cytometry data. (D) Representative kinetic flow cytometry analysis of mitochondrial Ca^{2+} level in CACNA1D KO KCL22 cells treated for 24 hours with or without 1 μM imatinib. Cells were stimulated with 2.5 μM thapsigargin during acquiring flow cytometry data. Error bars were shown as SDM+/- MFI of n=3 independent technical replicates. Statistical analysis was performed with one-way ANOVA and Tukey was performed to correct for multiple comparisons.

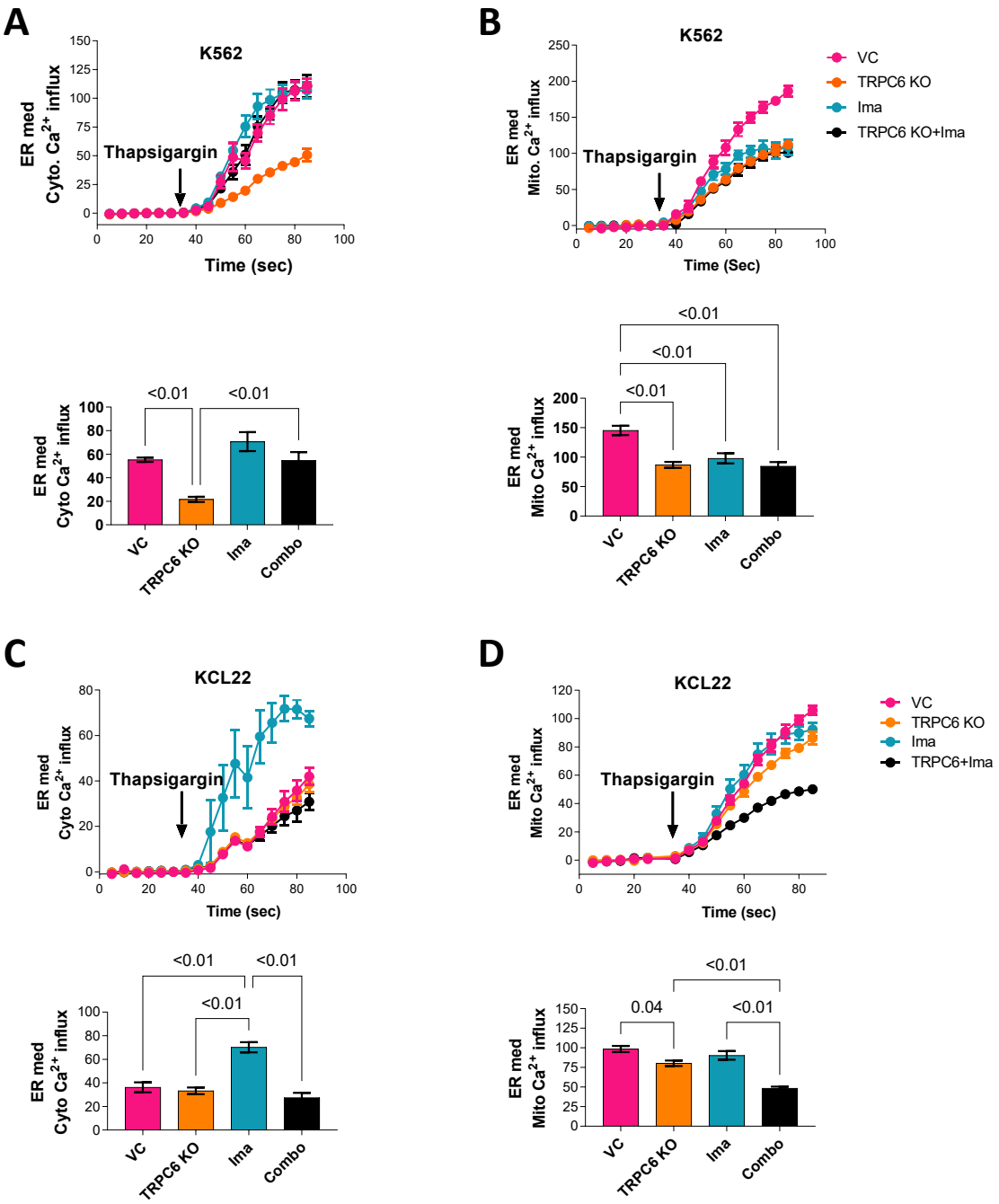

Figure 3-30: TRPC6 deletion inhibits ER Ca^{2+} mobilisation.

(A) Representative kinetic flow cytometry analysis of cytosolic Ca^{2+} level in TRPC6 KO K562 cells treated for 24 hours with or without 1 μM imatinib. Cells were stimulated with 2.5 μM thapsigargin during acquiring flow cytometry data. (B) Representative kinetic flow cytometry analysis of mitochondrial Ca^{2+} level in TRPC6 KO K562 cells treated for 24 hours with or without 1 μM imatinib. Cells were stimulated with 2.5 μM thapsigargin during acquiring flow cytometry data. (C) Representative kinetic flow cytometry analysis of cytosolic Ca^{2+} level in TRPC6 KO KCL22 cells treated for 24 hours with or without 1 μM imatinib. Cells were stimulated with 2.5 μM thapsigargin during acquiring flow cytometry data. (D) Representative kinetic flow cytometry analysis of mitochondrial Ca^{2+} level in TRPC6 KO KCL22 cells treated for 24 hours with or without 1 μM imatinib. Cells were stimulated with 2.5 μM thapsigargin during acquiring flow cytometry data. Error bars were shown as SDM+/- MFI of n=3 independent technical replicates. Statistical analysis was performed with one-way ANOVA and Tukey was performed to correct for multiple comparisons.

3.7.3 TRPC6 or CACNA1D deletion inhibits mitochondrial respiration

Next, investigating if TRPC6 or CACNA1D regulates Ca^{2+} mediated OXPHOS via acting as a cofactor for mitochondrial dehydrogenases was performed. The IDH enzyme has 3 isoforms: NADPH-dependent IDH1 (cytosolic), IDH2 (cytosolic and mitochondrial) and NADH-dependent IDH3 (mitochondrial). Thus, to avoid interference between cytosolic and mitochondrial IDH isoforms, mitochondrial IDH3 in TRPC6 KO, CACNA1D KO, or vector control K562 or KCL22 cells was measured after their exposure to imatinib for 4 hours. Imatinib does not alter IDH3 activity in vector control cells (Figure 3-31). TRPC6 or CACNA1D KO cells significantly reduces mitochondrial IDH3 activity and imprints this impact in KO cells exposed to imatinib. Our findings indicate a direct effect of TRPC6 or CACNA1D on Ca^{2+} ions availability for OXPHOS and inhibiting mitochondrial dehydrogenases.

Finally, the impact of TRPC6 or CACNA1D on mitochondrial respiration was measured by Seahorse mitostress analysis. Vector control, TRPC6 KO, and CACNA1D KO K562 and KCL22 cell lines were cultured for 12 hours in presence or absence of 1 μM imatinib (Figure 3-32). TRPC6 or CACNA1D KO cell lines shows significantly reduced OCR compared to vector control cells (Figure 3-33). Deleting TRPC6 or CACNA1D further reduces OCR in imatinib treated cells compared to imatinib treated vector control cells (Figure 3-33). Findings confirm dependency of mitochondrial respiration on Ca^{2+} ions coming from TRPC6 or CACNA1D.

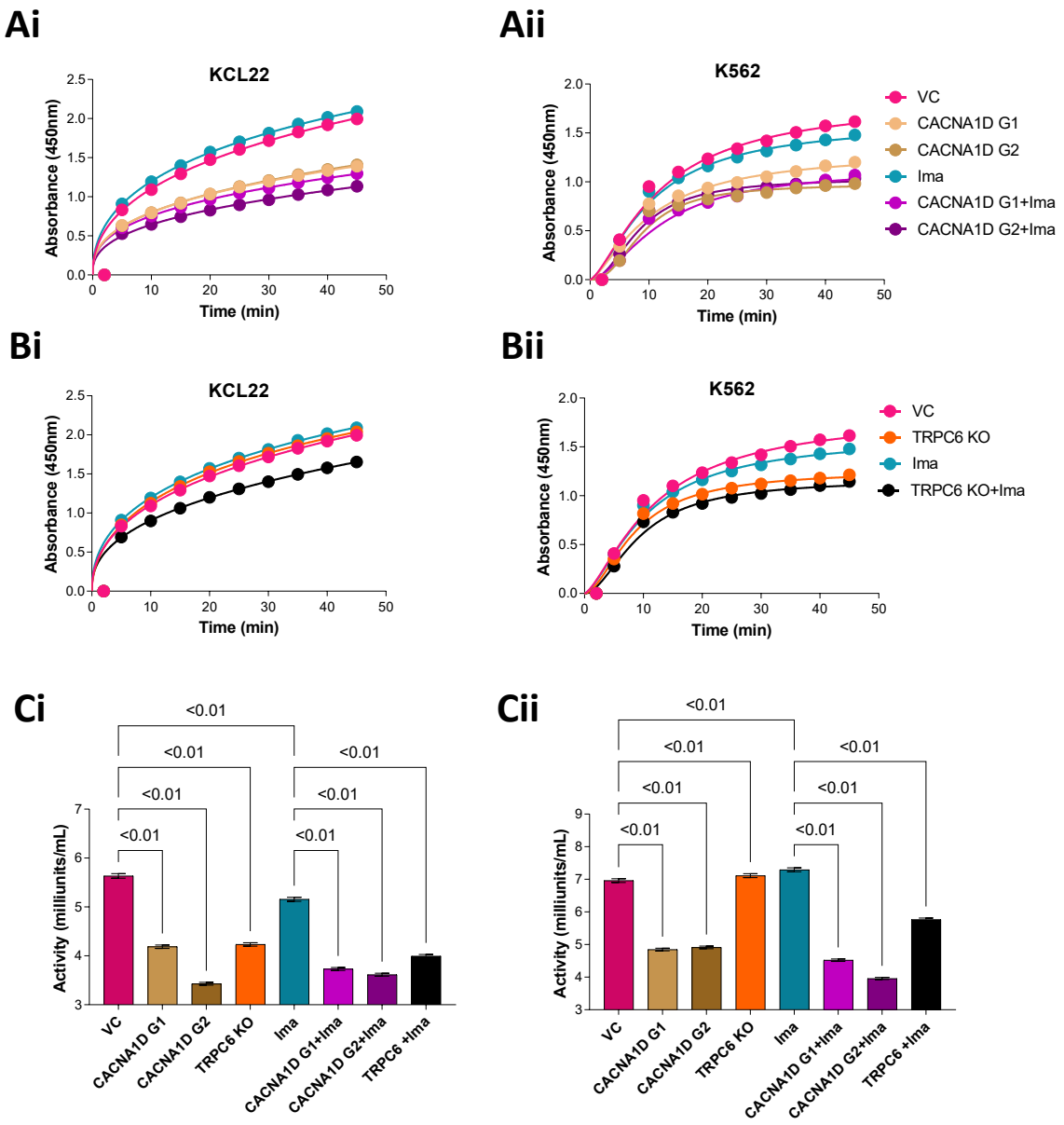

Figure 3-31: CACNA1D or TRPC6 deletion inhibits IDH3 activity.

(A) Representative kinetic absorbance that reflects IDH3 activity was measured colorimetrically in CACNA1D KO KCL22 cells (left panel) or K562 cells (right panel) treated with or without 1 μM imatinib for 12 hours. (B) Representative kinetic absorbance that reflects IDH3 activity was measured colorimetrically in TRPC6 KO KCL22 cells (left panel) or K562 cells (right panel) treated with or without 1 μM imatinib for 12 hours. (C) Quantification analysis of level of IDH3 activity in CACNA1D and TRPC6 KO K562 cells KCL22 cells (left panel) or K562 cells (right panel) treated with or without 1 μM imatinib for 12 hours (n=4 technical replicates). Statistical analysis was performed with one-way ANOVA and Tukey was performed to correct for multiple comparisons.

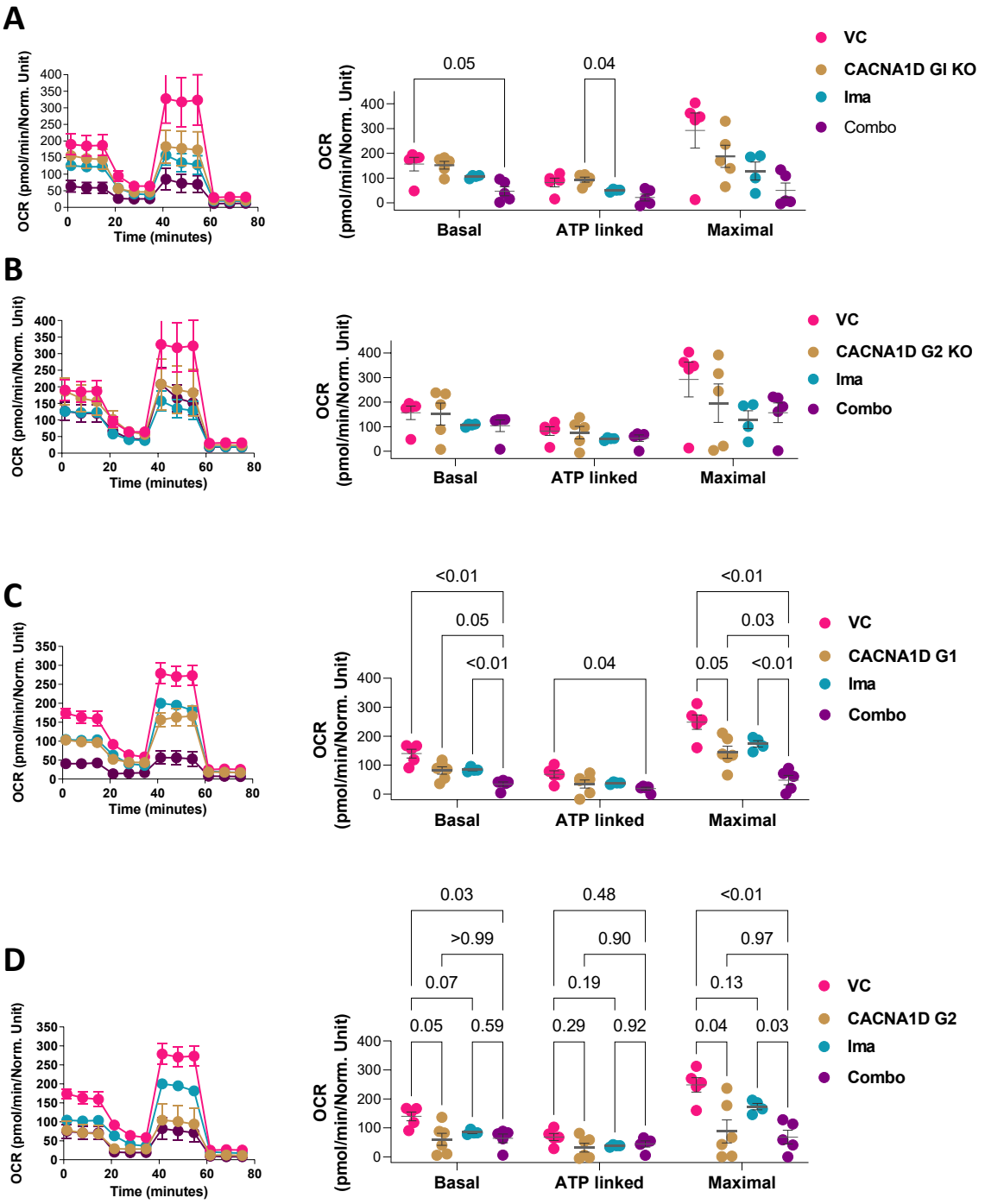

Figure 3-32: CACNA1D deletion inhibits respiration in imatinib treated cells.

(A) Respirometry analysis of CACNA1D KO KCL22 cells was treated for 12 hours, followed by quantification of basal, ATP-linked, and maximal OCR (n≥ 6 technical replicates). Respirometry analysis of CACNA1D KO KCL22 cells treated with indicated treatment for 12 hours. (B) Respirometry analysis of CACNA1D KO K562 cells was treated for 12 hours, followed by quantification of basal, ATP-linked, and maximal OCR (n≥ 6 technical replicates). (C) Respirometry analysis of CACNA1D KO K562 cells treated with indicated treatment for 12 hours. Statistical analysis was performed with two-way ANOVA and Tukey was performed to correct for multiple comparisons.

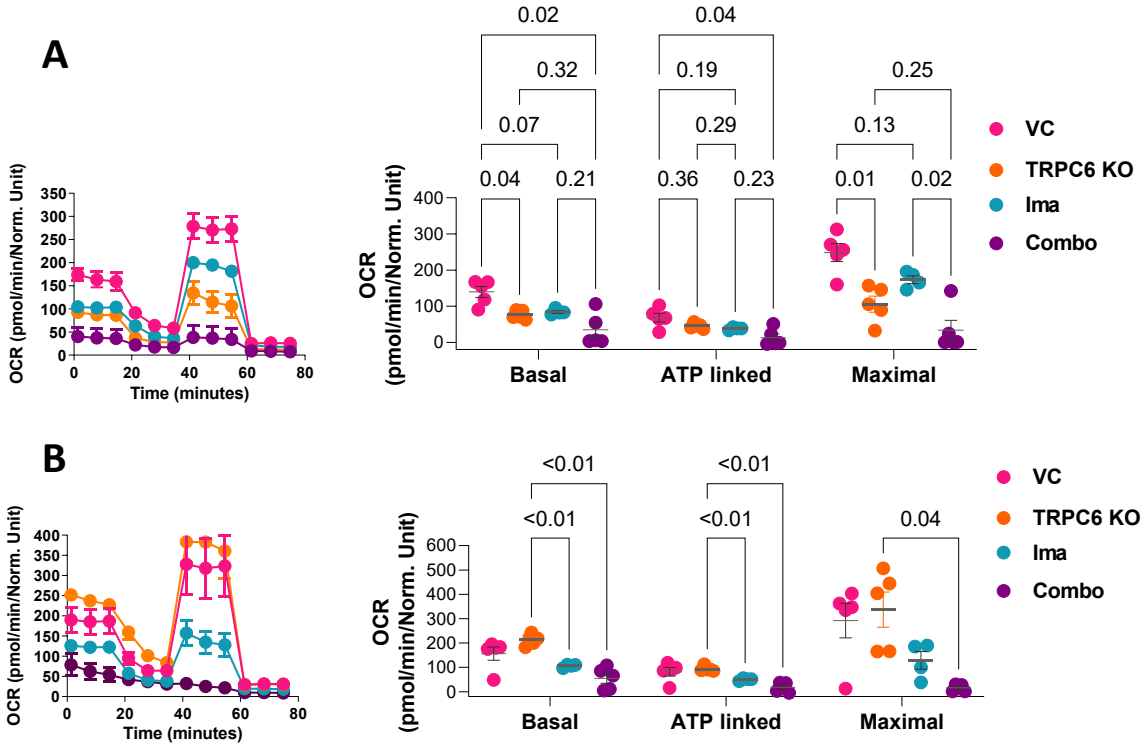

Figure 3-33: TRPC6 deletion inhibits respiration in imatinib treated cells.

(A) Respirometry analysis of TRPC6 KO K562 cells was treated with or without 1 μM imatinib for 12 hours, followed by quantification of basal, ATP-linked, and maximal OCR (n≥ 6 technical replicates). (B) Respirometry analysis of TRPC6 KO KCL22 cells was treated for 12 hours, followed by quantification of basal, ATP-linked, and maximal OCR (n≥ 6 technical replicates). Statistical analysis was performed with two-way ANOVA and Tukey was performed to correct for multiple comparisons.

3.8 Conclusion

In this chapter, publicly available transcriptome data sets of CD34+CD38- CML versus CD34+CD38- normal cells were analysed. The analyses revealed enrichment of mitochondrial hallmarks of OXPHOS and VGCC activities. The data analysis of single gene expressions showed upregulation of CACNA1D, CACNB4 and TRPC6 in CML versus normal counterparts. This led us to assume that TRPC6 and CACNA1D could participate in supporting CML cells with higher Ca^{2+} ions that could act as a cofactor for mitochondrial dehydrogenases. Comparable with findings from blood leukapheresis, differential expression of 584 genes (including CACNA1D as one of top hits) was found between CD34+CD38-Lin- cells from BM of individuals with CML and haematologically normal cells from patients undergoing orthopaedic hip surgery [233]. It is well known that not only mitochondria can buffer Ca^{2+} ions within mammalian cells, but ER is the main storage organelle, which can hold Ca^{2+} ions in millimolar range. Mitochondrial Ca^{2+} uptake requires sustained Ca^{2+} release from ER [28, 226].

Based on the role of mitochondria and ER in Ca^{2+} buffering and utilisation into metabolic processes, transcriptome analysis involved in the ER biological processes such as UPR, ER phagosome in LSCs and their normal counterparts were performed. Results showed that CML enriched ER related gene sets' transcriptome versus their normal counterparts. To support our *in-silico* findings, *ex vivo* and *in vitro* analysis has been performed to assess the mass level of ER and its Ca^{2+} ions buffering capacity in CD34+ cells isolated from CML or non-CML individuals.
Further current research assessed ER Ca^{2+} contribution to mitochondria in those CD34+ CML and CD34+ non-CML cells. As it was previously shown by Helgason lab that CML has higher mitochondrial mass, It also has been shown that CML has higher ER mass, and this reflects the capacity of CD34+ CML to buffer more Ca^{2+} within their ER, leading to significantly reduced levels within cytosol and increased within mitochondria. Also, CD34+ CML primary cells have a greater sensitivity towards Ca^{2+} influx to cytosol but not mitochondria when compared to their normal counterparts, indicating that CML has increased Ca^{2+} influx activity. However, most of this Ca^{2+} is buffered within ER and mitochondria.
Furthermore, Another transcriptome dataset of CD34+ CML treated with imatinib for 7 days versus untreated CML cells has been analysed. Results showed that

imatinib could not alter CACNA1D and TRPC6 expression levels but reduced mitochondrial OXPHOS and mitochondrial biogenesis hallmarks signature, indicating that imatinib affects the mitochondria of CML on a transcriptional level. The author also checked if imatinib treatment altered mitochondrial and ER mass. The author used CD34+ CML samples to check their corresponding mass levels. The author also labelled CML cell lines (K562 and KCL22) with both organelles' fluorescent markers that reflect their mass and to verify if they are involved in biological processes such as mitobiogenesis, mitophagy or ER-Phagy. Results showed that imatinib significantly reduced both ER and mitochondrial mass. This likely affects basal level of Ca^{2+} within mitochondria of CML when treated with imatinib (see subsequent chapters). Even though imatinib enhances ATG7 or ULK1 associated autophagy (macro autophagy), mitochondrial mass reduction and ER mass reduction seems to arise from either mitobiogenesis arrest or ATG7 or ULK1 independent ER-Phagy, respectively.

Given that Ca^{2+} is so important for OXPHOS, several questions in CML have not been answered yet, such as if TRPC6 and CACNA1D participate in supporting ER Ca^{2+} buffering and transfer to mitochondria. Also, it is unknown whether imatinib alters TRPC6 or CACNA1D mediated Ca^{2+} influx to either mitochondrion or ER itself. Furthermore, it has been shown for first time that CACNA1D and TRPC6 are important for CML mitochondrial metabolic phenotype. Using CRISPR Cas9 that causes at least genetic disruption, the author could generate KCL22 and K562 cells expressing non-functional TRPC6 or CACNA1D proteins. CACNA1D gene disruption inhibited FPL mediated Ca^{2+} influx to cytosol, ER, or mitochondria. The effect of TRPC6 knockdown was virtually identical, with cells nonresponsive to hyperforin stimulation. This reflects low ER and mitochondrial Ca^{2+} levels with subsequent inhibition of mitochondrial OXPHOS. In turn, inhibition of OXPHOS because of those gene deletions sensitised cells to apoptosis by imatinib. The findings indicate a critical role of these channels in promoting CML survival by sustaining mitochondrial metabolism with Ca^{2+} ions. Our results indicate TRPC6 and CACNA1D as new metabolic vulnerabilities to exploit alongside imatinib treatment. Further, it is worthy to specifically check if those Ca^{2+} channel inactivation or disruption could impact normal cells.

4 Lomerizine inhibits Ca^{2+} influx and OXPHOS *in vitro*

4.1 Introduction

CML LSCs rely on upregulated OXPHOS for survival and therapy persistence *in vitro* and *in vivo* [184] . However, current OXPHOS inhibitors have limitations, such as a short half-life or limited therapeutic index. The Helgason lab previously performed a drug repurposing screen to identify repurposed drugs that could inhibit mitochondrial metabolism in leukaemic cells. Amongst other hits, the screen identified lomerizine dihydrochloride as a candidate compound effective against OXPHOS-dependent CML cells. In the clinic lomerizine has been used as an anti-migraine L-type Ca^{2+} channel blocker. Leading on from our results that *TRPC6* and *CACNA1D* are significantly upregulated in CML LSCs (CD34+CD38-) which was not reversed by imatinib treatment, these increases could be inhibited by lomerizine treatment. The author will also investigate the impact of previously known mitochondrial complex I inhibitor (IACS-010759) as a control on mitochondrial respiration in CML cell lines and look at drawbacks that may limit its clinical applicability.

Furthermore, the research investigates whether lomerizine targets CML OXPHOS and if the effect of lomerizine is linked to Ca^{2+} regulation by lomerizine. The study mainly focuses on TRPC6 and CACNA1D Ca^{2+} modulation in CML cell lines. Finally, the study investigates if Ca^{2+} inhibition targets viability of CML cells and whether it induces more cell death in presence of imatinib.

4.2 OXPHOS inhibition targets CML cells proliferation

It has been previously shown that targeting OXPHOS sensitised CML to imatinib therapy [184]. IACS-010759, a known mitochondrial complex I inhibitor tested in AML as OXPHOS inhibitor, but not yet in CML [234]. Including IACS-010759 in assays was intended to get comparative insights between two OXPHOS inhibitors.
In our hands, IACS-010759 significantly inhibits cell growth expansion and induces apoptosis levels in K562 and KCL22, especially when combined with imatinib (Figure 4-1).

Given that IACS-010759 inhibits complex I, a resazurin assay was performed in K562 and KCL22 cells cultured in glucose or galactose in the presence of serial dilutions of IACS-010759 for 72 hours (Figure 4-2A) to assess its impact on cell viability. Results show that IACS-010759 does not alter the viability of cells in glucose; meanwhile, IACS-010759 has IC50s of 0.001 and 0.01 μM in K562 and KCL22, respectively, when these cells were cultured in galactose. This shows the specificity of IACS-010759 in targeting CML viability only when there is a reliance on OXPHOS. Furthermore, when combined, 10 nM IACS-010759 significantly lowers the IC50 of imatinib in K562 and KCL22 (Figure 4-2 B&C).

IACS-010759 alone or when combined with imatinib further reduces OCR in K562 and KCL22 cells after different time points; 60 minutes, 12 hours, 24 hours, and 48 hours, as measured by Seahorse mitostress assay (Figure 4-3).

Furthermore, IACS-010759 shows selective efficacy to target patient derived CML cells *in vitro,* which confirmed previous findings that OXPHOS inhibition sensitised LSCs to TKI therapy.

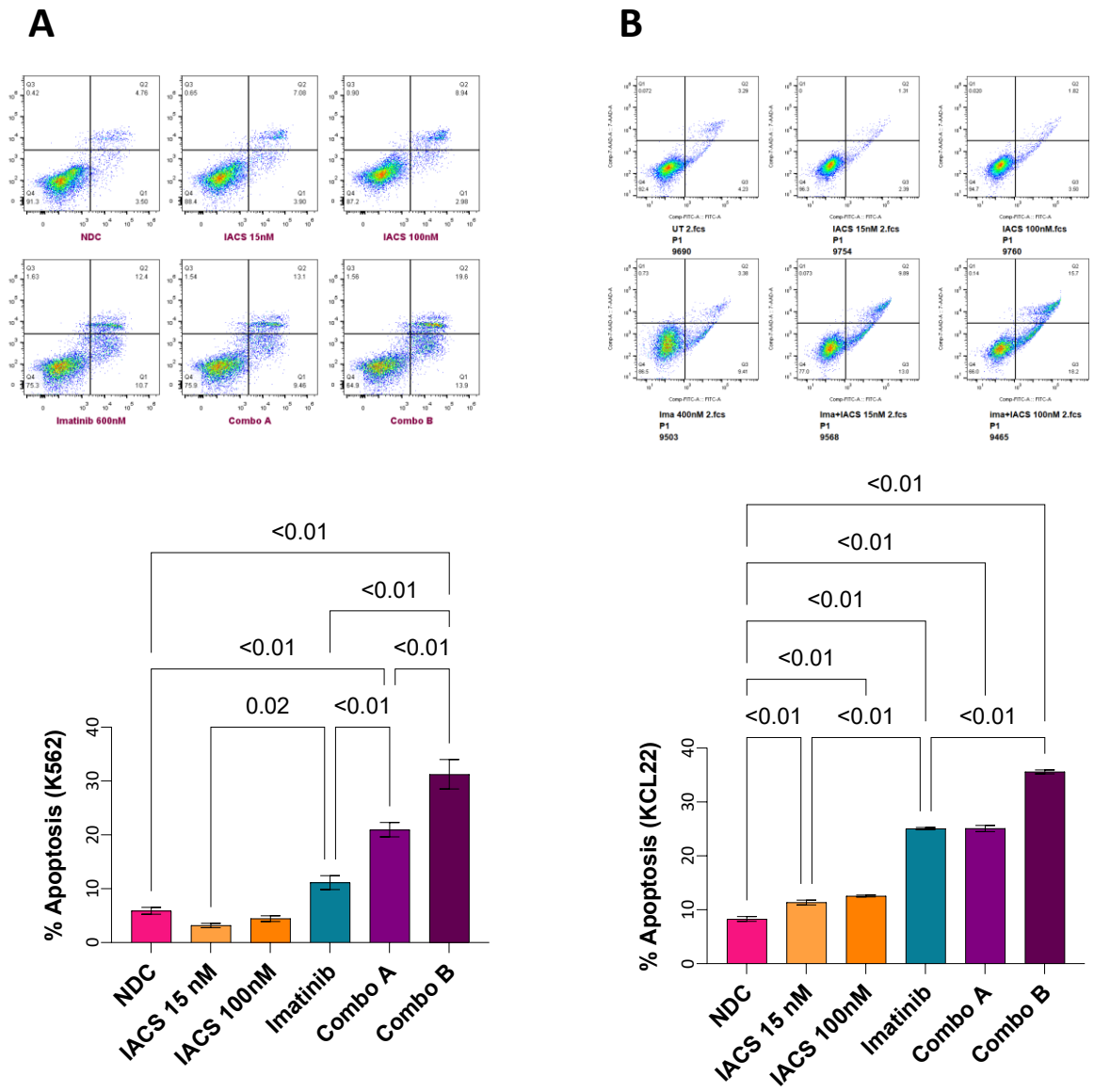

Figure 4-1: IACS-010759 induces imatinib apoptosis in KCL22 and K562 cells.

(A) Flow cytometry chart and bar plot illustrate enhanced apoptosis after 72 hours of IACS-010759 combination of 0.5 μM imatinib with 15 nM IACS (Combo A) or with 100 nM IACS (Combo B) in WT K562 cells. (B) Flow cytometry chart and bar plot illustrates enhanced apoptosis after 72 hours of IACS-010759 combination with 0.5 μM imatinib in WT K562 cells. Error bars are shown as SEM+/- MFI on n=3 technical replicates.

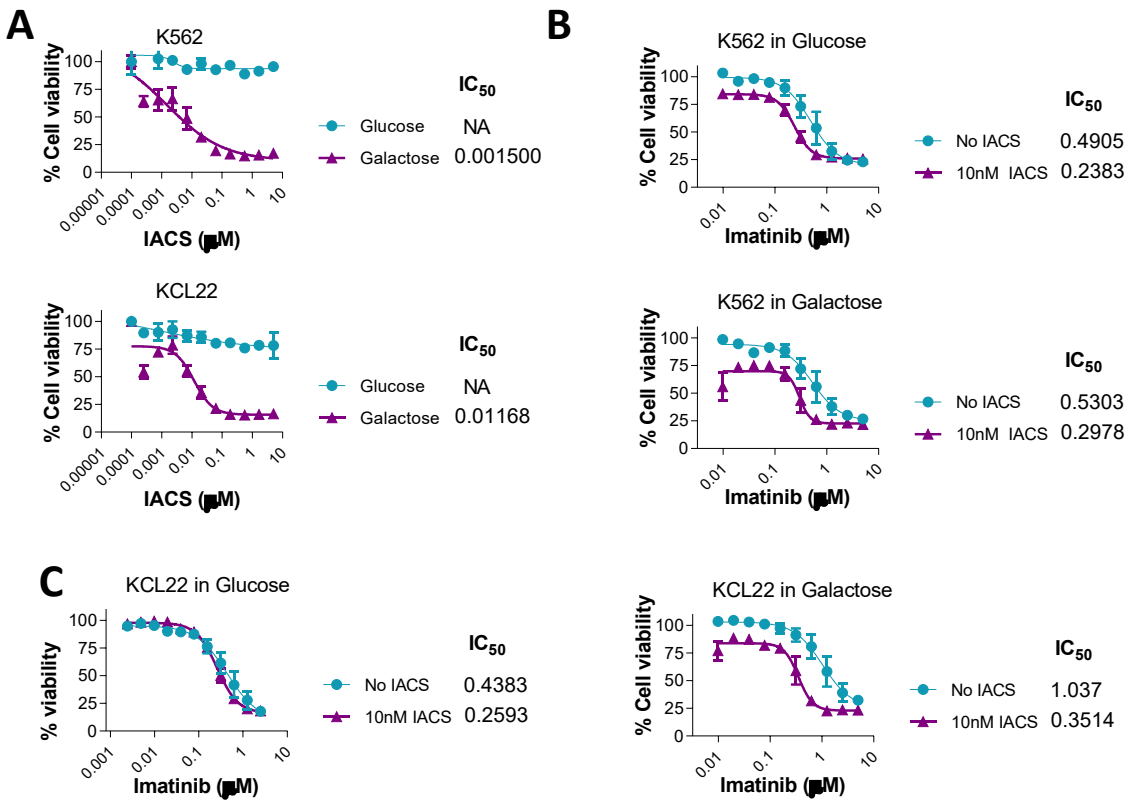

Figure 4-2: IACS-010759 reduces imatinib IC50 in CML cells.

(A) Resazurin cell viability curve in WT K562 and KCL22 was treated with a serial concentration of IACS-010759 upon incubating them either in glucose or galactose for 72 hours. (B) Resazurin cell viability curve in WT K562 treated with a serial concentration of imatinib with or without 10 nM IACS-010759 upon incubating them either in glucose or galactose for 72 hours. (C) Resazurin cell viability curve of WT KCL22 treated with either serial concentration of imatinib alone or 10 nM IACS-010759 for 72 hours in glucose or galactose. Sigmoidal curves error bars are shown as SDM+/-mean response of n=3 technical replicates. The concentration on X-axis of (A) represents serial concentrations of IACS, and of (B) and (C) represent serial concentration of imatinib with or without 10 nM of IACS.

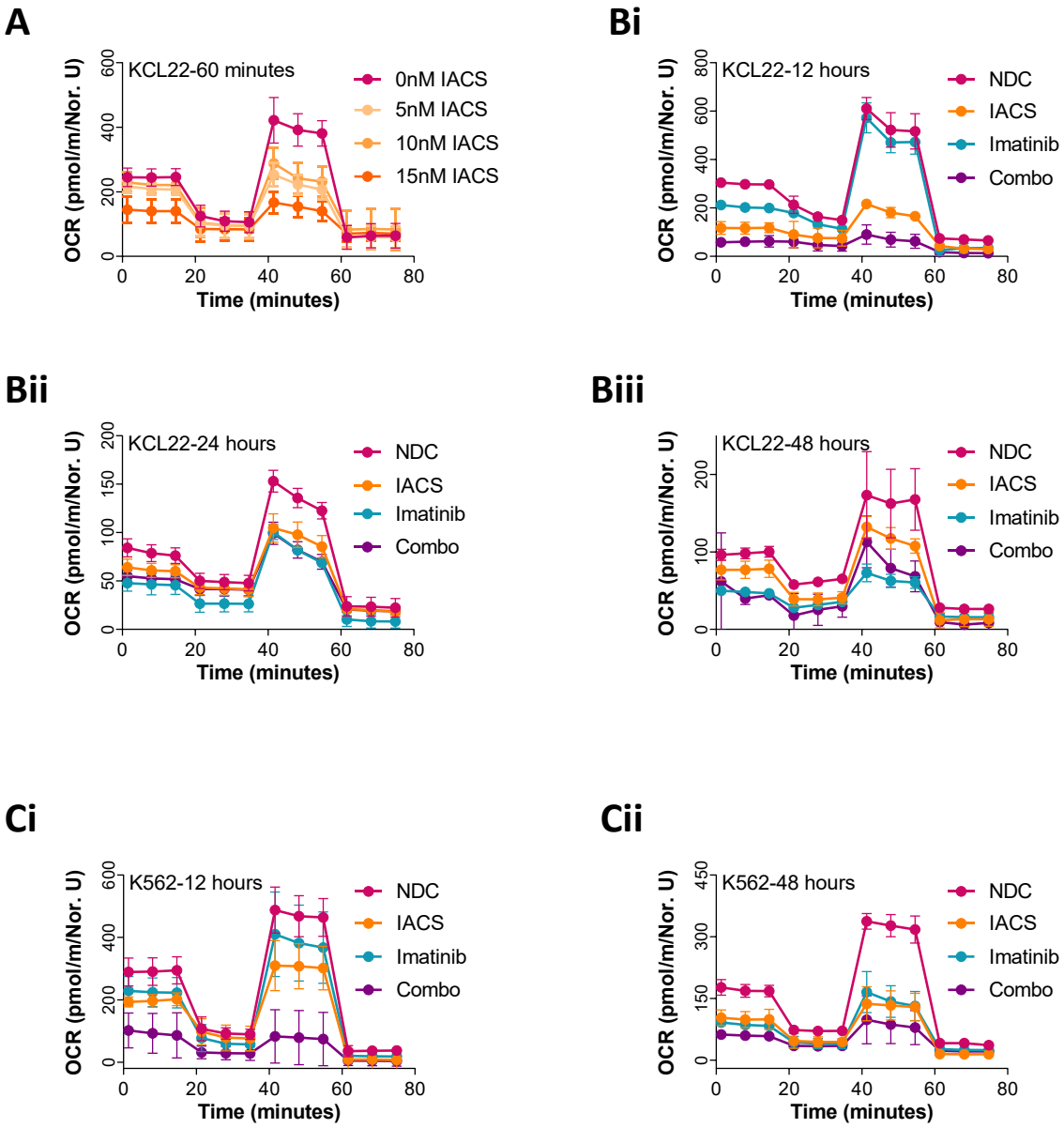

Figure 4-3: IACS-010759 inhibits respiration in CML cell lines.

(A) Respirometry analysis of WT KCL22 cells exposed to 5,10,15 nM IACS-010759 for 60 minutes, where n= 6-8 technical replicates. (B) Respirometry analysis of WT KCL22 cells exposed to 10 nM IACS-010759, 0.5 μM imatinib, or their combination for 12, 24, or 48 hours, Where n=6-8 technical replicates. (C) Respirometry analysis of WT K562 cells treated with 0.5 μM imatinib, 5 nM IACS or their combination for 12 or 48 hours, where n=6-8 technical replicates.

Besides fact that IACS-010759 can act as a potent OXPHOS inhibitor, it may enhance rate of glycolysis in those cells. In order to investigate this approach, glycostress assay was also performed in K562 and KCL22 cells treated with IACS-010759 for 12 hours. Results, however, indicate that IACS-010759 induces glycolysis and reverses imatinib induced glycolysis repression (Figure 4-4).

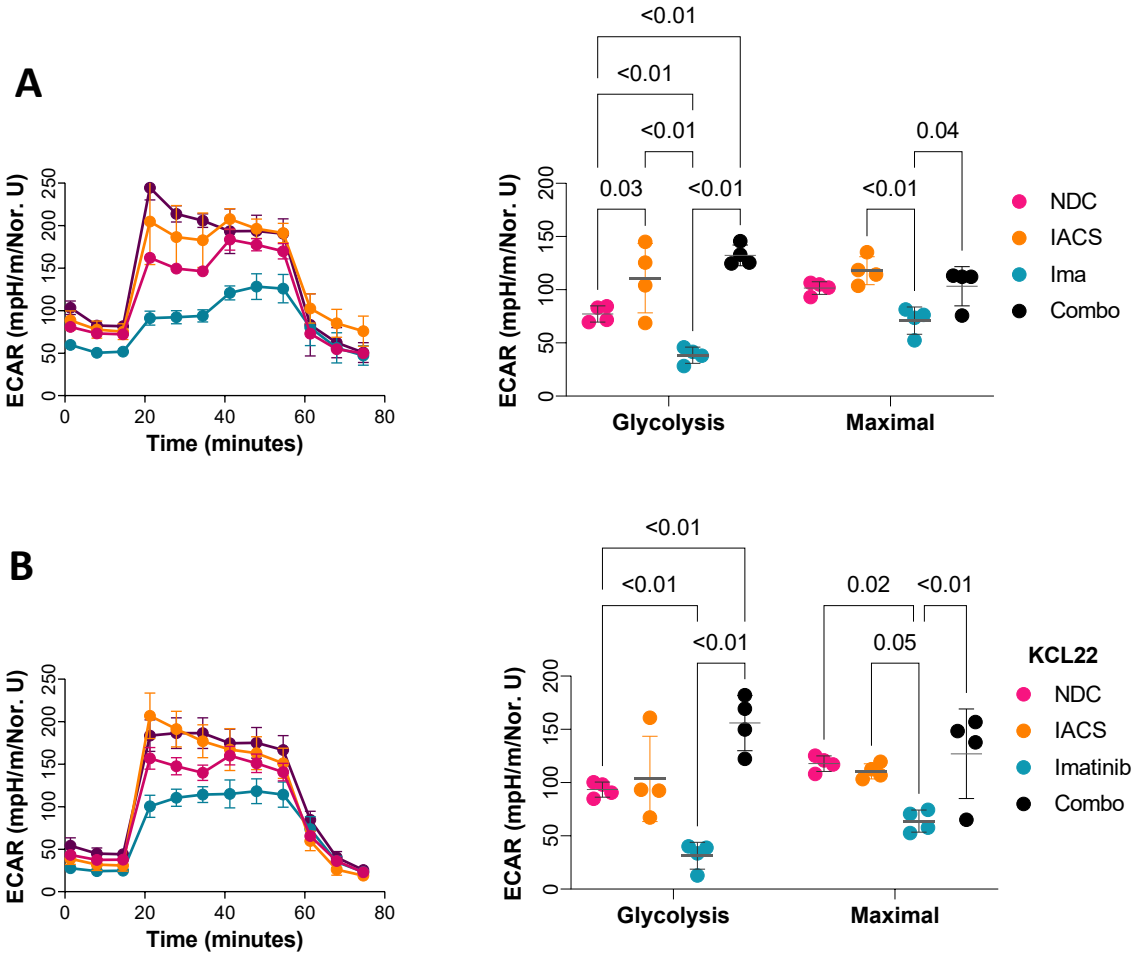

Figure 4-4: IACS-010759 reverses imatinib glycolytic inhibition.

(A) Glycostress profile of K562 cell lines exposed to 10nM IACS-010759, 0.5 μM imatinib, and their combination for 12 hours, followed by analysing the glycolysis and maximal glycolysis. (B) Glycostress profile of KCL22 cell lines exposed to 10nM IACS, 0.5 μM imatinib, and their combination for 12 hours, followed by analysing glycolysis and maximal glycolysis. Both Glycostress tests were performed using n= 4 technical replicates for K562 and n=8 technical replicates for KCL22 cells. The Error bars present SDM+/-Mean response and two-way ANOVA was used to calculate statistical significance and Tukey's test for multiple corrections.

4.3 Lomerizine enhances CML cells sensitivity to imatinib

Given that LSCs rely on OXPHOS for survival, Helgason lab designed an approach to find new OXPHOS inhibitors through drug repurposing screening. The screening analysis indicated lomerizine as a suitable candidate [210]. Lomerizine is known Ca^{2+} inhibitor used for migraine treatment [235].

To investigate if lomerizine affects CML viability through targeting OXPHOS, KCL22 cells were cultured in (glucose-free) RPMI media supplemented with galactose or grown in regular glucose-containing RPMI and exposed to a combination of lomerizine and imatinib. The cells were treated with a serial dilution of imatinib in the presence or absence of 5 μM lomerizine, followed by resazurin assay in KCL22 (Figure 4-5A) and in K562 cells (Figure 4-5B). Results show that incubating cells with glucose or galactose medium does not alter imatinib's IC50 in either K562 or KCL22 cells. However, lomerizine significantly lowers the IC50 of imatinib for both K562 and KCL22 cells cultured in media supplemented with either glucose or galactose.

Furthermore, the IC50 of imatinib in cells exposed to combination of galactose containing medium was significantly lower when compared to the IC50 of imatinib in cells treated with the combination of glucose. Lomerizine lowering the IC50 of imatinib in galactose medium more than the IC50 of cells in glucose reflects these cells solely relying on OXPHOS. Therefore, these cells are more sensitive to the inhibitory effect of lomerizine.

Leading on from our results, further investigation if lomerizine exposure will sensitise CML cell lines to apoptosis by imatinib was performed. Apoptosis and cell growth expansion levels in K562 and KCL22 cells exposed to lomerizine, imatinib, or the combination for 3 days were measured (Figure 4-6). Lomerizine combination with imatinib significantly reduces cell growth expansion and significantly increases apoptosis level in those cells, indicating a beneficial combination impact on CML death.

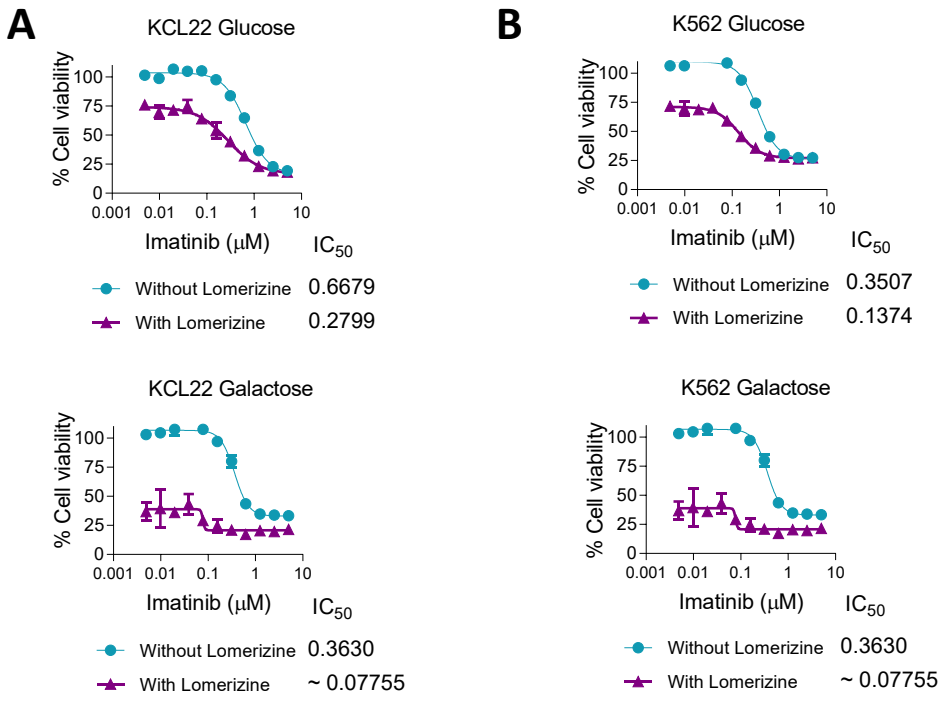

Figure 4-5: Lomerizine enhances CML cells sensitivity to imatinib.

(A) Resazurin cell viability assay curve in WT KCL22 treated with either serial concentration of imatinib alone or 5 μM lomerizine for 72 hours in glucose or galactose. (B) Resazurin cell viability curve of WT KCL22 treated with either serial concentration of imatinib alone or 5 μM lomerizine for 72 hours in glucose or galactose. Sigmoidal curves error bars are shown as SDM+/-mean response of n=3 technical replicates.

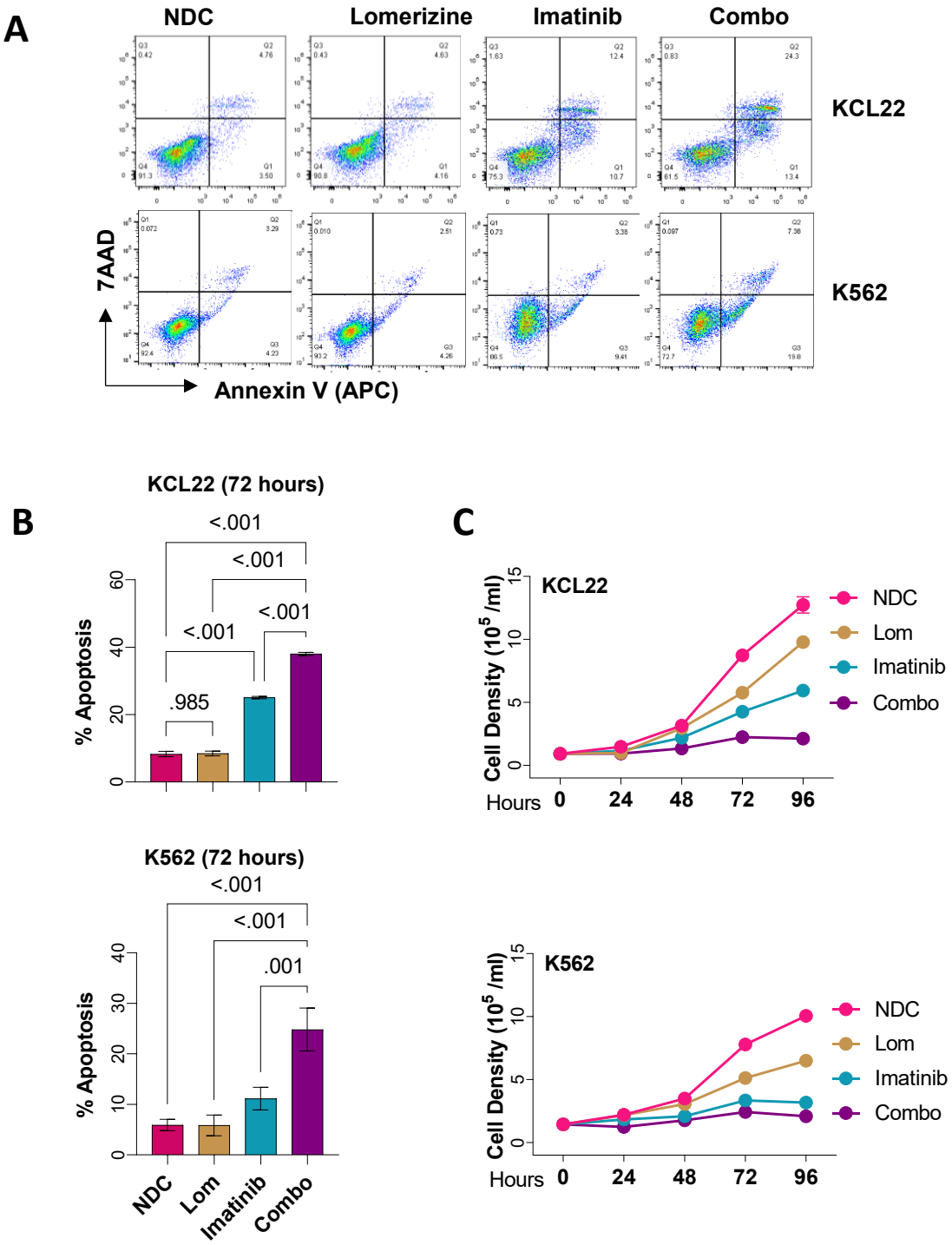

Figure 4-6: Lomerizine sensitises cell lines to imatinib induced apoptosis.

(A) Flow cytometry chart illustrating enhanced apoptosis after 72 hours of 5 μM lomerizine combination with 0.5 μM imatinib treatment in KCL22 and K562 cells. (B) Apoptosis levels in KCL22 and K562 exposed to indicated treatments for 72 hours, error bars are represented as SDM +/- mean response, where n=3 technical replicates. The line graph shows 72 hours of apoptosis level and different time points for cell density in WT KCL22 and K562 cells. Statistical analysis was performed with one-way ANOVA and Tukey was performed to correct for multiple comparisons.

4.4 Lomerizine inhibits respiration in CML cell lines

Further, the appropriate lomerizine dose required to show an effect on mitochondrial respiration were investigated. For this approach, Agilent Seahorse mitostress flux assay was established. This assay relies on the ability of cells to consume oxygen from growth media when they respire using the mitochondrial machinery. The cells' OCR change is measured in response to acute (chemical) inhibition of mitochondrial complexes. KCL22 cells were exposed to different concentrations of lomerizine for 60 minutes, followed by respirometry analysis using Agilent Seahorse mitostress assay. Lomerizine treatment inhibits OCR at 2-8 μM strengths (Figure 4-7A).

To expand on this, K562 cells were exposed to 5 μM lomerizine in the presence or absence of glucose for 12 hours, followed by mitostress analysis. Cells consistently show reduced OCR levels with or without glucose in response to lomerizine treatment compared to untreated cells (Figure 4-7 B&C). These findings indicate that lomerizine blocks mitochondrial respiration in a dose dependent manner, regardless the carbon sources that fuel TCA cycle.

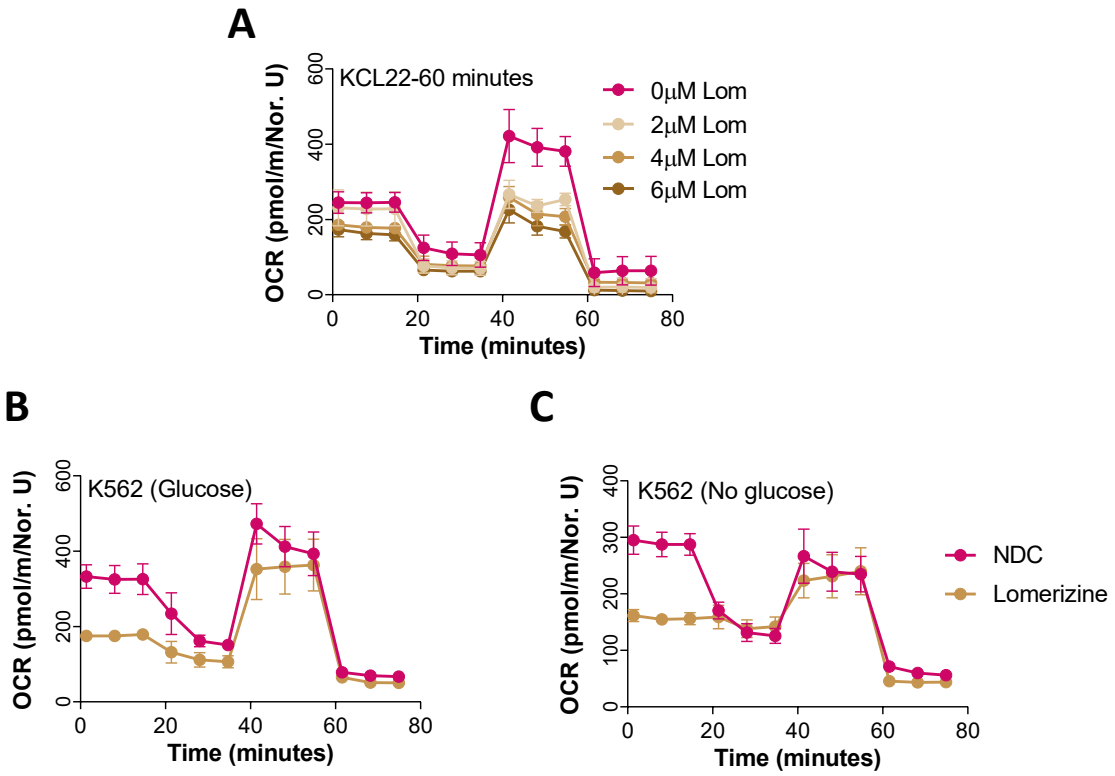

Figure 4-7: Lomerizine inhibits respiration in CML cell lines.

(A) Respirometry profile of KCL22 cells treated with different concentrations of lomerizine for 60 minutes. Respirometry profile of K562 cells cultured in glucose and exposed to 5 µM lomerizine for 12 hours in presence of 11 mM glucose (B) or in the absence of glucose from culture medium for 12 hours (C), where n= 8 technical replicates.

4.4.1 Lomerizine inhibits $CaCl_2$-mediated OCR in K562 cells

Despite promising results lomerizine shows regards the inhibition of OXPHOS, it is not clear yet if this effect arises from lomerizine mediated Ca^{2+} regulation.
Initially, to investigate the correlation between mitochondrial OXPHOS and Ca^{2+} ions, K562 cells were exposed to either 2 mM $CaCl_2$ or 10 µM EGTA (extracellular Ca^{2+} ion chelator) for 12 hours, followed by measuring OCR using mitostress assay. Cells significantly increase their OCR in response to $CaCl_2$ supplementation and significantly blocks OCR in response to EGTA compared to untreated cells (Figure 4-8A).

Going further, EGTA significantly impacts cell expansion and viability after 72 hours compared to cells exposed to $CaCl_2$ or untreated cells. Cells probably enhance internal Ca^{2+} stores utilisation to compensate for scavenging of extracellular Ca^{2+} shortly after exposing cells to EGTA, which may lead to depletion on long-term exposure (Figure 4-8B). Our findings indicate that deprivation of Ca^{2+} ion content significantly impacts CML viability in the longer term.

Given that lomerizine has been reported to block plasma membrane Ca^{2+} channels such as VGCC [236], it can be predicted that lomerizine will block the increase in OCR when culturing cells in higher $CaCl_2$. To test this, K562 cells were cultured in either 2 mM $CaCl_2$, 200 nM EGTA, 5 µM lomerizine or a combination, followed by OCR assessment (Figure 4-8 C&D). Lomerizine significantly blocks $CaCl_2$ induced OCR, indicating that lomerizine blocks OXPHOS, potentially through inhibiting extracellular Ca^{2+} influx to mitochondria which will be investigated shortly.

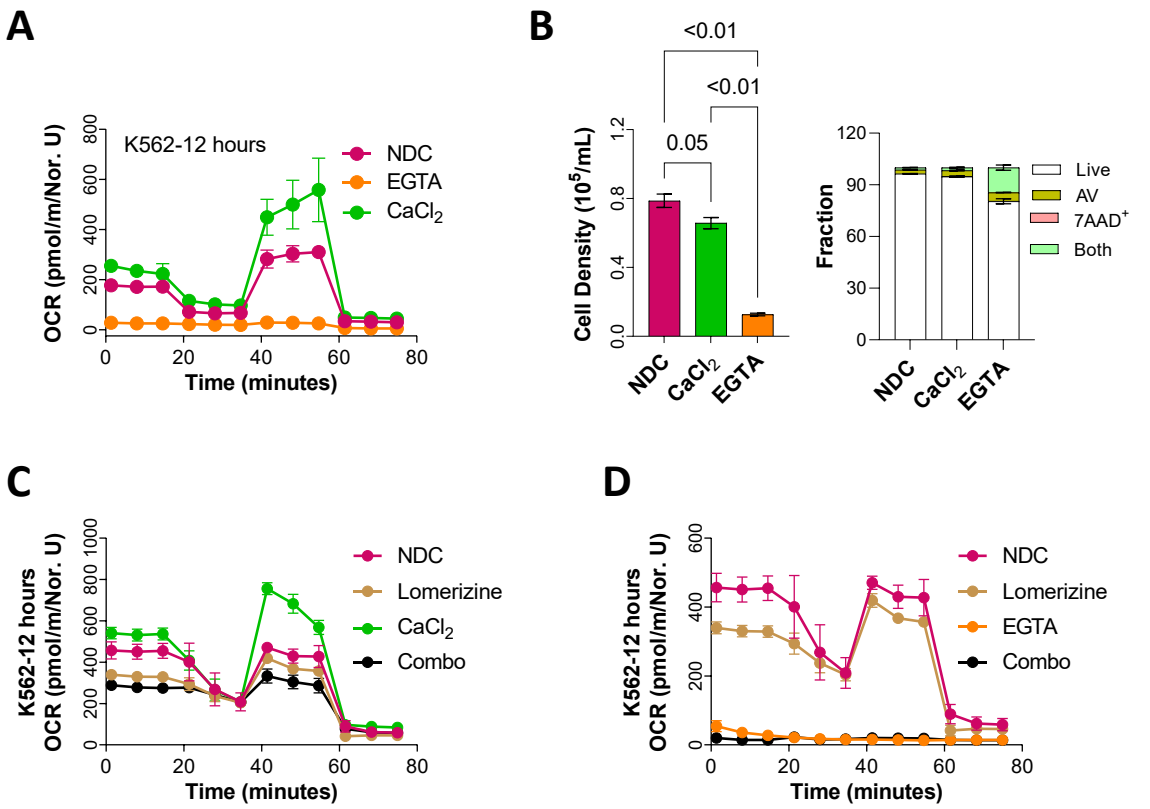

Figure 4-8: Lomerizine inhibits Ca^{2+} mediated respiration in K562 cells.

(A) Representative respirometry of WT K562 cells treated with 200 nM EGTA or 2 mM CaCl2 for 12 hours, measured with Agilent Seahorse mitostress test (n=5 technical replicates). (B) Cell expansion levels in WT K562 cells were treated with an additional 2 mM CaCl2 or 200 nM EGTA for 72 hours. Level of apoptosis after staining cells with APC-annexin V and 7-AAD using flow cytometry (n=3 technical replicates). (C) Respirometry profile of WT K562 exposed to 5 µM lomerizine, 2 mM $CaCl_2$ or their combination for 12 hours. N=4 technical replicates. (D) Respirometry profile of WT K562 exposed to 5 µM lomerizine, 200 nM EGTA or their combination for 12 hours. N=4 technical replicates. Error bars were presented as SDM+/- mean response. Statistical analysis of (B) was performed with one-way ANOVA and LSD exact test was performed to correct for multiple comparisons.

Next, the effect of imatinib on OCR levels in K562 and KCL22 cells exposed to high Ca^{2+} level (2 mM $CaCl_2$) or low Ca^{2+} level (200 nM EGTA) for 12 hours were investigated (Figure 4-9). Imatinib does not alter EGTA's impact on severely lowering OCR on either cell line (Figure 4-9A). Also, in combination with $CaCl_2$, imatinib significantly reduces OCR level compared to $CaCl_2$ alone (Figure 4-9B). However, KCL22 cells, but not K562 cells, cultured with a combination of imatinib and $CaCl_2$ have significant higher maximal OCR when compared to cells exposed to imatinib alone, indicating that $CaCl_2$ can partially rescue some of imatinib effects on mitochondrial respiration. This may indicate that imatinib can reduce OCR independently from Ca^{2+} influx to mitochondria.

The lasting effect of lomerizine on mitochondrial respiration was confirmed by measuring OCR on K562 and KCL22 exposed to lomerizine, imatinib, or their combination for 12 hours and 48 hours. Results confirm that imatinib inhibits maximal OCR level only after 48 hours (Figure 4-10). Lomerizine significantly reduces OCR at 12 hours and 48 hours alone or in combination with imatinib when compared to untreated or imatinib treated cells. Those findings indicate that lomerizine acts faster than imatinib on inhibition and significantly impacts OCR alone and when combined with imatinib.

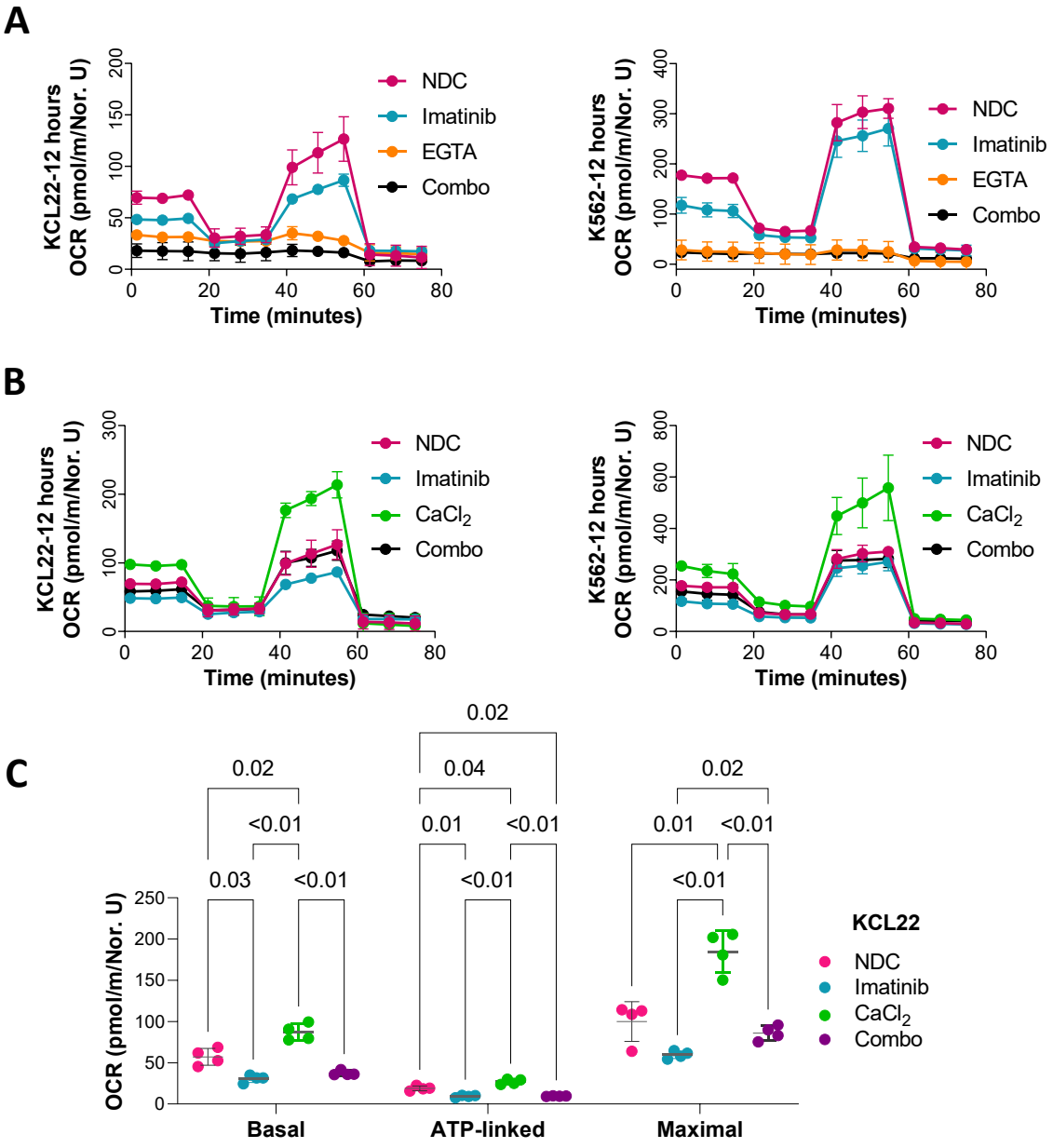

Figure 4-9: $CaCl_2$ rescues maximal respiration in imatinib treated cells.

(A) Respirometry profile of KCL22 and K562 cells treated with 0.5 µM imatinib, 200 nM EGTA, or their combinations for 12 hours. (B) Respirometry profile of KCL22 and K562 cells treated with 0.5 µM imatinib, 2mM $CaCl_2$, or their combinations for 12 hours. (C) Analysis of respirometry profile of KCL22 cells treated with 0.5 µM imatinib, 2mM $CaCl_2$, or their combinations for 12 hours shows that CaCl2 ameliorates maximal respiration compared to imatinib treated cells. Error bars are presented as SDM+/- mean response of n= 4 technical replicates. Statistical analysis was performed with two-way ANOVA and Tukey was performed to correct for multiple comparisons.

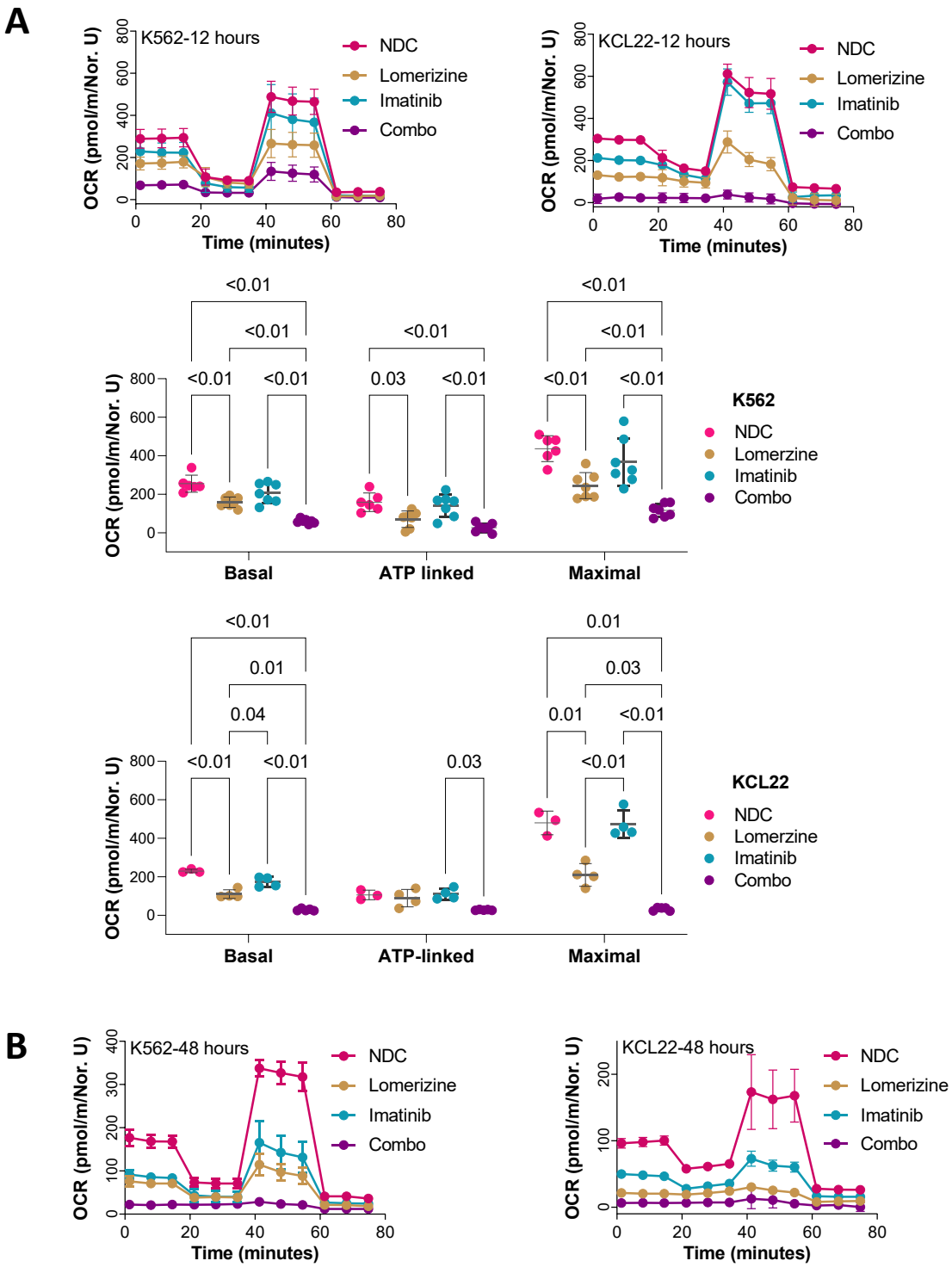

Figure 4-10: Lomerizine inhibits respiration in imatinib treated cells.

(A) Respirometry analysis of WT K562 and KCL22 cells exposed to lomerizine for 12 hours, followed by quantification of basal, ATP-linked, and maximal OCR (n = 7 for K562 and n=4 technical replicates in KCL22 cells). Statistical analysis was performed with two-way ANOVA and Tukey was performed to correct for multiple comparisons (B) Respirometry analysis of WT K562 and KCL22 cells treated with 5 μM lomerizine, 0.5 μM imatinib or their combination for 48 hours.

4.4.2 Lomerizine does not target mitochondrial complexes

However, it was still unclear if lomerizine inhibits OXPHOS by directly inhibiting mitochondrial ETC complexes.
Author addressed this question by optimising a modified respirometry analysis using Agilent Seahorse flux analyser. The idea is to permeabilise live cells' plasma membrane and exposes cells to a high concentration of a specific mitochondrial complex's substrates, such as succinate, to activate complex II [204]. The impact of injecting those substrates on OCR reflects a particular complex activity and can indicate a direct blockade of a complex by the inhibitor.

It is assumed that analysis should be performed on cells exposed to treatment for 4 hours maximum to avoid any late point impact on mitochondrial activities. To confirm successful cell membrane permiabilisation with saponin, we feed intact and cell membrane permeabilised cells with cell membrane impermeable succinate (Figure 4-11A). Permeabilised membrane allows cells to respond to succinate acute injection, while intact cells do not alter cell response to succinate injections, indicating successful membrane permiabilisation with saponin.

To investigate the effect of lomerizine and imatinib on the level of mitochondrial complexes (I, II, IV), K562 cells were exposed to treatments for 4 hours, followed by measuring their activity. Results indicate that neither imatinib nor lomerizine directly impacts mitochondrial complexes' activities, in contrast to the specific complex I inhibitor (IACS-010759) that obviously shuts complex I and maximises other complexes activities (Figure 4-11 B-D). These findings indicate that impact of imatinib or lomerizine on OXPHOS is indirect, such as blocking Ca^{2+} ions or reducing mitochondrial mass in the case of lomerizine or imatinib, respectively.

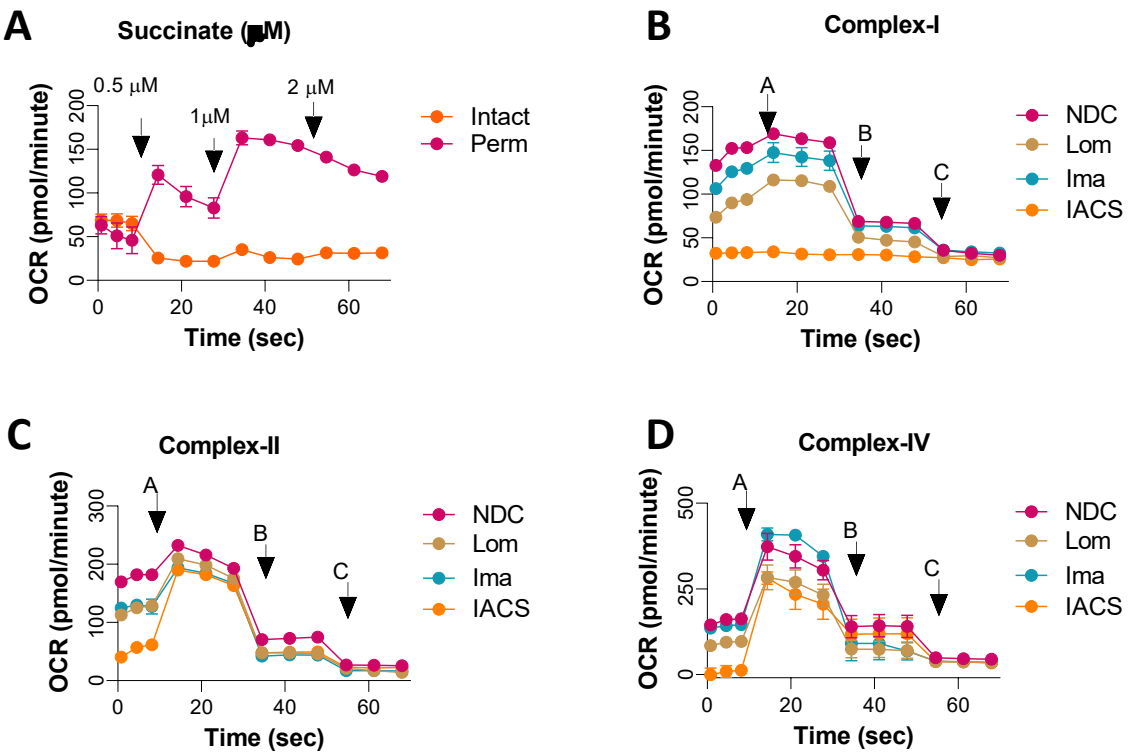

Figure 4-11: Lomerizine or imatinib does not alter complex activities.

(A) Optimisation of the method through injecting 0.5 µM, 1 µM, and 2 µM succinate in either intact or permeabilised cells. (B) Measurement of complex I activity. (C) Measurement of complex II activity. (D) Measurement of complex-IV activity. Figures (A, B, and C) represent results of n=4 independent replicates. Error bars are shown as SEM+/-mean.

4.4.3 Lomerizine does not alter basal glycolysis in CML cells

It is well known that imatinib reduced the level of glycolytic activities [237]. Author decided to investigate the role of lomerizine in the glycolysis level using Seahorse Glycostress analysis (Figure 4-12). Imatinib reduces level of glycolysis after 12 hours. Further, lomerizine significantly reduces maximum glycolytic capacity without altering the basal glycolysis level in K562 cells. In addition, lomerizine does not alter the response of imatinib mediated glycolysis inhibition.

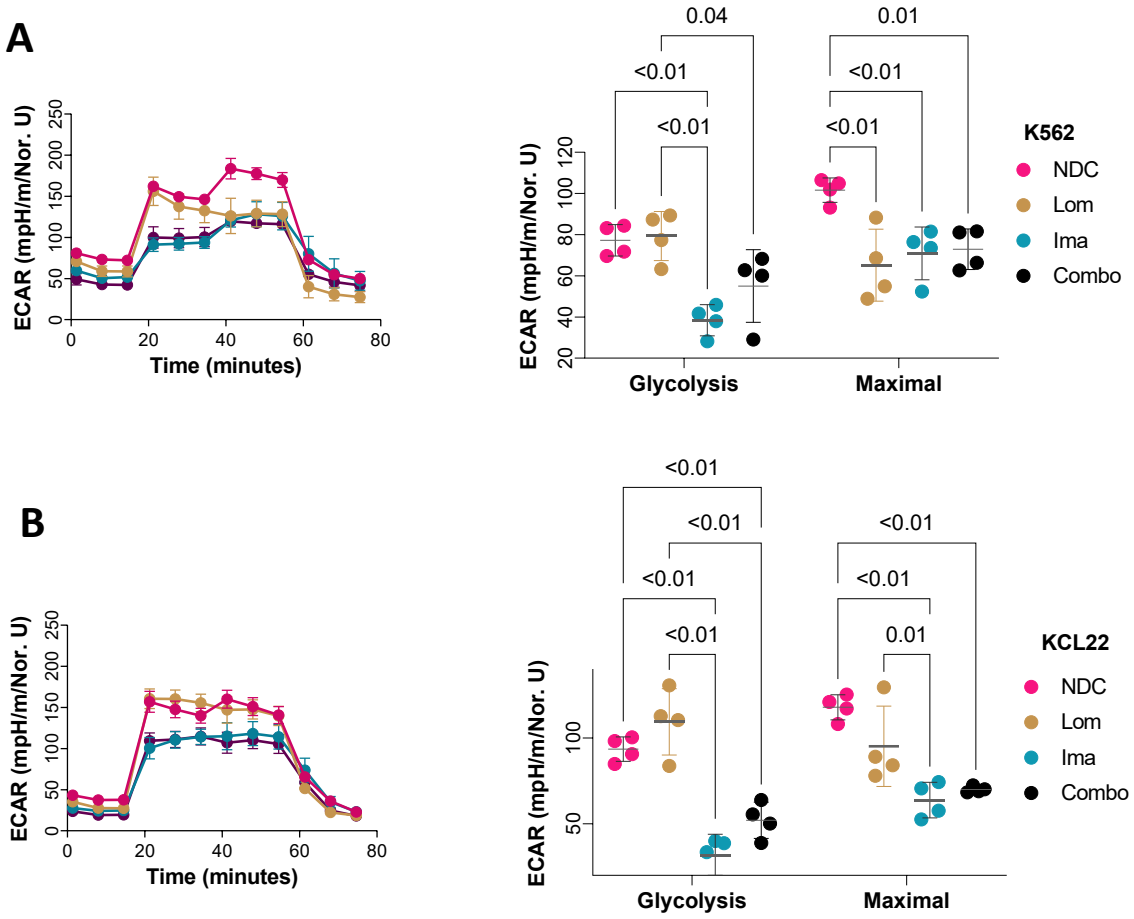

Figure 4-12: Lomerizine cannot reverse glycolysis inhibition by imatinib.

(A) Glycostress profile of K562 cell lines exposed to 5 μM lomerizine, 0.5 μM imatinib, and their combination for 12 hours, followed by analysing glycolysis and maximal glycolysis. (B) Glycostress profile of KCL22 cell lines exposed to 5 μM lomerizine, 0.5 μM imatinib, and their combination for 12 hours, followed by analysing glycolysis and maximal glycolysis. Error bars are shown as SDM +/- mean response. Statistical analysis was performed with two-way ANOVA and Tukey was performed to correct for multiple comparisons.

4.4.4 Lomerizine reduces TCA metabolites levels *in vitro*

It is likely that lomerizine will impact the TCA cycle intermediate levels, given the lomerizine mediated dehydrogenase activity inhibition. IACS-010759, which is known to inhibit complex I activity and used as an OXPHOS inhibitor control, is also likely to interrupt TCA integrity. To test this, TCA intermediate levels were tracked by culturing K562 cells with heavy labelled [$^{13}C_6$] glucose isotope instead of regular glucose for 24 hours. IACS-010759 inhibits labelled glucose integration into TCA cycle metabolites (Figure 4-13). IACS-010759 treatment further increases the level of M+3 lactate in the intracellular fraction and in the culture medium (Figure 4-13). In addition, IACS-010759 significantly increases NADH levels, which is expected due to inability of cells to consume NADH after complex I inhibition (Figure 4-13).

On the other hand, lomerizine treatment reduces level of intracellular TCA cycle intermediates. In addition, lomerizine does not increase intracellular glycolytic intermediates, such as lactate and pyruvate (Figure 4-13). Further, lomerizine significantly decreases level of nucleotides pool size, reflecting energetic supply shortage in those cells upon exposure to lomerizine. In addition, the level of aspartate is significantly reduced in cells exposed to lomerizine or IACS-010759, reflecting potential inhibition of nucleotide synthesis, besides stalled OXPHOS mediated ATP machinery, which could finally deteriorate cell proliferation.

Following on this lead, investigating if OXPHOS inhibition by lomerizine will drive stress signalling in response to energetic status disruption was carried out. To address this, the level of AMPK phosphorylation in K562 cells after 12 hours of lomerizine exposure was measured. AMPK acts as a metabolic sensor, where increased AMP/ATP ratio leads to AMPK phosphorylation which leads to inhibition of anabolic processes that require ATP consumption. Results show that lomerizine and imatinib significantly enhances AMPK phosphorylation with subsequent trend increase in phosphorylation of ACC enzyme down stream of AMPK (Figure 4-14).

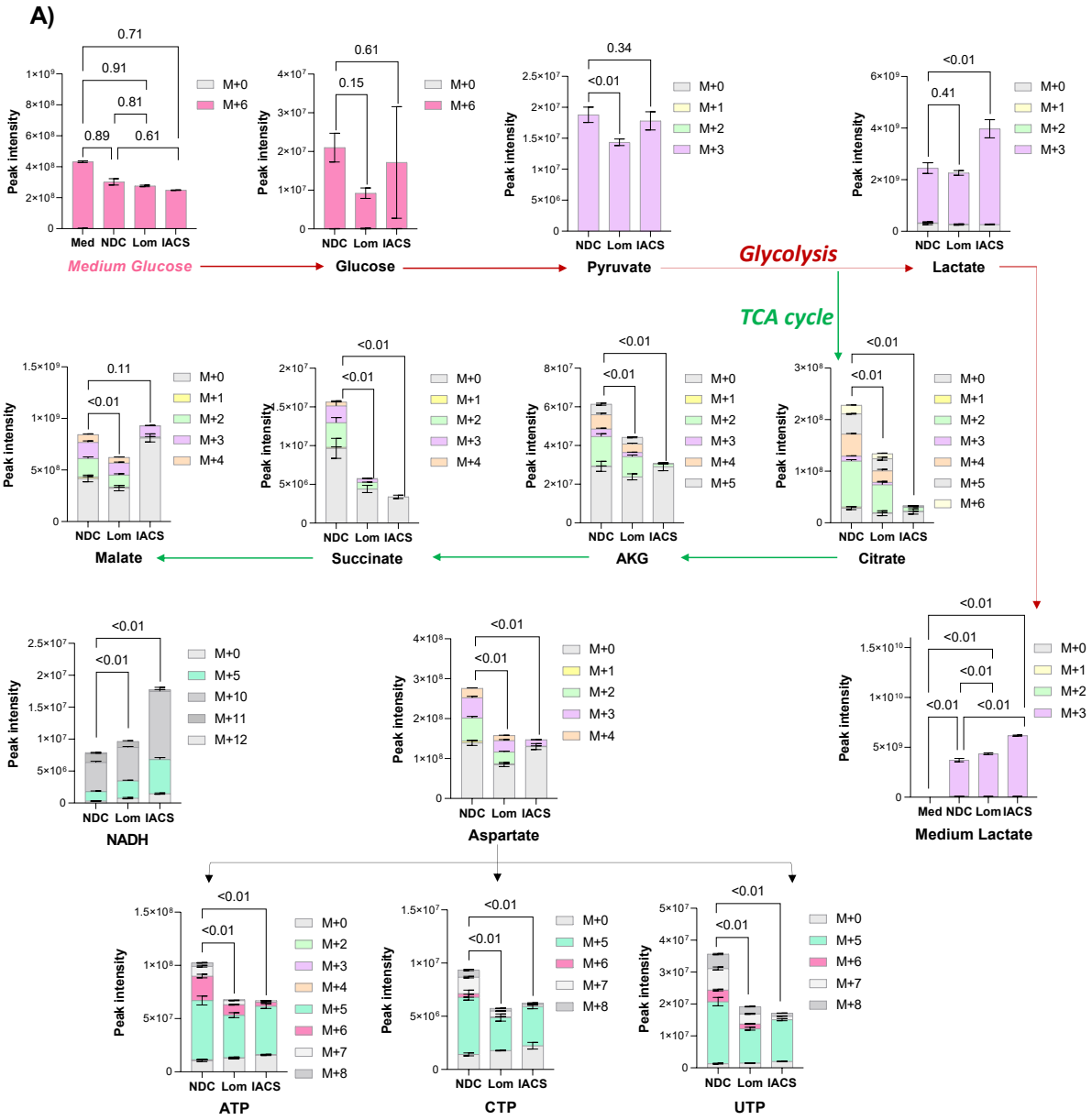

Figure 4-13: Lomerizine reduces TCA metabolite in K562 cells.

$^{13}C_6$ glucose isotope labelling in glycolysis and TCA cycle metabolites extracted from K562 WT cells treated with 5 μM lomerizine or 20 nM IACS for 24 hours, n=3 technical replicates. Statistical analysis was performed with one-way ANOVA and Tukey was performed to correct for multiple comparisons.

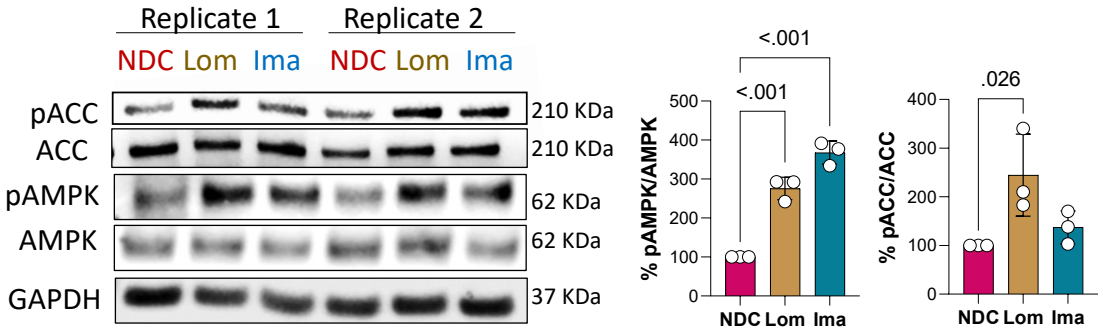

Figure 4-14: Lomerizine enhances AMPK phosphorylation in K562 cells.

Western blot shows the level of pThr172 AMPK, subsequent pACC, and their corresponding total levels in K562 cells treated with 5 μM lomerizine or 1μM imatinib for 12 hours. Statistical analysis was performed using one-way ANOVA and Dunnett's test for multiple comparisons correction. Analysis was estimated from n=3 technical replicates and error bar are shown as mean+/- SDM.

4.4.5 Lomerizine inhibits IDH3 in K562 cells

Further investigation if lomerizine blocks OXPHOS due to its effect on enzymatic activity of mitochondrial dehydrogenases was required, such as IDH. IDH has 3 isoforms; mitochondrial NADPH-dependent IDH2, NADH-dependent IDH3 and cytosolic NADPH-dependent IDH1 [238]. Author measured mitochondrial IDH3 in K562 cells exposed to lomerizine, imatinib, or their combination for 12 hours. Despite lack of imatinib impact on IDH3 activity, lomerizine significantly reduces mitochondrial IDH3 activity and significantly inhibits IDH3 in cells exposed to imatinib, indicating the effect of lomerizine on OXPHOS through inhibiting mitochondrial dehydrogenases (Figure 4-15).

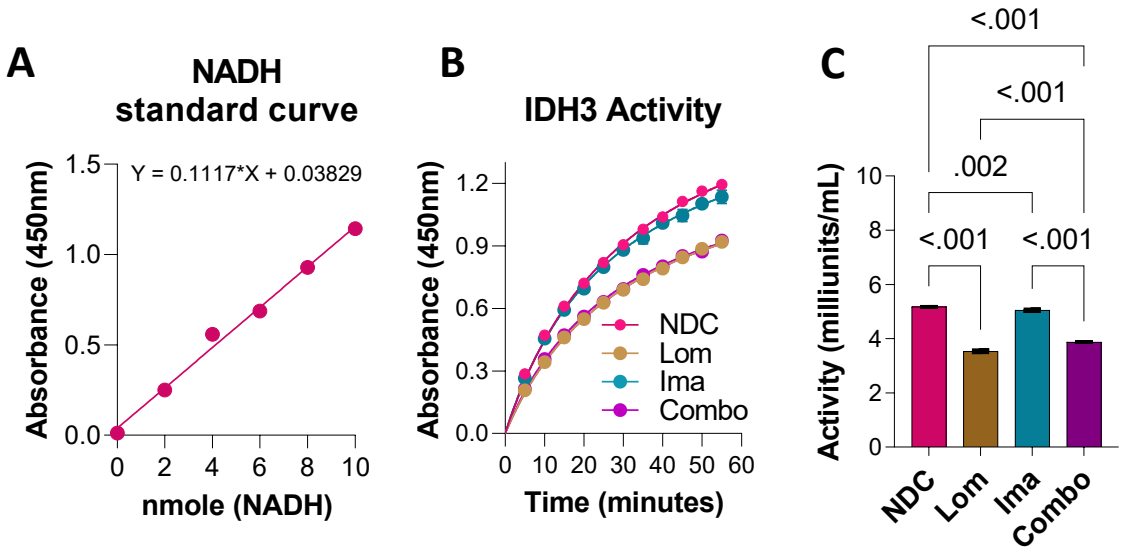

Figure 4-15: Lomerizine inhibits IDH3 activity in K562 cells.

(A) Standard curve analysis of NADH level. (B) Representative kinetic absorbance that reflects IDH3 activity was measured colorimetrically in WT K562 cells treated with 5μM lomerizine, 1 μM imatinib or their combination for 12 hours. (C) Quantification analysis of level of IDH3 activity (n=4 technical replicates and error bars are shown as SDM +/- mean response). Statistical analysis was performed with one-way ANOVA and Tukey was performed to correct for multiple comparisons.

4.5 Lomerizine acts by inhibiting Ca^{2+} influx to CML cells

As previously shown, Ca^{2+} ion availability is a prerequisite for maximal mitochondrial dehydrogenase catalytic activities [93, 224]. Next, it is aimed to address if lomerizine regulates Ca^{2+} in CML. This approach was delivered by measuring cytosolic and mitochondrial Ca^{2+} ions levels using specific Ca^{2+} indicators, namely Indo-1 and Rhod-2, followed by quantification of Ca^{2+} levels by flow cytometry (Figure 4-16). While measuring Ca^{2+} levels on flow cytometer, cells were also stimulated for Ca^{2+} influx through spiking 25 μM 1,2-dioctanoyl-cn-glycerol (DOG), a nonspecific Ca^{2+} influx stimulator that acts through activation of TRPC6 (this requires intact lipid raft and Src signalling) and L-type of VGCC, such as CACNA1D [239, 240].

Exploiting this approach using K562 cells exposed to lomerizine or imatinib for 24 hours revealed that imatinib does not alter basal cytosolic Ca^{2+} levels or influx in response to DOG stimulation. In addition, lomerizine significantly reduces cytosolic and mitochondrial basal Ca^{2+} levels and abolishes DOG effect on Ca^{2+} influx to cytosol and mitochondria (Figure 4-17 A&B).
These findings indicate that lomerizine blocks Ca^{2+} influx via TRPC6 and CACNA1D, while imatinib does not alter this process. In contrast, imatinib significantly reduces basal mitochondrial and Ca^{2+} influx to mitochondria in response to DOG (Figure 4-17B).

4.5.1

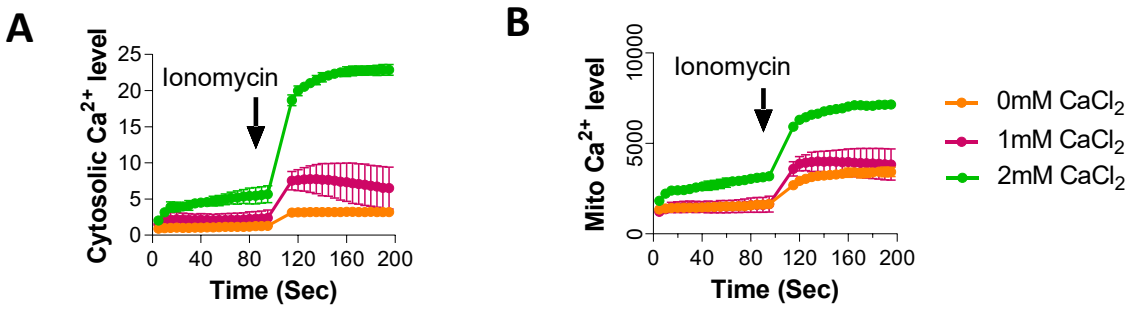

Figure 4-16: Optimisation of Ca^{2+} level assay.

Flow cytometry analysis shows (A) Cytosolic and (B) mitochondrial Ca^{2+} level in K562 cells upon exposure to 0, 1 mM, or 2 mM $CaCl_2$. Cells were exposed to acute stimulation with 2.5 µM ionomycin.

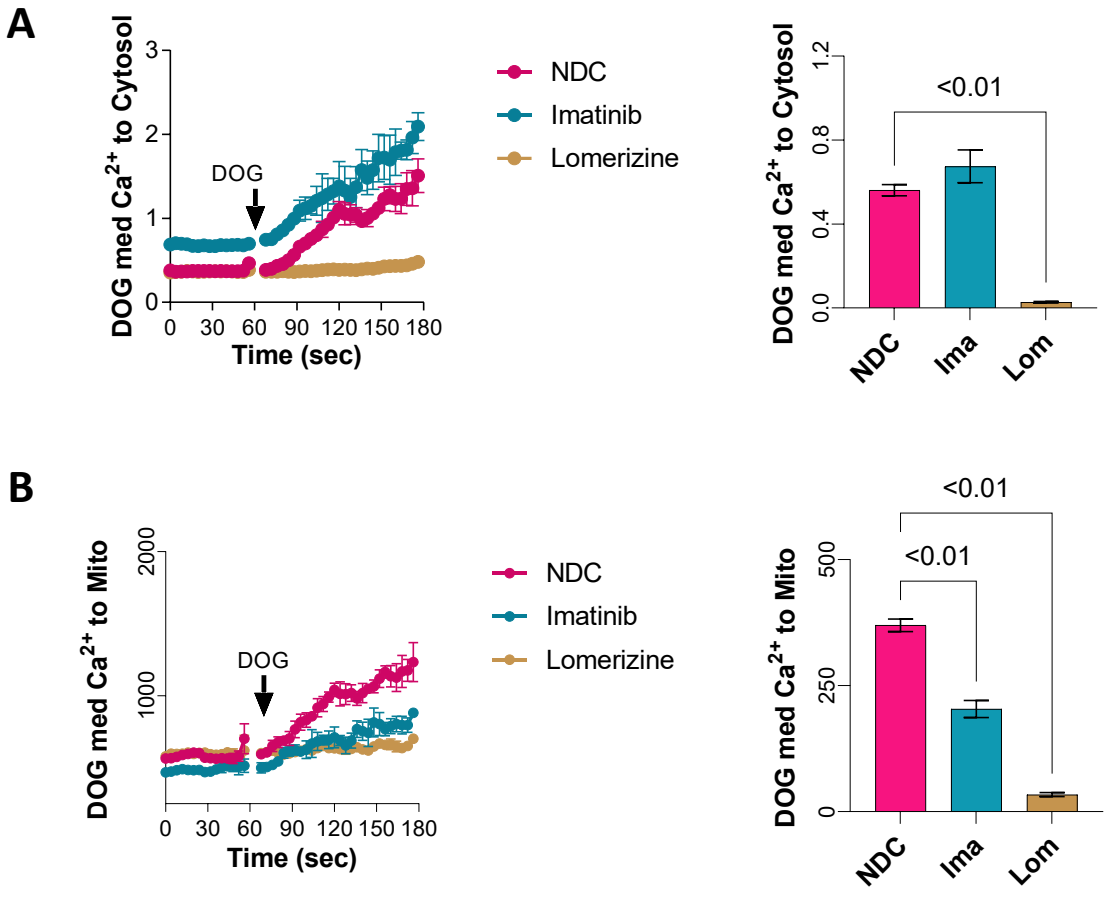

Figure 4-17: Lomerizine inhibits DOG-mediated Ca^{2+} influx in K562 cells.

Representative kinetic flow cytometry analysis of cytosolic Ca^{2+} level (A) and mitochondrial Ca^{2+} levels (B) in WT K562 cells treated for 24 hours with 10 µM lomerizine, or 1 µM imatinib. Cells were stimulated with 25 µM DOG instantly during acquiring flow cytometry data. Error bars are shown as SEM+/- MFI where n=3 independent experiments. Statistical analysis was performed with one-way ANOVA and Tukey was performed to correct for multiple comparisons.

4.5.2 Lomerizine inhibits TRPC6 and CACNA1D mediated Ca^{2+} influx

To address if lomerizine blocks Ca^{2+} influx by targeting TRPC6 channel, author followed the same approach to measure Ca^{2+} influx, replacing DOG with 50 μM hyperforin, a specific TRPC6 stimulator [220]. K562 cells were treated with 2 μM BI749327, another TRPC6 blocker, as a positive control [213]. Lomerizine and BI749327, but not imatinib, almost abolishes hyperforin mediated Ca^{2+} influx to cytosol and mitochondria alone or combined with imatinib (Figure 4-18).
The impact of hyperforin on OCR in K562 cells was confirmed.

To go further, the effect of lomerizine on CACNA1D-mediated Ca^{2+} influx was investigated. The same approach was used using 50 μM FPL to stimulate CACNA1D Ca^{2+} influx [221]. K562 cells were treated with 10 μM nicardipine, which selectively blocks CACNA1D Ca^{2+} influx [222]. Results show that lomerizine and nicardipine, but not imatinib alone, significantly inhibits FPL mediated Ca^{2+} influx to cytosol when combined to imatinib (Figure 4-19A). Also, as a single agent, lomerizine and nicardipine reduces mitochondrial Ca^{2+} influx in response to FPL stimulation (Figure 4-19B).

Overall, this indicates that lomerizine, but not imatinib inhibits Ca^{2+} influx to cells by inhibiting both TRPC6 and CACNA1D channels. The mode of action that results in the dual channels' inhibition by lomerizine is still unclear though.

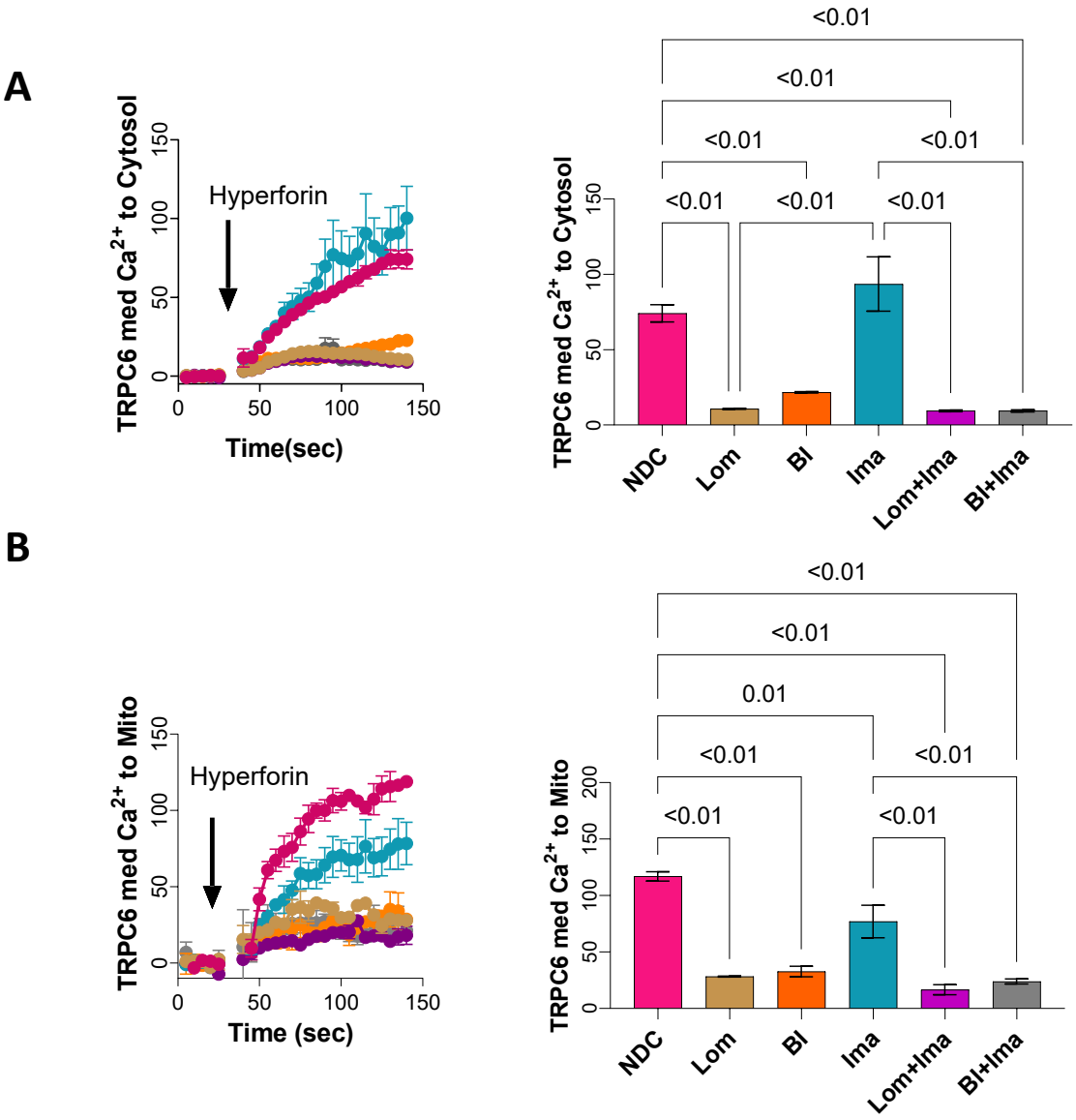

Figure 4-18: Lomerizine inhibits TRPC6-mediated Ca^{2+} influx in K562 cells.

Representative kinetic flow cytometry analysis of cytosolic Ca^{2+} level (A) and mitochondrial Ca^{2+} levels (B) in WT K562 cells treated for 24 hours with 10 μM lomerizine, 5 μM BI (TRPC6 inhibitor) or 1 μM imatinib or their combination with imatinib. Cells were stimulated with 25 μM Hyperforin instantly during acquiring flow cytometry data. Error bars are shown as SEM+/- MFI where n=3 independent experiments. Statistical analysis was performed with one-way ANOVA and Tukey was performed to correct for multiple comparisons.

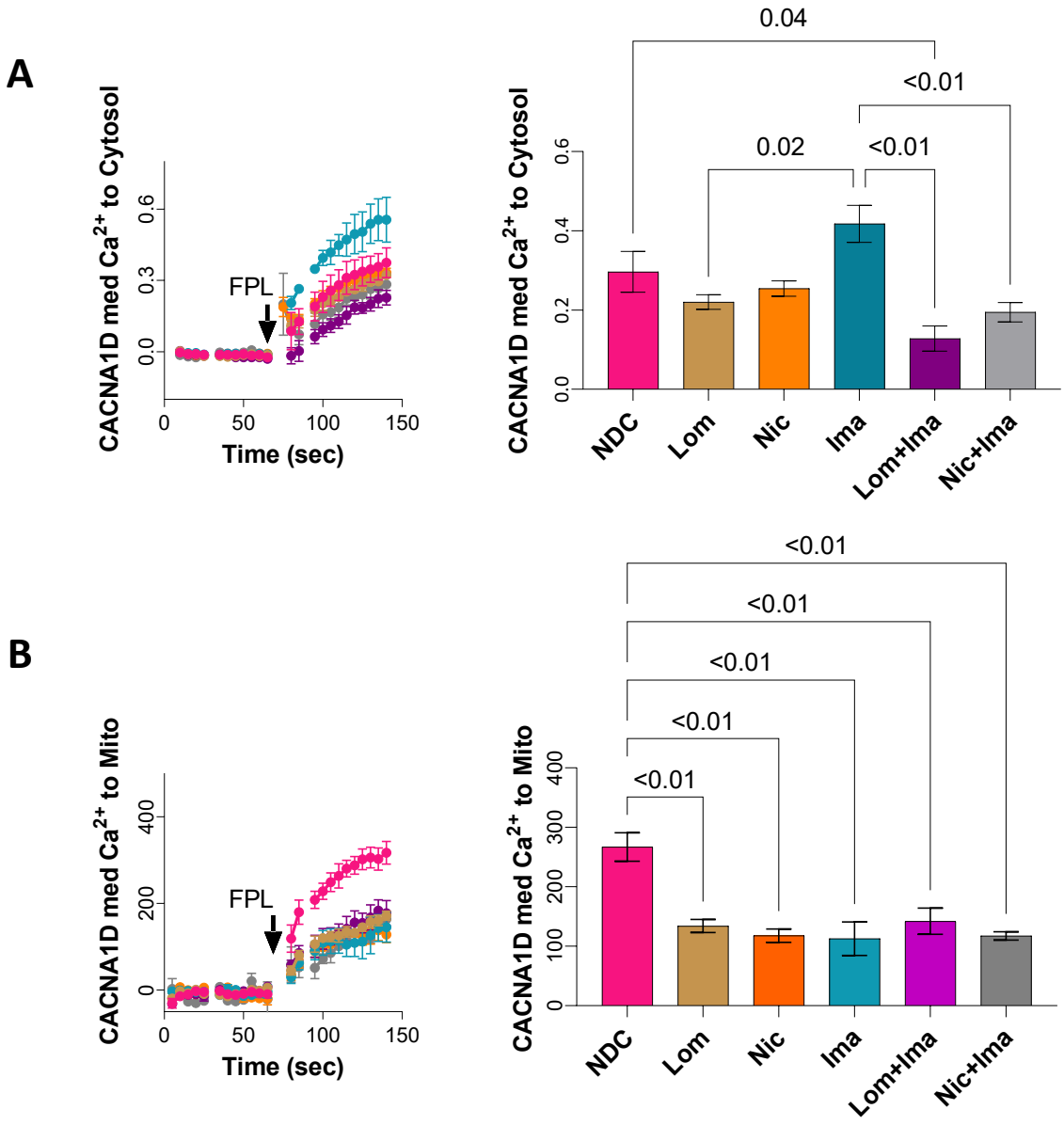

Figure 4-19: Lomerizine inhibits CACNA1D Ca^{2+} influx in K562 cells.

Representative kinetic flow cytometry analysis of cytosolic Ca^{2+} level (A) and mitochondrial Ca^{2+} levels (B) in WT K562 cells treated for 24 hours with 10 µM lomerizine, 10 µM nicardipine (CACNA1D inhibitor) or 1 µM imatinib or their combination with imatinib. Cells were stimulated with 25 µM FPL instantly during acquiring flow cytometry data. Error bars are shown as SEM+/- MFI where n=3 independent experiments. Statistical analysis was performed with one-way ANOVA and Tukey was performed to correct for multiple comparisons.

4.5.3 Lomerizine inhibits ER Ca^{2+} transfer to mitochondria

It has been shown that most intracellular Ca^{2+} ions (~800 µM) are stored within ER sheets [241]. Mitochondrial Ca^{2+} ions require a continuous transfer from ER to mitochondria [242].

It is critical to investigate if lomerizine regulates Ca^{2+} ion storage capacity of ER and whether lomerizine regulates transfer of ER Ca^{2+} to mitochondria. To test this, K562 cells that expresses a genetically encoded protein called GCAMPER was generated [243] (Figure 4-20). The mechanism of action of GCAMPER is based on its ER-targeted design that emits green fluorescence upon binding to Ca^{2+} ions at µM range (low binding affinity). In turn, the fluorescence intensity reflects level of ER Ca^{2+}. Also, green fluorescence is lost in response to acute Ca^{2+} mobilisation from ER.

To measure the maximum Ca^{2+} storage capacity of ER, it is tended to retain Ca^{2+} inside ER by treating GCAMPER K562 cells with 2APB, known as IP3R inhibitor, for 24 hours, followed by acutely mobilise this Ca^{2+} with high concentration of m3-M3FBS that can reverse 2APB mediated IP3R inhibition. The reason behind this is that 2APB has been reported to indirectly inhibit IP3R and for being unable to alter IP3 binding to IP3R [244] (Figure 4-21). Thus, after 24 hours of cell exposure to treatments, GCAMPER fluorescence intensity reduction was quantified upon spiking cells with 50 µM m3-M3FBS.

In terms of lomerizine effect on ER Ca^{2+} level, GCAMPER K562 cells were exposed to 10 µM lomerizine, 1 µM imatinib, or a combination for 24 hours, followed by measurement of fluorescence intensity of green (ER Ca^{2+} level) with flow cytometry in PBS (Ca^{2+} free). Imatinib does not alter progressive green signal reduction compared to untreated cells (Figure 4-22 B&C).

Interestingly, lomerizine alone or combined with imatinib significantly inhibits the reduction of the green signal in response to ER Ca^{2+} mobilisation, indicating either IP3R inhibition or ER Ca^{2+} depletion. However, the high concentration at 50 µM 3m-3MFBS should suffice to reverse any IP3R inhibition caused by lomerizine. Also, lomerizine significantly reduces the effect of different stimulators such as

ionomycin or thapsigargin, that forcedly mobilise ER Ca^{2+} to cytosol or mitochondria. This assumes that lomerizine impacts Ca^{2+} level rather than IP3R inhibition.

As reported and explained in Figure 4-21, GCAMPER K562 cells were further pre-treated with 5 μM 2-aminoethoxydiphenyl borate (2APB) for 24 hours which inhibits Ca^{2+} mobilisation through IP3R [245]. 2APB treated cells were co-treated with imatinib, or lomerizine.
Results reveal the ability of 2APB to significantly reduce green fluorescence in response to IP3R stimulation, indicating 2APB can retain more Ca^{2+} within ER when compared to untreated cells. Imatinib cannot reverse the 2APB effect, in contrast with lomerizine, which significantly reduces 2APB-mediated reduction in green fluorescence intensity (Figure 4-22 B&C). Findings reveal the ability of lomerizine to inhibit the release of ER Ca^{2+} ions.

To verify that retaining ER Ca^{2+} ions in response to lomerizine directly impacts the level of Ca^{2+} levels in the cytosol and mitochondria, corresponding Ca^{2+} levels in WT K562 and KCL22 cells was measured after 24 hours of exposure to lomerizine or imatinib. Cells were stimulated with 2.5 μM thapsigargin, which is known to mobilise Ca^{2+} ions from ER instantly. This reveals a consistently significant reduction in Ca^{2+} mobilisation from ER to the cytosol or mitochondria in response to lomerizine (Figure 4-23). However, imatinib significantly increases Ca^{2+} mobilisation from ER to cytosol this time. This contradicts our previous GCAMPER findings that imatinib does not regulate ER Ca^{2+} release (Figure 4-23). This contradiction likely derives from the difference in sensitivity of the Indo-1 Ca^{2+} indicator compared to the GCAMPER protein, detecting Ca^{2+} levels in the nM and μM range, respectively [243, 246]
This shows that lomerizine represents an additive value for imatinib treatment, as lomerizine combination can inhibit plasma membrane Ca^{2+} influx and ER Ca^{2+} transfer to mitochondria.

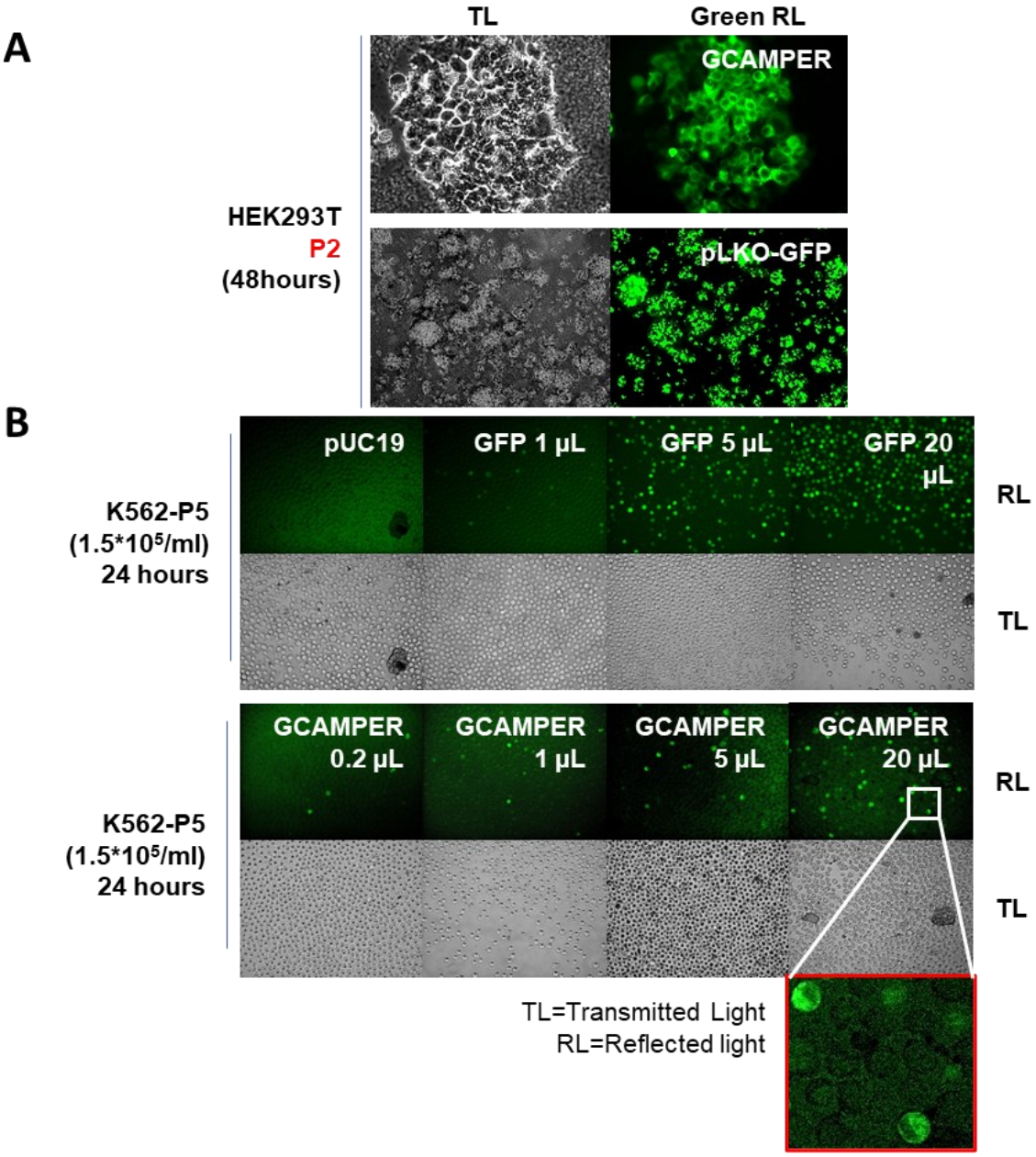

Figure 4-20: Generation of GCAMPER expressing K562 cells.

(A) Images show a successful HEK293FT transfection with the lentiviral GCAMPER construct. (B) Images show the successful transduction of increasing volumes of lentivirus GCAMPER concentrate in WT K562 cells. Viral particles of pLKO-GFP were used as a control.

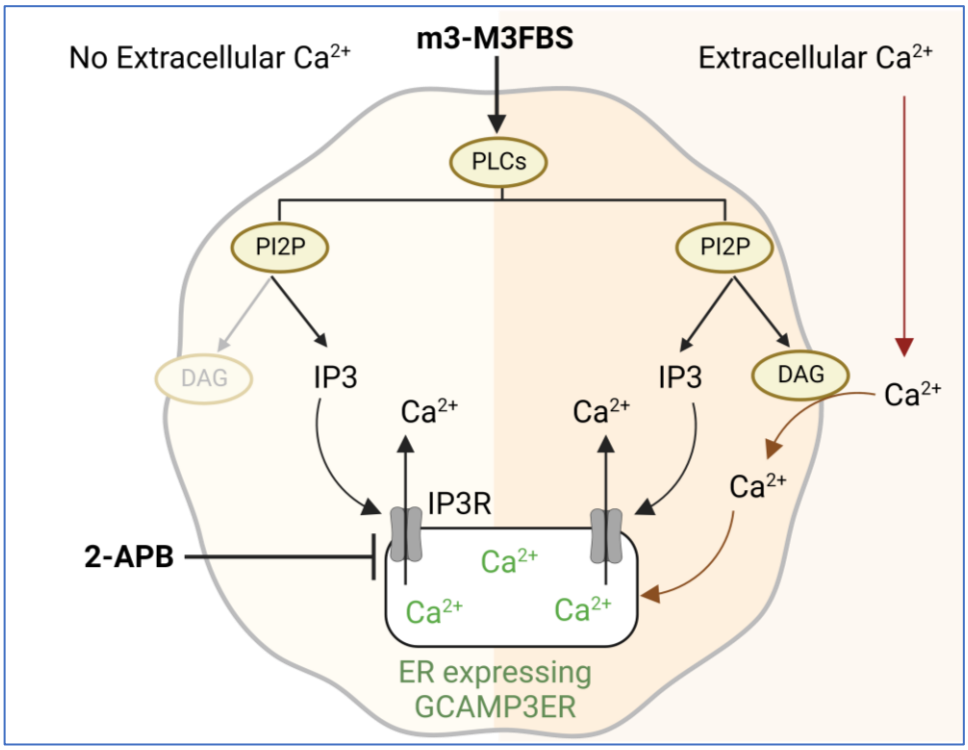

Figure 4-21: 2-APB and m3-M3FBS effect on GCAMPER expressing K562 cells.

ER Ca^{2+} can be quantified through expressing GCAMPER construct that gets localised and binds to ER Ca^{2+}. Upon binding to ER Ca^{2+}, GCAMPER produces fluorescence detected in GFP spectrum. Given that ER Ca^{2+} mobilisers reduce the level of ER Ca^{2+}, they are subsequently expected to reduce the fluorescence intensity. For example, m3-M3FBS mobilises ER Ca^{2+} through nonspecific activation of PLC enzymes responsible for plasma membrane PI2P lysis into DAG and IP3 (IP3R on ER direct ligand). DAG also causes extracellular Ca^{2+} influx through plasma membrane channels. Technically, Author set up ER Ca^{2+} assay in the absence of extracellular Ca^{2+} to eliminate the DAG effect and specifically measure the level of IP3R activity after acute exposure to m3-M3FBS. Further, to quantify the capacitive ER Ca^{2+} storage, ER Ca^{2+} was retained in ER through pre-treating cells for 24 hours with IP3R inhibitor (2APB) followed by measuring maximum ER Ca^{2+} after acute exposure to m3-M3FBS.

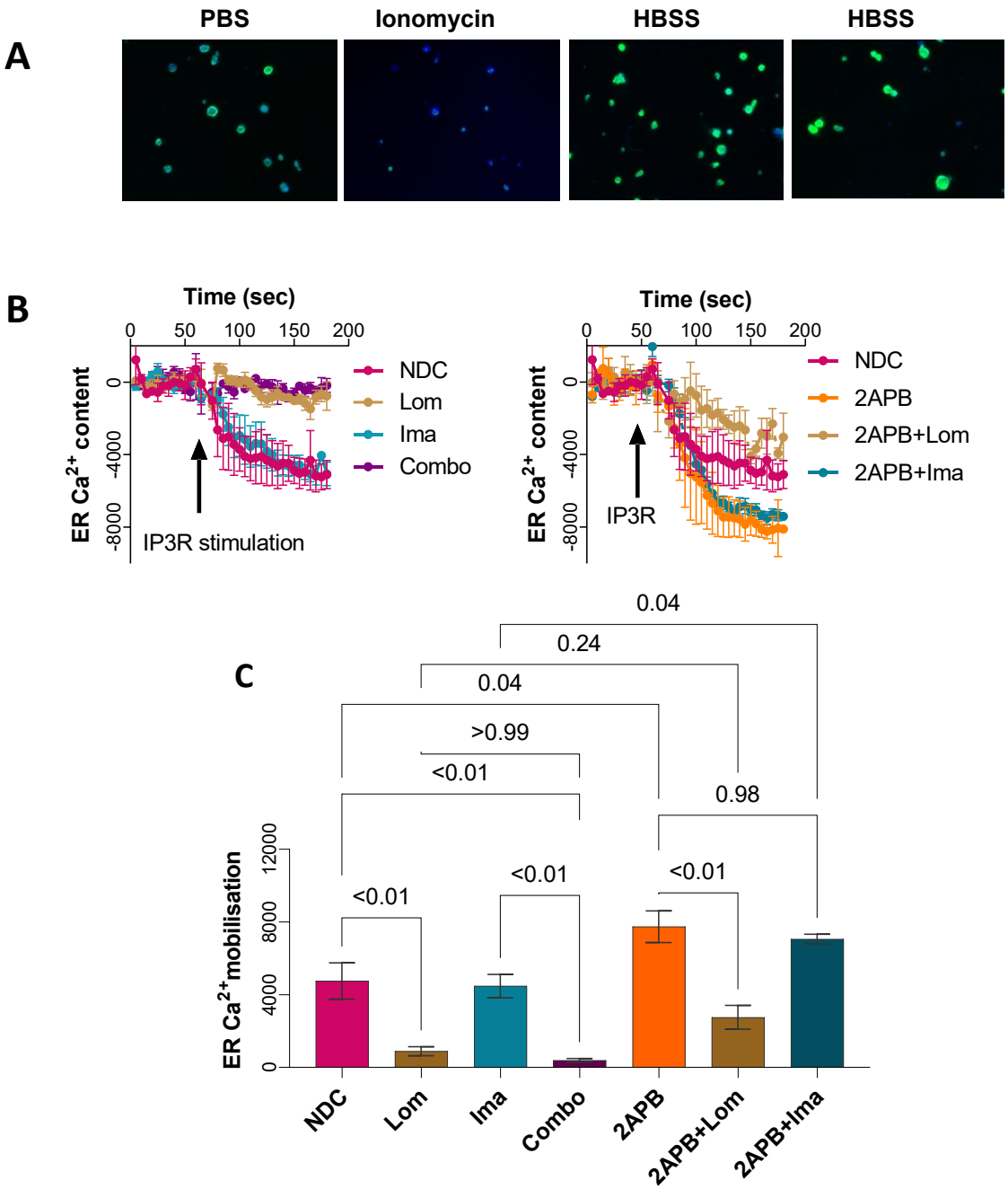

Figure 4-22: Lomerizine reduces ER Ca^{2+} content in K562 cells.

(A) Validation of GCAMPER expressing K562 through depletion of ER content with ionomycin or induction of Ca^{2+} accumulation with HBSS (2 mM $CaCl_2$). (B) Representative kinetic flow cytometry of Ca^{2+} levels in WT K562 expressing GCAMPER and treated with 10 µM lomerizine, 5 µM 2APB, 1 µM imatinib or their combinations for 24 hours (2APB control was used to inhibit ER Ca^{2+} content release). Basal ER Ca^{2+} level was acquired, followed by stimulating cells with 25 µM m-3M3FBS (activates I3PR in the absence of extracellular Ca^{2+}) (n=3 independent experiments). (C) Statistical analyses of (B), where n=4 independent replicates and error bars are shown as SEM+/- means. Statistical analysis was performed with one-way ANOVA and Tukey was performed to correct for multiple comparisons.

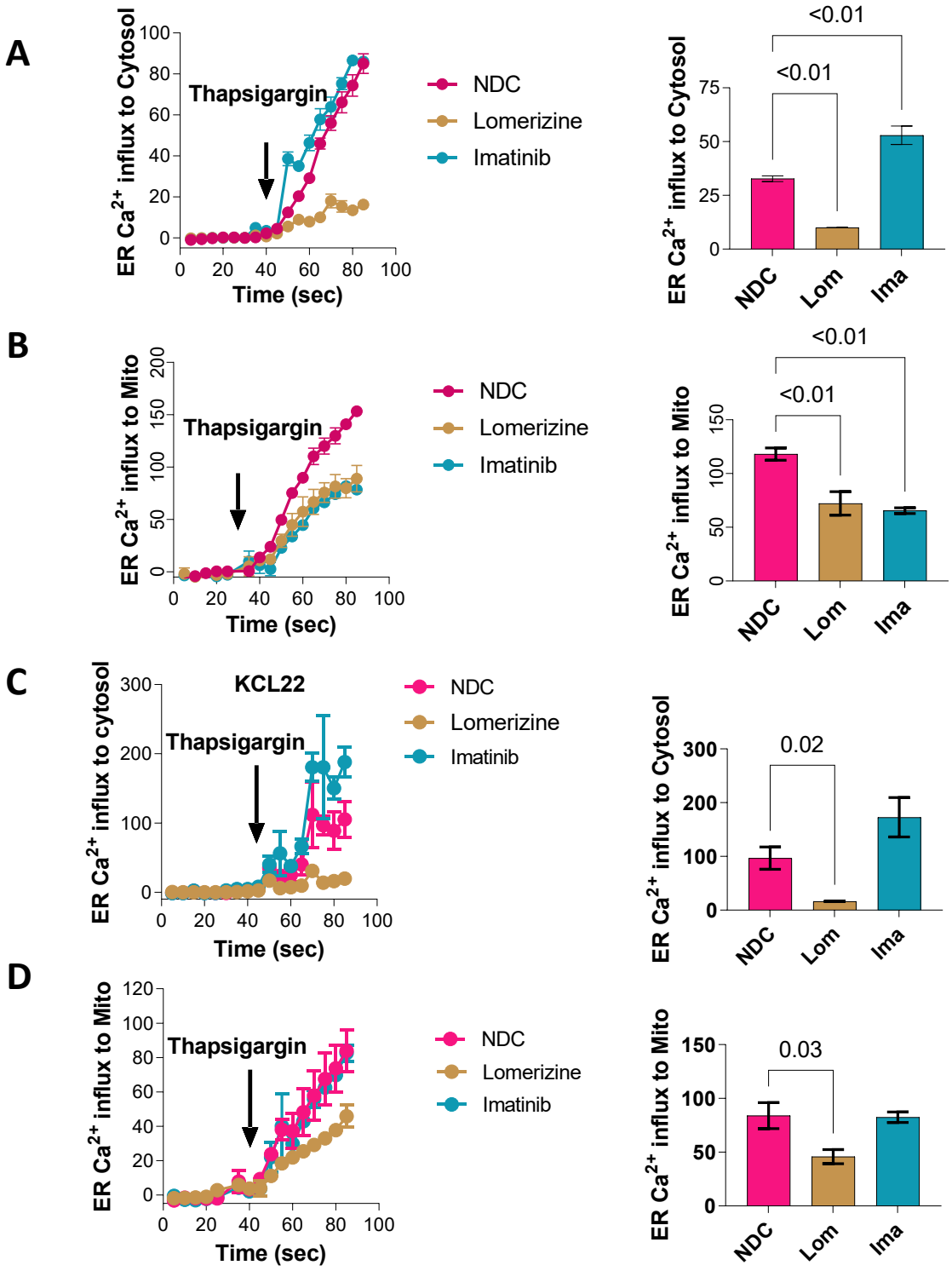

Figure 4-23: Lomerizine inhibits ER mobilisation.

Representative kinetic flow cytometry analysis of cytosolic Ca^{2+} level (A) and mitochondrial Ca^{2+} level (B) in WT K562 cells. (C) Representative kinetic flow cytometry analysis of cytosolic Ca^{2+} level (C) and mitochondrial Ca^{2+} level (D) in WT KCL22 cells. Cells were stimulated with 2.5 µM thapsigargin instantly during acquiring flow cytometry data. Where n=4 independent replicates, SD+/-mean. Statistical analysis was performed with one-way ANOVA and Tukey was performed to correct for multiple comparisons.

4.6 Lomerizine inhibits proliferation of imatinib resistant cells

Resistance to imatinib therapy in CML results from point mutation within *Abl* that results in replacement of one of amino acids of BCR::ABL, such as T315I BCR::ABL. Other mutation independent therapy resistance has been reported.
Yet, the level of mitochondrial and ER content, as major organelles for Ca^{2+} buffering, have not been investigated in imatinib resistant CML. Further, it has not been investigated yet if Ca^{2+} may play a role in survival of imatinib resistance.

To determine the level of therapy resistant CML cells reliance on mitochondrial function, mitochondrial mass, reactive oxygen species (ROS), and potential was evaluated in imatinib sensitive KCL22 cells, and imatinib resistant KCL22 cells that harbour T315I BCR::ABL (T315I KCL22 cells) or does not have BCR::ABL mutations but have other non-mutational dependent imatinib resistance. Ponatinib resistant KCL22 cells showed resistance to multiple TKIs including imatinib and ponatinib and is considered as non-mutation dependent therapy resistant KCL22; Pon-Res KCL22 cells).

Interestingly, Pon-Res KCL22 cells possess higher mitochondrial mass, ROS, and mitochondrial potential compared to imatinib sensitive KCL22 cells (Figure 4-24 A-C). In contrast to imatinib sensitive KCL22 cells, T315I KCL22 cells have decreased mitochondrial bulk mass, ROS, and mitochondrial potential (Figure 4-24 A-C). In addition, ER mass was assessed where there was no difference between imatinib sensitive and Pon-Res KCL22 cells but a significant decrease in ER mass of T315I KCL22 cells relative to imatinib sensitive KCL22 cells (Figure 4-24D).

Also, Ca^{2+} level homeostasis based on initial findings of mitochondrial and ER mass in therapy resistant cells is investigated. The level of Ca^{2+} influx into cytosol and mitochondria in response to DOG was then assessed (Figure 4-24E). While neither resistant nor sensitive cell lines exhibit a change in DOG-induced cytosolic Ca^{2+} influx, they exhibit a significant decrease in mitochondrial Ca^{2+} influx. It is anticipated that most mitochondrial Ca^{2+} would originate from ER rather than cytoplasm. To test this hypothesis, cells were treated with thapsigargin to

mobilise ER Ca^{2+} content. Considerable increase in release of ER Ca^{2+} into cytosol between resistant and susceptible cell lines is observed ((Figure 4-24F).

Interestingly, ER Ca^{2+} transport to mitochondria is dramatically reduced in T315I cells but not in ponatinib resistant cells relative to sensitive cells. These findings demonstrate importance of ER in Ca^{2+} transport in non-mutation resistant cells with greater mitochondrial bulk and function (Figure 4-24F).

Previous studies demonstrated that T315I mutation decreased mitochondrial respiration [247]. However, nothing is known about effects of mutation independent resistance on mitochondrial respiration. Therefore, whether TKI-resistant cells have dysregulated OXPHOS is examined and, if so, whether lomerizine could affect this. Pon-Res KCL22 cells exhibits enhanced OXPHOS and that lomerizine significantly reverses (Figure 4-24G).

Finally, the effect of combining lomerizine or other examples of Ca^{2+} inhibitors, such as BI or nicardipine with imatinib on proliferation of T315I and TKI-resistant cells is examined. Results show that all Ca^{2+} inhibitors significantly inhibit cell growth, regardless the BCR::ABL mutations (Figure 4-24H). This suggests that targeting Ca^{2+} may be efficient way to eradicate resistant CML populations.

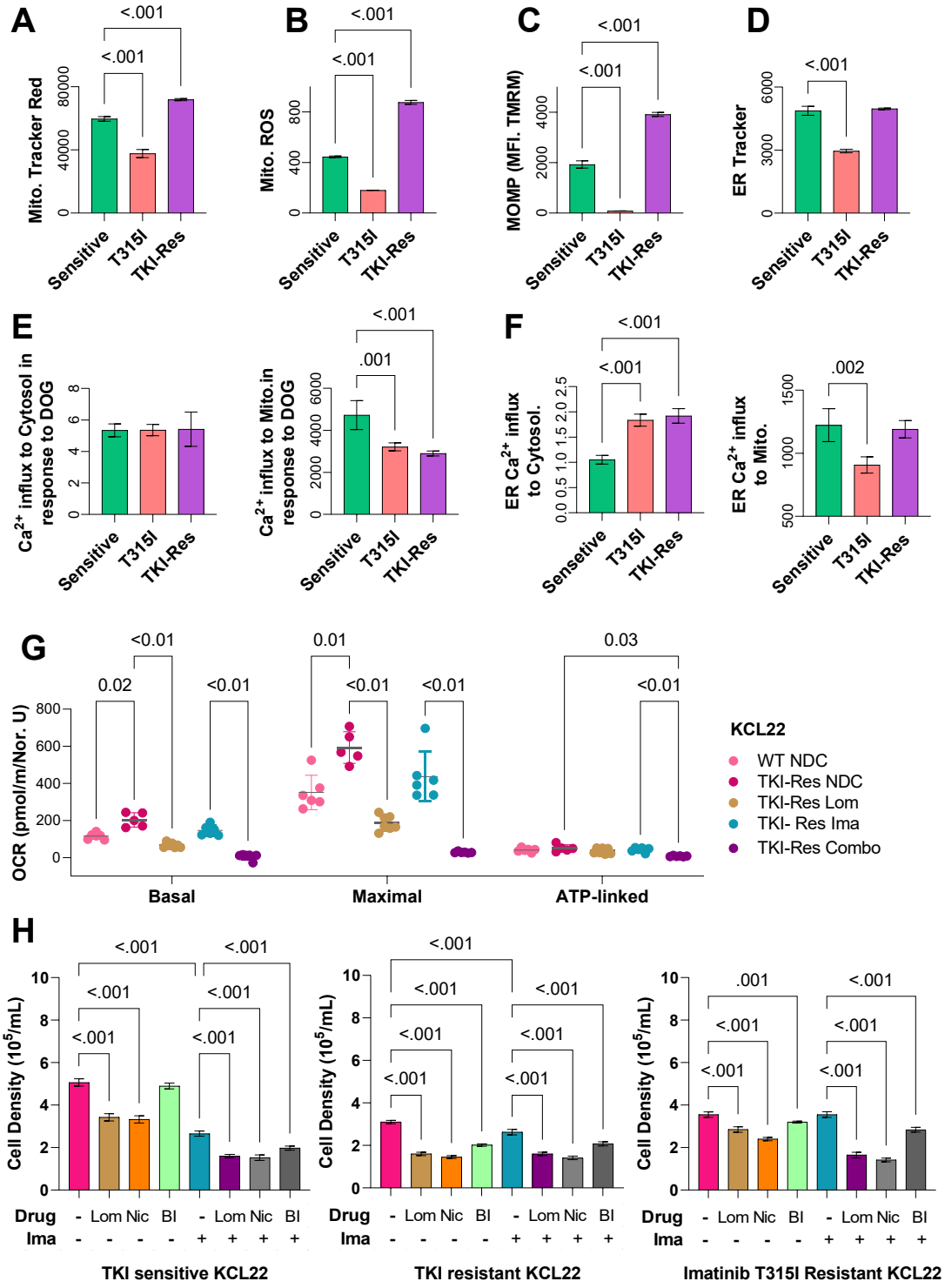

Figure 4-24: Mitochondria and ER mass in T315I and Pon-Res KCL22 cells.

(A-F) Flow cytometry analyses in sensitive and resistant cell lines after exposure to 1 µM imatinib for 24 hours. (G) OCR of PonRes KCL22 cells after 24 hours of treatment with 1 µM imatinib, 10 µM lomerizine or their combination. (H) Cell count of sensitive and resistant cell line after 72 hours of exposure to 10 µM lomerizine, 10 µM nicardipine, 5 µM BI, in combination with or without 1 µM imatinib. Statistical analysis was performed with one-way ANOVA (A-F and H) and two-way ANOVA for (H). Tukey was performed to correct for multiple comparisons.

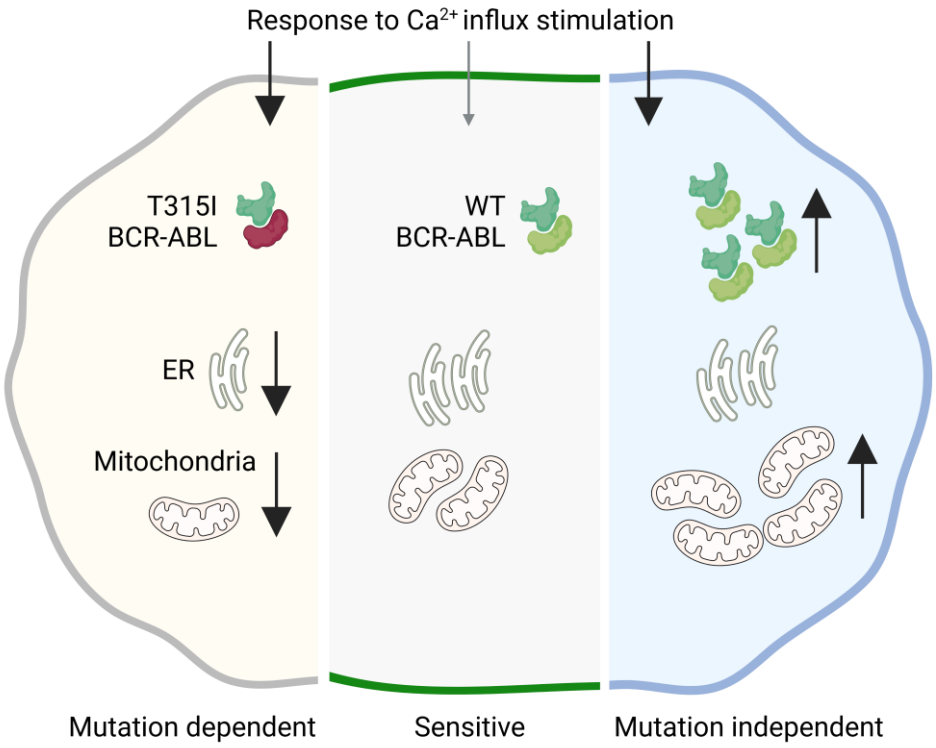

Figure 4-25: T315I and Pon-Res KCL22 cells mitochondrial and ER mass.

The reason behind dissimilarities in imatinib resistant cells is not known yet and this requires further investigation. Possible enhanced BCR::ABL expression in Pon-Res cells could drive changes on transcriptional level, such as mitobiogenesis. In contrast, T315I KCL22 cells have lower mitochondrial activity and mass because of possible ability of those cells to adapt after long-term culture in imatinib through initiating T315I mutation and adopting other signalling and metabolic pathways enabling them to skip imatinib effect on their survival. However, this assumption is still speculative and requires through investigation.

4.7 Conclusion

In this chapter, authors introduced the Ca^{2+} channel blocker lomerizine, a hit from a previous drug repurposing screen aimed at identifying OXPHOS inhibitor candidates that might be better tolerated in the clinic. The mechanism of action of lomerizine is likely to modulate TRPC6 activity, as well as CACNA1D mediated Ca^{2+} influx to either ER or mitochondria. Lomerizine also significantly reduced IDH activity and expectedly to impact other Ca^{2+} dependent dehydrogenases.

Further, BCR::ABL mutation independent therapy resistance CML cells, as seen in Pon-Res KCL22 cells, exhibited increased mitochondrial levels and mitochondrial respiration compared to imatinib sensitive KCL22 cells, suggesting metabolic vulnerabilities of these populations. However, there was different dependency on mitochondrial respiration in BCR::ABL mutation dependent cells, as seen in T315I KCL22 cells. Despite metabolic differences, resistant KCL22 cells of non-mutational and mutational therapy resistance did not show any differences in their sensitivity to Ca^{2+} influx to cytosol. Thus, cell proliferation was halted when those KCL22 cells were exposed to Ca^{2+} inhibitors.

The impact of targeting OXPHOS with IACS-010759 as complex I inhibitor enhanced CML cell lines growth reduction and induced more apoptosis. In addition, IACS-010759 significantly inhibited OCR, a measure that reflects mitochondrial respiration. Thus, combining IACS-010759 with imatinib potentiated apoptosis level and blocked almost any residual mitochondrial respiration. These findings are consistent with previous findings that targeting OXPHOS eradicated most therapy resistant LSCs that rely on OXPHOS for survival [184]. However, as it has been shown, IACS-010759 has a narrow therapeutic margin because it causes rewiring of cancer cells' metabolic phenotype towards glycolysis, which leads to undesirable acidosis found in reported clinical trial [248]. Despite some clinical trials showing that IACS-010759 did not cause acidosis [249], it is still considered an excluding criterion of individuals with initial high lactate levels from clinical trials. Here, IACS-010759 induced glycolysis in CML cell lines and enhanced accumulation of lactate. Lomerizine, in contrary, showed a potent effect on inhibiting mitochondrial respiration in CML cell lines at 60 minutes of treatment without impacting the basal glycolysis nor inducing lactate secretion.

5 Lomerizine targets CML LSCs *in vitro* and *in vivo*

5.1 Introduction

Our previous findings showed that lomerizine significantly reduced cytosolic, ER, and mitochondrial Ca^{2+} levels. Lomerizine treatment also inhibited mitochondrial OXPHOS in CML cell lines. It is assumed that lomerizine targets both TRPC6 and CACNA1D. This is consistent with previous findings that lomerizine allosterically engages to different sites on 1,4 dihydropyridine binding site [250]. However, it is not known how lomerizine inhibits TRPC6 mediated Ca^{2+} influx. The impact of those channels on CML cell lines viability has been shown, confirming similar findings as seen with lomerizine treatment.

Next, the study aims to investigate the impact of lomerizine on CD34+ CML metabolism. The study also aims to measure impact of lomerizine on level of tumour burden *in vivo* using KCL22 xenograft model. Finally, the study aims to address the impact of lomerizine on level of engraftment of stem cells *in vivo* in a PDX model.

5.2 Lomerizine inhibits CD34+ CML OXPHOS *in vitro*

To measure the impact of lomerizine on CD34+ CML mitochondrial OXPHOS, CD34+ CML cells were cultured in SFM supplemented with growth factors. Moreover, cells were exposed to lomerizine, imatinib, or a combination of both for 24 hours, followed by measuring their OCR respirometry (Figure 5-1A). This experiment included 100 nM IACS-010759 as an OXPHOS inhibitor control (Figure 5-1A).

Results show that, in line with what author found with cell lines, lomerizine or IACS-010759 significantly reduce OCR compared to untreated cells. Lomerizine and IACS-010759 significantly reduce the OCR of imatinib treated cells compared to imatinib alone. These findings confirm global effect of lomerizine as an OXPHOS inhibitor in CD34+ CML cells.

5.2.1 Lomerizine reduces Ca^{2+} influx in CD34+ CML cells

Next, the study investigated if lomerizine alters Ca^{2+} levels in CD34+ CML cells. To deliver this approach, CD34+ CML cells were cultured in SFM supplemented with growth factors and exposed to lomerizine, imatinib or a combination for 24 hours. Ca^{2+} levels were detected by staining cells with Ca^{2+} indicators and quantified by flow cytometry. Cells were stimulated with ionomycin during flow cytometry data acquisition.

Consistent with cell lines findings, imatinib does not alter cytosolic Ca^{2+} response to ionomycin but significantly reduces mitochondrial Ca^{2+} level (Figure 5-2). Lomerizine significantly reduces both cytosolic and mitochondrial Ca^{2+} influx compared to untreated cells. Lomerizine also significantly reduces cytosolic and mitochondrial Ca^{2+} levels compared to cells treated with imatinib as a single agent.

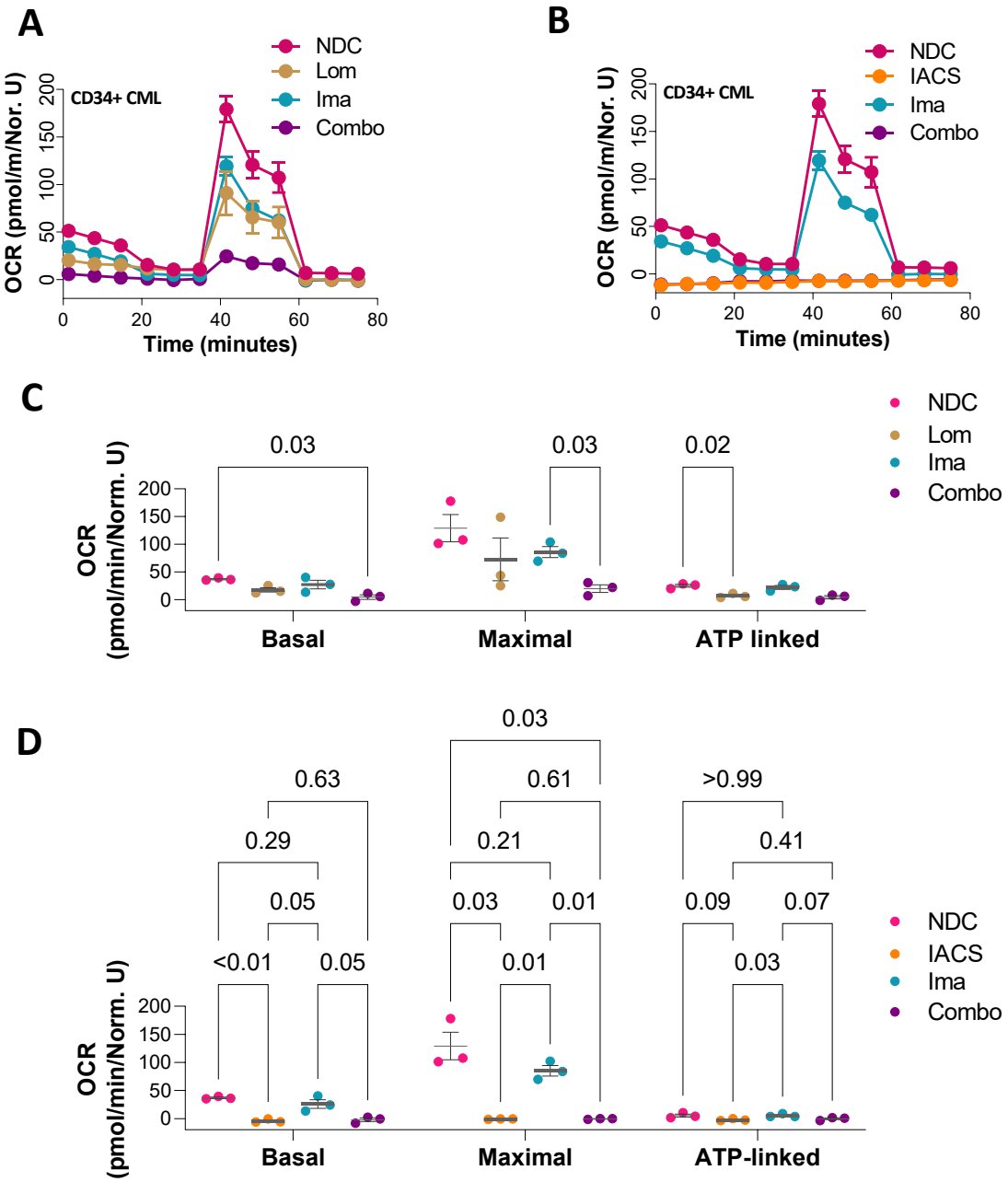

Figure 5-1: Lomerizine inhibits respiration in CD34+ CML cells.

(A, B) Respirometry profile of CD34+ CML cells treated with 5 μM lomerizine or 20 IACS-010759, 1 μM imatinib, or their combination for 24 hours, n=3 CML biological patient samples. (C, D) Statistical analysis of A and B. Statistical analysis was performed with two-way ANOVA and Tukey was performed to correct for multiple comparisons.

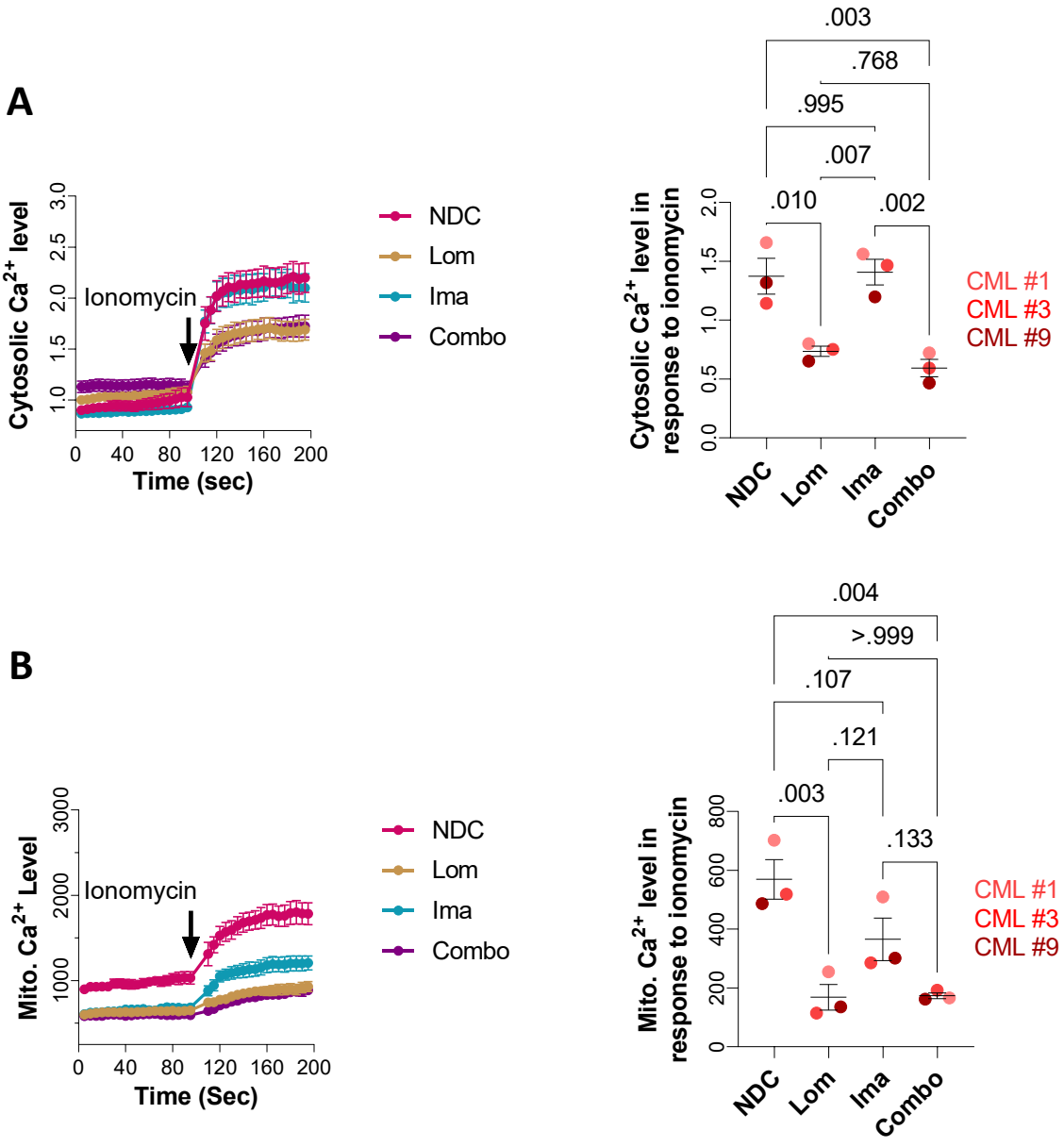

Figure 5-2: Lomerizine inhibits Ca^{2+} influx in CD34+ CML cells *in vitro.*

(A) Representative kinetic flow cytometry analysis of cytosolic Ca^{2+} level in CD34+ CML cells treated for 24 hours. Cells were stimulated with 2.5 µM ionomycin instantly during acquiring flow cytometry data. (B) Representative mitochondrial Ca^{2+} level of same cells. Statistical analyses were performed using one-way ANOVA, and error bars were shown as SEM, where n=3 biological patient samples. Multiple comparisons were performed using Tukey test.

5.3 Lomerizine targets patient derived CML cells *in vitro*

Next, the study investigated the effect of lomerizine on CD34+ CML cell expansion, apoptosis, and level of residual stem cells. CD34+ CML cells were cultured in SFM supplemented with physiological growth and exposed to lomerizine, imatinib, or their combination for 72 hours. Endpoint cell density was measured, followed by performing an apoptosis assay and stem cell quantification assay by measuring expression level of stem cell markers on live cells (APC-CD34 and PE-CD38) by flow cytometry.

Lomerizine shows non-significant trend reduction in cell proliferation compared to untreated cells (Figure 5-3 A&B). It does not alter level of apoptosis when compared to untreated cells. Also, lomerizine does not alter level of LSCs when compared to untreated cells (Figure 5-3C). However, combination of lomerizine and imatinib significantly reduces cell expansion, increases apoptosis, and significantly reduces LSC population enrichment compared to untreated or single-treated CD34+ CML cells (Figure 5-3 A-C). These findings show the ability of lomerizine to target CML CD34+ proliferation when combined with imatinib by increasing apoptosis and inducing exhaustion of the stem cell pool.

To further substantiate the impact of combination on progenitor and stem cell pool exhaustion, CFC and LTC-IC were performed. CD34+ CML cells were treated with lomerizine, imatinib, or a combination of both for 72 hours in SFM supplemented with growth factors. Results show that lomerizine significantly reduces CFC colony counts compared to untreated CD34+ CML cells (Figure 5-3 D&F). Furthermore, combination of lomerizine with imatinib significantly reduces CFC count compared to imatinib only treated CD34+ CML cells (Figure 5-3 D&F). These findings confirm ability of lomerizine to halt short- and long-term potential of progenitor and stem cell population, which reflects beneficial additive effect of lomerizine with imatinib to sensitise therapy resistant stem cells to TKI treatment.

The same functional assays (cell density, apoptosis, stem cell enrichment by flow cytometry, CFC and LTC-IC) were performed by treating CD34+ CML with IACS-010759 instead of lomerizine (Figure 5-4). IACS-010759 shows non-significant

impact CD34+ CML proliferation. IACS-010759 significantly reduces stem cell pool enrichment similarly to lomerizine, confirming critical role of OXPHOS in CML stem cell proliferation and exploiting OXPHOS as a vulnerability to enhance eradication by imatinib.

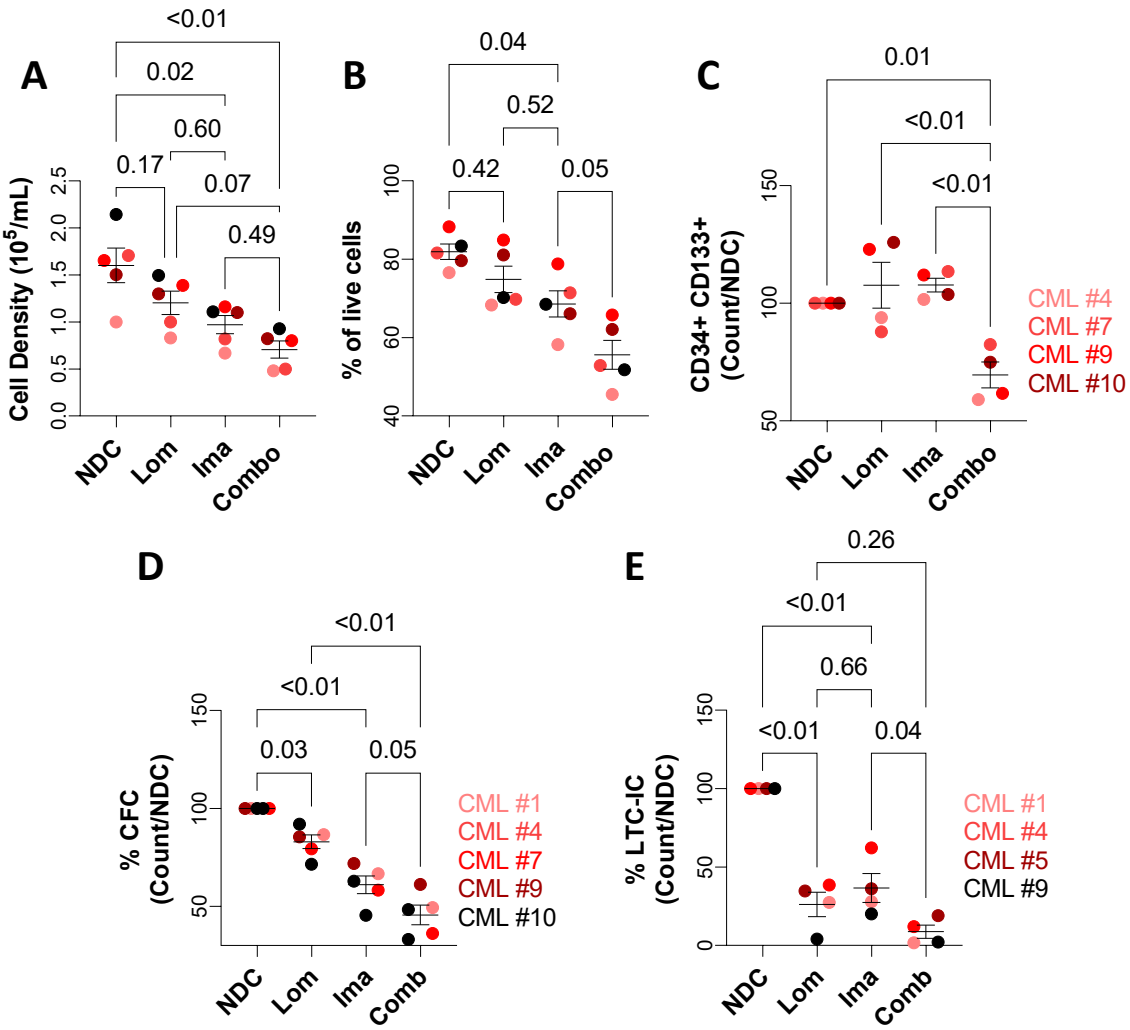

Figure 5-3: Lomerizine targets LSC viability and clonal expansion *in vitro*.

(A) Cell count of CD34+ CML treated with lomerizine, imatinib or their combination for 72 hours (n=5). (B) Live cells assay was measured by staining cells with 7-AAD, and Annexin V in CD34+ CML treated for 72 hours with 5 μM lomerizine, 0.6 μM imatinib, or their combination (n=5 CML patients' samples). (C) Level of stem cell (CD34+ and CD133+) enrichment in live events of CD34+ CML treated for 3 days followed by labelling with APC-CD34 and PE-CD133 surface markers antibodies and measuring their levels using flow cytometry. Results were normalised to cell density to get absolute values (n=4 CML patients' samples). (D) Colony-forming images and representative statistical analysis in CD34+ CML cells after culturing same cell numbers in semi-solid Methocult for another 14 days (n=3 CML patients' samples). (E) Level of long-term colony-initiating capacity (LT-IC) after culturing cells in MyeloCult for another 4 weeks, followed by culturing them in Methocult semi-solid medium (n=4 CML patients' samples). Statistical analysis was performed with one-way ANOVA and Tukey was performed to correct for multiple comparisons.

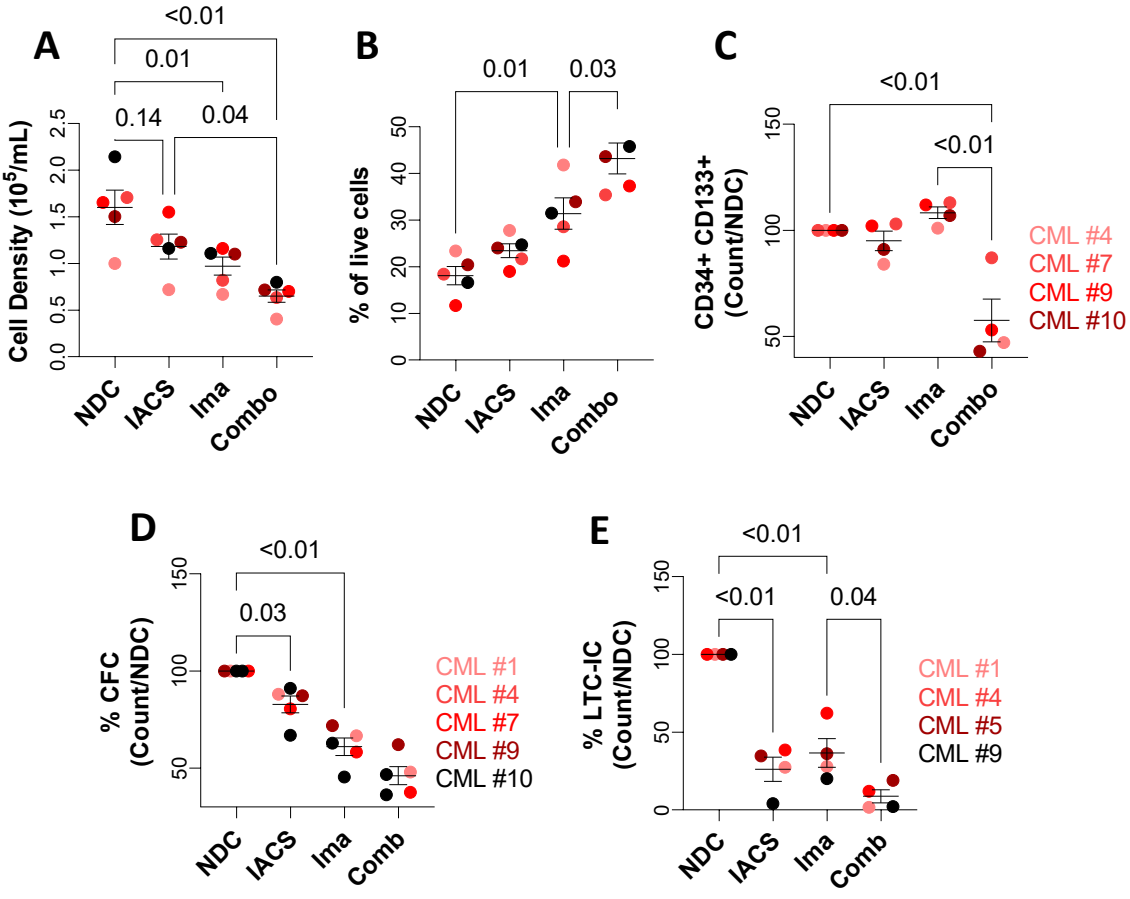

Figure 5-4: IACS-010759 targets LSC viability and clonal expansion.

(A) Cell count of CD34+ CML treated with 100 nM IACS-010759, 1 μM imatinib or their combination for 72 hours (n=5 CML patients' samples). (B) Live cells assay was measured by staining cells with 7-AAD, and Annexin V in CD34+ CML treated for 72 hours (n=5 patients' samples). (C) Level of stem cell (CD34+ and CD133+) enrichment in live events of CD34+ CML treated for 72 hours followed by labelling with APC-CD34 and PE-CD133 surface markers antibodies and measuring their levels using flow cytometry. Results were normalised to cell density to get absolute values (n=4 CML patients' samples). (D) Colony-forming images and representative statistical analysis in CD34+ CML cells after culturing same cell numbers in semi-solid Methocult for another 14 days (n=3 CML patients' samples). (E) Level of long-term colony-initiating capacity (LT-IC) after culturing cells in MyeloCult for another 4 weeks, followed by culturing them in Methocult semi-solid medium (n=4 CML patients' samples).

5.3.1 Lomerizine exhausts early primitive CD34+ CML cells.

To measure the dividing potential of CD34+ CML cells following lomerizine treatment, CD34+ CML cells were stained with cell trace violet (CTV) that get distributed between dividing daughter cells which can be traced by flow cytometry. Following cultured cells in SFM supplemented with physiological growth factors and exposure to lomerizine, imatinib, or a combination of both for 72 hours, CTV staining was fluorescently measured by flow cytometry. Cells were co-stained cells with APC-CD34 expression marker antibody at day 0 and day 3, followed by assessment by flow cytometry.

Cell staining with CTV and APC-CD34 antibody reveals that CD34+ CML cells proliferate in culture and expand towards CD34- population without losing CD34+ population during cell division within 72 hours (Figure 5-5).

In addition, imatinib does not alter overall CD34+ CML cell division as measured by comparable CTV of the undivided population (D0) compared to untreated CML cells (Figure 5-5). Also, imatinib does not reduce the CD34+ CML cells in (D3), indicating persistence of CD34+ enriched CML cells despite imatinib treatment, possibly LSCs. Lomerizine, as a single treatment or when combined with imatinib, dramatically reduces absolute cell numbers in every cell division, including undivided cells (D0). Also, lomerizine was able to eradicate persistent CD34+ CML in (D3) alone or as combined with imatinib compared to untreated or imatinib alone. This finding reflects the effect of lomerizine on targeting CML stem cell division possibly through reducing stem cells' pool size *in vitro*.

Of note, CD34+ CML cells can differentiate from being CMP into succeeding progenitors, GMP or MEP. The MEP population is responsible for enrichment of blood with mature erythrocytes. Erythrocyte numbers are significantly lower in CML patients due to primitive CMP differentiation into RBCs blockage, which causes anaemia in CML patients.

To investigate if lomerizine induces differentiation, CD34+ CML were exposed to lomerizine, imatinib, or their combination in SFM supplemented with physiological growth factors for 5 days. Following this, cells were stained with erythrocytic

maturation markers PE-CD71 and PerCP-GlyA surface marker expression antibodies, followed by flow cytometry analysis.

The results show that lomerizine alone or when combined with imatinib, induces erythrocyte maturation. However, imatinib alone does not induce this maturation compared to untreated cells (Figure 5-6).

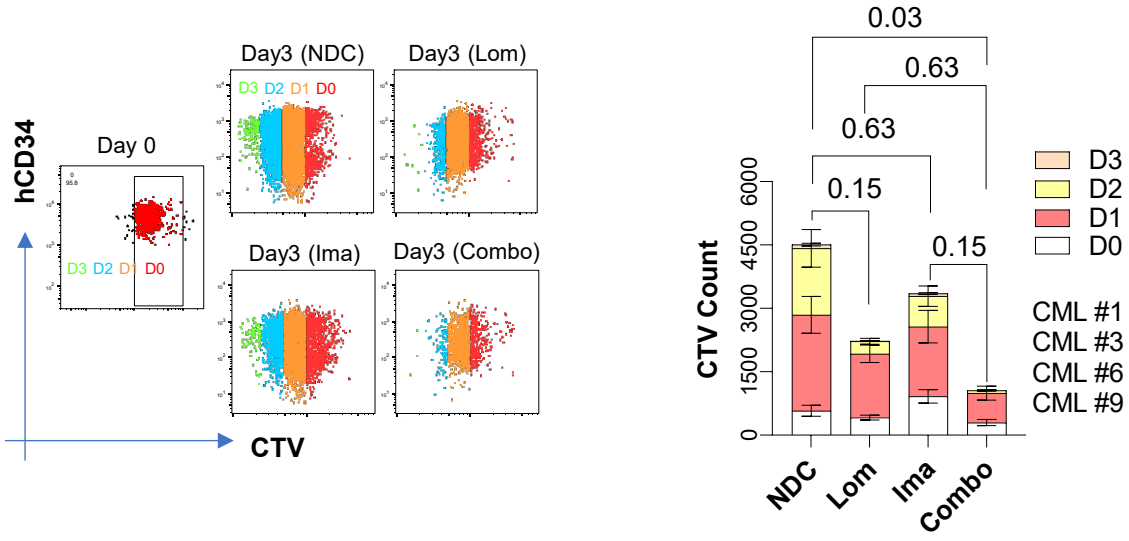

Figure 5-5: Lomerizine reduces undivided and dividing CD34+ CML cells.

Representative flow cytometry plot outlining CTV gating of CML CD34+ cells treated for 72hr. CTV tracked proliferation of CD34+ cells where input represents number of cells inside every gate (D0-D3), D0 represents undivided cells, and D1-D3 is number of divisions measured as dilution of fluorescence intensity of CTV dye. Data representative of mean ± SE, n=3 individual patient samples. P-values were calculated with a paired one-way ANOVA using Tukey test.

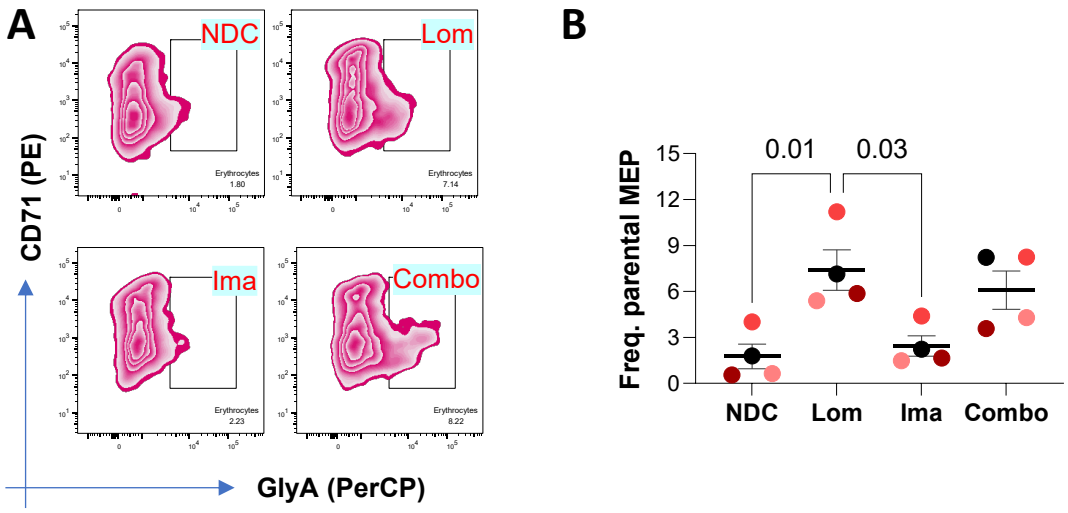

Figure 5-6: Lomerizine enhances CD34+ CML erythroblast differentiation.

(A) Representative flow cytometry plot illustrates GlyA and CD71 expression in CD34+ CML exposed to treatment for 72 hours. (B) Bar graph illustrates representative frequencies of CD71+GlyA+ population in CD34+ CML exposed to treatment for 72 hours. Data were plotted as mean+/-SEM. Of n=3 different individuals' CML samples, P. values were calculated using paired one-way ANOVA test with Tukey test.

5.3.2 Lomerizine targets LSCs after 6 days of treatment

Due to lack of lomerizine effect on LSC pool size after 3 days, the study aimed to address if we could verify the impact of lomerizine on LSC pool size at longer treatment time point. author measured percentage of stem cells (CD34 and CD38 expression level with flow cytometry) in CD34+ CML cultured in SFM with physiological growth factors and exposed to lomerizine, imatinib and their combination for 6 days. Lomerizine does not alter the fraction of CD34+ CML population (Figure 5-7 A&C). However, the fraction of CD34+CD38- expressing population becomes significantly lower following lomerizine treatment (Figure 5-7 B&D).

Imatinib by itself decreases CD34+ percentage. Despite this, imatinib does not alter the level of CD34+CD38- cells compared to untreated CML cells (Figure 5-7 B&D). Findings indicate that imatinib targets more differentiating progenitor-like CML and lomerizine targets more stem-like CML cells *in vitro*. Thus, lomerizine and imatinib combination significantly induces more apoptosis and significantly decreases the CD34+ population and percentage of CD34+CD38- cells.

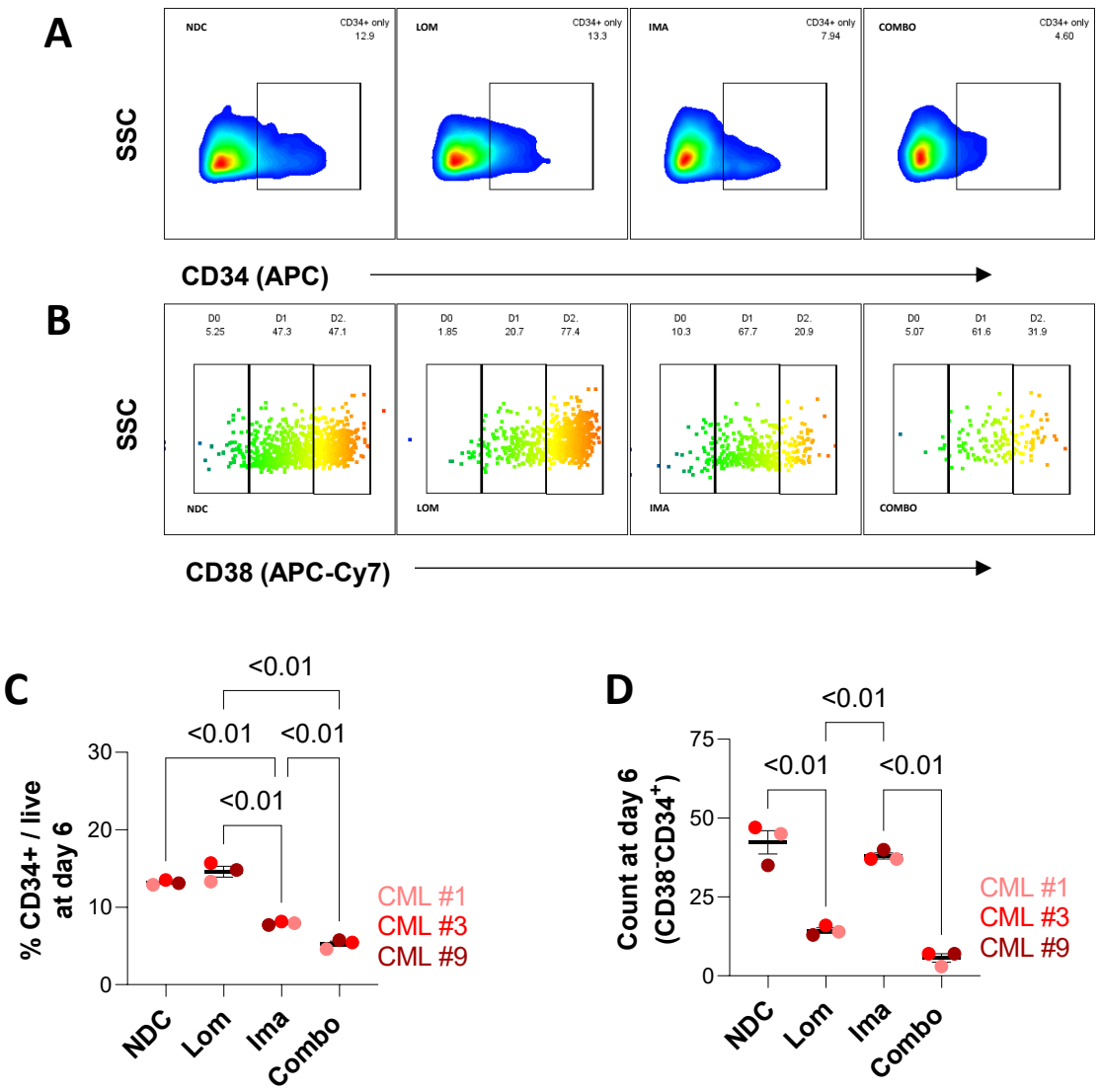

Figure 5-7: Lomerizine reduces primitive CD34+CD38- cells at day 6 *in vitro*.

(A) Flow cytometry plot illustrates APC CD34 expression level and gating strategy of CD34+ populations in CD34+ CML exposed to treatments for 6 days. (B) Flow cytometry plot of CD34+ from (A) illustrates APC-Cy7 CD38 expression level and gating strategy of CD38- (labelled as green) population in CD34+ CML exposed to treatments for 6 days. (C) Bar plot illustrates level of CD34+ in CD34+ CML following 6 days of treatments. (D) Bar plot illustrates level of CD34+CD38- in CD34+ CML following 6 days of treatment. Data from (C, D) were plotted as mean+/- SEM, where P. value was calculated with a one-way ANOVA test; Tukey test for multiple comparisons, n=3 patient samples.

5.4 Lomerizine does not impact CD34+ normal cells *in vitro*

The fact that LSCs upregulate *TRPC6* and *CACNA1D* when compared to HSCs, suggests lomerizine is an ideal candidate to inhibit CML proliferation and block stem cell survival. It is assumed that CML cells require higher Ca^{2+} ion levels compared to normal counterparts.

To investigate this further, CD34+ cells collected from non-CML individuals (further referred to as normal) were cultured in SFM with growth factors and exposed to lomerizine, imatinib or their combination for 72 hours followed by a cell density assay, a viability assay using 7-AAD staining, stem cell enrichment analysis (CD34 and CD133 expression level assay by flow cytometry), and a CFC assay (Figure 5-8).

In normal CD34+ cells, neither lomerizine, imatinib, nor combination alters expansion, apoptosis, stem cell enrichment or CFC clonal expansion (Figure 5-9). Author used omacetaxine, transcriptional protein inhibitor, as a control. Similarly, targeting normal CD34+ cells with IACS-010759 reveals identical findings to lomerizine. This suggests that targeting OXPHOS is selectively detrimental to LSCs without any obvious effect on their normal counterparts.

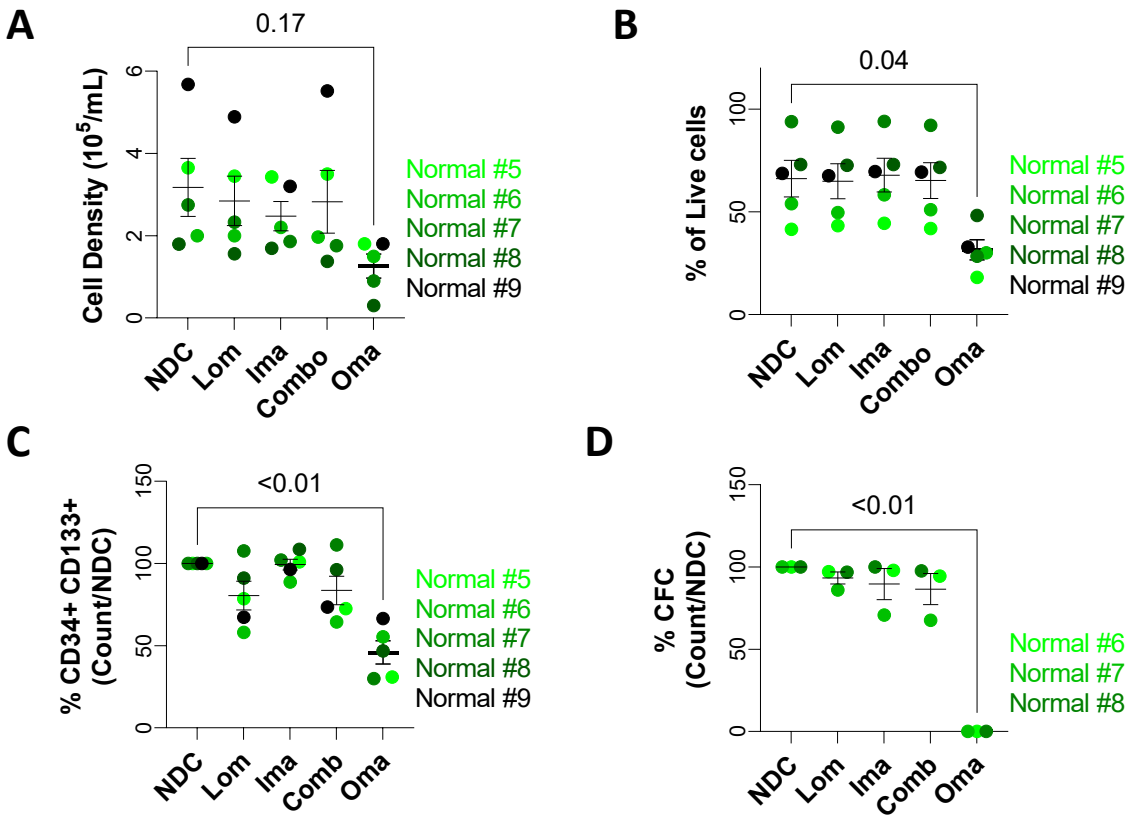

Figure 5-8: Lomerizine does not alter proliferation of normal CD34+ cells.

(A) Bar plot illustrates cell density in CD34+ non-CML following 3 days of treatment with 5 µM lomerizine, 0.6 µM imatinib, or their combination, n=5 individual human samples. Bar plot illustrates live events in Cd34+ non-CML following 3 days of treatment, stained with 7-AAD, and measured viable events (7-AAD- population), n=5 individual samples. (B) Level of stem cell (CD34+ and CD133+) enrichment in live events of CD34+ non-CML treated for 3 days followed by labelling with APC-CD34 and PE-CD133 surface markers antibodies and measuring their levels using flow cytometry. Results were normalised to cell density to get absolute values (n=4 individual human samples). (C) Colony-forming images and representative statistical analysis in CD34+ non-CML cells after culturing same cell numbers in semi-solid Methocult for another 14 days (n=3 individual human samples). All data were plotted as mean +/- SEM. The P. value was calculated using a one-way ANOVA test, and Tukey test was used for multiple comparisons.

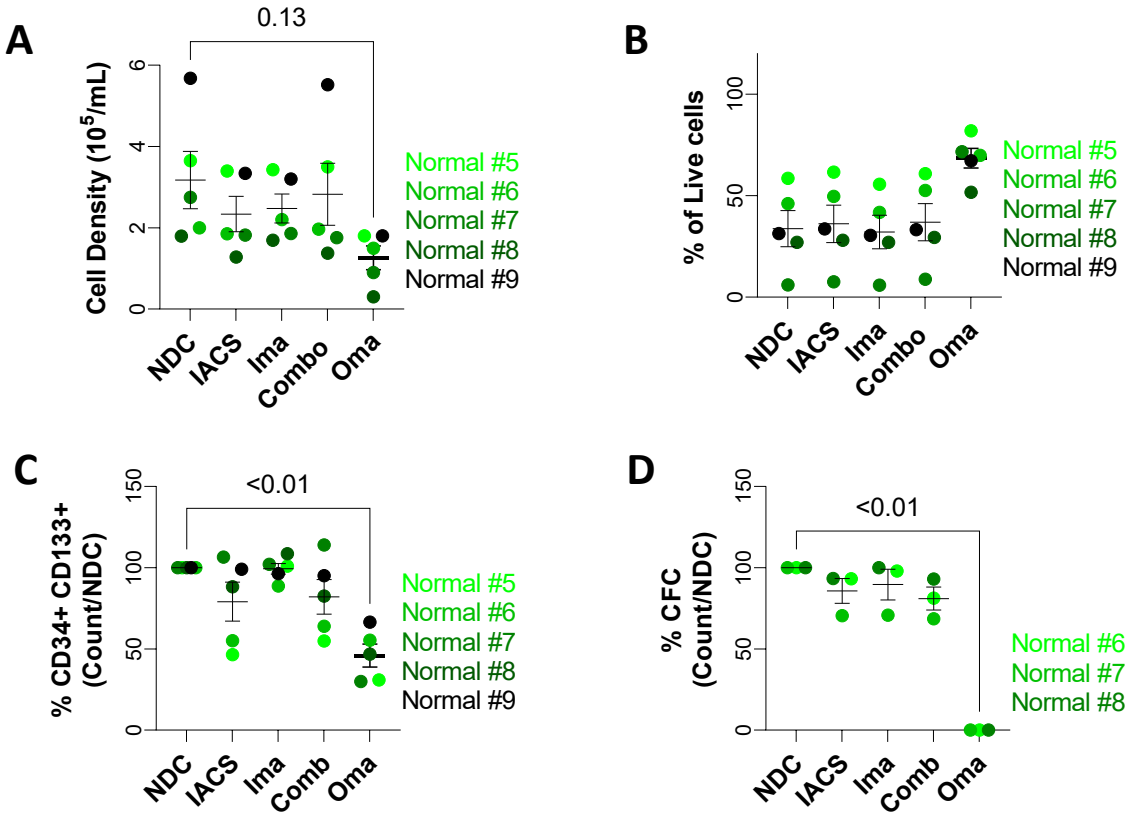

Figure 5-9: IACS-010759 does not alter proliferation of CD34+ normal cells.

(A) Bar plot illustrates cell density in CD34+ non-CML following 3 days of treatment with 100 nM IACS-010759, 0.6 μM imatinib, or their combination, n=5 individual samples. (B) Bar plot illustrates live events in CD34+ non-CML following 3 days of treatment, stained with 7-AAD, and measured viable events (7-AAD- population), n=5 individual samples. (C) Level of stem cell (CD34+ and CD133+) enrichment in live events of CD34+ non-CML treated for 3 days followed by labelling with APC-CD34 and PE-CD133 surface markers antibodies and measuring their levels using flow cytometry. Results were normalised to cell density to get absolute values (n=4). (D) Colony-forming images and representative statistical analysis in CD34+ non-CML cells after culturing same cell numbers in semi-solid Methocult for another 14 days (n=3). All data were plotted as mean +/- SEM. Where P. value was calculated using a one-way ANOVA test and Tukey test was used for multiple comparisons.

5.5 Lomerizine reduces KCL22 tumour burden *in vivo*

Leading on from promising *in vitro* results with lomerizine, author continued investigating the effect of lomerizine in an *in vivo* mouse model. Prior to main experiment, a dose escalation was established using NOD.Cg-*Rag1*^{tm1Mom} *Kit*$^{W-41J}$ *Il2rg*^{tm1Wjl}/EavJ (NRGW41) mice strain. This mouse strain was developed to support haematopoietic cells engraftment with or without irradiation. Lomerizine injections were prepared to be administered intraperitoneally once daily at increasing weekly doses; 10, 20, 40, and 80 mg/kg (4 dose strengths at 4 weeks total). Mice weights were recorded 3 times weekly, and a health scoring system was established to monitor health status of mice receiving lomerizine and control mice. The drug dose escalation study shows that mice tolerate lomerizine well at a maximum dose of 80 mg/kg without significant impact on mice's weight or health status (Figure 5-10A).

Of note, 30-40 µL of tail vein blood was collected at end of every weekly dose (one hour after dose administration). Blood was also collected 5 and 24 hours after last dosing at end of 4th week. All blood serum samples were lysed, and lomerizine concentration was analysed by LCMS and compared to a concentration standard of lomerizine (Figure 5-10B).
Findings show that serum from last dose regimen at 80 mg/kg results in a blood concentration of nearly 2 µM lomerizine, which is enough to inhibit functional processes in CML cell lines *in vitro*. Author decided to use an 80 mg/kg lomerizine dose for our next *in vivo* experiment.

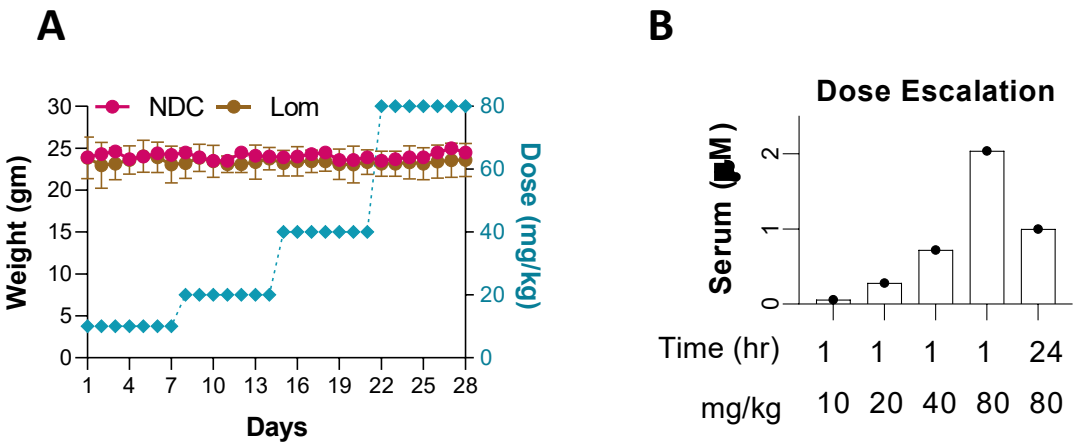

Figure 5-10: Lomerizine shows tolerability at 80 mg/kg in NRGW41 mice.

(A) Line graph showing dose escalation of lomerizine from 10 mg/kg following doubling of dose every week till 80 mg/kg was reached. Mice weights were recorded and plotted during experiment; n=1 vehicle mouse and 2 mice were treated with lomerizine. (B) Bar graph illustrates level of lomerizine detected by LCMS and corrected according to standard samples. Samples were prepared following serum collection via tail bleeding after an hour of drug administration on last day of every dose regimen. Last day of treatment (80 mg/kg), serum samples were collected after 1 hour, 5 hours, and 24 hours of drug administration.

The Helgason lab previously generated firefly luciferase expressing KCL22 that enables live imaging of these cells *in vivo* by injecting luciferin into mouse.
To test the impact of lomerizine on CML transplantation *in vivo*, NRGW41 female mice were transplanted with 4 million KCL22 luciferase cells and imaged them weekly using IVIS (Figure 5-11A). Two weeks after transplantation, mice received vehicle, 80 mg/kg lomerizine I.P. once daily (+water oral gavage), 50 mg/kg imatinib by oral gavage twice daily (+2.5% DMSO + 5% tween80 + 85% saline I.P.), or a combination of lomerizine and imatinib treatment for 4 weeks.

Mice were maintained to assess the impact of treatment on survival. Mice were culled on reaching a humane endpoint, where a visible or measurable tumour growth approached but did not yet exceed 1.3 cm. After sacrificing, tumours were collected. Imaging results showed that lomerizine, but not imatinib, reduced luciferase signal as detected by IVIS after week 3 of treatment (Figure 5-11B).

Mice were culled throughout survival analysis due to severity limits being reached, followed by measuring tumour burden by inspecting collected tumours per mouse and counting them.
Results reveal that lomerizine significantly reduces tumour burden by reducing the number of tumours per mouse compared to vehicle mice (Figure 5-11C). The combination of lomerizine and imatinib further significantly reduces the number of tumours compared to untreated and imatinib only treated mice. Findings illustrate the ability of lomerizine to inhibit KCL22 expansion *in vivo*.

The lomerizine and imatinib combination also significantly extends survival of mice compared to imatinib alone or untreated mice (P.= 0.007, Log-rank Mantel-Cox) (Figure 5-11D). Despite the trend increase in lomerizine treated mice compared to untreated mice, the overall survival of lomerizine treated mice (median survival= 65) is not significantly altered compared to untreated mice (median survival= 42), indicating necessity of combining imatinib with lomerizine to maximise therapeutic impact *in vivo* (median survival= 114).

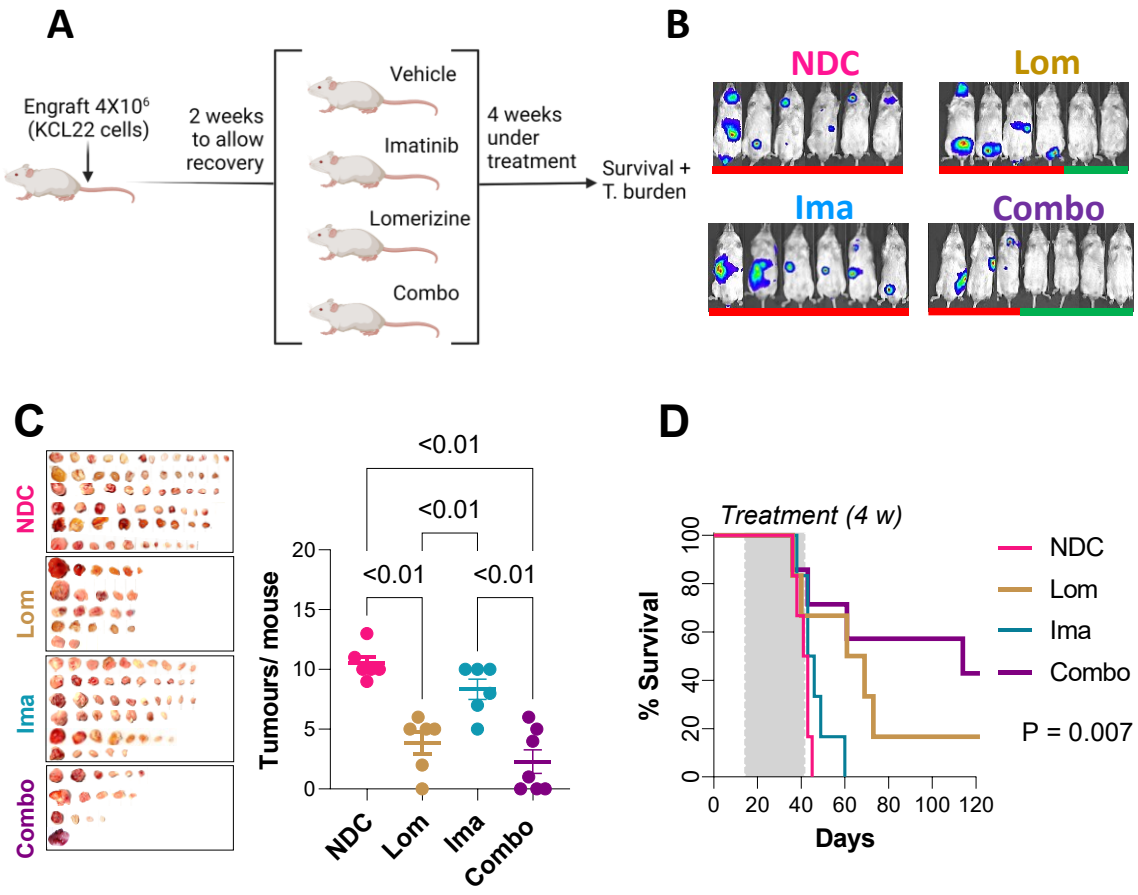

Figure 5-11: Lomerizine reduces KCL22 tumorigenesis *in vivo*.

(A) Diagram summaries of experimental timeline. NRGW41 mice were transplanted with luciferase+ KCL22 cells. Images of IVIS at weeks 5 following transplantation of luciferase expressing KCL22 cells. (B) Images and numbers of extramedullary tumours harvested from each mouse simultaneously parallel to survival studies. (C) The number of tumours harvested at different time points for indicated treated mice. Statistical analysis was performed with one-way ANOVA and Tukey was performed to correct for multiple comparisons. (D) Flow cytometry illustrates that dissected tumours are of human nature (huCD45+). Overall survival was monitored by Kaplan-Meier analysis. P-values were calculated using log-rank (Mantel-Cox) test, referring to lomerizine + imatinib versus vehicle mice.

5.6 Lomerizine reduces patient derived LSC BM engraftment

After demonstrating that treatment with lomerizine *in vivo* affects tumour burden of KCL22 cells, it was next hypothesised that lomerizine could target human CML LSCs *in vivo*. To investigate this, CD34+ CML cells were transplanted into sub-lethally irradiated and immuno-deficient NRGW41 female mice in a PDX study (Figure 5-12A). Eight weeks post-transplant, mice were divided into four treatment arms (vehicle, lomerizine, imatinib, and a combination of lomerizine and imatinib) and treated for another 4 weeks (Figure 5-12B). After 4 weeks of treatment, mice was sacrificed on last day of treatment and dissected to collect bones (tibias, femurs, and hip bones), blood, and spleens.

Those harvested tissues were then processed and analysed by flow cytometry to measure human CD45, human CD34+, and human CD34+CD38- (LSC markers) levels of each mouse (Figure 5-14A).

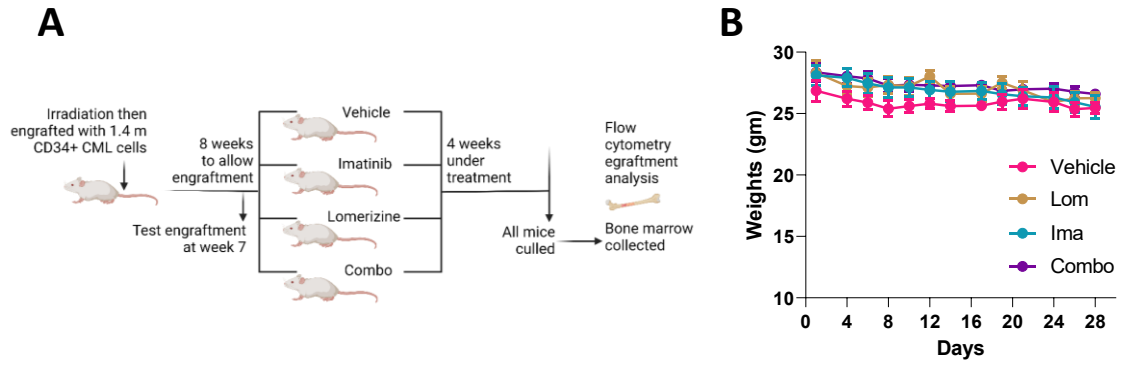

Figure 5-12: PDX strategy in NRGW41 mice model.

(A) Experimental plan of PDX. (B) Mice weights during treatment regimen of 4 weeks.

Engraftment of human cells was confirmed 7 weeks after transplantation by flow cytometry analysis of human leucocyte surface marker (CD45) and human myeloid marker (CD33) in BM (Figure 5-13).

Absolute counts of population were calculated by correcting % of human CD45+, CD34+, and CD34+CD38- from flow cytometry analyses to cell count of BM cell density. The absolute cell counts show that lomerizine and imatinib significantly reduces total count of human CD45, CD34+, and CD34+CD38- in BM compared to vehicle control mice (Figure 5-14 B, Figure 5-15 A-C). In addition, combination of lomerizine and imatinib significantly reduced level of human CD45, CD34+, and CD34+CD38- total counts compared to imatinib treatment. All data so far demonstrates that combining imatinib with lomerizine significantly enhances imatinib's ability to eradicate primitive LSCs.

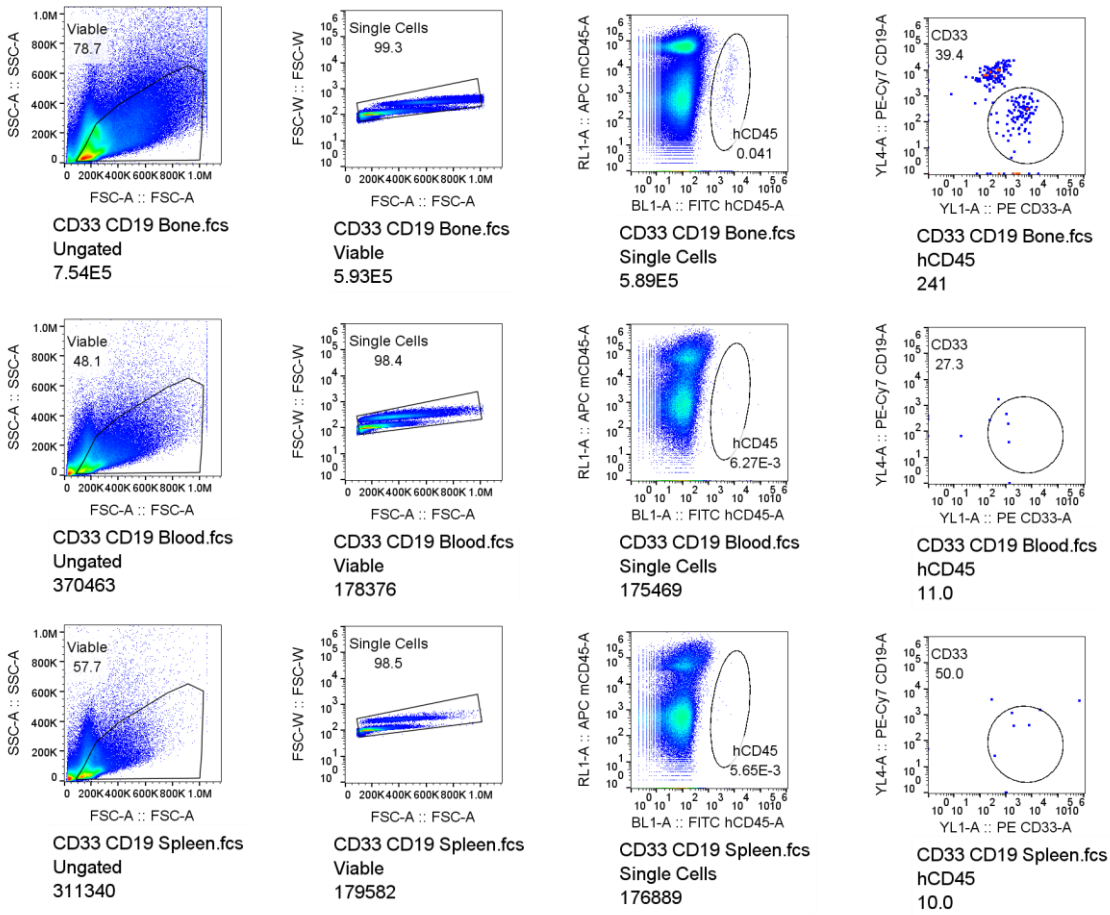

Figure 5-13: Myeloid engraftment in mice BM at week 7.

Flow cytometry profile shows level of CD33 (myeloid marker) and CD19 (lymphoid marker) in blood, spleen, and BM 7 weeks after CD34+ CML transplantation in NRGW41 mice.

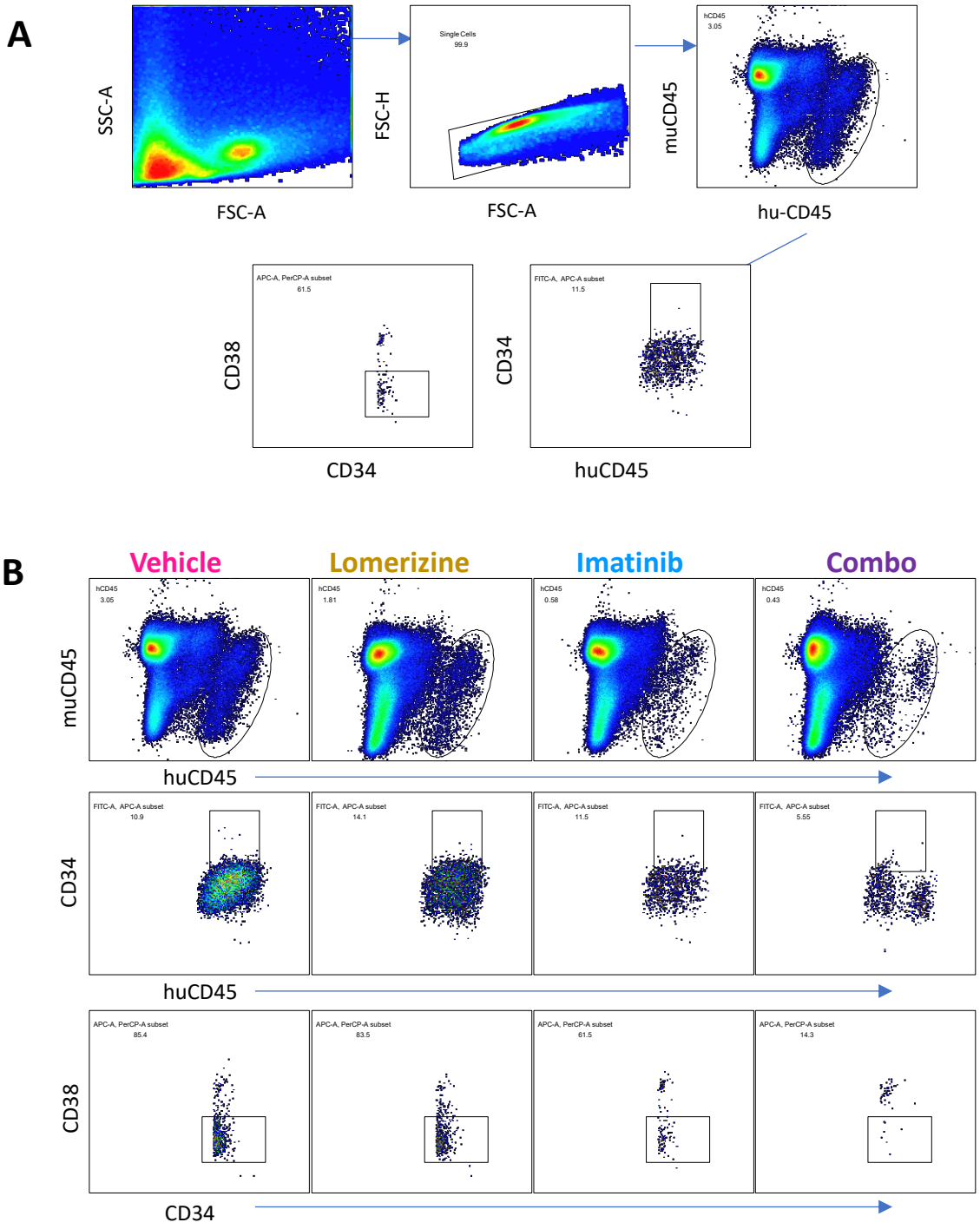

Figure 5-14: Gating strategy for assessment of LSCs in PDX model.

Flow cytometry gating strategy of hu CD45+ CD34+ CD38- population of BM followed by flow cytometry panel illustrates changes in hu CD45, CD34+ and CD34+CD38- expression levels. Samples were isolated from mice treated with vehicle, lomerizine, imatinib or combination.

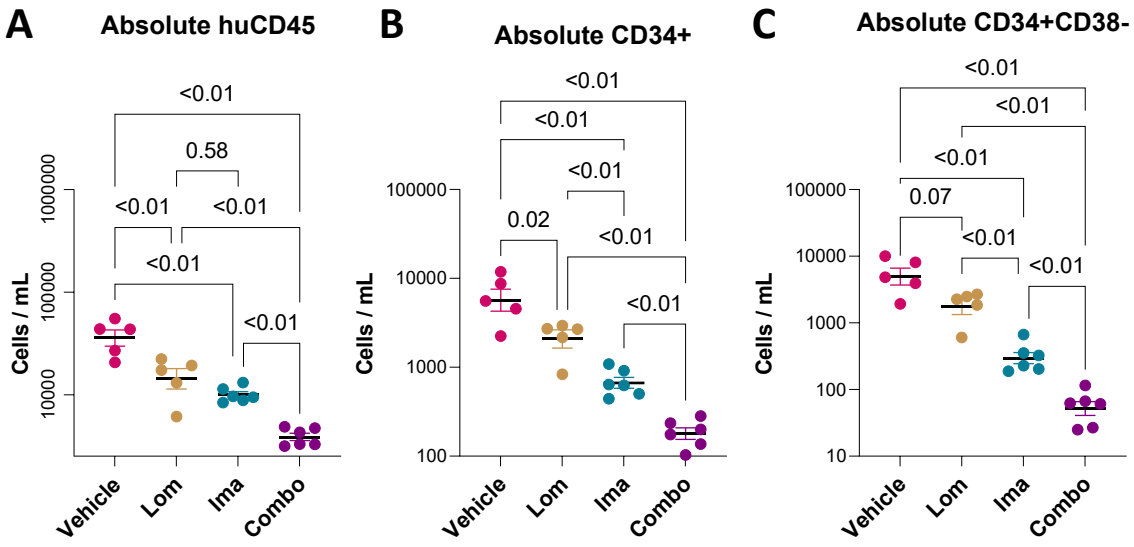

Figure 5-15: Lomerizine reduces patient LSCs in mice BM.

Absolute counts of population expressing (A) hu CD45, (B) CD34+, and (C) CD34+CD38- in mice treated with indicated treatments for 4 weeks. Error bars were shown as SEM+/-mean. One-way ANOVA was performed, and multiple comparisons were corrected with Bonferroni method. Dot blot was shown as log 10 values on Y axis for normal distribution assurance.

5.7 Conclusions

In this chapter, the effect of lomerizine on CML tumour burden *in vivo* was investigated. To achieve this, KCL22 cells were injected into NRGW41 mice strain and treated them with lomerizine, imatinib or their combination. The results from this experiment indicated that lomerizine could reduce CML tumour burden over time and enhance imatinib effect in reducing number of tumours and subsequently enhance survival in mice receiving combination treatment. Author also established another *in vivo* experiment to investigate impact of lomerizine on LSC survival in BM of NRGW41 mice. Similarly, lomerizine combination with imatinib significantly reduced level of CD34+CD38- cells in BM compared to imatinib alone, indicating more effective strategy to eradicate those therapy resistant LSCs from BM. This reflected similar findings *in vitro* when lomerizine reduced short- and long-term potential of LSCs. Lomerizine also increased apoptosis level in CD34+ CML after exposure to combination of lomerizine with imatinib when compared to imatinib as a single therapy. It is assumed that this arises from ability of lomerizine to reduce CD34+ CML mitochondrial Ca^{2+}, which impacts mitochondrial respiration. This does not seem to be same scenario in CD34+ CML cells treated with imatinib which has been shown to impact mitochondrial Ca^{2+} due to reduced mitochondrial mass but not impact Ca^{2+} influx to cytosol and presumably to mitochondria. Besides important role ER plays in Ca^{2+} transfer to mitochondria, ER-Phagy has been proposed as a reason for ER mass reduction in CML cell lines upon imatinib treatment, indicating a novel approach to investigate CML LSCs in the future. Our research showed that lomerizine did not measurably alter behaviour of the normal cell. In normal cells, lomerizine did not induce cell apoptosis and it did not alter cell expansion or short-term stem cell potential *in vitro*. This encouragingly suggests selectivity of lomerizine in targeting LSCs while sparing normal HSCs. Furthermore, the impact of Ca^{2+} influx inducers on CD34+ CML cell expansion, viability, and short-term potential of LSCs was examined. In addition, hyperforin, TRPC6 stimulator induced cell apoptosis, reduced cell expansion, significantly eradicated CD34+ CD133+ LSCs, and significantly reduced clonality of LSCs, as shown by reduced CFC count. However, many studies have highlighted that Ca^{2+} overload is also detrimental to HSCs. Therefore, Ca^{2+} depletion using lomerizine is likely safer approach to eradicate LSCs while selectively spare HSCs.

6 Discussion and Future work

In this thesis, study aimed to investigate the role of intracellular Ca^{2+} in CML mitochondrial metabolism and how this may expose a novel vulnerability to eradicate LSCs in combination with TKI treatment. Below this chapter discusses recent findings in field of Ca^{2+} signalling in normal HSCs and CML LSCs. Furthermore, the study discusses recent findings in CML LSC's mitochondrial metabolism.

6.1 Discussion

6.1.1 LSCs rely on OXPHOS for their survival

Since development of imatinib, first FDA approved TKI, in 2001, overall survival of CML patients has dramatically enhanced by 90%. However, approximately a quarter of CML individuals develop resistance to TKIs [251]. Over 25% of CML patients will switch TKIs due to intolerance or resistance. Mutations in BCR kinase ABL domain are most investigated mechanism of TKI resistance in CML. However, these mutations only account for 20–40% of resistant cases [252]. Thus, one of main therapeutic burdens in leukaemia is still to find a cure for those with either minimal residual disease or resistance to therapy. This resistance is unclear if it arises inherently as a profound feature of LSCs or if resistance occurs secondarily due to therapy selection process.

Nevertheless, in both cases, LSCs resist TKI treatment due to their unique characteristics. For example, their existence in BM niche offers them an extra layer of protection from treatment due to many extrinsic factors, such as immunological landscape of BM. However, reason for LSCs resistance expands to involve intrinsic features of LSCs. Previously Kuntz *et al*. revealed that CML LSCs have higher OXPHOS levels than normal HSCs or other CD34- CML progenitors. Our transcriptome data analysis confirmed that CD34+CD38- LSC-enriched population had enriched OXPHOS, ETC and even glycolysis compared to their normal counterparts. This highlighted possible role of OXPHOS in CML LSC survival and therapy resistance, as confirmed by Kuntz *et al*. [184]. Kuntz *et al*. used tigecycline as an effective therapy that can inhibit CML LSC OXPHOS, which has been shown to sensitise therapy resistant LSCs to eradication by imatinib.

However, previously tested OXPHOS inhibitors, including tigecycline, showed poor *in vivo* characteristics or adverse effects such as a short metabolic half-life, which limits tigecycline clinical efficacy [253]. Another currently available OXPHOS inhibitor, IACS-010759, has been shown to induce lactic acidosis, which limits its clinical applicability or excludes patients who profoundly suffer from high level of acidosis [89]. In our hands, IACS-010759 could inhibit OXPHOS and target LSC clonality *in vitro*. However, CD34+ CML cells increased level of intracellular lactate detected by heavy isotope glucose labelling in response to 20 nM IACS-010759 exposure for 24 hours. Therefore, there is an unmet need for an OXPHOS inhibitor that can be safely administered in clinics.

Helgason lab previously performed a drug repurposing screen by testing over 1300 FDA approved compounds to identify potential OXPHOS inhibitors [210]. The concept behind repurposing screen was that when cell is cultured in glucose, it can perform both OXPHOS and glycolysis. When glucose is replaced with galactose, cells cannot perform glycolysis and rely on OXPHOS as sole energy source. The replacement of glucose with galactose in culture medium *in vitro* results in a deficiency of ATP and intermediate metabolites, which is compensated for by mitochondrial respiration [254]. Thus, galactose grown CML cells are sensitive to OXPHOS inhibition. This screen revealed several hits, including lomerizine, a Ca^{2+} channel blocker, currently used clinically for the treatment of migraines. Previous findings indicated Ca^{2+} ions as a cofactor of mitochondrial dehydrogenases [224]. Therefore, we asked if CML LSCs rely on Ca^{2+} to perform OXPHOS and whether this reliance of LSCs on calcium driven OXPHOS allows them to reduce impact of imatinib treatment.

6.1.2 Ca^{2+} ions' role in HSCs and LSC OXPHOS

LT-HSCs have a low basal energy level that relies on glycolysis [109, 110]. However, cells keep mitochondrial mass as a reservoir that allows LT-HSCs to respire, proliferate, and reconstitute BM niche during stress conditions [71, 111]. Even though OXPHOS is seemingly dispensable for HSCs, it does not seem to be case in CML LSCs, which display significantly higher levels of OXPHOS [184]. LSCs of AML were also found to rely on mitochondrial OXPHOS [184, 255]. Zhong *et al.* uncovered role of oxysterol binding protein-related protein 4L (ORP4L) as a mediator for PIP2 extraction from plasma membrane and chaperoning it to PLCβ3

in T-ALL and AML LSCs [256, 257]. Subsequently, ORP4L signalling ultimately enhances LSC mitochondrial respiration [256, 257]. All these findings emphasise potential role of extracellular and intracellular Ca^{2+} signalling in CML or AML LSC survival, proliferation, and therapy resistance. Even though critical role of mitochondrial metabolism has been suggested, it is not clear in CML or CLL yet if Ca^{2+} is involved [258, 259]. In this study, a mainly focussed on CML LSCs. The transcriptome analysis of CD34+CD38- LSCs and their normal HSCs counterparts revealed that *CACNA1D*, *TRPC6*, and almost all ER gene sets are enriched in CD34+CD38- LSCs compared to their non-CML counterparts. Our subsequent results further substantiated these transcriptome findings, in that ER mass, ER Ca^{2+} content, and mitochondrial Ca^{2+} content is higher in CD34+ CML cells *ex vivo* than their normal counterparts.

6.1.3 Targeting Ca^{2+} signalling in LSCs and therapy resistant CML cells

Previous findings have shown that disrupting Ca^{2+} levels or targeting Ca^{2+} related signalling can eradicate myeloid LSCs. For example, Gregory *et al*. performed an RNAi-based synthetic lethal screen with imatinib treated CML cells, which showed involvement of Wnt/Ca^{2+}/NFAT signalling pathway in enhanced imatinib lethality when antagonised [260]. In line with this result, *in vivo* studies demonstrated that dasatinib, combined with NFAT inhibitor cyclosporin A, could effectively eradicate BCR::ABL+ leukaemias that were refractory to dasatinib single treatment [260]. Affecting NFAT signalling and inhibiting Ca^{2+} binding proteins such as CaMKII reduces LSC self-renewal, whereas CaMKII overexpression has opposite effect, without affecting normal HSCs [261]. Furthermore, CaMKIIγ has been reported to participate in CML disease progression to blast crisis and resistance to imatinib treatment [261]. Berbamine binds into ATP binding pocket of CaMKII, blocking its phosphorylation, and induces apoptosis in leukaemic cells [262]. Berbamine analogues also inhibit growth of imatinib resistant CML cells, $CD34^{+}$ cells, and T315I mutant BCR::ABL CML cell clones [262, 263]. Not only targeting Ca^{2+} binding proteins but also targeting Ca^{2+} stores could eradicate therapy resistant and residual LSCs in myeloid leukaemia. For example, imatinib induced Ca^{2+} mobilisation from ER can induce autophagy in murine and human CML cells [165]. It was shown that Ca^{2+} chelation inhibited this imatinib induced autophagy. Given that LSCs rely more on autophagy following imatinib for their survival [229],

connection between Ca^{2+} induced autophagy and LSCs therapy resistance possibly phenocopies CML cell line responses. However, this remains to be investigated in LSCs.

In this study, imatinib does not alter CACNA1D or TRPC6 mediated Ca^{2+} influx, as shown in cell line models. Imatinib induces a higher basal level of ER Ca^{2+} ions in CML cell lines. Using primitive CD34+ CML cells, lomerizine reduced LSC clonality and proliferation without affecting CD34+ normal cells. In addition, genetic knockout of *CACNA1D* and *TRPC6* in CML cell line models significantly increased sensitivity of CML cells to imatinib treatment, with a subsequent reduction in ER Ca^{2+} content and ER-mitochondria Ca^{2+} transfer, leading to a progressive reduction of mitochondrial respiration.

Finally, combined imatinib and lomerizine treatment significantly reduced CML tumour burden and LSC engraftment in CML *in vivo* models. Our findings further substantiate a rationale for effective eradication of CML by targeting previously reported OXPHOS dependency in CML cells.

6.1.4 Ca^{2+} depletion for selective LSC eradication

Previous studies have highlighted that Ca^{2+} level overload can lead to oxidative stress and apoptosis in various leukaemias. Luo *et al*. showed that pharmacological activation of TRPC6 with 6′-Hydroxy justicidin B slowed K562 cell growth and increased apoptosis through stimulating Ca^{2+} overload [264]. Justicidin B was found to reduce mitochondrial potential and indirectly upregulate expression of *caspase 8*, *9*, and *p53*.

Thus, it may be concluded that therapeutic perturbation in Ca^{2+} homeostasis, either by depletion or overload, can sensitise leukaemic cells to eradication. In our hands, treatment of CD34+ CML cells with a TRPC6 stimulator, hyperforin nearly eradicated CD34+CD133+ LSCs pool size compared to untreated samples. Also, this significantly impacted short-term potential of LSCs exposed to hyperforin, as shown in reduced CFC count. Not only hyperforin but also FPL CACNA1D stimulator had same impact on CD34+, CD133+ and CFC count levels. Researchers have known for some time that inhibiting *in vitro* or *in vivo* Ca^{2+} influx is not detrimental to HSCs and allows undifferentiated HSC division [70, 73]. This highlights a promising Ca^{2+} targeting strategy for leukaemic cells without affecting

normal cells as Ca^{2+} overload or exhaustion will more specifically target leukaemia cells.

However, persistent Ca^{2+} overload could also lead to a loss of maintenance of HSCs and speed up HSC differentiation. For instance, persistent Ca^{2+} influx via CACNA1B led to switching mitochondrial respiration and ultimately differentiated those quiescent HSCs [265]. Barbosa *et al*. also supported these findings when they reported that Ca^{2+} signalling induces HSCs cycling, leading to exhaustion of murine HSCs and myeloid/granulocyte fraction [266]. HSCs and BM resident cells would also favour low Ca^{2+} for their maintenance while simultaneously targeting leukaemia. For example, chimeric antigen receptor (CAR) T cells were known to provide a protective immune response against tumours when mice received SOCE Ca^{2+} influx inhibitor, which then boosted antitumour activity *in vivo* against a ALL xenograft model [267]. In general, inhibiting Ca^{2+} influx *in vivo* results in expansion of engrafted human HSCs and enhanced BM mouse resident cell proliferation [268]. To our knowledge, Soboloff *et al*., for the first time, revealed that inhibiting Ca^{2+} influx in a mixture of normal and leukaemia cells led to selective elimination of leukaemia cells without halting normal cells [269]. Soboloff *et al*., showed that competitive transplanting of murine BM cells with leukaemia cell line P815 into irradiated mice led mice to survive for 2-4 weeks. At week 4, the level of P815 cells were 38 % of BM cells and 11 % of spleen cells. However, prior treatment of BM cells mixed with P815 with 12 μM econazole for 2 hours as a SOCE inhibitor prior to their engraftment led to extended survival of mice over 14 weeks without reporting any P815 cells [269]. However, their findings must be revisited and broadly investigated to include a wide range of leukaemic and LSC advanced models and a more specific targeted approach alongside pharmacological approach. Overall, this supports notion that low Ca^{2+} signalling supports HSC maintenance, the role of BM niche resident cells and highlights the role of Ca^{2+} inhibition as a strategy to inhibit OXPHOS and subsequent eradication, rather than Ca^{2+} overload, as more suitable strategy for targeting leukaemia without affecting normal microenvironmental components, including HSCs.

6.2 Future work

Despite our advanced knowledge regarding Ca^{2+} regulation *in vitro* and *in vivo*, the translation of Ca^{2+} signalling research into leukaemia clinical trials is still in its infancy. Several recent studies have reported off-target effects for compounds that purportedly targeted a specific part of Ca^{2+} signalling. Therefore, it may be more prudent to use more precise therapeutic targeting based on genetic read out of cancerous cell population, or through using of specific monoclonal antibodies to target Ca^{2+} channels, Ca^{2+} binding proteins, or Ca^{2+} signalling to target upregulated Ca^{2+} signalling in leukaemia progression more specifically. Another important area of future investigation will be to study how Ca^{2+} participates in cell cycling and maintaining DNA repair mechanisms in HSCs, and whether leukaemia initiation occurs in response to Ca^{2+} dysregulation in the BM niche. The resistance towards therapy due to either extra features in LSCs or the mutational landscape that acquire cell resistance remains a significant challenge in therapeutic options for leukaemia. It has been proven that Ca^{2+} levels and signalling are dysregulated in many blood cancers. However, little has been done to relate Ca^{2+} level and mitochondrial metabolism in ALL and AML, both of which likely utilise Ca^{2+} signalling via ORP4L to perform mitochondrial respiration.

Further, as shown from transcriptome analysis, ER content and activity is upregulated in LSCs. Thus, investigating ER-mediated regulatory processes is still imperative in CML research. For example, resident proteins between ER and mitochondria regulate Ca^{2+} transfer. Yet, none of these regulatory proteins has been evaluated regarding leukaemia progression.

ER integrity, which allows sustained ER activity such as Ca^{2+} transfer to mitochondria, fatty acid synthesis, and fatty acid recycling through phagophore formation and autophagy (Figure 6-1). For example, the ER is known to be involved in phagophore membrane formation and autophagy activation that modulates fatty acid availability for OXPHOS [270]. Further, fatty acid recycling and autophagy support mitochondrial OXPHOS [271]. Both processes have been shown to play an important role in CML survival and therapy resistance.

ER-Phagy, another ER regulatory process, also plays a role in keeping ER integrity. One of mechanisms that help maintain a functional ER has been shown to be through ER stress. This was also reported in CML after exposure to imatinib,

indicating a possible role in ER stress in regulating response of LSCs to therapy. Finally, current findings showed that imatinib induced ER-Phagy that is known to clear out defective ER and maintain functional ER. Most of these aspects still require further investigation in the context of CML LSC therapy resistance.
Further, as this research project expands on OXPHOS as a vulnerability that could be targeted to eradicate LSCs. Preliminary data shows the differences between therapy resistance CML cell lines. Author found that non-mutational therapy resistance, as shown in Pon-Res cells, has higher mitochondrial content and activity. However, mutational dependent therapy resistance, as shown in T315I cells, has lower mitochondrial content and activity. This dissimilarity represents novel findings that potentially reflects dependency on metabolic rewiring to skip imatinib treatment. However, these interesting findings still require further investigation.

Our results highlight that pharmacological Ca^{2+} inhibition by lomerizine can selectively target LSCs without impacting normal HSCs, reinforcing to consider these findings for selective maintenance of HSCs *ex vivo*.
However, LSCs are shown to be exhausted in the presence of both Ca^{2+} inhibitors or Ca^{2+} inducers. It is expected that Ca^{2+} induction will drive differentiation in HSCs which potentially imply unfavourable pharmacological vulnerabilities to CML patients. Despite such fact, the impact of hyperforin as Ca^{2+} inducer on eradicating LSCs is worth further investigation. It is also still needed to expand on investigating the impact of pharmacological Ca^{2+} induction on normal HSCs maintenance and try to identify selective approaches to utilise this as a tool to eradicate LSCs but not HSCs (like Trojan Horse treatment to locate therapy in cancer without impacting or causing normal systematic tissues or cells). Researchers may find an approach to safely deliver Ca^{2+} inducer to LSCs based on differential surface marker expression as shown in recent study which reintroduced exogenous MS4A3 to LSCs [272].
Despite the progress made in this project, There is still thrive to answer more research questions which will allow us to better understand mechanistic insights to cure CML disease.

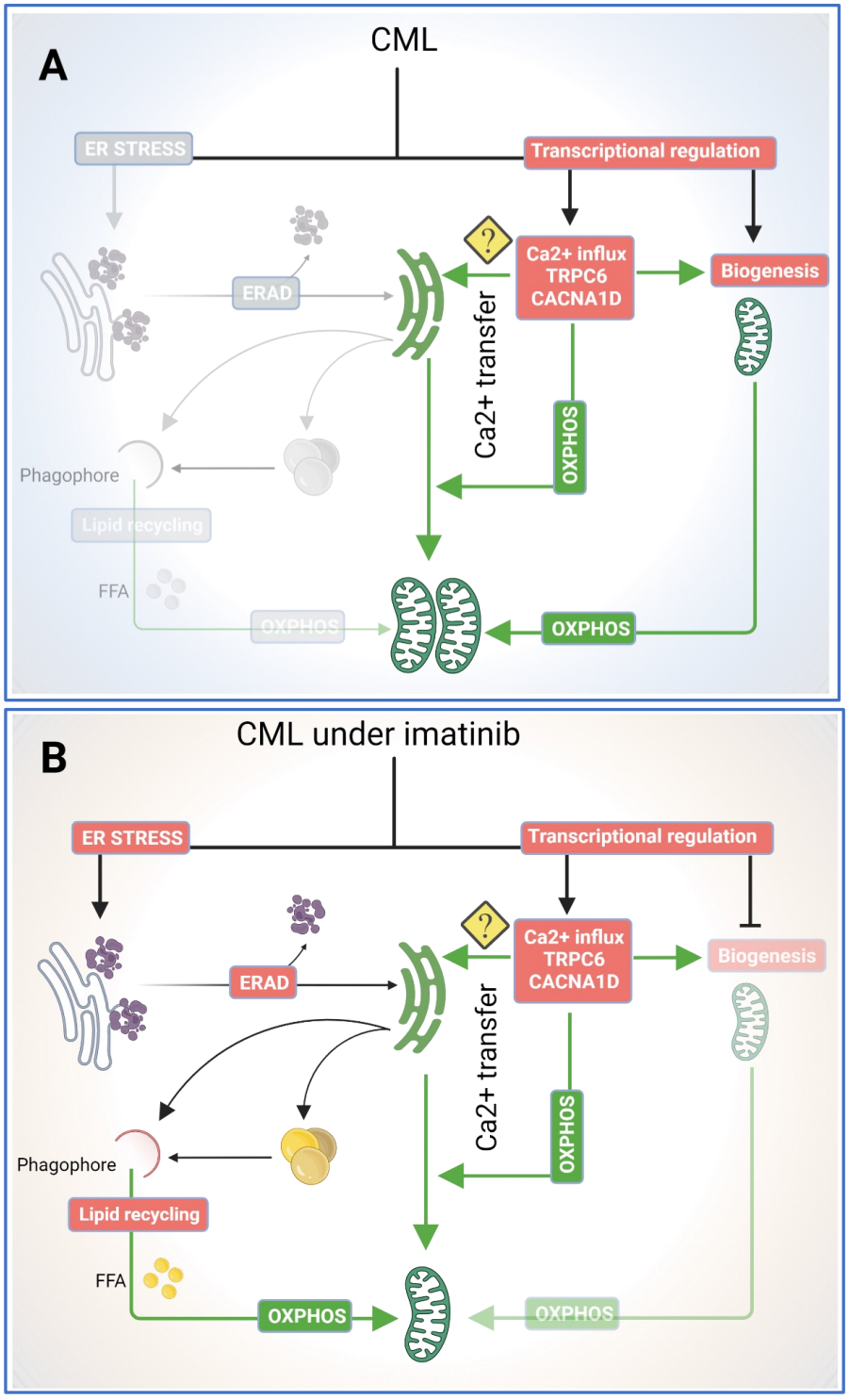

Figure 6-1: Proposed Ca^{2+} vulnerability in imatinib treated CML cells.

(A) In brief, this figure illustrates the potential impact of imatinib treatment on OXPHOS in CML cells. The transcriptome data analysis showed that CML cells upregulate TRPC6 and CACNA1D levels. In addition, processes that represent ER quality control, such as ER-Phagy and ER related fatty acid recycling, have been shown to become higher in CML (maybe not active until ER is stressed). Furthermore, ER and mitochondrial mass are significantly higher in CML compared to normal cells. (B) However, imatinib treatment does not alter CACNA1D or TRPC6 expression levels indicating possible sustained Ca^{2+} influx to mitochondria. Imatinib, further, seems to trigger ER stress, as shown by Bellodi *et al.* [273]. Consequently, ER stress may allow cells to adapt stress through activating ER-Phagy. It is also possible that ER supports fatty acid recycling because autophagy induction and phagophore formation by ER activity (not yet investigated in CML).

6.3 Concluding remark

The result in this thesis validates lomerizine as OXPHOS inhibitor to eradicate CML LSCs, which was identified from drug repurposing screen (Figure 6-2). The results further highlight how Ca^{2+} is regulated in CML LSCs and this reveals ER as a novel druggable target in the future CML research field.

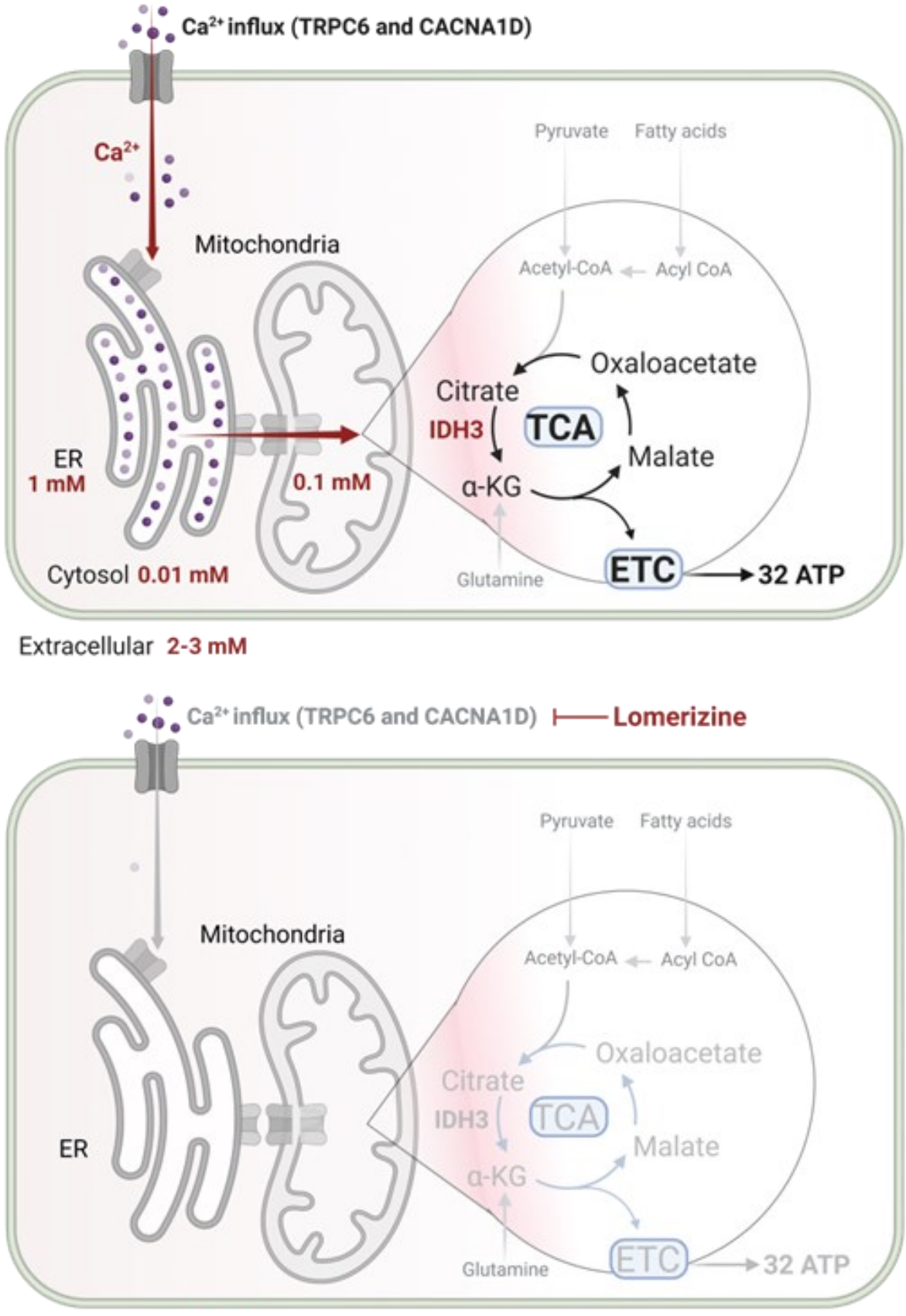

Figure 6-2: CML LSCs rely on Ca^{2+} to perform OXPHOS which is targetted by lomerizine .

List of References

1. Zambidis, E.T., et al., *Emergence of human angiohematopoietic cells in normal development and from cultured embryonic stem cells.* Ann N Y Acad Sci, 2007. **1106**: p. 223-32.
2. Giancotti, A., et al., *Functions and the Emerging Role of the Foetal Liver into Regenerative Medicine.* Cells, 2019. **8**(8).
3. Julien, E., R. El Omar, and M. Tavian, *Origin of the hematopoietic system in the human embryo.* FEBS Lett, 2016. **590**(22): p. 3987-4001.
4. Till, J.E. and E.A.J.R.r. McCulloch, *A direct measurement of the radiation sensitivity of normal mouse bone marrow cells.* 1961. **14**(2): p. 213-222.
5. Morrison, S.J., et al., *The biology of hematopoietic stem cells.* 1995. **11**(1): p. 35-71.
6. Pellin, D., et al., *A comprehensive single cell transcriptional landscape of human hematopoietic progenitors.* Nature Communications, 2019. **10**(1): p. 2395.
7. Zhang, Y., et al., *Hematopoietic hierarchy-an updated roadmap.* 2018. **28**(12): p. 976-986.
8. Haylock, D., et al., *Ex vivo expansion and maturation of peripheral blood CD34+ cells into the myeloid lineage.* 1992.
9. Schoedel, K.B., et al., *The bulk of the hematopoietic stem cell population is dispensable for murine steady-state and stress hematopoiesis.* 2016. **128**(19): p. 2285-2296.
10. Akashi, K., et al., *A clonogenic common myeloid progenitor that gives rise to all myeloid lineages.* 2000. **404**(6774): p. 193-197.
11. Andrews, R.G., J.W. Singer, and I.D.J.B. Bernstein, *Monoclonal antibody 12-8 recognizes a 115-kd molecule present on both unipotent and multipotent hematopoietic colony-forming cells and their precursors.* 1986. **67**(3): p. 842-845.
12. Krause, D.S., et al., *CD34: structure, biology, and clinical utility [see comments].* 1996.
13. Baum, C.M., et al., *Isolation of a candidate human hematopoietic stem-cell population.* 1992. **89**(7): p. 2804-2808.
14. Terstappen, L., et al., *Sequential generations of hematopoietic colonies derived from single nonlineage-committed CD34+ CD38-progenitor cells.* 1991.
15. Hess, D.A., et al., *Selection based on CD133 and high aldehyde dehydrogenase activity isolates long-term reconstituting human hematopoietic stem cells.* 2006. **107**(5): p. 2162-2169.
16. Deryugina, E. and C.J.C.r.i.i. Müller-Sieburg, *Stromal cells in long-term cultures: keys to the elucidation of hematopoietic development?* 1993. **13**(2): p. 115-150.
17. Eaves, A.C., et al., *Unregulated proliferation of primitive chronic myeloid leukemia progenitors in the presence of normal marrow adherent cells.* 1986. **83**(14): p. 5306-5310.
18. Ogawa, M., *Differentiation and proliferation of hematopoietic stem cells.* 1993.
19. Uchida, N., et al., *Rapid and sustained hematopoietic recovery in lethally irradiated mice transplanted with purified Thy-1.1lo Lin-Sca-1+ hematopoietic stem cells.* Blood, 1994. **83**(12): p. 3758-79.

20. Erdman Jr, J.W., I.A. Macdonald, and S.H. Zeisel, *Present knowledge in nutrition*. 2012: John Wiley & Sons.
21. Luo, G., et al., *Spontaneous calcification of arteries and cartilage in mice lacking matrix GLA protein*. 1997. **386**(6620): p. 78-81.
22. Wang, S., et al., *pH effects on measurements of ionized calcium and ionized magnesium in blood*. Arch Pathol Lab Med, 2002. **126**(8): p. 947-50.
23. Prakriya, M. and R.S.J.P.r. Lewis, *Store-operated calcium channels*. 2015. **95**(4): p. 1383-1436.
24. Ashby, M.C. and A.V. Tepikin. *ER calcium and the functions of intracellular organelles*. in *Seminars in cell & developmental biology*. 2001. Elsevier.
25. Catterall, W.A., et al., *International Union of Pharmacology. XLVIII. Nomenclature and structure-function relationships of voltage-gated calcium channels*. Pharmacol Rev, 2005. **57**(4): p. 411-25.
26. Bush, E.W., et al., *Canonical transient receptor potential channels promote cardiomyocyte hypertrophy through activation of calcineurin signaling*. J Biol Chem, 2006. **281**(44): p. 33487-96.
27. Szabadkai, G., et al., *Chaperone-mediated coupling of endoplasmic reticulum and mitochondrial Ca2+ channels*. 2006. **175**(6): p. 901-911.
28. Szabadkai, G., A.M. Simoni, and R. Rizzuto, *Mitochondrial Ca2+ uptake requires sustained Ca2+ release from the endoplasmic reticulum*. Journal of Biological Chemistry, 2003. **278**(17): p. 15153-15161.
29. Ljubojevic, S. and D.M.J.J.o.c.p. Bers, *Nuclear calcium in cardiac myocytes*. 2015. **65**(3): p. 211.
30. Lewis, R.S.J.C.S.H.p.i.b., *Store-operated calcium channels: from function to structure and back again*. 2020. **12**(5): p. a035055.
31. Rowell, J., N. Koitabashi, and D.A. Kass, *TRP-ing up heart and vessels: canonical transient receptor potential channels and cardiovascular disease*. J Cardiovasc Transl Res, 2010. **3**(5): p. 516-24.
32. Putney Jr, J.W. and R.R.J.B. McKay, *Capacitative calcium entry channels*. 1999. **21**(1): p. 38-46.
33. Nilius, B., et al., *Transient receptor potential cation channels in disease*. Physiol Rev, 2007. **87**(1): p. 165-217.
34. Medina, D.L. and A.J.A. Ballabio, *Lysosomal calcium regulates autophagy*. 2015. **11**(6): p. 970-971.
35. Dolphin, A.C., *A short history of voltage-gated calcium channels*. British journal of pharmacology, 2006. **147 Suppl 1**(Suppl 1): p. S56-S62.
36. Lacerda, A.E., et al., *Normalization of current kinetics by interaction between the a 1 and ß subunits of the skeletal muscle dihydropyridine-sensitive Ca 2+ channel*. 1991. **352**(6335): p. 527-530.
37. Williams, M.E., et al., *Structure and functional expression of a1, a2, and B subunits of a novel human neuronal calcium channel subtype*. 1992. **8**(1): p. 71-84.
38. Castellano, A., et al., *Cloning and expression of a third calcium channel beta subunit*. 1993. **268**(5): p. 3450-3455.
39. Huang, H., et al., *Modest Ca V 1.3 42-selective inhibition by compound 8 is ß-subunit dependent*. 2014. **5**(1): p. 1-7.
40. Berjukow, S., et al., *Molecular mechanism of calcium channel block by isradipine. Role of a drug-induced inactivated channel conformation*. J Biol Chem, 2000. **275**(29): p. 22114-20.

41. Stanika, R., et al., *Splice variants of the Ca V 1.3 L-type calcium channel regulate dendritic spine morphology*. 2016. **6**(1): p. 1-17.
42. Dunlap, K., J.I. Luebke, and T.J. Turner, *Exocytotic Ca2+ channels in mammalian central neurons*. Trends Neurosci, 1995. **18**(2): p. 89-98.
43. Putney, J.W.J.P.o.t.N.A.o.S., *TRP, inositol 1, 4, 5-trisphosphate receptors, and capacitative calcium entry*. 1999. **96**(26): p. 14669-14671.
44. Clapham, D.E.J.N., *TRP channels as cellular sensors*. 2003. **426**(6966): p. 517-524.
45. Dupont, G. and L.J.F. Combettes, *Fine tuning of cytosolic Ca 2+ oscillations*. 2016. **5**.
46. Elíes, J., et al., *An update to calcium binding proteins*. 2020: p. 183-213.
47. Kar, P. and A.B.J.M.c. Parekh, *Distinct spatial Ca2+ signatures selectively activate different NFAT transcription factor isoforms*. 2015. **58**(2): p. 232-243.
48. Li, H., A. Rao, and P.G.J.T.i.c.b. Hogan, *Interaction of calcineurin with substrates and targeting proteins*. 2011. **21**(2): p. 91-103.
49. Medina, D.L., et al., *Lysosomal calcium signalling regulates autophagy through calcineurin and TFEB*. 2015. **17**(3): p. 288-299.
50. Takuwa, N., W. Zhou, and Y. Takuwa, *Calcium, calmodulin and cell cycle progression*. Cellular Signalling, 1995. **7**(2): p. 93-104.
51. Backs, J., et al., *Histone deacetylase 5 acquires calcium/calmodulin-dependent kinase II responsiveness by oligomerization with histone deacetylase 4*. 2008. **28**(10): p. 3437-3445.
52. Schäfer, B.W. and C.W.J.T.i.b.s. Heizmann, *The S100 family of EF-hand calcium-binding proteins: functions and pathology*. 1996. **21**(4): p. 134-140.
53. Donato, R., et al., *Functions of S100 proteins*. 2013. **13**(1): p. 24-57.
54. Strobl, S., et al., *The crystal structure of calcium-free human m-calpain suggests an electrostatic switch mechanism for activation by calcium*. 2000. **97**(2): p. 588-592.
55. Rasmussen, K.D., K.J.G. Helin, and development, *Role of TET enzymes in DNA methylation, development, and cancer*. 2016. **30**(7): p. 733-750.
56. Tong, Y. and F.J.A. Song, *Intracellular calcium signaling regulates autophagy via calcineurin-mediated TFEB dephosphorylation*. 2015. **11**(7): p. 1192-1195.
57. Roach, P.J.J.M. and c. biology, *AMPK→ uLK1→ autophagy*. 2011. **31**(15): p. 3082-3084.
58. Carrión, A.M., et al., *DREAM is a Ca2+-regulated transcriptional repressor*. Nature, 1999. **398**(6722): p. 80-4.
59. Forostyak, O., et al., *Physiology of Ca2+ signalling in stem cells of different origins and differentiation stages*. 2016. **59**(2-3): p. 57-66.
60. Lehotsky, J., et al., *The role of plasma membrane Ca2+ pumps (PMCAs) in pathologies of mammalian cells*. Front Biosci, 2002. **7**: p. d53-d84.
61. Wuytack, F., L. Raeymaekers, and L. Missiaen, *Molecular physiology of the SERCA and SPCA pumps*. Cell calcium, 2002. **32**(5-6): p. 279-305.
62. Yeh, S.-C., et al., *Quantification of bone marrow interstitial pH and calcium concentration by intravital ratiometric imaging*. 2022. **13**(1): p. 1-13.
63. Adams, G.B., et al., *Stem cell engraftment at the endosteal niche is specified by the calcium-sensing receptor*. 2006. **439**(7076): p. 599-603.

64. Lam, B.S., C. Cunningham, and G.B.J.B. Adams, *Pharmacologic modulation of the calcium-sensing receptor enhances hematopoietic stem cell lodgment in the adult bone marrow*. 2011. **117**(4): p. 1167.
65. Wu, Q., et al., *Extracellular calcium increases CXCR4 expression on bone marrow-derived cells and enhances pro-angiogenesis therapy*. 2009. **13**(9b): p. 3764-3773.
66. Schajnovitz, A., et al., *CXCL12 secretion by bone marrow stromal cells is dependent on cell contact and mediated by connexin-43 and connexin-45 gap junctions*. 2011. **12**(5): p. 391-398.
67. Bowie, M.B., et al., *Hematopoietic stem cells proliferate until after birth and show a reversible phase-specific engraftment defect*. 2006. **116**(10): p. 2808-2816.
68. Kelly, E.K., L. Wang, and L.B. Ivashkiv, *Calcium-activated pathways and oxidative burst mediate zymosan-induced signaling and IL-10 production in human macrophages*. The Journal of Immunology, 2010. **184**(10): p. 5545-5552.
69. McCabe, A., et al., *Interleukin-10 Signaling in Hematopoietic Stem and Progenitor Cells Maintains Stem Cell Function and Regulates Inflammation-Induced Myeloid Cell Output*. Blood, 2018. **132**: p. 2407.
70. Luchsinger, L.L., et al., *Harnessing hematopoietic stem cell low intracellular calcium improves their maintenance in vitro*. 2019. **25**(2): p. 225-240. e7.
71. Fukushima, T., et al., *Discrimination of dormant and active hematopoietic stem cells by G0 marker reveals dormancy regulation by cytoplasmic calcium*. 2019. **29**(12): p. 4144-4158. e7.
72. Stella Jr, S.L., E.J. Bryson, and W.B.J.J.o.n. Thoreson, *A2 adenosine receptors inhibit calcium influx through L-type calcium channels in rod photoreceptors of the salamander retina*. 2002. **87**(1): p. 351-360.
73. Umemoto, T., et al., *Ca2+-mitochondria axis drives cell division in hematopoietic stem cells*. Journal of Experimental Medicine, 2018. **215**(8): p. 2097-2113.
74. Hirata, Y., et al., *CD150high bone marrow Tregs maintain hematopoietic stem cell quiescence and immune privilege via adenosine*. Cell stem cell, 2018. **22**(3): p. 445-453. e5.
75. Breitbach, M., et al., *In vivo labeling by CD73 marks multipotent stromal cells and highlights endothelial heterogeneity in the bone marrow niche*. 2018. **22**(2): p. 262-276. e7.
76. Cipolleschi, M.G., P. Dello Sbarba, and M. Olivotto, *The role of hypoxia in the maintenance of hematopoietic stem cells*. Blood, 1993. **82**(7): p. 2031-7.
77. Parmar, K., et al., *Distribution of hematopoietic stem cells in the bone marrow according to regional hypoxia*. Proc Natl Acad Sci U S A, 2007. **104**(13): p. 5431-6.
78. Broxmeyer, H.E., et al., *The importance of hypoxia and extra physiologic oxygen shock/stress for collection and processing of stem and progenitor cells to understand true physiology/pathology of these cells ex vivo*. 2015. **22**(4): p. 273-278.
79. Mantel, Charlie R., et al., *Enhancing Hematopoietic Stem Cell Transplantation Efficacy by Mitigating Oxygen Shock*. Cell, 2015. **161**(7): p. 1553-1565.

80. Suda, T., K. Takubo, and Gregg L. Semenza, *Metabolic Regulation of Hematopoietic Stem Cells in the Hypoxic Niche*. Cell Stem Cell, 2011. **9**(4): p. 298-310.
81. Luchsinger, L.L., et al., *Mitofusin 2 maintains haematopoietic stem cells with extensive lymphoid potential*. 2016. **529**(7587): p. 528-531.
82. Bonora, M., et al., *ATP synthesis and storage*. Purinergic Signal, 2012. **8**(3): p. 343-57.
83. Wiskich, J.T., *6 - Control of the Krebs Cycle**Abbreviations F1-ATPase; the mitochondrial ATP-synthesizing complex; NAD, nicotinamide adenine dinucleotide (oxidized form-NAD+; reduced form-NADH); NADP, nicotinamide adenine dinucleotide phosphate*, in *Metabolism and Respiration*, D.D. Davies, Editor. 1980, Academic Press. p. 243-278.
84. Mitchell, P.J.N., *Coupling of phosphorylation to electron and hydrogen transfer by a chemi-osmotic type of mechanism*. 1961. **191**(4784): p. 144-148.
85. Salway, J.G., *Metabolism at a Glance*. 2016: John Wiley & Sons.
86. Matés, J.M., et al., *Glutamine homeostasis and mitochondrial dynamics*. 2009. **41**(10): p. 2051-2061.
87. Warburg, O.J.S., *On the origin of cancer cells*. 1956. **123**(3191): p. 309-314.
88. Ito, K. and K.J.E.h. Ito, *Hematopoietic stem cell fate through metabolic control*. 2018. **64**: p. 1-11.
89. de Beauchamp, L., E. Himonas, and G.V. Helgason, *Mitochondrial metabolism as a potential therapeutic target in myeloid leukaemia*. Leukemia, 2022. **36**(1): p. 1-12.
90. Jouaville, L.S., et al., *Regulation of mitochondrial ATP synthesis by calcium: evidence for a long-term metabolic priming*. 1999. **96**(24): p. 13807-13812.
91. Denton, R., P. Randle, and B.J.B.J. Martin, *Stimulation by calcium ions of pyruvate dehydrogenase phosphate phosphatase*. 1972. **128**(1): p. 161.
92. McCORMACK, J.G., A.P. Halestrap, and R.M.J.P.r. Denton, *Role of calcium ions in regulation of mammalian intramitochondrial metabolism*. 1990. **70**(2): p. 391-425.
93. McCORMACK, J.G. and R.M.J.B.J. Denton, *The effects of calcium ions and adenine nucleotides on the activity of pig heart 2-oxoglutarate dehydrogenase complex*. 1979. **180**(3): p. 533-544.
94. Harris, D.A., *Regulation of the mitochondrial ATP synthase in rat heart*. 1993, Portland Press Ltd.
95. Scholz, T.D., R.S.J.A.J.o.P.-H. Balaban, and C. Physiology, *Mitochondrial F1-ATPase activity of canine myocardium: effects of hypoxia and stimulation*. 1994. **266**(6): p. H2396-H2403.
96. Territo, P.R., et al., *Ca2+ activation of heart mitochondrial oxidative phosphorylation: role of the F0/F1-ATPase*. 2000. **278**(2): p. C423-C435.
97. MILDAZIENE, V., et al., *Ca2+ stimulates both the respiratory and phosphorylation subsystems in rat heart mitochondria*. 1996. **320**(1): p. 329-334.
98. Friel, D. and R.J.J.o.N. Tsien, *An FCCP-sensitive Ca2+ store in bullfrog sympathetic neurons and its participation in stimulus-evoked changes in [Ca2+] i*. 1994. **14**(7): p. 4007-4024.

99. Moreau, B. and A.B.J.C.B. Parekh, *Ca2+-dependent inactivation of the mitochondrial Ca2+ uniporter involves proton flux through the ATP synthase*. 2008. **18**(11): p. 855-859.
100. Przedborski, S. and V.J.M.d.o.j.o.t.M.D.S. Jackson-Lewis, *Mechanisms of MPTP toxicity*. 1998. **13**: p. 35-38.
101. del Arco, A. and J.J.J.o.B.C. Satrústegui, *Molecular cloning of Aralar, a new member of the mitochondrial carrier superfamily that binds calcium and is present in human muscle and brain*. 1998. **273**(36): p. 23327-23334.
102. Contreras, L., et al., *Ca2+ Activation kinetics of the two aspartate-glutamate mitochondrial carriers, aralar and citrin: role in the heart malate-aspartate NADH shuttle*. 2007. **282**(10): p. 7098-7106.
103. Lasorsa, F.M., et al., *Recombinant expression of the Ca2+-sensitive aspartate/glutamate carrier increases mitochondrial ATP production in agonist-stimulated Chinese hamster ovary cells*. 2003. **278**(40): p. 38686-38692.
104. Safer, B., et al., *Control of the transport of reducing equivalents across the mitochondrial membrane in perfused rat heart*. 1971. **2**(2): p. 111-124.
105. Kitsos, C.M., et al., *Calmodulin-dependent Protein Kinase IV Regulates Hematopoietic Stem Cell Maintenance*. 2005. **280**(39): p. 33101-33108.
106. Racioppi, L., et al., *Calcium/calmodulin-dependent kinase kinase 2 regulates hematopoietic stem and progenitor cell regeneration.* Cell Death Dis, 2017. **8**(10): p. e3076.
107. Grahn, T.H.M., et al., *S100A6 is a critical regulator of hematopoietic stem cells.* 2020. **34**(12): p. 3323-3337.
108. Lagasse, E. and I.L. Weissman, *Mouse MRP8 and MRP14, two intracellular calcium-binding proteins associated with the development of the myeloid lineage*. 1992.
109. Suda, T., K. Takubo, and G.L.J.C.s.c. Semenza, *Metabolic regulation of hematopoietic stem cells in the hypoxic niche*. 2011. **9**(4): p. 298-310.
110. Ito, K. and T.J.N.r.M.c.b. Suda, *Metabolic requirements for the maintenance of self-renewing stem cells.* 2014. **15**(4): p. 243-256.
111. Takihara, Y., et al., *High mitochondrial mass is associated with reconstitution capacity and quiescence of hematopoietic stem cells.* Blood advances, 2019. **3**(15): p. 2323.
112. Ansó, E., et al., *The mitochondrial respiratory chain is essential for haematopoietic stem cell function.* 2017. **19**(6): p. 614-625.
113. Bejarano-García, J.A., et al., *Sensitivity of hematopoietic stem cells to mitochondrial dysfunction by SdhD gene deletion.* 2016. **7**(12): p. e2516-e2516.
114. Richardson, M.K. and G.J.B.R. Keuck, *The revolutionary developmental biology of W ilhelm H is, Sr*. 2022. **97**(3): p. 1131-1160.
115. Bennett, J.H., *Case of Hypertrophy of the Spleen and Liver, in*
Which Death Took Place From Suppuration of the Blood. Edinburgh Med Surg J, 1845. **64:413-423**.
116. R., V., *Weisses blut*. Froriep's Notizen. , 1846. **1845;36:151-156.**
117. Bauduer, F., et al., *Chronic myeloid leukemia as a secondary neoplasm after anti-cancer radiotherapy: a report of three cases and a brief review of the literature*. 2002. **43**(5): p. 1057-1060.
118. Vlaanderen, J., et al., *Occupational benzene exposure and the risk of chronic myeloid leukemia: A meta-analysis of cohort studies incorporating study quality dimensions*. 2012. **55**(9): p. 779-785.

119. Argiropoulos, B. and R.K. Humphries, *Hox genes in hematopoiesis and leukemogenesis*. Oncogene, 2007. **26**(47): p. 6766-76.
120. Wang, Y., et al., *The Wnt/beta-catenin pathway is required for the development of leukemia stem cells in AML*. Science, 2010. **327**(5973): p. 1650-3.
121. Nowell, P.C. and D.A.J.J.o.t.N.C.I. Hungerford, *Chromosome studies on normal and leukemic human leukocytes*. 1960. **25**(1): p. 85-109.
122. Rowley, J.D., *Letter: A new consistent chromosomal abnormality in chronic myelogenous leukaemia identified by quinacrine fluorescence and Giemsa staining*. Nature, 1973. **243**(5405): p. 290-3.
123. Raskind, W.H. and P.J. Fialkow, *The use of cell markers in the study of human hematopoietic neoplasia*. Adv Cancer Res, 1987. **49**: p. 127-67.
124. Daley, G.Q., R.A. Van Etten, and D. Baltimore, *Induction of chronic myelogenous leukemia in mice by the P210bcr/abl gene of the Philadelphia chromosome*. Science, 1990. **247**(4944): p. 824-30.
125. Sawyers, C.L., *Chronic myeloid leukemia*. N Engl J Med, 1999. **340**(17): p. 1330-40.
126. UK, C.R., *Chronic myeloid leukaemia (CML) incidence statistics*.
. Cancer Research UK. 2015. https://www.cancerresearchuk.org/health, (accessed 14 Feb 2020). **professional/cancer-statistics/statistics-by-cancer-type/leukaemia cml/incidence**

127. Höglund, M., F. Sandin, and B.J.A.o.h. Simonsson, *Epidemiology of chronic myeloid leukaemia: an update*. 2015. **94**(2): p. 241-247.
128. Warsch, W., et al., *High STAT5 levels mediate imatinib resistance and indicate disease progression in chronic myeloid leukemia*. 2011. **117**(12): p. 3409-3420.
129. Skorski, T., et al., *Transformation of hematopoietic cells by BCR/ABL requires activation of a PI-3k/Akt-dependent pathway*. 1997. **16**(20): p. 6151-6161.
130. Mayerhofer, M., et al., *BCR/ABL induces expression of vascular endothelial growth factor and its transcriptional activator, hypoxia inducible factor-1a, through a pathway involving phosphoinositide 3-kinase and the mammalian target of rapamycin*. 2002. **100**(10): p. 3767-3775.
131. Sattler, M., et al., *Critical role for Gab2 in transformation by BCR/ABL*. 2002. **1**(5): p. 479-492.
132. Jain, P., et al., *Prognostic factors and survival outcomes in patients with chronic myeloid leukemia in blast phase in the tyrosine kinase inhibitor era: Cohort study of 477 patients*. Cancer, 2017. **123**(22): p. 4391-4402.
133. Perrotti, D., et al., *Chronic myeloid leukemia: mechanisms of blastic transformation*. J Clin Invest, 2010. **120**(7): p. 2254-64.
134. Kumar, R. and D.S.J.F.R. Krause, *Recent advances in understanding chronic myeloid leukemia: where do we stand?* 2021. **10**.
135. Goldman, J.M. and G.Q. Daley, *Chronic Myeloid Leukemia — A Brief History*, in *Myeloproliferative Disorders*, J.V. Melo and J.M. Goldman, Editors. 2007, Springer Berlin Heidelberg: Berlin, Heidelberg. p. 1-13.
136. Fefer, A., et al., *Disappearance of Ph1-positive cells in four patients with chronic granulocytic leukemia after chemotherapy, irradiation and marrow transplantation from an identical twin*. 1979. **300**(7): p. 333-337.

137. Barrett, A.J. and S. Ito, *The role of stem cell transplantation for chronic myelogenous leukemia in the 21st century.* Blood, 2015. **125**(21): p. 3230-5.
138. Bonifazi, F., et al., *Chronic myeloid leukemia and interferon-a: a study of complete cytogenetic responders.* 2001. **98**(10): p. 3074-3081.
139. Hehlmann, R., et al., *Randomized comparison of busulfan and hydroxyurea in chronic myelogenous leukemia: prolongation of survival by hydroxyurea. The German CML Study Group.* 1993.
140. Hehlmann, R., et al., *Randomized comparison of interferon-alpha with busulfan and hydroxyurea in chronic myelogenous leukemia. The German CML Study Group [see comments].* 1994.
141. Roy, L., et al., *Survival advantage from imatinib compared with the combination interferon-a plus cytarabine in chronic-phase chronic myelogenous leukemia: historical comparison between two phase 3 trials.* Blood, 2006. **108**(5): p. 1478-1484.
142. Druker, B.J., et al., *Efficacy and safety of a specific inhibitor of the BCR-ABL tyrosine kinase in chronic myeloid leukemia.* 2001. **344**(14): p. 1031-1037.
143. Hochhaus, A., et al., *Long-Term Outcomes of Imatinib Treatment for Chronic Myeloid Leukemia.* N Engl J Med, 2017. **376**(10): p. 917-927.
144. Mahon, F.-X., et al., *Discontinuation of imatinib in patients with chronic myeloid leukaemia who have maintained complete molecular remission for at least 2 years: the prospective, multicentre Stop Imatinib (STIM) trial.* 2010. **11**(11): p. 1029-1035.
145. Ross, D.M., et al., *Safety and efficacy of imatinib cessation for CML patients with stable undetectable minimal residual disease: results from the TWISTER study.* 2013. **122**(4): p. 515-522.
146. Galinsky, I. and S.J.J.o.t.a.p.i.o. Buchanan, *Guide to interpreting disease responses in chronic myeloid leukemia.* 2012. **3**(4): p. 225.
147. Society, L.a.L., *Treatment outcome in CML.* Leukaemia and Lymphoma Society, 2022.
148. Branford, S., et al., *High frequency of point mutations clustered within the adenosine triphosphate-binding region of BCR/ABL in patients with chronic myeloid leukemia or Ph-positive acute lymphoblastic leukemia who develop imatinib (STI571) resistance.* Blood, 2002. **99**(9): p. 3472-5.
149. Gorre, M.E., et al., *Clinical resistance to STI-571 cancer therapy caused by BCR-ABL gene mutation or amplification.* Science, 2001. **293**(5531): p. 876-80.
150. Hochhaus, A., et al., *Dasatinib induces notable hematologic and cytogenetic responses in chronic-phase chronic myeloid leukemia after failure of imatinib therapy.* 2007. **109**(6): p. 2303-2309.
151. Cortes, J.E., et al., *Safety and efficacy of bosutinib (SKI-606) in chronic phase Philadelphia chromosome-positive chronic myeloid leukemia patients with resistance or intolerance to imatinib.* 2011. **118**(17): p. 4567-4576.
152. Kantarjian, H.M., et al., *Nilotinib (formerly AMN107), a highly selective BCR-ABL tyrosine kinase inhibitor, is effective in patients with Philadelphia chromosome–positive chronic myelogenous leukemia in chronic phase following imatinib resistance and intolerance.* 2007. **110**(10): p. 3540-3546.

153. Smith, S.J.A.M.S.J., *Imatinib resistance in chronic myeloid leukaemia caused by Bcr-Abl kinase domain and non-Bcr-Abl mutations: a comparison and review*. 2017. **8**(1).
154. O'Hare, T., et al., *AP24534, a pan-BCR-ABL inhibitor for chronic myeloid leukemia, potently inhibits the T315I mutant and overcomes mutation-based resistance*. 2009. **16**(5): p. 401-412.
155. Saussele, S. and R.T.J.A.o.h. Silver, *Management of chronic myeloid leukemia in blast crisis*. 2015. **94**(2): p. 159-165.
156. Lipton, J.H., et al., *Ponatinib versus imatinib for newly diagnosed chronic myeloid leukaemia: an international, randomised, open-label, phase 3 trial*. Lancet Oncol, 2016. **17**(5): p. 612-21.
157. Hughes, T.P., et al., *Asciminib in chronic myeloid leukemia after ABL kinase inhibitor failure*. 2019.
158. Jones, J.K. and E.M. Thompson, *Allosteric Inhibition of ABL Kinases: Therapeutic Potential in Cancer*. Mol Cancer Ther, 2020. **19**(9): p. 1763-1769.
159. Dhillon, S., *Olverembatinib: First Approval*. Drugs, 2022. **82**(4): p. 469-475.
160. Jiang, Q., et al., *Olverembatinib (HQP1351), a well-tolerated and effective tyrosine kinase inhibitor for patients with T315I-mutated chronic myeloid leukemia: results of an open-label, multicenter phase 1/2 trial*. 2022. **15**(1): p. 1-17.
161. Qian, J., et al., *Updated safety and efficacy results of phase 1 study of olverembatinib (HQP1351), a novel third-generation BCR-ABL tyrosine kinase inhibitor (TKI), in patients with TKI-resistant chronic myeloid leukemia (CML)*. 2021. **138**: p. 311.
162. Marin, D., et al., *Adherence is the critical factor for achieving molecular responses in patients with chronic myeloid leukemia who achieve complete cytogenetic responses on imatinib*. J Clin Oncol, 2010. **28**(14): p. 2381-8.
163. Eadie, L.N., T.P. Hughes, and D.L.J.L. White, *Patients with low OCT-1 activity and high ABCB1 fold rise have poor long-term outcomes in response to tyrosine kinase inhibitor therapy*. 2018. **32**(10): p. 2288-2291.
164. Okumu, D.O., *LYN Regulates Drug Resistance Mechanisms in Chronic Myelogenous Leukemia (CML)*. 2018, The University of North Carolina at Chapel Hill.
165. Bellodi, C., et al., *Targeting autophagy potentiates tyrosine kinase inhibitor–induced cell death in Philadelphia chromosome-positive cells, including primary CML stem cells*. 2009. **119**(5): p. 1109-1123.
166. Bellodi, C., et al., *Targeting autophagy potentiates tyrosine kinase inhibitor–induced cell death in Philadelphia chromosome-positive cells, including primary CML stem cells*. 2013. **123**(8): p. 3634-3634.
167. Hurtz, C., et al., *BCL6-mediated repression of p53 is critical for leukemia stem cell survival in chronic myeloid leukemia*. J Exp Med, 2011. **208**(11): p. 2163-74.
168. Pellicano, F., et al., *The antiproliferative activity of kinase inhibitors in chronic myeloid leukemia cells is mediated by FOXO transcription factors*. Stem Cells, 2014. **32**(9): p. 2324-37.
169. Naka, K., et al., *TGF-beta-FOXO signalling maintains leukaemia-initiating cells in chronic myeloid leukaemia*. Nature, 2010. **463**(7281): p. 676-80.
170. Ilander, M., C. Hekim, and S. Mustjoki, *Immunology and immunotherapy of chronic myeloid leukemia*. Curr Hematol Malig Rep, 2014. **9**(1): p. 17-23.

171. Huntly, B.J., et al., *MOZ-TIF2, but not BCR-ABL, confers properties of leukemic stem cells to committed murine hematopoietic progenitors.* Cancer Cell, 2004. **6**(6): p. 587-96.
172. Hochhaus, A., et al., *Long-term outcomes of imatinib treatment for chronic myeloid leukemia.* 2017. **376**(10): p. 917-927.
173. Eisterer, W., et al., *Different subsets of primary chronic myeloid leukemia stem cells engraft immunodeficient mice and produce a model of the human disease.* 2005. **19**(3): p. 435-441.
174. Jørgensen, H. and T.J.B.S.T. Holyoake, *Characterization of cancer stem cells in chronic myeloid leukaemia.* 2007. **35**(5): p. 1347-1351.
175. Houshmand, M., et al., *Chronic myeloid leukemia stem cells.* Leukemia, 2019. **33**(7): p. 1543-1556.
176. Kinstrie, R., et al., *CD93 is expressed on chronic myeloid leukemia stem cells and identifies a quiescent population which persists after tyrosine kinase inhibitor therapy.* Leukemia, 2020. **34**(6): p. 1613-1625.
177. Herrmann, H., et al., *Dipeptidylpeptidase IV (CD26) defines leukemic stem cells (LSC) in chronic myeloid leukemia.* 2014. **123**(25): p. 3951-3962.
178. Hamilton, A., et al., *Chronic myeloid leukemia stem cells are not dependent on Bcr-Abl kinase activity for their survival.* 2012. **119**(6): p. 1501-1510.
179. Giustacchini, A., et al., *Single-cell transcriptomics uncovers distinct molecular signatures of stem cells in chronic myeloid leukemia.* 2017. **23**(6): p. 692-702.
180. Holyoake, T., et al., *Isolation of a highly quiescent subpopulation of primitive leukemic cells in chronic myeloid leukemia.* 1999. **94**(6): p. 2056-2064.
181. Corbin, A.S., et al., *Human chronic myeloid leukemia stem cells are insensitive to imatinib despite inhibition of BCR-ABL activity.* 2011. **121**(1): p. 396-409.
182. Vander Heiden, M.G., L.C. Cantley, and C.B.J.s. Thompson, *Understanding the Warburg effect: the metabolic requirements of cell proliferation.* 2009. **324**(5930): p. 1029-1033.
183. Bost, F., et al., *Energy disruptors: rising stars in anticancer therapy?* 2016. **5**(1): p. e188-e188.
184. Kuntz, E.M., et al., *Targeting mitochondrial oxidative phosphorylation eradicates therapy-resistant chronic myeloid leukemia stem cells.* 2017. **23**(10): p. 1234-1240.
185. Abraham, A., et al., *SIRT1 regulates metabolism and leukemogenic potential in CML stem cells.* 2019. **129**(7): p. 2685-2701.
186. Ye, H., et al., *Leukemic stem cells evade chemotherapy by metabolic adaptation to an adipose tissue niche.* 2016. **19**(1): p. 23-37.
187. Abraham, A., et al., *SIRT1 regulates metabolism and leukemogenic potential in CML stem cells.* 2019. **129**(7): p. 2685-2701.
188. Kuntz, E.M., et al., *Targeting mitochondrial oxidative phosphorylation eradicates therapy-resistant chronic myeloid leukemia stem cells.* 2017. **23**(10): p. 1234.
189. Simsek, T., et al., *The distinct metabolic profile of hematopoietic stem cells reflects their location in a hypoxic niche.* 2010. **7**(3): p. 380-390.
190. Giorgi, C., et al., *PML regulates apoptosis at endoplasmic reticulum by modulating calcium release.* 2010. **330**(6008): p. 1247-1251.

191. Ellgaard, L. and E.-M. Frickel, *Calnexin, calreticulin, and ERp57.* Cell Biochemistry and Biophysics, 2003. **39**(3): p. 223-247.
192. Myhill, N., et al., *The subcellular distribution of calnexin is mediated by PACS-2.* 2008. **19**(7): p. 2777-2788.
193. Simmen, T., et al., *PACS-2 controls endoplasmic reticulum–mitochondria communication and Bid-mediated apoptosis.* 2005. **24**(4): p. 717-729.
194. Szabadkai, G.r., et al., *Chaperone-mediated coupling of endoplasmic reticulum and mitochondrial Ca2+ channels.* 2006. **175**(6): p. 901-911.
195. Lombardi, A.A., et al., *Mitochondrial calcium exchange links metabolism with the epigenome to control cellular differentiation.* 2019. **10**(1): p. 1-17.
196. Cai, L., et al., *Acetyl-CoA induces cell growth and proliferation by promoting the acetylation of histones at growth genes.* 2011. **42**(4): p. 426-437.
197. Kuntz, E.M., *An investigation of metabolic vulnerabilities in chronic myeloid leukaemic stem cells*. 2017, University of Glasgow.
198. Mitchell, R., *Exploring BCR-ABL-independent mechanisms of TKI-resistance in chronic myeloid leukaemia*. 2017, University of Glasgow.
199. Henderson, M.J., et al., *A Low Affinity GCaMP3 Variant (GCaMPer) for Imaging the Endoplasmic Reticulum Calcium Store.* PLoS One, 2015. **10**(10): p. e0139273.
200. Xiao, J., et al., *2-Aminoethoxydiphenyl borate, a inositol 1,4,5-triphosphate receptor inhibitor, prevents atrial fibrillation.* Exp Biol Med (Maywood), 2010. **235**(7): p. 862-8.
201. Wang, C.J.C.p.i.c.b., *A sensitive and quantitative mKeima assay for mitophagy via FACS.* 2020. **86**(1): p. e99.
202. Martín-Maestro, P., et al., *Slower dynamics and aged mitochondria in sporadic Alzheimer's disease.* 2017. **2017**.
203. Liang, J.R., et al., *A genome-wide ER-phagy screen highlights key roles of mitochondrial metabolism and ER-resident UFMylation.* 2020. **180**(6): p. 1160-1177. e20.
204. Salabei, J.K., A.A. Gibb, and B.G.J.N.p. Hill, *Comprehensive measurement of respiratory activity in permeabilized cells using extracellular flux analysis.* 2014. **9**(2): p. 421-438.
205. Miller, P.H., et al., *Analysis of parameters that affect human hematopoietic cell outputs in mutant c-kit-immunodeficient mice.* 2017. **48**: p. 41-49.
206. Irizarry, R.A., et al., *Exploration, normalization, and summaries of high density oligonucleotide array probe level data.* 2003. **4**(2): p. 249-264.
207. Smyth, G.K.J.S.a.i.g. and m. biology, *Linear models and empirical bayes methods for assessing differential expression in microarray experiments.* 2004. **3**(1).
208. Benjamini, Y. and Y.J.J.o.t.R.s.s.s.B. Hochberg, *Controlling the false discovery rate: a practical and powerful approach to multiple testing.* 1995. **57**(1): p. 289-300.
209. Subramanian, A., et al., *Gene set enrichment analysis: a knowledge-based approach for interpreting genome-wide expression profiles.* 2005. **102**(43): p. 15545-15550.
210. Robert de Beauchamp, L., *Investigating and targeting metabolic dependencies in myeloid leukaemia*. 2020, University of Glasgow.

211. Selt, M., et al., *Limited restoration of visual function after partial optic nerve injury; a time course study using the calcium channel blocker lomerizine*. 2010. **81**(4-5): p. 467-471.
212. Ishii, M., et al., *Inhibitory effect of lomerizine, a prophylactic drug for migraines, on serotonin-induced contraction of the basilar artery*. 2009: p. 0909250284-0909250284.
213. Lin, B.L., et al., *In vivo selective inhibition of TRPC6 by antagonist BI 749327 ameliorates fibrosis and dysfunction in cardiac and renal disease*. Proc Natl Acad Sci U S A, 2019. **116**(20): p. 10156-10161.
214. Ward, P.D., et al., *Phospholipase C-γ modulates epithelial tight junction permeability through hyperphosphorylation of tight junction proteins*. 2002. **277**(38): p. 35760-35765.
215. Brauner, P. and B. Fridlender, *Use of chelating agents as terminators of alkaline phosphatase activity in enzyme-linked immunosorbent assay (ELISA) tests*. J Immunol Methods, 1981. **42**(3): p. 375-9.
216. Thastrup, O., et al., *Thapsigargin, a tumor promoter, discharges intracellular Ca2+ stores by specific inhibition of the endoplasmic reticulum Ca2 (+)-ATPase*. 1990. **87**(7): p. 2466-2470.
217. Liu, C. and T.E. Hermann, *Characterization of ionomycin as a calcium ionophore*. J Biol Chem, 1978. **253**(17): p. 5892-4.
218. Bae, Y.-S., et al., *Identification of a compound that directly stimulates phospholipase C activity*. 2003. **63**(5): p. 1043-1050.
219. Aires, V., et al., *Activation of TRPC6 calcium channels by diacylglycerol (DAG)-containing arachidonic acid: a comparative study with DAG-containing docosahexaenoic acid*. 2007. **89**(8): p. 926-937.
220. Leuner, K., et al., *Hyperforin—a key constituent of St. John's wort specifically activates TRPC6 channels*. 2007. **21**(14): p. 4101-4111.
221. Baxter, A.J., et al., *Discovery and synthesis of methyl 2, 5-dimethyl-4-[2-(phenylmethyl) benzoyl]-1H-pyrrole-3-carboxylate (FPL 64176) and analogs: the first examples of a new class of calcium channel activator*. 1993. **36**(19): p. 2739-2744.
222. Thellung, S., et al., *Apoptotic cell death and impairment of L-type voltage-sensitive calcium channel activity in rat cerebellar granule cells treated with the prion protein fragment 106-126*. Neurobiol Dis, 2000. **7**(4): p. 299-309.
223. Vande Voorde, J., et al., *Improving the metabolic fidelity of cancer models with a physiological cell culture medium*. Sci Adv, 2019. **5**(1): p. eaau7314.
224. Denton, R.M., *Regulation of mitochondrial dehydrogenases by calcium ions*. Biochimica et Biophysica Acta (BBA) - Bioenergetics, 2009. **1787**(11): p. 1309-1316.
225. Tu, G., et al., *Expressional and prognostic value of S100A16 in pancreatic cancer via integrated bioinformatics analyses*. 2021. **9**.
226. de la Fuente, S., et al., *Ca2+ homeostasis in the endoplasmic reticulum measured with a new low-Ca2+-affinity targeted aequorin*. 2013. **54**(1): p. 37-45.
227. Bustos, G., et al., *Endoplasmic reticulum–mitochondria calcium communication and the regulation of mitochondrial metabolism in cancer: a novel potential target*. 2017. **7**: p. 199.
228. Mauvezin, C. and T.P. Neufeld, *Bafilomycin A1 disrupts autophagic flux by inhibiting both V-ATPase-dependent acidification and Ca-P60A/SERCA-*

dependent autophagosome-lysosome fusion. Autophagy, 2015. **11**(8): p. 1437-8.
229. Ianniciello, A., et al., *ULK1 inhibition promotes oxidative stress-induced differentiation and sensitizes leukemic stem cells to targeted therapy.* 2021. **13**(613): p. eabd5016.
230. Gottlieb, R.A. and A.J.J.o.M.M. Stotland, *MitoTimer: a novel protein for monitoring mitochondrial turnover in the heart.* 2015. **93**(3): p. 271-278.
231. Klein, S., et al., *Modulation of transient receptor potential channels 3 and 6 regulates osteoclast function with impact on trabecular bone loss.* 2020. **106**(6): p. 655-664.
232. Talbot, B.E., et al., *Transmembrane insertases and N-glycosylation critically determine synthesis, trafficking, and activity of the nonselective cation channel TRPC6.* J Biol Chem, 2019. **294**(34): p. 12655-12669.
233. Avilés-Vázquez, S., et al., *Global gene expression profiles of hematopoietic stem and progenitor cells from patients with chronic myeloid leukemia: the effect of in vitro culture with or without imatinib.* 2017. **6**(12): p. 2942-2956.
234. Molina, J.R., et al., *An inhibitor of oxidative phosphorylation exploits cancer vulnerability.* 2018. **24**(7): p. 1036-1046.
235. Iwasaki, S., et al., *Migraine-associated vertigo: clinical characteristics of Japanese patients and effect of lomerizine, a calcium channel antagonist.* 2007. **127**(sup559): p. 45-49.
236. Fitzgerald, M., et al., *Secondary retinal ganglion cell death and the neuroprotective effects of the calcium channel blocker lomerizine.* 2009. **50**(11): p. 5456-5462.
237. De Rosa, V., et al., *Coordinate Modulation of Glycolytic Enzymes and OXPHOS by Imatinib in BCR-ABL Driven Chronic Myelogenous Leukemia Cells.* 2019. **20**(13): p. 3134.
238. Wallace, D.C., M.T. Lott, and V. Procaccio, *10 - Mitochondrial Biology and Medicine*, in *Emery and Rimoin's Principles and Practice of Medical Genetics and Genomics (Seventh Edition)*, R.E. Pyeritz, B.R. Korf, and W.W. Grody, Editors. 2019, Academic Press. p. 267-322.
239. Aires, V., et al., *Activation of TRPC6 calcium channels by diacylglycerol (DAG)-containing arachidonic acid: A comparative study with DAG-containing docosahexaenoic acid.* Biochimie, 2007. **89**(8): p. 926-937.
240. Schreur, K.D. and S.J.A.J.o.P.-C.P. Liu, *1, 2-Dioctanoyl-sn-glycerol depresses cardiac L-type Ca2+ current: independent of protein kinase C activation.* 1996. **270**(2): p. C655-C662.
241. Samtleben, S., et al., *Direct imaging of ER calcium with targeted-esterase induced dye loading (TED).* 2013(75): p. e50317.
242. Rutter, G.A. and R. Rizzuto, *Regulation of mitochondrial metabolism by ER Ca2+ release: an intimate connection.* Trends in Biochemical Sciences, 2000. **25**(5): p. 215-221.
243. Henderson, M.J., et al., *A low affinity GCaMP3 variant (GCaMPer) for imaging the endoplasmic reticulum calcium store.* 2015. **10**(10): p. e0139273.
244. Missiaen, L., et al., *2-Aminoethoxydiphenyl borate affects the inositol 1,4,5-trisphosphate receptor, the intracellular Ca2+pump and the non-specific Ca2+leak from the non-mitochondrial Ca2+stores in permeabilized A7r5 cells.* Cell Calcium, 2001. **29**(2): p. 111-116.

245. Maruyama, T., et al., *2APB, 2-aminoethoxydiphenyl borate, a membrane-penetrable modulator of Ins (1, 4, 5) P3-induced Ca2+ release*. 1997. **122**(3): p. 498-505.
246. Rabinovitch, P., et al., *Heterogeneity among T cells in intracellular free calcium responses after mitogen stimulation with PHA or anti-CD3. Simultaneous use of indo-1 and immunofluorescence with flow cytometry*. 1986. **137**(3): p. 952-961.
247. Lu, Z., et al., *Inhibition of autophagy enhances the selective anti-cancer activity of tigecycline to overcome drug resistance in the treatment of chronic myeloid leukemia*. 2017. **36**(1): p. 1-14.
248. Konopleva, M., et al., *Targeting Oxidative Phosphorylation with a Mitochondrial Complex I Inhibitor is limited by Mechanism-based Toxicity*. 2022.
249. Yap, T.A., et al., *Phase I trial of IACS-010759 (IACS), a potent, selective inhibitor of complex I of the mitochondrial electron transport chain, in patients (pts) with advanced solid tumors*. 2019, American Society of Clinical Oncology.
250. Iwamoto, T., et al., *Effects of KB-2796, a new calcium antagonist, and other diphenylpiperazines on [3H]nitrendipine binding*. Jpn J Pharmacol, 1988. **48**(2): p. 241-7.
251. Talati, C. and J.J.C.O.i.H. Pinilla-Ibarz, *Resistance in chronic myeloid leukemia: definitions and novel therapeutic agents*. 2018. **25**(2): p. 154-161.
252. Steegmann, J.L., et al., *European LeukemiaNet recommendations for the management and avoidance of adverse events of treatment in chronic myeloid leukaemia*. Leukemia, 2016. **30**(8): p. 1648-71.
253. Reed, G.A., et al., *A Phase 1 study of intravenous infusions of tigecycline in patients with acute myeloid leukemia*. Cancer Med, 2016. **5**(11): p. 3031-3040.
254. Marroquin, L.D., et al., *Circumventing the Crabtree effect: replacing media glucose with galactose increases susceptibility of HepG2 cells to mitochondrial toxicants*. 2007. **97**(2): p. 539-547.
255. Lagadinou, E.D., et al., *BCL-2 inhibition targets oxidative phosphorylation and selectively eradicates quiescent human leukemia stem cells*. 2013. **12**(3): p. 329-341.
256. Zhong, W., et al., *ORP4L Extracts and Presents PIP2 from Plasma Membrane for PLCβ3 Catalysis: Targeting It Eradicates Leukemia Stem Cells*. 2019. **26**(8): p. 2166-2177. e9.
257. Zhong, W., et al., *ORP4L is essential for T-cell acute lymphoblastic leukemia cell survival*. 2016. **7**(1): p. 1-14.
258. Nie, Y., et al., *Targeting metabolic reprogramming in chronic lymphocytic leukemia*. 2022. **11**(1): p. 1-13.
259. de Beauchamp, L., E. Himonas, and G.V.J.L. Helgason, *Mitochondrial metabolism as a potential therapeutic target in myeloid leukaemia*. 2022. **36**(1): p. 1-12.
260. Gregory, M.A., et al., *Wnt/Ca2+/NFAT signaling maintains survival of Ph+ leukemia cells upon inhibition of Bcr-Abl*. 2010. **18**(1): p. 74-87.
261. Gu, Y., et al., *Aberrant activation of CaMKIIγ accelerates chronic myeloid leukemia blast crisis*. 2016. **30**(6): p. 1282-1289.
262. Gu, Y., et al., *CaMKII γ, a critical regulator of CML stem/progenitor cells, is a target of the natural product berbamine*. 2012. **120**(24): p. 4829-4839.

263. Xu, R., et al., *Berbamine: a novel inhibitor of bcr/abl fusion gene with potent anti-leukemia activity*. 2006. **30**(1): p. 17-23.
264. Luo, J., et al., *6′-Hydroxy Justicidin B Triggers a Critical Imbalance in Ca2+ Homeostasis and Mitochondrion-Dependent Cell Death in Human Leukemia K562 Cells*. 2018. **9**: p. 601.
265. Wang, N., et al., *TWIST1 preserves hematopoietic stem cell function via the CACNA1B/Ca2+/mitochondria axis*. Blood, 2021. **137**(21): p. 2907-2919.
266. Barbosa, C.M.V., et al., *Extracellular annexin-A1 promotes myeloid/granulocytic differentiation of hematopoietic stem/progenitor cells via the Ca2+/MAPK signalling transduction pathway*. Cell Death Discovery, 2019. **5**(1): p. 135.
267. Shao, M., et al., *Inhibition of Calcium Signaling Prevents Exhaustion and Enhances Anti-Leukemia Efficacy of CAR-T Cells via SOCE-Calcineurin-NFAT and Glycolysis Pathways*. 2022. **9**(9): p. 2103508.
268. Uslu, M., E. Albayrak, and F.J.J.o.c.p. Kocabaş, *Temporal modulation of calcium sensing in hematopoietic stem cells is crucial for proper stem cell expansion and engraftment*. 2020. **235**(12): p. 9644-9666.
269. Soboloff, J., et al., *Sensitivity of myeloid leukemia cells to calcium influx blockade: application to bone marrow purging*. 2002. **30**(10): p. 1219-1226.
270. Bosc, C., et al., *Autophagy regulates fatty acid availability for oxidative phosphorylation through mitochondria-endoplasmic reticulum contact sites*. Nature Communications, 2020. **11**(1): p. 4056.
271. Lee, J.-S., et al., *Targeting oxidative phosphorylation reverses drug resistance in cancer cells by blocking autophagy recycling*. 2020. **9**(9): p. 2013.
272. Zhao, H., et al., *MS4A3 promotes differentiation in chronic myeloid leukemia by enhancing common ß-chain cytokine receptor endocytosis*. Blood, 2022. **139**(5): p. 761-778.
273. Bellodi, C., et al., *Targeting autophagy potentiates tyrosine kinase inhibitor-induced cell death in Philadelphia chromosome-positive cells, including primary CML stem cells*. J Clin Invest, 2009. **119**(5): p. 1109-23.